Nonequilibrium Thermodynamic Signatures Of Some Complex Dynamical Systems

Thesis submitted for the degree of
Doctor of Philosophy (Science)
in Physics (Theoretical)

by
Premashis Kumar

Department of Physics
University of Calcutta
2024

Nonequilibrium Thermodynamic Signatures Of Some Complex Dynamical Systems

Abstract

Understanding complex systems' behaviors is crucial in various fields. Chemical reaction networks (CRNs) offer a framework to describe complex systems, further developed into reaction-diffusion systems (RDSs), encompassing spatial and temporal dimensions. This RDS encapsulates exotic behaviors, patterns, and emergent phenomena in real-world complex systems. While research often focuses solely on the dynamical perspectives of these behaviors, understanding the thermodynamic cost of far-from-equilibrium phenomena becomes crucial in practical situations. This thesis sheds light on the connection between the dynamics and thermodynamics of a complex system by exploring the nonequilibrium thermodynamic signatures of different phenomena.

For the deterministic CRNs, we employ a stochastic thermodynamics-motivated nonequilibrium thermodynamic formalism that also leverages the network properties of the CRN. For nonlinear reaction dynamics with the general RDS in the presence of self and cross diffusion, the amplitude equation formalism is employed for the dynamical description near the onset of instability, which makes our approach analytically tractable at the single system level. The dynamic entity is translated into a thermodynamic picture to obtain associated entropy production rate (EPR), nonequilibrium thermodynamic potentials, or nonconservative work.

We analyze the effect of cross-diffusion coefficients and chemostatted species concentration on dynamic and thermodynamic entities by studying Turing-Hopf

overlapping and traveling waves. In this context, our findings uncover a proportional relationship between the total EPR and the global concentration dynamics of the RDS. The complexity of different patterns and the existence of finite boundary effects are evident from the contrasting nature of the thermodynamic potential variations. We further investigate the emergence of a counterintuitive chimera state in a globally coupled chemical system and also identify the equivalence between chimera energetics and the Gabor representation. Extending this study to states around the chimera state, we discover some intriguing resemblances between dynamic and thermodynamic quantities. We additionally explore the interplay between dissipation, thermodynamic potential, and accuracy by implementing this framework in kinetic proofreading networks of core biological events.

This powerful formalism captures arbitrarily intricate dynamics and far-from-equilibrium thermodynamics, both qualitatively and quantitatively. This line of investigation can open avenues for understanding, controlling, comparing, and utilizing complex systems and their behaviors.

List of publications

1. **Premashis Kumar** and Gautam Gangopadhyay. Energetic and entropic cost due to overlapping of Turing-Hopf instabilities in the presence of cross diffusion. Phys. Rev. E, 101:042204, Apr 2020.

2. **Premashis Kumar** and Gautam Gangopadhyay. Nonequilibrium thermodynamics of glycolytic traveling wave: Benjamin-feir instability. Phys. Rev. E, 104:014221, Jul 2021.

3. **Premashis Kumar** and Gautam Gangopadhyay. Nonequilibrium thermodynamic characterization of chimeras in a continuum chemical oscillator system. Phys. Rev. E, 105:034208, Mar 2022.

4. **Premashis Kumar** and Gautam Gangopadhyay. Nonequilibrium thermodynamic signatures of collective dynamical states around chimera in a chemical reaction network. Phys. Rev. E, 108:044218, Oct 2023.

5. **Premashis Kumar**, Kinshuk Banerjee, and Gautam Gangopadhyay. Interplay of energy, dissipation, and error in kinetic proofreading: Control via concentration and binding energy. Physica A, 603:127735, 2022.

6. * **Premashis Kumar** and Gautam Gangopadhyay. Glycolytic wave patterns in a simple reaction-diffusion system with inhomogeneous influx: Dynamic transitions. ChemPhysChem, 24(5):e202200643, 2023. (*Not included in this thesis)

Contents

LIST OF FIGURES

LIST OF TABLES

To the memory of Didibhai, my maternal grandmother, whose unwavering belief in my potential continues to fuel my determination.

Acknowledgments

I express my gratitude to my Ph.D. thesis advisor, Prof. Gautam Gangopadhyay, for introducing me to nonequilibrium thermodynamics and granting me the freedom to explore different research avenues through analytical work. This approach has contributed to my growth as a researcher. I also extend my appreciation to my master's thesis guide, Prof. Manish Dev Shrimali, for introducing me to the world of nonlinearity.

My time at the S.N. Bose National Centre for Basic Sciences (SNBNCBS) was enriching, thanks to the robust research framework and excellent living facilities. Yet, the true highlight was the exceptional company of my colleagues. I am deeply grateful to Tanmoy, Prasun, Krishnendu Sinha, Krishnendu Patra, and Dibyendu for their unwavering support, both academic and personal, throughout my PhD journey. Tanmoy's ability to engage in stimulating discussions, both scientific and casual, proved to be a constant source of intellectual exchange. I thank Prasun for being a reliable source of clarity regarding complex topics. Krishnendu Sinha, with his unique and simplistic approach to explaining intricate topics, was akin to a 'biochemistry Made Easy'. Krishnendu Patra's humor and entertaining nature in the face of adversity were invaluable antidotes to dullness and boredom. Dibyendu emerged as the go-to solution for all my technical and computational issues. Through numerous tea breaks, lunch conversations, sports activities, and shared snacks, I gained a wealth of knowledge and valuable insights from these remarkable individuals. I am also grateful for the company of Debayan, Shobhan, Susmita Changdar, Biswajit Panda, Nur, and Anish since the beginning of my journey at this institute. Their presence and countless casual interactions broadened my perspective and enriched my PhD journey. I am very fortunate to have lots of enthusiastic

junior PhD scholars around me, including Sayan, Samir, Anirban Pal, Anutosh, Riju, Manodip, Shivam Misra, Sayari, Sabuj, Shubhajit, Aniruddha, and Sutanu. I learned many new things from them in the academic field. Special thanks to Sayan for our engaging discussions and all kind gestures. I also acknowledge my lab juniors, Krishanu, Jayarshi, and Pallabi, for their enthusiasm and contributions to the lab environment.

The invaluable learnings I gained from people from my master's days, Sauvik, Apoorv, Pradeep, Bhavana, Vinay, Bidhisha Di, Abhaya, Anjali, Rohit, Surbhi, Tulchi, Abhishek, Gunjan, Sandhya, and Sudipta have shaped me both personally and professionally. I am especially thankful to Sauvik and Apoorv for lending me an ear and keeping my morale high during the lowest points of my Ph.D. journey. I also cherish the enduring friendship with Sauvanik and Shirshendu from my bachelor's days, who have always encouraged me to push my boundaries. My heartfelt appreciation also goes to Musaraf, Atanu, Shibu, Arijit, Sk Suraj, Supriyo, Shubham, Manoj, Tanuj, and many others from those unforgettable school days for the shared laughter that echoed through the years and the enduring friendship that made this journey all the more meaningful.

I am indebted to many terrific teachers, including Shrikanta Mishra, Biplab Mishra, Manoj Kumar, Dhritiman Bagchi, Mansur Rahaman, Biplab Jha, Sarat Kumar, Rajib Kumar, Dr. Girish Tiwary, Dr. Rakesh Kumar, Dr. Rajneesh Kumar, and Dr. Sandip Kumar. Without their guidance and support, I could not have begun this journey.

I am incredibly fortunate to have parents who have supported me through every challenging situation during this journey. My brother, Prince, has been my confidant, with whom I share all my crazy goals, plans, and dreams. In addition to my immediate family, I am fortunate to have a wonderful extended family whose love and affection have made me stronger. I am thankful to all the senior members of my extended family, especially Didibhai, Jethu Baba, Pinaki Kaku, Choto Mama, and Ful Masimoni. Affection and love from my cousins, including, Arnab, Daiya, Puja Didi, Trinath, Riju, Sonai, Soumya, Tanay, and Rik, have been the non-decaying driving force in my oscillating journey. This acknowledgment would be incomplete without mentioning the Nike Training Club app, which helped me sustain my mental and physical fitness.

It is by avoiding the rapid decay into the inert state of 'equilibrium' that an organism appears so enigmatic

- Erwin Schrödinger

1 Introduction

Our universe is home to a vast array of living organisms and nonliving entities whose behaviors, structures, evolution, or collective manifestations appear immensely captivating yet defy straightforward descriptions and predictions. Therefore, these organisms, entities, or their fragments have attracted the attention of researchers from different disciplines, from biology, chemistry, and physics to mathematics, computer science, economics, and beyond. This diverse pursuit necessitates a truly interdisciplinary approach that utilizes various tools, descriptions, and terminologies offered by different domains. By embracing this interdisciplinary lens, it is possible to elucidate those behaviors, structures, etc. in a more general and useful way. By identifying these organisms, entities, or their fractions as complex systems, one can frame the interdisciplinary approach, utilizing the collective wisdom of various fields to convincingly comprehend different aspects of them, as a complex system study.

Complex systems are usually described by multiple components, with intricate dependencies, interactions, feedback loop formation, and competitions amongst their com-

ponents and with their surrounding environment. These characteristics of complex systems lead to rich dynamics and fascinating emergent behavior in the system operating far from equilibrium. Proper modeling and description of these intricate relationships among components can encapsulate spatial[1], temporal[2,3] or spatiotemporal patterns[4,5,6] yielded in animal coat, living tissues[7], cellular rhythms[8], development of an organism[9], natural phenomena[10] and many other situations[11]. In living systems, these patterns play a crucial role in processing and spreading biological information and thus dictate the coordination among diverse phenomena in the system. Dynamical perspectives reveal that these patterns can originate due to various factors. These factors include instabilities, the coexistence of multiple states or pathways, or symmetry-breaking scenarios. These factors can be triggered by specific values of systems' components, initial conditions, or coupling parameters in the case of collective dynamics. This dynamical understanding has fueled extensive research aimed at identifying transitions or bifurcations[10], controlling certain behaviors or precisely selecting a desirable outcome from many possibilities, uncovering the pivotal factors and key interactions behind a complex behavior, or recognizing intricate emergent phenomena. Especially when nonlinearity exists, as is often the case in chemical and biological systems, these studies become not only difficult and exotic but also require accessing a significantly wider range of phenomena and behaviors compared to linear systems. However, capturing the proper dynamic features or gaining dynamic insights might be inadequate or incomplete knowledge in terms of finding proper real-world implications, optimizing the performance and operation, specifying an efficient pathway, or designing experimental settings of an arbitrarily complex system. Indeed, in practical situations, when complex systems operate within a limited-resource environment, the thermodynamic cost of far-from-equilibrium phenomena can set a crucial constraint on the system's performance. For instance, in the biosynthesis process, a trade-off between accuracy and the thermodynamic cost[12] determines the fate of the process. Another example can be the design of metabolic pathways[13], where one should focus both on the amount of biochemical compounds produced in a particular pathway and the thermodynamic cost and feasibility of that

pathway[14,15]. An understanding of both reaction dynamics and thermodynamics is key to the regulation of metabolic pathways, selection between different pathways, or specification of the optimal performance regimes, scenarios, and architecture of the network. Additionally, something that appears trivial in an equilibrium system, can be very tricky in a nonequilibrium environment. For instance, wave number selection of a dynamical behavior within an out-of-equilibrium finite system can be highly non-trivial due to the intricate dependence of the wave number on the system parameter values, boundary conditions, perturbation, and methodologies. Thus, the macroscopic patterns in the concentration dynamics of species can be modulated based on these requirements. In these contexts, unraveling the proper connection between thermodynamic and dynamic entities of a complex system within the nonequilibrium environment is elusive. The systematic nonequilibrium thermodynamic characterization, signatures, and cost of dynamical phenomena in complex systems can shed light on this important avenue. Nevertheless, from a theoretical point of view, it is still challenging to develop a systematic thermodynamic approach to deal with an arbitrary nonequilibrium process and thus extract nonequilibrium thermodynamic signatures of different instabilities and responses within some generic complex systems.

In the thermodynamic picture, a system of interest is often divided into two parts: the 'system' and 'environment', separated by a real or imaginary 'boundary'. 'Systems' often exchange matter and energy with the 'environment' through the 'boundary'. Depending on the type of exchange between 'system' and 'environment', we can identify the following three different classes of systems:

(i) **Isolated system:** No exchange of energy or matter occurs.

(ii) **Closed system:** Only energy exchange is allowed.

(iii) **Open system:** Both energy and matter can be exchanged.

The schematic of these three system types is shown in Fig. 1.1. Among these systems, open systems are most prevalent. All living systems around us, ranging from a single cell to an ecosystem, are described as open systems. In this context, tools like chemical

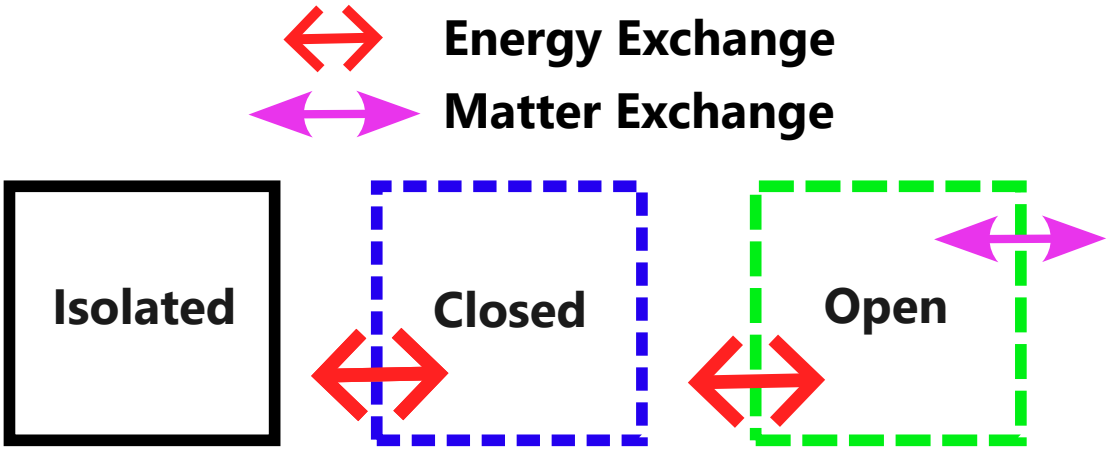

Figure 1.1: Three types of thermodynamic systems based on exchange between 'system' and 'environment': isolated, closed, and open.

reaction networks (CRNs)[16] can be powerful for representing various complex systems. A schematic of an open CRN representation where chemical species are exchanged between the system and reservoirs is illustrated in Fig. 1.2. A CRN can also be described within a closed system framework. However, the ultimate fate of a closed system is the state of equilibrium. So dynamical behaviors in the CRN appear as a transient phenomenon on the way to the system equilibrium. To properly capture the rich dynamics of CRNs, including the possibility of sustained behavior, we need to consider them within the description of open systems. For instance, the Belousov–Zhabotinsky (BZ) reaction[17,11] is a CRN that exhibits oscillatory behavior in the concentrations of its chemical species. As a closed system, this CRN can only produce damped oscillations, whereas an open system description allows the possibility of sustained oscillations. Open CRNs can exhibit a transition to an oscillatory state or spatial pattern-forming state at the expense of dissipation. These self-organized 'ordered' structures are known as dissipative structures[18,19,20].

The CRN representation of the complex system can be further taken to a higher dimension by adding a spatial dimension to the network picture. This representation is generally called a spatially extended system. In the simplest case, this spatial dimension can be a single line. In the presence of spatial coordinates, chemical species associated

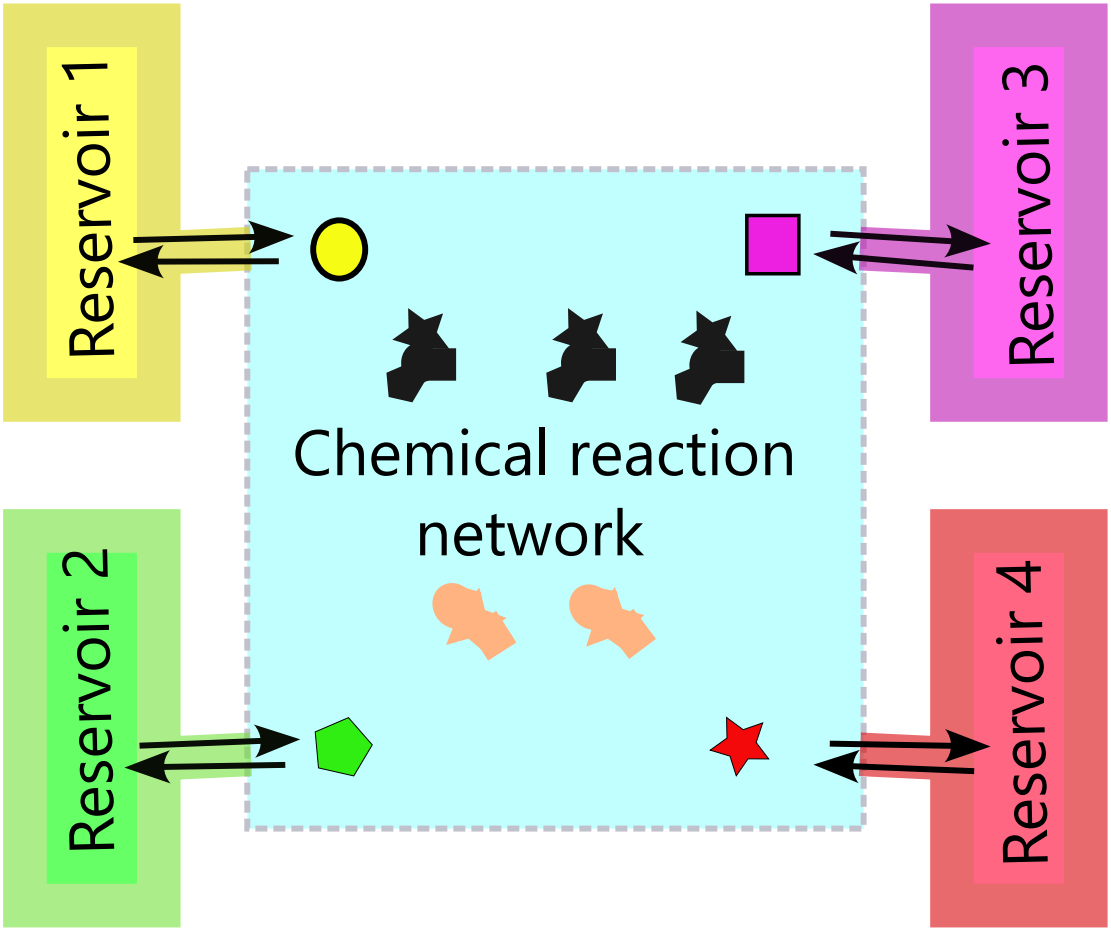

Figure 1.2: Open chemical reaction network representation with multiple reservoirs. Four different species are exchanged between the system and reservoirs. Two other species are also present within the system.

with the reaction network can now diffuse along the length. This kind of modeling of the complex system with the possibility of simultaneous occurrence of reaction and diffusion of species is known as reaction-diffusion system (RDS)[1,21,11,4,7,6]. The reaction rates and diffusion coefficients set the length and time scale of the RDS. Although we can have even one-component RDS[22,23], two or more component RDS with chemical species identified as activators and inhibitors[1,21,7], we can achieve diverse and interesting patterns. Thus, the RDS representation of a complex system is a ubiquitous way to visualize the formation of dissipative structures far from equilibrium, along the spatial and temporal coordinates. Nevertheless, most RDS representations of complex systems

only concern the self-diffusion of a species, and thus cross diffusions[24,20] of species are often ignored. Since the role of cross diffusion in altering the dynamics of biological and chemical systems is still under-investigated, acquiring the influence of cross diffusion on complex system patterns will be very interesting. In the presence of both self and cross diffusion of the species along the spatial coordinate, one can construct a general RDS to showcase the capability of cross diffusion in dictating the dynamic and consequently the thermodynamic fate of the system to some extent. Furthermore, in the coupled RDS, consideration of spatial coordinates in the system dynamics facilitates the generation of a range of collective behaviors along spatial dimensions. Taking various ranges and strengths of coupling environments, one can develop different collective states ranging from coherence and incoherence to counterintuitive chimera state[25,26] and cluster state. By comparing their respective dynamic and thermodynamic signatures, one may understand the basic underlying mechanisms, emergence, and exclusiveness of these collective behaviors.

A standard numerical method of solving RDS is the finite differences method. However, an amplitude equation formalism[4] related to the different instabilities and coupling scenarios in the RDS can be employed to encapsulate the essential nonlinear characteristics near the onset of instabilities. For example, the heuristic complex Ginzburg Landau equation (CGLE)[5,27,28] and the Turing amplitude equation (TAE)[4] can be exploited to capture the salient features of Hopf[10] and Turing pattern[1], respectively. One of the main advantages of amplitude equation formalism is that one can explore the possibility of universality within the spatially extended system. The universality of amplitude equation formalism offers more insights into the dynamic features irrespective of the specific system, and the explicit relation between system parameters and coefficients of the amplitude equation provides flexibility in exploring and predicting the behaviors of a complex system. Moreover, in the presence of multiple instabilities and their interactions within a parameter regime, this formalism allows the simplified investigation of complex systems by focusing on one or two specific instabilities by considering only relevant amplitude equations. In this method, combining amplitude and phase extracted

from the heuristic amplitude description of the RDS with the linearization picture[10] of a nonlinear RDS, one can capture the experimentally measurable entity from the conventional deterministic equations. This formalism can be analytically tractable at a single RDS level. However, for studying collective dynamics, these amplitude equations need to be modified, and in the presence of various coupling scenarios, modern computational techniques like a pseudospectral method with an exponential time differencing algorithm[29] need to be invoked for obtaining the solution from this modified amplitude equation of the system. These modified amplitude equations[30,31] then can aid in obtaining the dynamical entities of collective behaviors like chimera and many other states.

The conventional thermodynamic approach defines entities like entropy, energy, work, and temperature at thermal equilibrium. These entities are associated with the fundamental laws of thermodynamics. The Zeroth law of thermodynamics gives the idea of empirical temperature. While the first law of thermodynamics is essentially the law of conservation of energy in a closed system, the second law of thermodynamics is concerned with entropy. Nevertheless, within the framework of conventional thermodynamics, all transformations are considered to be infinitely slow processes, and thermodynamic description does not involve any time[32]. However, many processes within complex systems occur for a finite time, and so the corresponding change in thermodynamic entities will be related to the time interval. Time was incorporated in the thermodynamic description of the system at nonequilibrium. Especially, in the far-from-equilibrium thermodynamics, time description was associated with different levels from the irreversibility to instabilty[33]. In this thesis, we will employ a particular nonequilibrium thermodynamics framework at the nonequilibrium steady state (NESS) and beyond it. Most importantly, this framework differs from other similar approaches[34] by leveraging the network properties of CRNs[16,35] to construct a nonequilibrium description specifically tailored to deterministic CRN dynamics. Thus, within the nonequilibrium thermodynamic framework mentioned above, one can acquire the central entities of nonequilibrium thermodynamics, like entropy production, nonequilibrium thermo-

dynamic potential, or nonconservative work, from the dynamics of a complex system. Importantly, the reaction driving force for RDS operating far from equilibrium is acquired here directly from the elementary chemical reactions, often including nonlinear autocatalytic reactions, in contrast to linear nonequilibrium thermodynamics where the driving force is linearly connected to the flux via Onsager coefficients[36] near equilibrium.

One should also take care of concepts like state functions and extensive and intensive properties while describing the nonequilibrium thermodynamics of a complex system. At thermodynamic equilibrium, the state of a system is often described by specifying macroscopic state variables, i.e., temperature, volume, pressure, and amount of a specific chemical species. Functions of multiple state variables are regarded as state functions, provided they depend only on the current thermodynamic state of the system. Variables and functions with magnitudes independent of the system size are categorized as intensive properties. Thus, temperature and pressure are intensive properties of the system. On the other hand, properties depending on the system size are called extensive properties. Volume, amount of chemical species, entropy, internal energy, Gibbs free energy, etc. are examples of extensive properties. Some extensive properties quantify conserved entities of thermodynamic processes. While some other extensive properties do not represent conserved entities. Meanwhile, the ratio of two extensive properties, results in an intensive property. So, by dividing entropy or Gibbs free energy by the volume of the system, we can acquire intensive properties, entropy density, or Gibbs free energy density. For nonequilibrium systems, where the concentration of species is known at each point of the system, one can define the densities of thermodynamic entities at those points. This entropy density, or Gibbs free energy density, is often loosely called the entropy and Gibbs free energy of the nonequilibrium systems. Some changes in an extensive property can affect a particular intensive property. By multiplying these two properties, we can obtain the dimension of energy, and these properties are called conjugate properties. Any of these two conjugate properties can be treated as independent state variables of the system. With this foundation, we can now delve into the historical perspective of how the dynamics and thermodynamics of complex systems

have been explored.

1.1 Historical perspective

The discovery and improvement of steam engines fueled the need to understand heat and work, leading to Sadi Carnot's principle of efficiency limitations in 1824[37]. In 1845, J. P. Joule established the equivalence between heat and mechanical effort, contributing to the development of the first Law of Thermodynamics by H. V. Helmholtz in 1847[38]. Recognizing the significance of these ideas, William Thomson (Lord Rayleigh) wrote[39],

> the whole theory of the motive power of heat is founded on ... two ... propositions, due respectively to Joule, and to Carnot and Clausius.

In this regard, he coined the term 'thermo-dynamics' and also proposed a version of the second law. Thomson applied his thermodynamic knowledge to study coupled irreversible processes like thermoelectric phenomena and provided reciprocal relations[40] as conjecture. Another important contribution by Thomson in 1852 was the introduction of the dissipation function, which quantifies the energy loss in the presence of friction force proportional to velocity[41].

In the context of the second law of thermodynamics, Rudolf Clausius laid the groundwork for entropy in the early 1850s[42]. Clausius introduced a notation 'N' to represent the only positive 'uncompensated transformation' in irreversible processes and asserted that 'uncompensated transformations must always be positive '[43]. However, he formally introduced the term 'entropy' in 1865[44]. The Clausius inequility[43], $dS \geq \frac{dQ}{T}$ for an isothermal system at temperature T, recognizes irreversible transformation, where dQ is the exchange of heat between the system and thermal reservoir, and dS is the change in the system entropy. Leveraging these developments, Josiah Willard Gibbs first conceptualized the chemical potential, one of the most fundamental concepts in thermodynamics, while considering a heterogeneous system comprising several homogeneous parts having different substances[45]. Connecting the change in energy of a homogeneous part with the mass changes of substances, Gibbs introduced the definition of the chem-

ical potentials, μ_σ, in 1876. Gibbs also first formulated the basic stability conditions of classical thermodynamics. Around the same time, Ludwig Boltzmann's formulation of H-theorem in the context of gas theory in 1872[46] brought the concept of detailed balance based on the time reversibility of the microscopic equations of motion. Boltzmann further developed these ideas around 1877, solidifying the statistical interpretation of thermodynamics. Austrian chemist Rudolf Wegscheider later exploited the concept of detailed balancing in chemical kinetics and derived the explicit relation of reaction rates under the principle of detailed balance[47].

In equilibrium thermodynamics, a fluctuation could not grow in the presence of the extremum principle of thermodynamic potential. De Donder realized the need to study thermodynamics beyond the equilibrium situation and started working on the thermodynamic basis of chemical reactions. By then, the chemists already introduced the concept of affinity for describing the tendency of chemical species to participate in chemical reactions and form compounds. However, there was a lot of ambiguity regarding the clear notion and definition of affinity. In 1927, De Donder first formulated a proper description and definition of the affinity in chemical reactions based on chemical potential and indicated the connection between chemical affinity and Gibbs free energy[48,20]. In 1931, Lars Onsager explored the near equilibrium situation and formulated reciprocity relations by proving a general linear relation between flux and force[36,49], which is an important breakthrough in formulating linear thermodynamics of irreversible processes. Onsager described the condition of detailed balancing in a chemical single-molecular triangle reaction and showed the analogy between the reciprocal relations and relations obtained under the detailed balance condition[36] near equilibrium. Onsager's work provides a proper connection between detailed balancing conditions at the molecular and macroscopic levels. Then another important development in linear thermodynamics comes in terms of Prigogine's theory of least entropy production[50] which says that time-dependent states have always higher entropy production than the corresponding steady-states near equilibrium.

While Von Bertalanffy made significant advancements in the open system description

of the organisms since 1932, he was skeptical about the proper applicability of thermodynamic laws in the open system[51]. A key development came from Ilya Prigogine, who extended and generalized the second law applicable to the closed system to the open system by incorporating the concept of entropy production associated with irreversible processes[52]. Prigogine further recognized that the thermodynamic behavior could be quite distinct for structures around us and identified far-from-equilibrium situations as the source of this order. In far-from-equilibrium situation, fluctuation may grow significantly, and irreversible processes may result in new spatiotemporal structures which Prigogine tagged as 'dissipative structures'[18,33,53]. Ilya Prigogine utilized this concept of local equilibrium for developing a generalized thermodynamic description in the open system[52]. For the nonequilibrium thermodynamics of complex systems, this local equilibrium often allows the leverage of tools of equilibrium thermodynamics in nonequilibrium situations. The concept of local equilibrium, first introduced by Edward A. Milne in the context of stellar radiation[54], will be a cornerstone of the nonequilibrium thermodynamic description employed in this thesis.

Besides these developments in equilibrium and nonequilibrium thermodynamics, the relationship between information processing and thermodynamics also gained significant attention. A seminal contribution in this area came from James Clerk Maxwell's 1871 thought experiment, which seemingly violated the second law by exploiting the velocities and positions information of the gas particles[55]. Building on this idea, Leo Szilard, in 1929, quantified information processing in terms of work extraction within a single-molecule gas system[56]. Later, Léon Brillouin in 1951 captured the cost of measurement in some particular models[57]. A key principle was established by Rolf Landauer in 1961, who identified a fundamental theoretical minimum energy cost associated with information erasure[58]. Charles H. Bennett further investigated the connection between thermodynamics and information processing, examining the second law's validity in information processing contexts such as logical reversibility, proofreading, and other phenomena[59]. Some recent efforts formulate a proper link between the Landauer principle and the second law of thermodynamics in both quantum and classical regimes[60,61,62,63].

Some key elements of information theory utilized in the context of nonequilibrium thermodynamics of different phenomena in this thesis will now be discussed from a historical perspective. A crucial concept in information theory is the information diagram, introduced by Dennis Gabor in 1946[64]. This diagram utilizes time and frequency coordinates to represent signals, and Gabor formulated an uncertainty relation between a signal's frequency and duration. He also described elementary signals 'which occupy the smallest possible area in the information diagram '[64], now known as Gabor elementary function (GEF). Claude Shannon, in 1948, introduced the 'entropy' in information theory, analogous to the entropy formula of statistical thermodynamics, to measure the uncertainty in a message received through channel[65]. He also denoted this entropy as an H function and this H function can be viewed as a generalization of the H used in Boltzmann's H-theorem. Another key information theory concept, the relative entropy or Kullback-Leibler (KL) divergence was introduced by Solomon Kullback and Richard Leibler in 1951 to quantify the difference between two probability distributions[66].

Now if we focus on the nonequilibrium study's development, particularly Prigogine's study in far-from-equilibrium situations, one can see the chemical reactions result in reaching a 'nonlinear regime' and then bifurcation scenarios lead to dissipative structures. In this aspect, one crucial breakthrough was the empirical report of cyclic color change in a reaction mixture by Boris Belousov around 1960[67]. Then Anatol Zhabotinsky also reconfirmed this chemical oscillation with a detailed study[68]. This reaction mechanism is known as Belousov-Zhabotinsky (BZ) reaction. In the late 1960s, Prigogine and his collaborators at the Université Libre de Bruxelles proposed a simple theoretical chemical reaction model, the Brusselator that can exhibit oscillatory behavior far from equilibrium[18,53] due to Hopf bifurcation. In 1968, E E Sel'kov proposed a simple kinetic model of glycolysis that captured self-oscillatory behavior[69]. Later Irving Epstein and his collaborators formulated systematically the design of oscillatory behaviors in chemical reaction[70,71]. Although Alan Turing had depicted a two-variable reaction-diffusion system (RDS) and formulated a diffusion-driven instability to generate spatial patterns in 1952[1], his work got much attention in the connection of far-from-

equilibrium scenario investigation of chemical systems. The Brusselator reaction scheme was also studied as the RDS, and then Turing patterns besides the oscillatory behavior can also exist[33]. In 1990, Castets et al.[72] reported the first empirical evidence of a Turing pattern in a variant of the chlorite-iodide reaction within open spatial reactors.

Now, investigating dynamical behavior in nonlinear reaction-diffusion systems from an analytical viewpoint is connected with Landau's theory of second-order phase transitions and turbulence[73,74]. In 1950, V. Ginzburg and L. Landau gave the phenomenological equations for describing a superconductor's behavior within a magnetic field near the critical temperature[75]. Then, this Ginzburg-Landau theory is enriched by the work of Abrikosov and Gorkov. Then the complex-amplitude formulation of the nonlinear oscillating system was derived by J. T. Stuart in 1960 in the context of pattern-forming instability[76] and the equation is known as the Stuart–Landau equation. In 1969, A. C. Newell and J. A. Whitehead[77], and L. Segel[78] first derived the real Ginzburg-Landau equation, introducing the concept of a spatially extended system with diffusively coupled oscillators. slow amplitude modulation for the non-oscillatory instabilities in the context of Rayleigh–Bénard convection. For the oscillatory system, in 1971, Newell and Whitehead[79] phenomenologically acquired the first complete form of CGLE, and Stewartson and Stuart[80] derived it. In 1976, to study the propagation of concentration waves, Y. Kuramoto and T. Tsuzuki implemented the CGLE picture in the reaction-diffusion representation of chemical system[81]. In this regard, the finding of chimera state in the collective dynamics of the phase oscillators by Kuramoto et al.[25] is crucial to mention in the light of discussion in this thesis.

Since nonequilibrium thermodynamic study was closely associated with the system of differential equations corresponding to nonlinear chemical kinetics having diverse dynamical behavior, research regarding the analytical understanding of the structure corresponding to the underlying chemical reaction network and their connection to the dynamical behaviors eventually gained much attention. In this regard, R. Aris's work in 1965[82] laid the groundwork for applying algebraic methods to analyze systems of chemical reactions and their structures. Further, Horn et al.[83] and Martin Feinberg[84]

acquired the algebraic nature of the equilibrium conditions and put forward a generalization of detailed balancing, known as complex balancing, within the framework of a deterministic chemical reaction network (CRN). The necessary and sufficient condition for complex balancing analogous to the detailed balancing condition was also determined[85]. Especially, these works established a link between network topology and dynamics by formulating theorems like deficiency zero theorem[85,84] and many more. However, T. L. Hill, in 1966, first exploited the diagrammatic representation of unimolecular systems for calculating steady-state fluxes[86]. He also explored the relation between the fluxes and possible cycles of the basic diagram and extracted the flux-force equations from the diagram approach. J. Schnakenberg then utilized the network representation of the master equation to develop general microscopic and macroscopic theory[87]. The ingredients of nonlinear irreversible thermodynamics, entropy production, and the Glansdorff-Prigogine criterion of stability in terms of generalized flux and force are obtained within the network description of the system.

Later, instead of global balancing like detailed and complex balancing, Katz et al. first used the term local detailed balance[88] while investigating the nonequilibrium steady states of interacting particle systems under an external field. Then, the thermodynamic entities of stochastic systems within the framework of the linear master equation[89] were addressed for systems like CRNs[90,91,92]. In a NESS far from equilibrium, Evans et al. provided a relation regarding the probability of entropy fluctuations[93], known as the fluctuation theorem. Works by Gallavotti and Cohen[94], Kurchan[95], and Spohn[96] further established this fluctuation theorem. C. Jarzynski derived a remarkable relation connecting nonequilibrium work done to equilibrium free energy differences[97], from which G Crooks in the stochastic system found another fluctuation theorem[98]. Building on these fluctuations theorems and thermodynamic approaches of stochastic systems, the modern and consistent stochastic thermodynamic framework[99,100,101,102] was systematically developed for small systems embedded within aqueous solutions for analyzing colloidal systems, biopolymers, molecular motors, and many more. Within the stochastic thermodynamic framework, a constraint on the precision of the system set by the

thermodynamic cost, the thermodynamic uncertainty relation was also formulated[103]. Based on the wisdom of this stochastic thermodynamics and utilizing the topological properties of the CRN, a nonequilibrium thermodynamic formalism[104,105,106] on top of the deterministic dynamics of the CRNs has been recently formulated. This framework was then readily extended to RDS descriptions[107].

1.2 Scope of the thesis

(a) **Nonequilibrium system in isothermal condition:** Nonequilibrium states within the non-isothermal situations have drawn considerable interest with a simple example being a a system in contact with thermal reservoirs of different temperatures. However, this thesis mainly focuses on a nonequilibrium scenario of open isothermal system connected with multiple chemical reservoirs (Fig. 1.2) known as chemostats[104,106]. This nonequilibrium state has CRNs at the heart of it.

(b) **Representing complex systems as CRNs and RDSs:** We begin by representing complex systems as CRNs, which capture their reaction mechanisms. Subsequently, these CRNs are developed into corresponding RDSs, enabling the analysis of their spatiotemporal dynamics within the regime of some well-known interesting phenomena in the system. For example, traveling waves in a simple glycolytic RDS[69].

(c) **Analytical tractability near the onset of instability:** For the dynamical description near the bifurcation point, amplitude equation formalism is employed along with linearization for the general construction of RDS in the presence of self and cross diffusion, making our approach analytically tractable.

(d) **Extracting thermodynamic signatures by dynamical data:** Utilizing the generated dynamical data from the RDS, we systematically extract the thermodynamic costs and signatures associated with various interesting phenomena, such

as Turing-Hopf overlapping, traveling waves, chimera, etc., observed within the system. This method is conducted at both the single-system and collective-system levels.

(e) **Utilization of reaction network properties:** The nonequilibrium thermodynamic framework[104,106,107] considered in this thesis, has leveraged the reaction network structure and properties in a convenient way. In both dynamic and thermodynamic descriptions of the thesis, stoichiometric matrix representation associated with the network is heavily exploited. The transition from a closed system to an open system description can be completely elucidated utilizing these network properties. Besides the nonlinear chemical oscillatory network, this stoichiometric-based picture is also implemented successfully for kinetic proofreading[108] or copolymerization[109] of biochemical systems[110] at the nonequilibrium steady states (NESS).

(f) **Both qualitative and quantitative analysis:** Our chosen formalism is powerful enough to capture intricate dynamics and far-from-equilibrium thermodynamics both qualitatively and quantitatively. However, we emphasize more on the qualitative signatures.

(g) **Broadening the understanding of diverse systems:** Since this CRN and RDS are ubiquitous representations of real-world complex systems, this line of investigation can significantly broaden our understanding of the dynamics and thermodynamics of various phenomena across a wide range of systems. This knowledge can:

- Aid in identifying connections between the studied phenomena and other well-established phenomena.
- Pave the way for discovering purposeful applications of the identified dynamical states.

(h) **Controlling and manipulating systems:** Quantification of the thermodynamic cost of patterns within the RDS framework will aid in controlling and manipulating the efficiency and dissipation of the system far from equilibrium, which ultimately leads to a deeper understanding of the evolution of real-world chemical and biological systems in a larger sense.

(i) **Additional considerations:**

- **Terminology:** Since the thermodynamic investigation is one of the main motives of this thesis, we reserve the term 'equilibrium' in the context of a closed system. For the fixed point of the system, we prefer the term 'steady state'.
- **Weakly nonlinear regime and limitation of linearization:** We often implement the amplitude equation formalism and thus confine ourselves to the weakly nonlinear regime. Besides, the linear stability analysis has its own limitations, as it fails to tell the proper dynamics of a non-hyperbolic fixed point with zero as the real component of the eigenvalue[10].
- **Limited to elementary reactions and mass-action law:** We describe CRNs as collections of elementary reactions obeying the mass-action law. Although a similar thermodynamic framework has also been developed for the CRN comprising of non-elementary reactions and without obligation to follow mass-action law[111], we will not consider such CRN as the model systems in our study.
- **Diffusions obey Fick's law:** All diffusive phenomena, including cross diffusion, incorporated within the RDS description adhere to Fick's law of diffusion. We will elaborate on this further in the next chapter, along with the corresponding expressions.
- **Homogeneous concentration distribution:** This thesis solely considers homogeneous concentration distributions of the chemical species whose concentrations are externally controlled and held at constant levels. Although

inhomogeneous distribution can bring more exotic and intricate situations, like wave direction change, and chaotic or quasiperiodic behavior in the RDS[112], we will stick to the homogeneous distribution.

- **Thermal efficiency:** While we have acquired all the central entities of nonequilibrium thermodynamics, no explicit expression or illustration of thermal efficiency is presented in this thesis.

1.3 Thesis outline

- **Introduction:** This thesis delves into the intriguing intersection of dynamics and thermodynamics of complex systems operating far from equilibrium. The initial chapter lays the groundwork by:
  - Discussing dynamic and thermodynamic perspectives of complex systems and their associated frameworks.
  - Highlighting the principal aims and motivations of the thesis.
  - Providing a historical perspective on the evolution of nonequilibrium thermodynamics, and the CRN framework.
  - Pointing out the limitations and strengths of this thesis work.
- **Theoretical Framework: Chemical reaction network, reaction-diffusion system, and nonequilibrium thermodynamics:** Chapter 2 offers a comprehensive, systematic, and rigorous exploration of:
  - Theoretical foundations underpinning the CRN and RDS dynamics, and nonequilibrium thermodynamics associated with these representations.
  - Detailed derivations and examples related to these concepts.
- **Thermodynamic cost of the overlapping of Turing and Hopf patterns in the presence of cross diffusion:** In chapter 3, we will:

  - Investigate spatiotemporal patterns emerging from the overlapping of Turing and Hopf instabilities in three distinct scenarios.
  - Analyze the relationship between dynamics and thermodynamics associated with these patterns.
  - Emphasize the crucial role of cross diffusion in generating the Turing pattern.

- **Thermodynamics of traveling waves and Benjamin-Feir instability in glycolysis:** In chapter 4, we will:
  - Focus exclusively on the thermodynamic characterization of Hopf instability and traveling waves within a simplified glycolysis RDS in the presence of both cross and self diffusion.
  - Examine amplitude and phase dynamics, alongside wave number selection in glycolytic traveling waves around the Benjamin-Feir instability.
  - Capture the entropic and energetic costs associated with glycolytic patterns.

- **Thermodynamic characterization of chimeras in a coupled continuum system:** In chapter 5, we will:
  - Realize a counterintuitive chimera state using modified amplitude in a globally coupled chemical continuum system.
  - Characterizes this state using the lens of nonequilibrium thermodynamics.
  - Provide the possible guiding role of the information uncertainty principle on the thermodynamic potential related to the state.

- **Collective dynamical states around chimera: thermodynamic signatures:** In chapter 6, we will:
  - Extend the study of the previous chapter by generating various spatiotemporal states surrounding the chimera state within a similar system.

  - Compare the nonequilibrium thermodynamic properties of these diverse states.
  - Uncover some intriguing resemblances between essential dynamic and thermodynamic quantities, irrespective of collective behaviors.

- **Kinetic proofreading: elucidating the interplay among energy, dissipation, and error rate in CRN:** In chapter 7, we will:
  - Analyze kinetic proofreading networks through the CRN-based nonequilibrium thermodynamics framework.
  - Investigates the intricate link between nonequilibrium thermodynamic entities and substrate selection accuracy of the network
  - Identify different discriminatory regimes and introduce a new metric to quantify the overall performance of the network.

- **Conclusions and prospects:** The final chapter will conclude the thesis by summarizing the key findings and outlining potential future research directions based on the presented work.

We do not know what the rules of the game are; all we are allowed to do is to watch the playing. Of course, if we watch long enough, we may eventually catch on to a few of the rules. The rules of the game are what we mean by fundamental physics.

- Richard P. Feynman

2

Theoretical Framework: Chemical reaction network, reaction-diffusion system, and nonequilibrium thermodynamics

2.1 Complexities: Chemical reaction networks and ordinary differential equations

Chemical, mechanical, and biological systems are often described by a set of ordinary differential equations (ODEs)[10]. From this system of ODE, we can acquire crucial information about the system dynamics, ranging from the stability under various situations to the transition possibilities among different states. Given the intricacy of real

systems and the mostly nonlinear nature of ODEs, it is often useful to capture and predict the essential features of complex phenomena in biological and chemical settings by investigating the underlying appropriate chemical reaction networks (CRNs)[16]. The ODE picture and CRN representation are generally connected via mass-action kinetics[83]. Nevertheless, by comprehending the proper correspondence between the CRN and differential equation system, we can incorporate qualitative features of any phenomenon into one of these two descriptions as per our convenience and then map the feature into another one. The association between the solution of ODEs and the structure of the corresponding reaction network can be exploited for investigating complex systems in different settings and fields. In this chapter, we will shed light on the dynamic and thermodynamic frameworks and related elements, tools, and perspectives related to the CRN and corresponding reaction-diffusion system (RDS). These will be relevant for gaining insight into various instabilities, emergent behaviors, and so on in chemical and biological systems.

2.2 Chemical reaction network (CRN) Representation of Complex Systems

2.2.1 Elements of the CRN

A CRN can be fully delineated by the following three sets:

- a set of species (σ)
- a set of complexes ($\mathcal{C}$): Complexes are groups of species and appear on both sides of each reaction arrow as reactants or products.
- a set of reactions (ρ): Reactions, ρ generally indicate reversible reactions. We use '$+$' and '$-$' to separate the forward reaction, '$+\rho$' from the reverse reaction, '$-\rho$'.

One species and complex of CRN can be present in multiple reversible reactions. In this thesis, we consider that reactions of CRN happen within a reactor of a length, l.

Rate constants

The rate constants of forward and reverse directions are independent of chemical species concentrations. They can have temperature dependence according to the Arrhenius equation. However, we would not bother about this temperature dependence as an isothermal condition will be considered throughout this thesis. In a CRN, $k_{+\rho}$ and $k_{-\rho}$ denote the forward and reverse reaction rate constants, respectively, for reaction ρ.

Example of CRN: The following CRN is presented to clarify each element of CRN:

$$\begin{aligned} \rho = 1: \quad & \mathrm{P} + \mathrm{X} \underset{\mathrm{k_{-1}}}{\overset{\mathrm{k_1}}{\rightleftharpoons}} \mathrm{S}, \\ \rho = 2: \quad & \mathrm{X} + \mathrm{Q} \underset{\mathrm{k_{-2}}}{\overset{\mathrm{k_2}}{\rightleftharpoons}} \mathrm{V}. \end{aligned} \tag{2.1}$$

We have five different species, $\{P, X, S, Q, V\}$ and four distinct complexes, $\{\mathcal{C}_1 : P + X, \mathcal{C}_2 : S, \mathcal{C}_3 : X + Q, \mathcal{C}_4 : V\}$. Two forward and two reverse reactions, $\{+1 : P + X \to S, -1 : S \to P + X, +2 : X + Q \to V, -2 : V \to X + Q\}$ connect these complexes and species. $\mathrm{k_1}$ and $\mathrm{k_{-1}}$ are forward and reverse rate constants, respectively, for the reaction pathway $\rho = 1$. Similarly, $\mathrm{k_2}$ and $\mathrm{k_{-2}}$ represent forward and reverse rate constants, respectively, for reaction pathway $\rho = 2$ of the above CRN.

2.2.2 Matrices representation of CRNs

It is often convenient to adapt various matrix representations for investigating CRNs. We can acquire the following three matrix representations for a CRN:

Incidence matrix

In terms of complexes, $\mathcal{C}$, we can represent all the reactions in the chemical reaction network in unimolecular form, $\mathcal{C}_{(\rho)} \underset{\mathrm{k}_{-\rho}}{\overset{\mathrm{k}_\rho}{\rightleftharpoons}} \mathcal{C}_{(-\rho)}$. From this unimolecular representation, we can construct an incidence matrix, $B_\rho^{\mathcal{C}}$, which reveals the connection between

complexes. The incidence matrix can have three different entries. For a particular forward reaction $+\rho$, we have -1 or $+1$ as an entry, depending on whether the complex acts as a reactant complex or product complex, respectively. However, no participation of the complex in that particular forward reaction results in 0 as an entry.

By considering complexes as vertices and reaction pathways as edges, we can have a reaction graph corresponding to CRN. Then, the incidence matrix exhibits an association between the vertices and edges.

Example of incidence matrix: For the CRN in (2.1), we acquire,

$$B_{\rho}^{\mathcal{C}} = \begin{array}{c} \\ P+X \\ S \\ X+Q \\ V \end{array} \begin{array}{c} \begin{array}{cc} \rho=1 & \rho=2 \end{array} \\ \begin{pmatrix} -1 & 0 \\ 1 & 0 \\ 0 & -1 \\ 0 & 1 \end{pmatrix} \end{array}. \tag{2.2}$$

Stoichiometric matrix

An arbitrary CRN can be also represented as, $\sum_{\sigma} v_{+\rho}^{\sigma}\sigma \underset{\mathrm{k}_{-\rho}}{\overset{\mathrm{k}_{\rho}}{\rightleftharpoons}} \sum_{\sigma} v_{-\rho}^{\sigma}\sigma$ where $v_{\pm\rho}^{\sigma}$ are stoichiometric coefficients representing the molecule number of a participating species, σ in ρ reaction. The entries of the stoichiometric matrix are given by $S_{\rho}^{\sigma} = v_{-\rho}^{\sigma} - v_{+\rho}^{\sigma}$ which captures the net number of molecules of species involved in the forward ρ reaction and specifies the network topology. Thus species that participate as a product in the forward ρ reaction will have a positive entry, whereas involvement as a reactant species results in a negative entry in the matrix. The stoichiometric matrix has row and column numbers equal to the number of participating species and reversible reactions, respectively. If species are considered as vertices, and reaction pathways as arcs, then the CRN will have a structure similar to a hypergraph[113].

Example of stoichiometric matrix: For the CRN in (2.1), we obtain,

$$S_\rho^\sigma = \begin{array}{c} \\ P \\ X \\ S \\ Q \\ V \end{array} \begin{array}{c} \begin{array}{cc} \rho=1 & \rho=2 \end{array} \\ \begin{pmatrix} -1 & 0 \\ -1 & -1 \\ 1 & 0 \\ 0 & -1 \\ 0 & 1 \end{pmatrix} \end{array}. \tag{2.3}$$

Stoichiometric cycles: The right null eigenvectors, $\{C^\rho\}$ obtained from the stoichiometic matrix, S_ρ^σ represent the stoichiometric cycles of the CRN[114], i.e., $S_\rho^\sigma C^\rho = 0$ with $C^\rho \in \mathbb{R}^{\rho\times(\rho-\mathbf{w})}, \mathbf{w} = rank(S_\rho^\sigma)$. Entries of $\{C^\rho\}$ can be rescaled to an integer number, and they indicate the number of times each reaction takes place (negative signs mean backward reactions) for a specific transformation, which keeps the concentration of all species unchanged. Meanwhile, S_ρ^σ in (2.3) has no stoichiometric cycle.

Composition matrix

In CRN theory, another crucial matrix representation is the composition matrix, $\Gamma_\mathcal{C}^\sigma$, which reveals the structure of each complex in terms of species of the network. Hence, entries of this matrix are the molecular number of species, σ in complexes, $\mathcal{C}$.

Example of composition matrix: For the network in (2.1), we can express,

$$\Gamma_\mathcal{C}^\sigma = \begin{array}{c} \\ P \\ X \\ S \\ Q \\ V \end{array} \begin{array}{c} \begin{array}{cccc} P+X & S & X+Q & V \end{array} \\ \begin{pmatrix} 1 & 0 & 0 & 0 \\ 1 & 0 & 1 & 0 \\ 0 & 1 & 0 & 0 \\ 0 & 0 & 1 & 0 \\ 0 & 0 & 0 & 1 \end{pmatrix} \end{array}. \tag{2.4}$$

The stoichiometric matrix, S^{σ}_{ρ} can be expressed as a product of composition matrix, $\Gamma^{\sigma}_{\mathcal{C}}$ and incidence matrix, $B^{\mathcal{C}}_{\rho}$, of the CRN, $S^{\sigma}_{\rho} = \Gamma^{\sigma}_{\mathcal{C}} B^{\mathcal{C}}_{\rho}$. We will emphasize the stoichiometric matrix and provide more examples of it in upcoming sections as it is an integral element of dynamic and thermodynamic descriptions provided in this thesis.

2.2.3 Classification of species: Intermediate and chemostatted

The chemical species of a CRN can separated into the following two disjoint sets:

- **Intermediate species, I:** Chemical species having dynamic concentrations over the time of interest are the elements of the set, intermediate species, I.

- **Chemostatted species, C:** The rest of the species with constant concentration belong to the set of chemostatted species, C.

The concentration of all chemical species in the network thus can be represented as $z_{\sigma} = [z_I, z_C]$. Concentrations of chemostatted species can be controlled externally by using relevant chemical reservoirs known as chemostats[104,115,106] (the term 'chemiostats'[116] is also used in literature). The procedure of maintaining the fixed concentration of chemostatted species by allowing the exchange of matter between the system and chemostats is called chemostatting. This chemostatting can be achieved by the various direct (via some external reactions) and indirect (semipermeable membranes) controls.

Example: For a CRN, $\rho = 1 : \mathrm{X{+}P} \underset{\mathrm{k_{-1}}}{\overset{\mathrm{k_1}}{\rightleftharpoons}} 2\,\mathrm{Y}$, the species P can be identified as chemostatted species, and X and Y belong to the intermediate species set.

It is possible to modify the rate constant k_1 into the pseudo-first-order rate constant[117,118] by absorbing the chemostatted species concentration into the rate constant, $k_1{}' = k_1 p$. Then, the reaction network becomes $\rho = 1 : \mathrm{X} \underset{\mathrm{k_{-1}}}{\overset{\mathrm{k_1 p}}{\rightleftharpoons}} 2\,\mathrm{Y}$. We will discuss pseudo-first-order rate constants more in the later chapter on the kinetic proofreading.

2.2.4 CRN description in closed and open reactor

We discussed in the chapter 1 that a closed system does not exchange matter with the environment, whereas an open system does. By establishing the chemostatting in the system, we can go from a closed system to an open system description. In a closed reactor, compositional changes in chemical species occur only due to the chemical reactions within the reactor. Incorporating 'pseudo-reactions' into the chemical reactions picture of the closed reactor, we obtain the corresponding open reactor with chemostatting.

Example: A CRN in a closed reactor, $\rho = 1 : \mathrm{X} \underset{\mathrm{k_{-1}}}{\overset{\mathrm{k_1}}{\rightleftharpoons}} {}_2\mathrm{Y}$ is modified by two additional 'pseudo-reactions' to capture the dynamics in an open reactor, $\rho = 1 : \mathrm{X} \underset{\mathrm{k_{-1}}}{\overset{\mathrm{k_1}}{\rightleftharpoons}} 2\mathrm{Y}$; $\rho = 2 : 0 \underset{\mathrm{k_{-2}}}{\overset{\mathrm{k_2}}{\rightleftharpoons}} \mathrm{X}$; $\rho = 3 : \mathrm{Y} \underset{\mathrm{k_{-3}}}{\overset{\mathrm{k_3}}{\rightleftharpoons}} 0$. 0 is the zero complex.

2.2.5 Dynamics of CRN and rate equations

The dynamics of the CRN can be represented by the reaction rates, and these reaction rates follow the mass-action kinetics[83,16]. The reactions, ρ, are here considered to be elementary steps, with the rate of the reaction being connected to the stoichiometry. For a particular reaction pathway, ρ, directed concentration flux is given by

$$j_{\pm\rho} = k_{\pm\rho} \prod_{\sigma} z_{\sigma}^{v_{\pm\rho}^{\sigma}}, \tag{2.5}$$

with '$+$' and '$-$' label denoting the forward and backward reaction, respectively. Net reaction fluxes or currents of reversible chemical reactions are given as the difference between forward and reverse fluxes of reactions:

$$j_{\rho} = j_{+\rho} - j_{-\rho}. \tag{2.6}$$

Example of reaction flux: For a simple elementary reaction, $\rho = 1 : \mathrm{X{+}P} \underset{\mathrm{k_{-1}}}{\overset{\mathrm{k_1}}{\rightleftharpoons}} 2\,\mathrm{Y}$, $j_{+1} = \mathrm{k_1} xp$, and $j_{-1} = \mathrm{k_{-1}} y^2$ according to (2.5). Here, $x = [X]$, $p = [P]$, and $y = [Y]$,

denote concentrations of species.

Finally, the concentration dynamics of the species, σ of the CRN read,

$$\dot{z_\sigma} = \sum_\rho S_\rho^\sigma j_\rho + \delta_\sigma^C \mathcal{J}_C, \tag{2.7}$$

with δ_σ^C being the Kronecker delta and $\mathcal{J}_C$ being the external flux of the chemostatted species only. Thus, we obtain a differential equation for a general CRN. For a closed system, no external flux exists between the system and environment, and the rate equation is reduced to $\dot{z_\sigma} = \sum_\rho S_\rho^\sigma j_\rho$. If we consider the stoichiometric matrix as a discrete Laplacian operator, this $\dot{z_\sigma} = \sum_\rho S_\rho^\sigma j_\rho$ have the form of the continuity equation.

Steady state The steady state corresponding to the CRN dynamics can be obtained by setting $\dot{z_\sigma} = 0 \implies \sum_\rho S_\rho^\sigma j_\rho + \delta_\sigma^C \mathcal{J}_C = 0$. For the closed system this condition is modified to $\sum_\rho S_\rho^\sigma j_\rho = 0$. Using the relation, we acquire the steady state concentrations as $z_{\sigma,0}$. In general, a steady state does not demand j_ρ and J_C to be zero.

2.2.6 Detailed balance in CRN dynamics

A state of CRN will be detailed-balanced if all net current of elementary chemical reaction obtained by Eq. (2.6) individually vanishes, i.e., $j_\rho = 0$ for all ρ. In an open CRN, external fluxes, $\mathcal{J}_C = 0$ at equilibrium state. When detailed balancing is acquired at the steady state of CRN, the system will be at equilibrium state[35], and the equilibrium state depends on the stoichiometric number of the reaction[20].

Steady state + Detailed Balance ⇒ Equilibrium

.

The condition $j_\rho = 0$ for each ρ leads to the, $k_{+\rho} \prod_\sigma (z_\sigma^{eq})^{v_{+\rho}^\sigma} = k_{-\rho} \prod_\sigma (z_\sigma^{eq})^{v_{-\rho}^\sigma}$ from Eq. (2.5) and results in the definition of the equilibrium rate constant as,

$$k_{eq} = \frac{k_{+\rho}}{k_{-\rho}} = \prod_\sigma (z_\sigma^{eq})^{S_\rho^\sigma}. \tag{2.8}$$

A steady state with nonzero fluxes and broken detailed balance is called a nonequilibrium steady state (NESS)[117,118].

Example of detailed balance: We consider the following cyclic CRN presenting interconversion between three isomers X, Y, and Z,

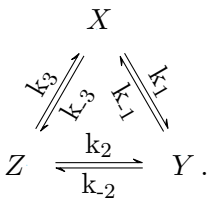

(2.9)

If the system in Eq. (2.9) is detailed balance, then leveraging Eq. (2.8), we find the following relations corresponding to three elementary reaction steps, $\frac{\mathrm{k}_1}{\mathrm{k}_{-1}} = \frac{y^{eq}}{x^{eq}}$; $\frac{\mathrm{k}_2}{\mathrm{k}_{-2}} = \frac{y^{eq}}{z^{eq}}$ and $\frac{\mathrm{k}_3}{\mathrm{k}_{-3}} = \frac{x^{eq}}{z^{eq}}$ (eq denotes equilibrium). From these three relations, we can assert that rate constants of this system need to obey the criteria, $\mathrm{k}_1\mathrm{k}_2\mathrm{k}_3 = \mathrm{k}_{-1}\mathrm{k}_{-2}\mathrm{k}_{-3}$ for equilibrium. Later, in the chapter on kinetic proofreading of this thesis, we will see a similar restriction posed by the detailed balance in the double-cyclic network.

A more general state of the CRN than the detailed balancing also exists and is called the complex balanced state[83]. A detailed balanced state of the CRN is complex-balanced, but the converse is not true in general.

2.2.7 Conservation laws of CRN

Now, we will discuss one of the most crucial concepts leveraged in this thesis to formulate the dynamic and thermodynamic pictures of the complex system under a nonequilibrium environment, and the topic is conservation laws. In the CRN, there exists a set of conservation laws[119] representing mass conservation. Identifying these conservation laws is crucial for a proper understanding of the system. The conservation matrix is referred to as the left null space of the stoichiometric matrix, $l^{\lambda}_{\sigma} S^{\sigma}_{\rho} = 0$, with $l^{\lambda}_{\sigma} \in \mathbb{R}^{(\sigma - \mathbf{w}) \times \sigma}, \mathbf{w} = rank(S^{\sigma}_{\rho})$. This conservation matrix is not unique for a CRN. Vectors

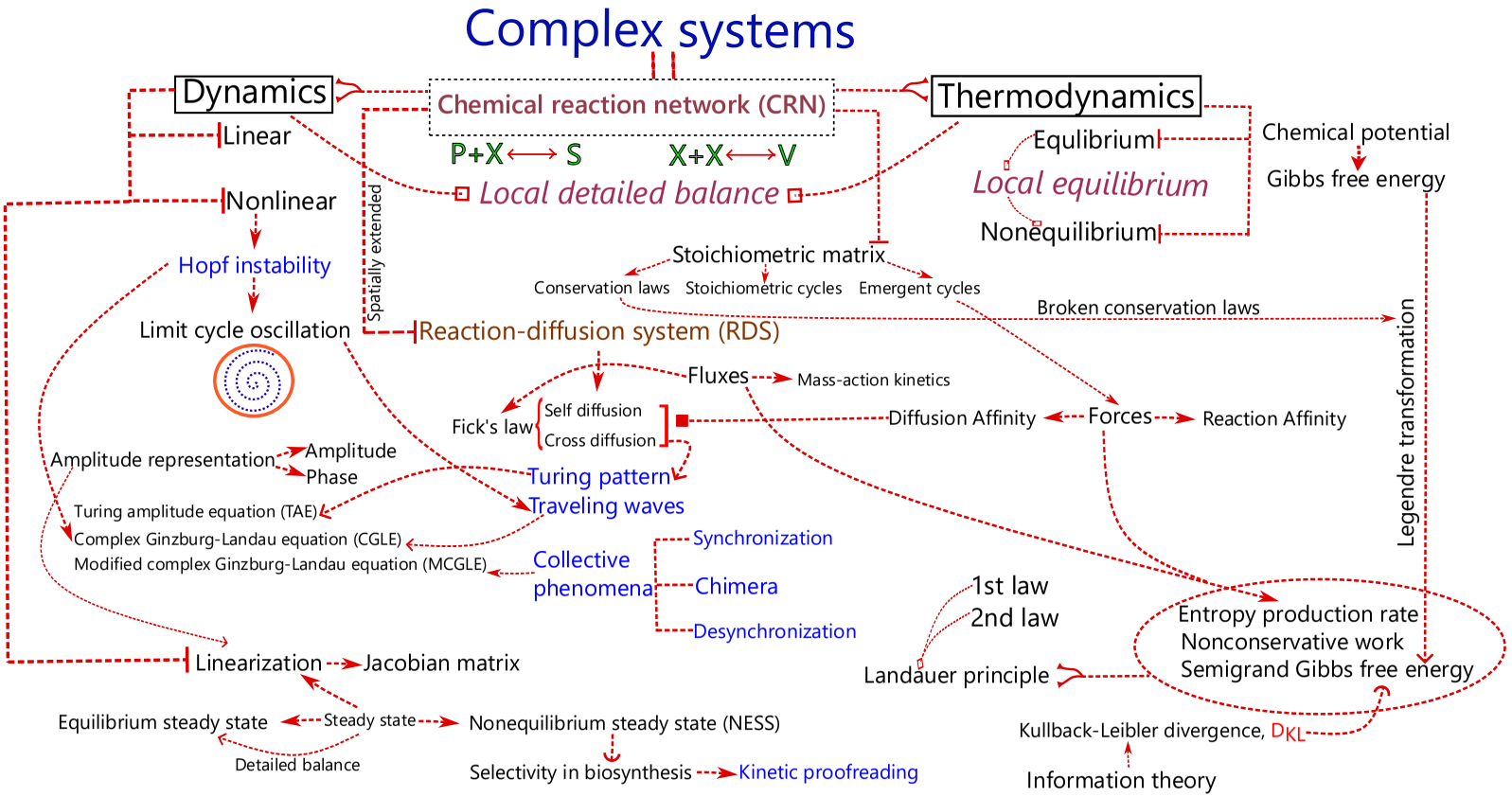

Figure 2.1: Overview of the elements of complex dynamical system and relevant nonequilibrium thermodynamics

corresponding to the conservation matrix are known as the conservation laws,

$$\sum_{\sigma} l_{\sigma}^{\lambda} S_{\rho}^{\sigma} = 0. \tag{2.10}$$

These conservation laws represent a conserved group of atoms known as moieties[120].

Example of conservation laws: From stoichiometric matrix (2.3), we obtain a 3×5 conservation matrix, and the following are conservation laws for the closed CRN (2.1),

$$l_{\sigma}^{\lambda=1} = \begin{array}{c} \begin{matrix} P & X & S & Q & V \end{matrix} \\ \begin{pmatrix} 1 & 0 & 1 & 0 & 0 \end{pmatrix} \end{array},$$

$$l_{\sigma}^{\lambda=2} = \begin{array}{c} \begin{matrix} P & X & S & Q & V \end{matrix} \\ \begin{pmatrix} 1 & -1 & 0 & 1 & 0 \end{pmatrix} \end{array},$$

and

$$l_{\sigma}^{\lambda=3} = \begin{array}{c} \begin{matrix} P & X & S & Q & V \end{matrix} \\ \begin{pmatrix} -1 & 1 & 0 & 0 & 1 \end{pmatrix} \end{array}.$$

Components

Using the conservation law, we can further obtain a globally conserved crucial quantity of a closed system known as the components[119]. Components can be expressed as, $L_{\lambda} = \sum_{\sigma} l_{\sigma}^{\lambda} z_{\sigma}$, where z_{σ} is the concentration of species, σ. The number of components in a closed system is unique and is given by the difference between the number of species and independent reactions in the CRN. The conservation matrix transforms species into components. Despite the number of species changes with reactions, components remain intact along reactions. Thus, for the closed system, we can write $\frac{d}{dt} L_{\lambda} = \sum_{\sigma} l_{\sigma}^{\lambda} \frac{dz_{\sigma}}{dt} = \sum_{\sigma} l_{\sigma}^{\lambda} S_{\rho}^{\sigma} j_{\rho} = 0$ (using the definition of conservation laws).

Example of components: For the CRN in (2.1), we have the following three components for the closed system, $L_1 = p + s$, $L_2 = p - x + q$ and $L_3 = -p + x + v$. These components capture concentrations of the moieties in the network.

2.2.8 Broken conservation laws in open system

In an open CRN, conservation laws play a crucial role in the construction of a proper nonequilibrium thermodynamic potential[104,106,107]. When a closed system is opened by attaching chemostats into the system, the relevant stoichiometric matrix of the CRN can be separated into two different parts: S_ρ^I associated with intermediate species and S_ρ^C related to chemostatted species. Thus, the general rate equation in Eq. (2.7) becomes

$$\begin{aligned} \dot{z_I} &= \sum_\rho S_\rho^I j_\rho \\ \dot{z_C} &= \sum_\rho S_\rho^C j_\rho + \mathcal{J}_C. \end{aligned} \tag{2.11}$$

Here, we do not consider the chemostatted species to be dynamic, and their concentrations are only controlled by the exchange of species between the system and chemostats.

Now, due to the split of the stoichiometric matrix, conservation laws of the system can be broken, and corresponding components no longer remain the globally conserved entity in the open system. These conservation laws are called broken conservation laws, $l_\sigma^{\lambda_b}$ and corresponding components are broken components, $L_{\lambda_b} = \sum_\sigma l_\sigma^{\lambda_b} z_\sigma$. In the open system, some conservation laws of the closed system can remain intact, and those conservation laws are identified as unbroken conservation laws. Unbroken conservation laws have null entries corresponding to the chemostatted species. Components corresponding to the unbroken conservation laws, L_{λ_u}, remain conserved entities in the open system. Therefore, the conservation laws in an open system can be specified more generally as

$$\sum_I l_I^\lambda S_\rho^I + \sum_C l_C^\lambda S_\rho^C = 0 \begin{cases} l_I^{\lambda_b} S_\rho^I \neq 0 & \text{broken CL,} \\ l_I^{\lambda_u} S_\rho^I = 0 & \text{unbroken CL} \end{cases} \tag{2.12}$$

where labels u and b stand for 'unbroken' and 'broken', respectively, and $l^{\lambda} = l^{\lambda_b} \bigcup l^{\lambda_u}$. We will show later in this chapter that Brusselator CRN admits two conservation laws, and when the system is opened by chemostatting, both conservation laws are broken.

Subsets of chemostatted species

Based on the role in breaking the conservation laws, we can disjoin the set of chemostatted species, C into two subsets, $C = C_b \bigcup C_u$. The minimal subset of chemostatted species, C_b (potential species), contains elements involved in breaking conservation laws. Therefore, the number of broken conservation laws is equal to the number of elements of the subset, C_b. The rest of the chemostatted species belong to the subset, C_u (force species), and elements of this subset do not break any conservation laws. By identifying the broken and unbroken conservation laws and corresponding chemostatted species, we can gain insight into mechanisms that keep the open system out of equilibrium.

By putting the entries of the broken conservation laws associated with the subset of chemostatted species, C_b, i.e., $l^{\lambda_b}_{C_b}$, we can generate a square and nonsingular matrix, $l^{\lambda_b}_{C_b}$. For instance, in the previous examples of conservation laws, if we consider that species, S, Q, and V belong to the subset, C_b, then we can represent the matrix, $l^{\lambda_b}_{C_b}$ as $\begin{pmatrix} 1 & 0 & 0 \\ 0 & 1 & 0 \\ 0 & 0 & 1 \end{pmatrix}$. We will see later that the broken conservation laws and related chemostatted species are essential for constructing the thermodynamic potential of the open RDS.

Emergent cycles

Another property related to the chemostatting of a closed system is the emergent cycle, which is a topological feature depending only on the number of chemostatted species[104,106]. These emergent cycles are linearly independent right null eigenvector of the stoichiometric matrix of the intermediate species, i.e., $S^I_\rho c^\rho_e = 0$. However, these eigenvectors are not right null eigenvectors of S^C_ρ, i.e., $S^C_\rho c^\rho_e \neq 0$, leading these emergent cycles to be linearly independent of the stoichiometric cycles. Similar to the stoichiomet-

ric cycles, entries of the emergent cycle also represent the number of times individual reaction happens. Along this emergent cycle, reactions keep the internal species constant while changing the concentration of chemostatted species. However, this concentration change will be compensated immediately due to the external chemostatting.

The number of chemostatted species is equal to the sum of the number of broken conservation laws and the number of emergent cycles[104], $\#C = \#l^{\lambda_b} + \#c_e^{\rho}$. However, it is worth noting that the first chemostatting species always breaks the conservation law as mass conservation is broken. Therefore, for an open CRN with one chemostatted species, we have, $\#C = \#l^{\lambda_b}$, implying no emergent cycle exists. These open CRNs with no emergent cycle are called unconditionally detailed balanced[106].

Example of conservation laws, and emergent cycle in MM CRN: The scheme of general Michaelis–Menten (MM) kinetics[121] for capturing the dynamics of enzyme-catalyzed reactions, can be represented via the following CRN,

$$\begin{aligned} \rho = 1: \quad & \mathrm{E} + \mathrm{S} \underset{\mathrm{k_{-1}}}{\overset{\mathrm{k_1}}{\rightleftharpoons}} \mathrm{ES}, \\ \rho = 2: \quad & \mathrm{ES} \underset{\mathrm{k_{-2}}}{\overset{\mathrm{k_2}}{\rightleftharpoons}} \mathrm{E{+}P}, \end{aligned} \tag{2.13}$$

where E, ES belong to the set of intermediate species, I, and $S, P \in C$ are regarded as chemostatted species. This MM CRN admits two conservation laws,

$$l_\sigma^{\lambda=1} = \begin{matrix} E & ES & S & P \end{matrix} \begin{pmatrix} 1 & 1 & 0 & 0 \end{pmatrix},$$

and

$$l_\sigma^{\lambda=2} = \begin{matrix} E & ES & S & P \end{matrix} \begin{pmatrix} -1 & 0 & 1 & 1 \end{pmatrix}.$$

When this closed CRN is opened by chemostatting, the conservation law, $l_\sigma^{\lambda=1}$, remains intact, while the conservation law $l_\sigma^{\lambda=2}$ gets broken. So $l_\sigma^{\lambda=1}$ is unbroken conservation law, and the corresponding component, $L_1 = e+es$, remains conserved in the open CRN of the MM. Whereas, $l_\sigma^{\lambda=2}$ will be broken by either, S or P. Here, we consider that S breaks the conservation law, and thus S belongs to the subset, C_b, and the species P includes in the subset, C_u. This P species is associated with the emergent cycle,

$$c_1 = \begin{matrix} 1 \\ 2 \end{matrix} \begin{pmatrix} 1 \\ 1 \end{pmatrix}.$$

2.2.9 Brusselator CRN and its network elements

We would conclude this section by providing CRN properties of the Brusselator[18,53], a minimal abstract model. Throughout this thesis, we often employ this model to illustrate different spatial, spatiotemporal, and collective behaviors. Therefore, it is crucial to present properties of the Brusselator CRN for future convenience.

Reversible Brusselator CRN

The following four elementary chemical reactions represent the reversible Brusselator,

$$\begin{aligned}
\rho = 1: &\quad \mathrm{A} \underset{\mathrm{k_{-1}}}{\overset{\mathrm{k_1}}{\rightleftharpoons}} \mathrm{X} \\
\rho = 2: &\quad \mathrm{B} + \mathrm{X} \underset{\mathrm{k_{-2}}}{\overset{\mathrm{k_2}}{\rightleftharpoons}} \mathrm{Y} + \mathrm{D} \\
\rho = 3: &\quad 2\,\mathrm{X} + \mathrm{Y} \underset{\mathrm{k_{-3}}}{\overset{\mathrm{k_3}}{\rightleftharpoons}} 3\mathrm{X} \qquad \text{(Autocatalytic)} \\
\rho = 4: &\quad \mathrm{X} \underset{\mathrm{k_{-4}}}{\overset{\mathrm{k_4}}{\rightleftharpoons}} \mathrm{E},
\end{aligned} \tag{2.14}$$

where $\{X, Y\} \in I$ are two intermediate species, and $\{A, B, D, E\} \in C$ are chemostatted species. Further, we recognize X as the activator and Y as the inhibitor.

Stoichiometric matrix of the Brusselator

From the CRN in (2.14), we acquire the stoichiometric matrix, S_ρ^σ as,

$$S_\rho^\sigma = \begin{array}{c} \\ X \\ Y \\ A \\ B \\ D \\ E \end{array} \begin{array}{c} \begin{array}{cccc} R_1 & R_2 & R_3 & R_4 \end{array} \\ \begin{pmatrix} 1 & -1 & 1 & -1 \\ 0 & 1 & -1 & 0 \\ -1 & 0 & 0 & 0 \\ 0 & -1 & 0 & 0 \\ 0 & 1 & 0 & 0 \\ 0 & 0 & 0 & 1 \end{pmatrix} \end{array}. \tag{2.15}$$

When the Brusselator CRN is opened by chemostatting, S_ρ^σ splits into the following parts,

$$S_\rho^I = \begin{array}{c} \\ X \\ Y \end{array} \begin{array}{c} \begin{array}{cccc} R_1 & R_2 & R_3 & R_4 \end{array} \\ \begin{pmatrix} 1 & -1 & 1 & -1 \\ 0 & 1 & -1 & 0 \end{pmatrix} \end{array} \tag{2.16}$$

, and

$$S_\rho^C = \begin{array}{c} \\ A \\ B \\ D \\ E \end{array} \begin{array}{c} \begin{array}{cccc} R_1 & R_2 & R_3 & R_4 \end{array} \\ \begin{pmatrix} -1 & 0 & 0 & 0 \\ 0 & -1 & 0 & 0 \\ 0 & 1 & 0 & 0 \\ 0 & 0 & 0 & 1 \end{pmatrix} \end{array}. \tag{2.17}$$

2.2.10 Brusselator conservation laws and components

The closed Brusselator network in Eq. (2.14) admits following two conservation laws,

$$l_{\sigma}^{\lambda=1} = \begin{array}{c} \begin{matrix} X & Y & A & B & D & E \end{matrix} \\ \begin{pmatrix} 1 & 1 & 1 & 0 & 0 & 1 \end{pmatrix} \end{array}$$

, and

$$l_{\sigma}^{\lambda=2} = \begin{array}{c} \begin{matrix} X & Y & A & B & D & E \end{matrix} \\ \begin{pmatrix} 0 & 0 & 0 & 1 & 1 & 0 \end{pmatrix} \end{array}.$$

Therefore, the corresponding components of the closed Brusselator CRN are $L_1 = x+y+a+e$ and $L_2 = b+d$. For the Brusselator CRN, we can select any of these combinations $(A, B), (A, D), (E, B)$, and (E, D) from the set of chemostatted species, C and that will break both of the conservation laws. Here, we have considered that the combination, (A, B) belongs to the subset, C_b. Therefore, we can write the square and nonsingular matrix, $l_{C_b}^{\lambda_b}$ for the Brusselator as, $l_{C_b}^{\lambda_b} = \begin{pmatrix} 1 & 0 \\ 0 & 1 \end{pmatrix}$.

In this thesis, we also implement a simple kinetic model proposed by E. E. Selkov for describing the dynamics of glycolysis[69]. We will discuss this model and its CRN representation in a later chapter.

2.3 Reaction dynamics and reaction-diffusion representation

2.3.1 Autocatalytic reactions: Feedback in CRN

A CRN often contains feedback with a product of one reaction step that can modify the other reaction steps of the network by activating or inhibiting them. Feedback is essential for having intricate temporal and spatial behavior in chemical and biological systems. In the context of chemical reactions, autocatalysis is an important instance of positive feedback that exists in most chemical oscillatory systems. According to

IUPAC[122], an autocatalytic reaction can be defined as, "A chemical reaction in which a product (or a reaction intermediate) also functions as a catalyst." In the following discussion, we will present some simple examples of autocatalytic reactions in CRN and interesting dynamic behaviors in those systems.

2.3.2 Two variable reaction dynamics

For exploring the chemical dynamics of a CRN with two intermediate species, we can categorize these two intermediate species into activators and inhibitors. Let us consider that the concentrations of activator, X, and inhibitor, Y, are represented by variables x and y, respectively. In the absence of any diffusion, concentration dynamics can be captured from the reactions of the system as

$$\frac{\partial x}{\partial t} = f(x, y), \tag{2.18a}$$

$$\frac{\partial y}{\partial t} = g(x, y), \tag{2.18b}$$

where f and g contain reaction rate expressions and are generally nonlinear. This system can reach its steady state when the concentrations of species become invariant with time, i.e., $f = 0$ and $g = 0$ simultaneously occur. Solving equations $f = 0$ and $g = 0$, we can determine the steady state of the system as (x_0, y_0). The stability of a particular steady state of the system can be checked by linearizing the steady state. In the following part, we will illustrate the dynamics of two-variable autocatalytic CRN.

A two-variable system with autocatalysis: Lotka's scheme

Lotka[123] hypothesized a minimal CRN comprised of three chemical reactions capable of generating permanent oscillations in chemical and biological systems. This CRN describes the transformation of chemical species P into species Q via two intermediate chemical species X and Y. Here, we consider the following reversible version of Lotka's

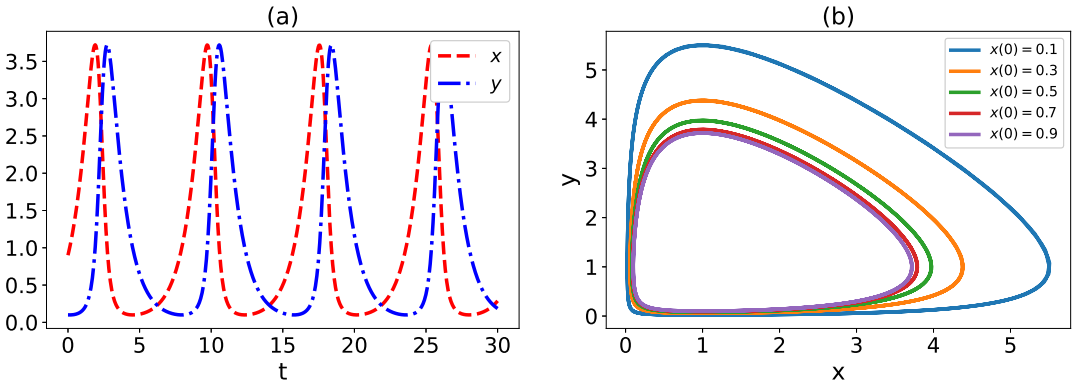

Figure 2.2: (a) Both x and y demonstrate periodic behavior in time. We have used all forward reaction rates equal to 1, i.e., $k_\rho = 1$, and reverse reaction rates are very small in comparison to forward ones, i.e., $k_{-\rho} = 10^{-5}$. Other parameters are $p = 1$, and $q = 1$ and initial condition is $[x(0) = 0.90, y(0) = 0.10]$. For the numerical integration, the time steps size is $\Delta t = 0.05$ (b) We obtain five cycles in the $x - y$ phase plane of the system corresponding to five different initial values of x, between $x(0) = 0.10$ and $x(0) = 0.90$ with an increment of 0.20 at each case. The initial value of y is fixed at $y(0) = 0.10$.

reaction scheme for thermodynamic consistency

$$\begin{aligned}
\rho = 1: &\quad \mathrm{P} + \mathrm{X} \underset{\mathrm{k_{-1}}}{\overset{\mathrm{k_1}}{\rightleftharpoons}} 2\mathrm{X}, \\
\rho = 2: &\quad \mathrm{X} + \mathrm{Y} \underset{\mathrm{k_{-2}}}{\overset{\mathrm{k_2}}{\rightleftharpoons}} 2\mathrm{Y}, \\
\rho = 3: &\quad \mathrm{Y} \underset{\mathrm{k_{-3}}}{\overset{\mathrm{k_3}}{\rightleftharpoons}} \mathrm{Q},
\end{aligned} \tag{2.19}$$

where the first two reactions are quadratic autocatalytic. The system dynamics of 2.19 evolves according to the rate of change of intermediate species concentration as,

$$\begin{aligned}
\dot{x} &= \mathrm{k_1} p x - \mathrm{k_{-1}} x^2 - \mathrm{k_2} x y + \mathrm{k_{-2}} y^2, \\
\dot{y} &= \mathrm{k_2} x y - \mathrm{k_{-2}} y^2 - \mathrm{k_3} y + \mathrm{k_{-3}} q,
\end{aligned} \tag{2.20}$$

where y and q are the concentration of species Y and Q, respectively.

The x and y dynamics illustrate periodic behavior with different phases along the time

coordinate in Fig. 2.2 (a). From the phase portrait in Fig. 2.2 (a), we observe multiple cycles corresponding to the different initial concentrations of species. This existence of the continuous family of stable cycles is structurally unstable and makes this scheme unrealistic[124,10]. In the illustrations of Fig. 2.2, we consider that reverse reaction rates are negligible in comparison to the forward reaction rates, $\mathrm{k}_\rho = 1 \gg \mathrm{k}_{-\rho} = 10^{-5}$. Under this limit, and proper consideration of the nondimensional variables, 2.20 can be reduced to a form known as the Lotka-Volterra model for predator-prey interactions[125].

Another two-variable autocatalytic CRN: limit cycle

Another important and often studied two-variable autocatalytic CRN in the isothermal CSTR is the Gray-Scott model[126,127] which originally comprises two irreversible reactions. Here, we considered a reversible version of this model to fit our description of the CRN. Following is the chemical reaction scheme we have considered,

$$\begin{aligned}
\rho = 1: &\quad \mathrm{P} \underset{\mathrm{k}_{-1}}{\overset{\mathrm{k}_1}{\rightleftharpoons}} \mathrm{X}, \\
\rho = 2: &\quad \mathrm{X} + 2\,\mathrm{Y} \underset{\mathrm{k}_{-2}}{\overset{\mathrm{k}_2}{\rightleftharpoons}} 3\mathrm{Y}, \\
\rho = 3: &\quad \mathrm{Y} \underset{\mathrm{k}_{-3}}{\overset{\mathrm{k}_3}{\rightleftharpoons}} \mathrm{Q},
\end{aligned} \tag{2.21}$$

where the second reaction is a cubic autocatalytic. Unlike the original reaction scheme $\mathrm{k}_{-\rho}$ are considered for thermodynamic consistency. Here, P and Q are the chemostatted species, and X and Y represent intermediate species. The kinetics of 2.21 can be captured by the rate of change of intermediate species under the condition $\mathrm{k}_\rho \gg \mathrm{k}_{-\rho}$ as,

$$\begin{aligned}
\dot{x} &= \mathrm{k}_1 p - \mathrm{k}_2 x y^2, \\
\dot{y} &= \mathrm{k}_2 x y^2 - \mathrm{k}_3 y,
\end{aligned} \tag{2.22}$$

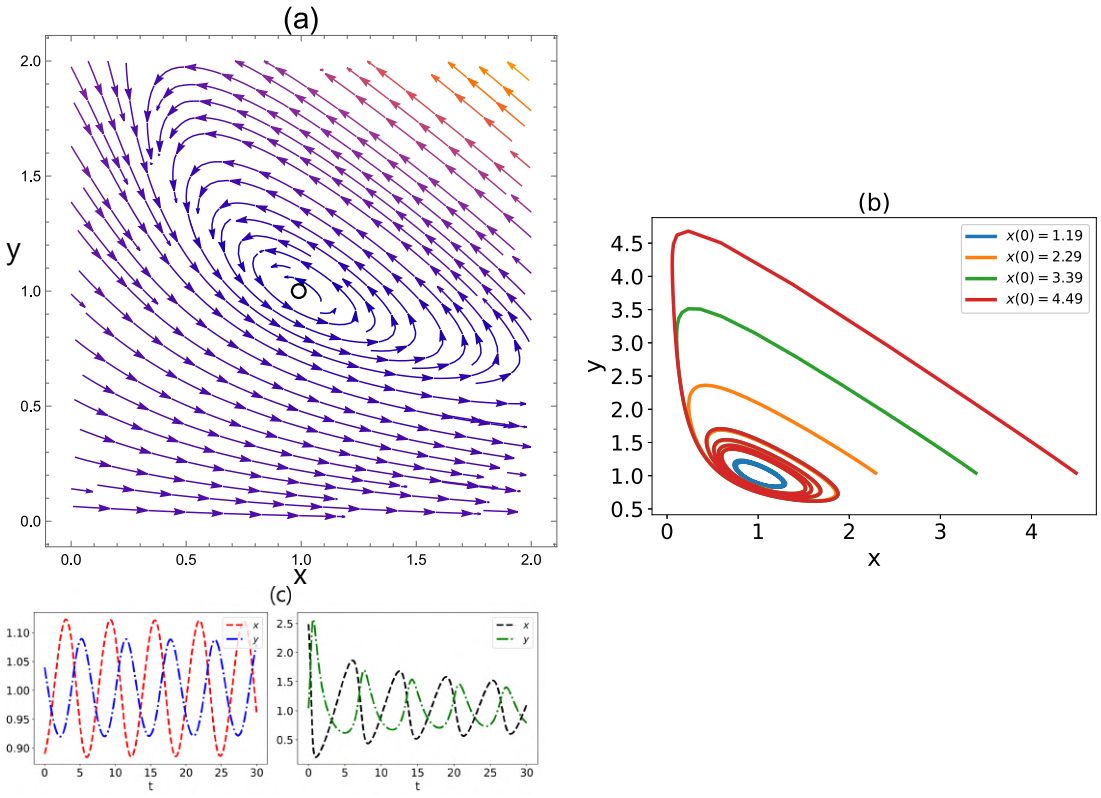

Figure 2.3: (a) The phase portrait in $y - x$ plane is presented. An open circle represents an unstable steady state. From the phase portrait, the existence of limit cycle behavior is anticipated. Two stable limit cycles are shown in (b). The first initial condition leads to the smaller limit cycle, and the remaining three initial conditions in x settle the system at the larger limit cycle. So, we have a particular bistability behavior known as birhythmicity. The temporal behavior of x and y concentrations is demonstrated in (c). Temporal behavior corresponding to smaller cycles is presented on the left, whereas concentration dynamics corresponding to the outer cycle are given on the right. We use all forward reaction rates equal to 1, i.e., $\mathrm{k}_\rho = 1$, and reverse reaction rates are very small in comparison to forward ones, i.e., $\mathrm{k}_{-\rho} = 10^{-5}$. The other parameter is $p = 1$. For the numerical integration, a time step size, $\Delta t = 0.05$, is used. The initial value of y is fixed at $y(0) = 1.04$.

where x, y and p are the concentration of species X, Y, and P, respectively. Dynamics of (2.22) has steady state at $(x_0 = \frac{\mathrm{k}_3{}^2}{\mathrm{k}_1\mathrm{k}_2 p}, y_0 = \frac{\mathrm{k}_1 p}{\mathrm{k}_3})$. However, this steady state is an unstable and is represented by an open cycle in Fig. 2.3 (a). The direction fields in the phase portrait in the same figure indicate the existence of limit cycles in the system. We have obtained a small-amplitude limit cycle in the phase plane for the initial condition near the unstable steady state of the system. Then, for the other three initial conditions further away from this limit cycle, we acquire another large-amplitude

limit cycle embracing the smaller-amplitude limit cycle as seen from Fig. 2.3 (b). So in this two variables system, we obtain birhythmicity for the same set of parameters with different initial conditions. The temporal natures of the concentration oscillation corresponding to small and large-amplitude limit cycles are illustrated in Fig. 2.3 (c). The figure on the left panel corresponds to the small amplitude limit cycle, and on the right, the time series corresponding to the larger limit cycle is demonstrated.

Brusselator rate equation

Another CRN with a similar cubic autocatalytic reaction is the Brusselator. The Brusselator CRN described in Eq. (2.14) admits the following rate equation,

$$\begin{aligned} \dot{x} &= k_1 a - (k_2 b + k_4 + k_{-1})x + (k_{-2} d + k_3 x^2)y - k_{-3} x^3 + k_{-4} e \\ \dot{y} &= k_2 b x - k_{-2} d y + k_{-3} x^3 - k_3 x^2 y \end{aligned} \tag{2.23}$$

with $x = [X]$, $y = [Y]$, $a = [A]$, $b = [B]$, $d = [D]$, $e = [E]$ denoting concentrations. The steady state of this system in Eq. (2.23) is acquired as, $x_0 = \frac{k_1 a + k_{-4} e}{k_{-1} + k_4}$, $y_0 = \frac{(k_2 b + k_{-3} x_0^2) x_0}{k_{-2} d + k_3 x_0^2}$. We will discuss Brusselator dynamics further from the next chapter onwards.

2.3.3 Linearization in two-variable nonlinear system

We will now discuss linear stability analysis leveraged extensively in this thesis for acquiring the solution of nonlinear systems. As we mentioned earlier, for the steady state of the two variable systems, we obtain $f(x_0, y_0) = 0$ and $g(x_0, y_0) = 0$ in Eq. (2.18a) and Eq. (2.18b), respectively. One can define small perturbations from the steady state, $x' = x - x_0$, $y' = y - y_0$. Now employing Taylor series expansion around the steady state of the system, we obtain $\dot{x'} = f(x_0 + x', y_0 + y') \approx x' \frac{\partial f}{\partial x}|_{(x_0, y_0)} + y' \frac{\partial f}{\partial y}|_{(x_0, y_0)}$, and $\dot{y'} = g(x_0 + x', y_0 + y') \approx x' \frac{\partial g}{\partial x}|_{(x_0, y_0)} + y' \frac{\partial g}{\partial y}|_{(x_0, y_0)}$ ignoring the higher order terms. Therefore, we can represent the evolution of the perturbation in terms of a linearized

system as

$$\begin{pmatrix} \dot{x'} \\ \dot{y'} \end{pmatrix} = \begin{pmatrix} \frac{\partial f}{\partial x} & \frac{\partial f}{\partial y} \\ \frac{\partial g}{\partial x} & \frac{\partial g}{\partial y} \end{pmatrix}_{(x_0,y_0)} \begin{pmatrix} x' \\ y' \end{pmatrix}, \tag{2.24}$$

where the matrix $\begin{pmatrix} \frac{\partial f}{\partial x} & \frac{\partial f}{\partial y} \\ \frac{\partial g}{\partial x} & \frac{\partial g}{\partial y} \end{pmatrix}$ is identified as the Jacobian matrix and will be denoted as

$$\mathcal{J} = \begin{pmatrix} J_{11} & J_{12} \\ J_{21} & J_{22} \end{pmatrix} \tag{2.25}$$

in the future discussion. J_{11}, J_{12}, J_{21}, and J_{22} are elements of Jacobian matrix. Using this Jacobian matrix, we derive characteristic equation by $det(A-\lambda I) = 0$, (I is identity matrix) and then eigenvalues, λ_1 and λ_2 are derived from this characteristic equation. For eigenvectors, U_1 and U_2 associated with eigenvalues, λ_1 and λ_2, respectively, the general time evolution of the concentration, x, reads $x(t) = C_1U_1 \exp(\lambda_1 t) + C_2U_2 \exp(\lambda_2 t)$ (t is temporal dimension) with C_1 and C_2 are complex coefficients.

The steady-state solution will be linearly stable if the real parts of both eigenvalues are negative, implying $Tr(\mathcal{J})$ is negative and $det(\mathcal{J})$ is positive. In the activator-inhibitor system[124] of the CRN, we can have different sign structures for this Jacobian matrix.

2.3.4 Hopf bifurcation in terms of linear stability analysis

Oscillation in the nonlinear chemical or biological system of two or more variables is often associated with the Hopf bifurcation[10]. Here, we will provide the conditions of Hopf bifurcation in terms of the linear stability analysis discussed above. In Hopf bifurcation, a stable steady state loses its stability locally as the control parameter is varied and generates oscillatory behavior. When the system is in a stable steady state, we can write from the aforementioned condition, $Tr(\mathcal{J}) < 0 \implies J_{11} + J_{22} < 0$ and $det\mathcal{J} > 0 \implies J_{11}J_{22} - J_{12}J_{21} > 0$. For a system with complex conjugate eigenvalues, Hopf instability arises when the trace of Jacobian changes from negative to positive with the variation of the control parameter, which implies eigenvalues cross the imaginary axis simultaneously. Therefore, at onset of the Hopf instability, $J_{11} + J_{22} = 0 \implies J_{11} = -J_{22}$, while the

determinant still remains the positive. The value of the control parameter at the onset of Hopf instability is called the critical value of the control parameter and is obtained using $J_{11} = -J_{22}$. The frequency of the oscillation near the onset of Hopf instability is approximately equal to the imaginary part of the eigenvalues at the onset of Hopf instability, which implies the critical frequency of the oscillation as $f_{cH} = \sqrt{det\mathcal{J}}$. The critical eigenvector associated with Hopf instability reads $U_{cH} = \begin{pmatrix} 1 + i\frac{\sqrt{det(\mathcal{J})}}{J_{11}} \\ \frac{J_{21}}{J_{11}} \end{pmatrix}$.

2.3.5 Fick's Law of diffusion

Besides chemical reactions, species of the CRN can also exhibit diffusion over spatial coordinates. This process obeys two fundamental laws proposed by Adolf Fick based on empirical results. Fick's first law states that diffusion current is proportional to the spatial gradient of the concentration of diffusing species. In general form, Fick's first law can be expressed in a one-dimensional system as

$$J_\sigma = -D_{\sigma\sigma'}\frac{\partial z_{\sigma'}}{\partial r}, \tag{2.26}$$

with J_σ and $D_{\sigma\sigma'}$ being the diffusion flux and the constant diffusion coefficient of the diffusing species σ, respectively. For self-diffusion coefficients, $\sigma' = \sigma$.

According to the continuity equation, the rate of change of the concentration of the species is captured by $\dot{z_\sigma} = -\frac{\partial J_\sigma}{\partial r}$. Inserting the J_σ from (2.26) and considering the constant diffusion coefficient, we obtain the expression of Fick's second law as,

$$\dot{z_\sigma} = D_{\sigma\sigma'}\frac{\partial^2 z_{\sigma'}}{\partial r^2}. \tag{2.27}$$

2.3.6 Cross diffusion

Cross diffusion is the generation of the diffusion flux of one species due to the gradient in the concentration of another chemical species present in the system. Coefficients of cross diffusion can be denoted as $D_{\sigma\sigma'}$, where $\sigma \neq \sigma'$ refers to σ and σ' as different

species. However, within a system involving electrolytes, microemulsions, etc., cross diffusion can play a crucial role, and even the slightest presence of this cross diffusion can modify the fate of spatial and spatiotemporal patterns generated in these systems[24].

These cross-diffusion coefficients generally exhibit concentration dependence. Notably, no flux of the species $\sigma(\sigma = 1, 2, ..)$ should exist when the concentration of the species, σ, is vanishingly low. Therefore, cross-diffusion coefficients $D_{\sigma\sigma'}$ must approach zero as the concentration, z_σ, tends to vanish, regardless of the concentration gradient $z_{\sigma'}$. So we can express the cross-diffusion coefficients[128] as,

$$D_{\sigma\sigma'}(z_\sigma) = \frac{D_{\sigma\sigma'} z_\sigma}{\eta + z_\sigma}. \tag{2.28}$$

In Eq. (2.28), $D_{\sigma\sigma'}$ always vanish, for $z_\sigma = 0$, satisfying the aforementioned demand. Furthermore, for the minimal η relative to concentrations (i.e., $\eta << z_\sigma$), $D_{\sigma\sigma'}(z_\sigma)$ effectively reduces to the constant $D_{\sigma\sigma'}$. Conversely, if $\eta >> z_\sigma$ is satisfied, $D_{\sigma\sigma'}(z_\sigma) = \frac{D_{\sigma\sigma'} z_\sigma}{\eta} = D'_{\sigma\sigma'} z_\sigma$ where $D'_{\sigma\sigma'} = \frac{D_{\sigma\sigma'}}{\eta}$. Consequently, the cross-diffusion coefficients exhibit a linear concentration dependence. For simplicity, we consider $(\eta << z_\sigma)$ corresponding to effective constant cross-diffusion coefficients throughout this thesis.

2.3.7 Reaction-diffusion system (RDS) of CRN

In the description of CRN, we assume a dilute ideal solution in which chemical species present as a well-mixed solute. The solution is kept within one spatial dimension, $r \in [0, l]$. In such spatially extended systems, species in a CRN system can diffuse over the spatial dimension as well as interact with other species. So the rate of change of species would be owing to both reaction and diffusion. Therefore, the concentration dynamics of CRN within a finite system will be captured by coupling the reaction terms with diffusion terms. This representation of species concentration dynamics is known as reaction-diffusion system (RDS)[1] and is a ubiquitous mathematical representation to describe and visualize various real-life phenomena involving spatial and temporal dynamics[124,4,129]. So using (2.7) and (2.27), we can have the general form of reaction-

diffusion corresponding to the chemical reaction network,

$$\dot{z_\sigma} = \sum_\rho S^\sigma_\rho j_\rho + \delta^C_\sigma \mathcal{J}_C + D_{\sigma\sigma}\frac{\partial^2 z_\sigma}{\partial r^2} + \sum_{\sigma'=\sigma} D_{\sigma\sigma'}\frac{\partial^2 z_{\sigma'}}{\partial r^2}, \tag{2.29}$$

where have also included cross-diffusion[130,131] related term (second term on the right) besides the usual self-diffusion of chemical species. For a two-variable system, these diffusion coefficients are elements of matrix $\begin{pmatrix} D_{11} & D_{12} \\ D_{21} & D_{22} \end{pmatrix}$ with diagonal elements are self-diffusion coefficients, and non-diagonal coefficients are cross-diffusion coefficients.

Example of RDS in the presence of self and cross diffusion: Under the assumption mentioned above, $k_\rho \gg k_{-\rho}$, we can represent the RDS of the Brusselator CRN in one spatial dimension $r \in [0, l]$ as

$$\begin{aligned} \dot{x} &= k_1 a - (k_2 b + k_4)x + k_3 x^2 y + D_{11} x_{rr} + D_{12} y_{rr} \\ \dot{y} &= k_2 b x - k_3 x^2 y + D_{21} x_{rr} + D_{22} y_{rr}. \end{aligned} \tag{2.30}$$

2.3.8 Turing pattern in a general RDS

Alan Turing, in his seminal work[1], reported that diffusion can create instability in an RDS and generate patterns. Specifically, a two-variable CRN, which is linearly stable in the absence of diffusion, can be destabilized by the introduction of diffusion in the system. In the presence of self diffusion only in the RDS, an activator-inhibitor system needs to satisfy local activation and lateral inhibition[7,4] condition, which means the self-diffusion coefficient of the inhibitor, D_{22}, is much greater than the self-diffusion coefficient of the activator, D_{11}, i.e., $D_{11} \ll D_{22}$ to cause Turing instability. However, in this thesis, we have investigated the Turing pattern in a more general RDS with both self- and cross-diffusion coefficients. In the presence of cross diffusion, Turing instability can arise even if the condition of local activation and lateral inhibition is not obeyed in the system. Indeed, the cross diffusion strongly modifies the Turing instability conditions, and we can have Turing instability even when the self-diffusion coefficient of the activator is

greater than the self-diffusion of the inhibitor[132]. Further, the Turing instability region in the presence of the cross-diffusion coefficients with a linear concentration dependence has been specified by acquiring universal conditions of the Turing instability[133]. Here,

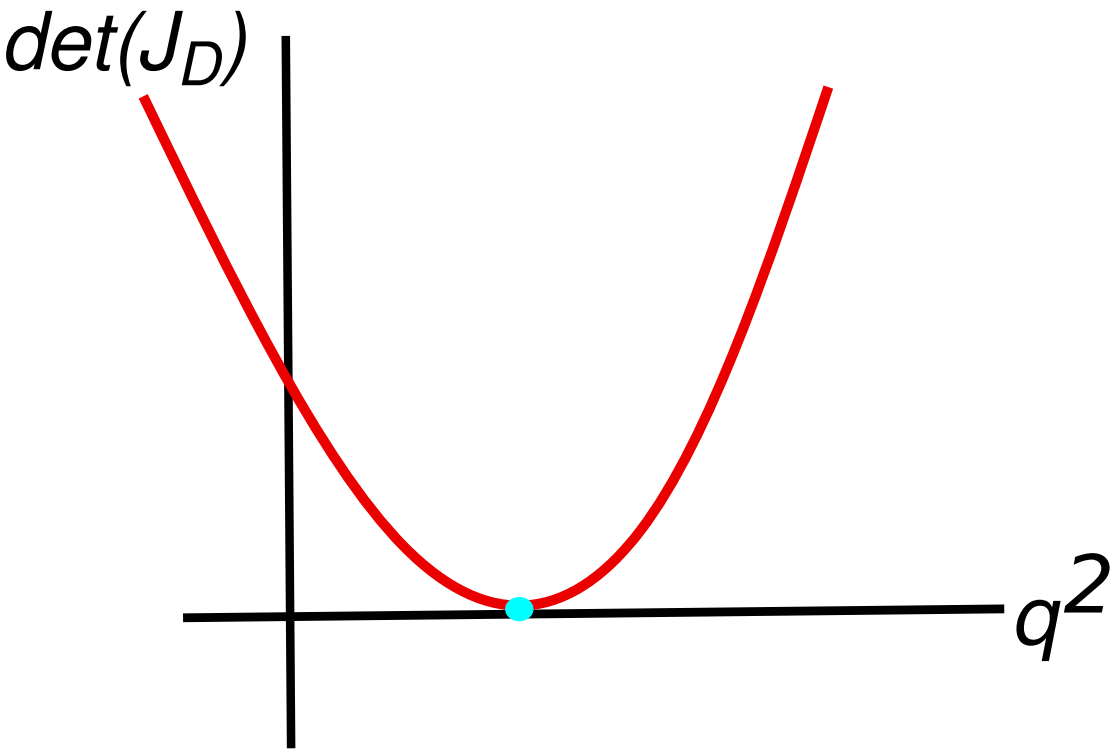

Figure 2.4: Illustration of the double root scenario at the onset (cyan dot) of Turing instability.

we obtain a critical value of the control parameter and wave number associated with the Turing pattern by determining conditions of Turing instability in the presence of both self and cross diffusion. Taking diffusion into consideration and applying a Fourier transform $g(r,t) \rightarrow g(q,t)$, the Jacobian matrix, $\mathcal{J}$ in 2.25 can be extended into

$$\begin{aligned} \mathcal{J}_{\mathcal{D}} &= \mathcal{J} - q^2\mathcal{D} \\ &= \begin{pmatrix} J_{11} & J_{12} \\ J_{21} & J_{22} \end{pmatrix} - q^2 \begin{pmatrix} D_{11} & D_{12} \\ D_{21} & D_{22} \end{pmatrix} \end{aligned} \tag{2.31}$$

where q is the wave number. Form Eq. (2.31), we obtain the trace of $\mathcal{J}_\mathcal{D}$ as: $Tr(\mathcal{J}_\mathcal{D})$. Whereas, the determinant of $\mathcal{J}_\mathcal{D}$ is acquired as the quadratic equation of q^2

$$det(\mathcal{J}_\mathcal{D}) = det(\mathcal{D})(q^2)^2 - [D_{11}J_{22} + D_{22}J_{11} - D_{12}J_{21} - D_{21}J_{12}]q^2 + det(\mathcal{J}). \quad (2.32)$$

Now, the eigenvalues λ of $\mathcal{J}_\mathcal{D}$ can be determined using the characteristic equation, $\lambda^2 - Tr(\mathcal{J}_\mathcal{D})\lambda + det(\mathcal{J}_\mathcal{D}) = 0$. Thus, eigenvalues in terms of determinant and trace can be written as,

$$\lambda_\pm = \frac{Tr(\mathcal{J}_\mathcal{D}) \pm \sqrt{Tr(\mathcal{J}_\mathcal{D})^2 - 4det(\mathcal{J}_\mathcal{D})}}{2}. \quad (2.33)$$

At a stable steady state, these eigenvalues will be complex conjugate pairs, $\lambda_\pm = \lambda_r \pm i\lambda_i$ given chemical concentrations are real quantities. The real parts of both of these eigenvalues need to be negative for the stability of the system, and this criterion demands, $Tr(\mathcal{J}_\mathcal{D}) < 0$ and $det(\mathcal{J}_\mathcal{D}) > 0$. We assume that the system remained at a stable steady state before the addition of the diffusion. Since $(D_{11} + D_{22})q^2 > 0$ is always true, the trace condition of the stability, $Tr(\mathcal{J}_\mathcal{D}) < 0$ remains intact even in the reaction-diffusion description of the system. Therefore, the only way to generate diffusion-driven instability in this RDS representation is by breaking the stability condition at the level of determinant. Thus, $det(\mathcal{J}_\mathcal{D}) < 0$ has to be satisfied within the instability regime, and at the onset of Turing instability, $det(\mathcal{J}_\mathcal{D}) = 0$. Since $det(\mathcal{D}) > 0$ is always true by the second law of thermodynamics, and $det(\mathcal{J}) > 0$ is satisfied for a stable steady state in the absence of the diffusion, the only way to obtain $det(\mathcal{J}_\mathcal{D}) < 0$ here is

$$[D_{11}J_{22} + D_{22}J_{11}] > [D_{12}J_{21} + D_{21}J_{12}]. \quad (2.34)$$

The above relation is a necessary condition to ensure that one of the real parts of eigenvalues crosses zero to become positive. However, this is not a sufficient condition to generate Turing instability in the presence of cross diffusion. However, this necessary condition in Eq. (2.34) suggests that the so-called local activation and lateral inhibition, $D_{22} \gg D_{11}$ for the traditional Turing pattern has not to be satisfied in the presence of

cross-diffusion. In that sense, the condition of having Turing instability gets diluted in the presence of cross diffusion.

Further, we have to ensure the existence of the real root of the quadratic equation (2.32) to acquire the necessary and sufficient condition of the Turing instability in the RDS. For that purpose, the discriminant of the quadratic equation should be positive, and hence the following condition must be obeyed

$$(D_{11}J_{22} + D_{22}J_{11} - D_{12}J_{21} - D_{21}J_{12})^2 - 4det(\mathcal{D})det(\mathcal{J}) > 0. \tag{2.35}$$

Therefore, at the onset of instability, the above condition in Eq. (2.35) results in the following equality,

$$(D_{11}J_{22} + D_{22}J_{11} - D_{12}J_{21} - D_{21}J_{12})^2 - 4det(\mathcal{D})det(\mathcal{J}) = 0. \tag{2.36}$$

From this equality, one can acquire the critical value of the control parameter by inserting explicit expressions of all the entities for a specific model.

Further, to have Turing instability, the necessary and sufficient condition also demands that the $det(\mathcal{J}_\mathcal{D})$ equation in (2.32) must allow double roots at the onset of the instability. For that purpose, the following two conditions should be satisfied simultaneously: $det(\mathcal{J}_\mathcal{D}) = 0$ and $\frac{d\{det(\mathcal{J}_\mathcal{D})\}}{d(q^2)} = 0$. These conditions yield the intrinsic critical wave number equation at the onset of Turing instability as,

$$q_{cT} = \left[\frac{det(\mathcal{J})}{det(\mathcal{D})}\right]^{\frac{1}{4}}. \tag{2.37}$$

This critical value of the wave number sets the length scale of the pattern formation as $\frac{2\pi}{q_{cT}}$. The general expression of the critical wave number suggests that q_{cT} have to be real and positive. This q_{cT} is the fastest-growing Fourier mode of the system and the growth rate corresponding to this critical wave number becomes zero for the first time at the critical value of the control parameter. We can also compare this critical wave number to the critical wave number for the RDS with the self diffusion only[132]. As

the critical wave number, q_{cT} reduces to $q_{cT}^0 = \left[\frac{det(\mathcal{J})}{D_{11}D_{22}}\right]^{\frac{1}{4}}$ in the absence of the cross diffusion, we can write $q_{cT} = q_{cT}^0\left[\frac{D_{11}D_{22}}{det(\mathcal{D})}\right]^{\frac{1}{4}}$.

At the onset of Turing instability, eigenvalues can be expressed as, $\lambda_+ = Tr(\mathcal{J}_\mathcal{D})$ and $\lambda_- = 0$. The negative value of $Tr(\mathcal{J}_\mathcal{D})$ suggests that eigenvalue $\lambda_- = 0$ at the onset of Turing instability will govern the whole system dynamics.

2.3.9 Amplitude equation formalism

In the presence of the different instabilities mentioned above, the concentration dynamics of the nonlinear RDS will be described in this thesis by incorporating relevant amplitudes into the linear stability picture of the system. These amplitudes, generally complex entities, obey some particular amplitude equation based on the nature of instabilities and coupling scenarios. This amplitude equation formalism is utilized to faithfully capture essential nonlinear features and effects of spatial and temporal patterns near the onset of instabilities and has a universal form[4].

Complex Ginzburg-Landau equation (CGLE)

The complex Ginzburg-Landau equation[5,27] (CGLE) provides the description and qualitative insights of RDS dynamics near the Hopf bifurcation point. The normal form of the CGLE[134,4] in a spatially extended system is

$$\frac{\partial Z}{\partial t} = \lambda Z - (1 - i\beta) \mid Z \mid^2 Z + (1 + i\alpha)\partial_r^2 Z, \tag{2.38}$$

with Z being the complex amplitude field and λ, β, and α being coefficients containing the RDS parameters. This complex amplitude can be expressed as $Z = \mathcal{A}\exp(-i\phi)$, where $\mathcal{A}$ and ϕ are amplitude and phase, respectively. Explicit equations of amplitude and phase are acquired in the next chapter in the context of Brusselator RDS.

Krylov-Bogolyubov (KB) method

The coefficients of the amplitude equations encapsulate the parameters of a specific RDS. Therefore, it is important to capture the explicit form of these coefficients in a particular RDS. In the presence of cross diffusion, it is cumbersome to acquire these coefficients using the usual multiscale method[4,5]. So, here, we implement the Krylov-Bogolyubov (KB) method, a standard technique in nonlinear mechanics for analyzing oscillations[135]. The essential concept behind this averaging method involves considering the very slow variation of the amplitude in time and space so that the averaged system can be almost equivalent to the exact dynamics. We will discuss and demonstrate this KB method in detail when employing it successfully in constructing the unscaled amplitude equation related to the Brusselator and Selkov RDS in the next two chapters.

Modified amplitude equation for globally coupled system

In this thesis, we have explored the scenario of global coupling in a continuum chemical oscillatory system. For that purpose, we enforce the coupling at the level of amplitude of the system. We assume that such a globally coupled chemical system near the onset of Hopf instability can be effectively represented by a modified complex Ginzburg-landau equation (MCGLE)[136,137,31,138,139] with a nonlinear global coupling.

$$\begin{aligned}\frac{\partial Z}{\partial t} &= \lambda Z - (1-i\beta) \mid Z \mid^2 Z + (1+i\alpha)\partial_r^2 Z \\ &\quad -(\lambda + i\nu)\langle Z\rangle + (1-i\beta)\left\langle \mid Z \mid^2 Z\right\rangle, \end{aligned} \tag{2.39}$$

with $\langle ... \rangle$ denoting the spatial average. This nonlinear global coupling scheme yields an oscillatory mean field following the spatial average over (2.39). This oscillatory mean field is $\langle Z\rangle = Z_0 = \eta \exp(-i\nu t)$ with η and ν being the amplitude and the frequency of the oscillation, respectively. A discrete counterpart of the continuum system in (2.39) can be represented by a globally coupled Stuart Landau oscillator system without diffusive coupling[31]. In this thesis, we will solve this MCGLE using a numerical method.

We will discuss more about the MCGLE when we investigate the thermodynamics of the chimera in the chemical system.

In this context, it is important to mention another crucial amplitude equation known as the Turing amplitude equation (TAE)[4] associated with the Turing instability. This amplitude equation can be seen as the real counterpart of the CGLE. In the next chapter, we will leverage this amplitude equation for investigating Turing-Hopf overlapping.

2.4 Framework and elements of nonequilibrium thermodynamics

All thermodynamic entities are defined in the RT unit, except explicitly noted otherwise.

2.4.1 Local equilibrium assumption

For the nonequilibrium thermodynamic description, we can formulate the intensive variables in elemental volume using the equilibrium thermodynamic definitions. For extensive variables, we can define their densities. These assumption is called the local equilibrium[140,20]. For a spatially extended system, we divide the space and time dimensions of the system into infinitesimal elemental parts where equilibrium hold, and we acquire the spatiotemporal variation of the thermodynamic variables under a nonequilibrium environment. In this thesis, with a slight abuse of the nomenclature, we use the names of the extensive variables, dropping 'densities' from the corresponding variables.

2.4.2 Nonequilibrium chemical potential

In this thesis, the chemical system is described as a well-mixed ideal dilute solution, with the solvent being abundant relative to the solute, the reacting species. For the dilute solution of chemicals, a chemical potential corresponding to species, σ, contained in the solution is[141] $\mu_\sigma = \mu_\sigma^o + \ln \frac{z_\sigma}{z_{total}}$, where μ_σ^o is standard-state chemical potential. Under the dilute solution approximation, the total concentration of the solution can be approximately represented by the solvent concentration, z_0, i.e., $z_{total} \backsimeq z_0$. Therefore, the chemical potential expression becomes $\mu_\sigma = \mu_\sigma^o + \ln \frac{z_\sigma}{z_0}$. We assume that the sol-

vent does not interact with solutes and that the solvent concentration, z_0, is constant. Absorbing it into μ_σ^o, the chemical potential expression becomes

$$\mu_\sigma = \mu_\sigma^o + \ln z_\sigma. \tag{2.40}$$

For z_σ being the nonequilibrium concentration, μ_σ can be identified as nonequilibrium chemical potential. The solvent of the dilute chemical solution acts as a thermal reservoir and maintains the system at local thermal equilibrium at temperature T.

2.4.3 Nonequilibrium Gibbs free energy

Gibbs free energy[45] is a crucial thermodynamic entity to employ for processes at constant pressure. For a dilute solution of chemical species, Gibbs free energy of the solution can be defined in terms of the chemical potential as[141], $G = \sum_\sigma z_\sigma \mu_\sigma$ where $\sigma = 0$ corresponds to the solvent and $\sigma \neq 0$ refers to the solute of the solution. The chemical potential characterizing the solute species can be obtained from Eq. (2.40). Now treating the solvent as a special chemostatted species, we can use the definition of the chemical potential given above as $\mu_0 = \mu_0^o + \ln \frac{z_0}{z_{total}} \implies \mu_0 = \mu_0^o - \ln \frac{z_0 + \sum_{\sigma\neq 0} z_\sigma}{z_0} = \mu_0^o - \ln\left(1 + \frac{\sum_{\sigma\neq 0} z_\sigma}{z_0}\right)$. Since $1 \gg \frac{\sum_{\sigma\neq 0} z_\sigma}{z_0}$, we can expand $\ln\left(1 + \frac{\sum_{\sigma\neq 0} z_\sigma}{z_0}\right)$ and neglect the higher order terms. Thus, we arrive at the final expression of the chemical potential of the solvent as $\mu_0 = \mu_0^o - \frac{\sum_{\sigma\neq 0} z_\sigma}{z_0}$. By inserting the chemical potential expressions of solute and solvent into the definition of the Gibbs free energy, one can achieve the Gibbs free energy of the whole dilute solution, $G = \mu_0^o z_0 + \sum_{\sigma\neq 0}(z_\sigma \mu_\sigma - z_\sigma)$[106,107]. After considering $G_0 = \mu_0^o z_0$, the final expression of Gibbs free energy emerges as

$$G = G_0 + \sum_{\sigma\neq 0} (z_\sigma \mu_\sigma - z_\sigma), \tag{2.41}$$

where terms G_0 and $\sum_{\sigma\neq 0} z_\sigma$ appear due to the solvent. When z_σ represents the nonequilibrium concentration distribution, Eq. (2.41) is identified as the expression of the nonequilibrium Gibbs free energy.

2.4.4 Reaction affinity

The driving force involved in the chemical reaction is known as reaction affinities and can be expressed as[142] $f_\rho = -\sum_\sigma S_\rho^\sigma \mu_\sigma$, where $S_\rho^\sigma = v_{-\rho}^\sigma - v_{+\rho}^\sigma$ being the stoichiometric coefficient of species. A nonzero affinity of a reaction system indicates that the system is in a nonequilibrium thermodynamic state. Affinity vanishes at an equilibrium state.

Example of reaction affinity: For a simple elementary reaction step, $\rho = 1$: $\mathrm{X+Y} \underset{\mathrm{k_{-1}}}{\overset{\mathrm{k_1}}{\rightleftharpoons}} 2\,\mathrm{Y}$, the affinity becomes $f_1 = \mu_X - \mu_Y$, where μ_X and μ_Y are chemical potential of species X and Y, respectively.

Gibbs free energy of reaction

Affinity can also be interpreted as the negative change in Gibbs free energy along each reaction pathway, known as the Gibbs free energy of reaction,[119,20] $\Delta G_\rho = -f_\rho = \sum_\sigma S_\rho^\sigma \mu_\sigma$. Inserting the expression of chemical potential from Eq. (2.40) into the definition of affinity, we acquire

$$f_\rho = -\Delta G_\rho^o - \sum_\sigma S_\rho^\sigma \ln z_\sigma, \tag{2.42}$$

where $\Delta G_\rho^o = \sum_\sigma S_\rho^\sigma \mu_\sigma^o$ is called standard Gibbs energy of reaction. It is important to note that despite the resemblance between the affinity and Gibbs free energy along the reaction pathway, they have completely different conceptual origins. While Gibbs free energy is essentially associated with reversible processes and equilibrium states, affinity is particularly connected with irreversible processes.

2.4.5 Local detailed balance condition

Since the affinity vanishes for the equilibrium state, we can write from Eq. (2.42), $\sum_\sigma S_\rho^\sigma \ln z_\sigma^{eq} = -\Delta G_\rho^o \implies \prod_\sigma (z_\sigma^{eq})^{S_\rho^\sigma} = \exp\left(-\Delta G_\rho^o\right)$. This relation is obtained from the thermodynamic equilibrium situation. Incorporating the equilibrium rate constant

definition in Eq. (2.8), obtained using the dynamic equilibrium scenario, we appear at

$$\ln \frac{k_{+\rho}}{k_{-\rho}} = -\Delta G^o_\rho. \tag{2.43}$$

Thus, Eq. (2.43) connects the dynamics and thermodynamics, and this condition is the local detailed balance condition for a nonequilibrium system. Exploiting this local detailed balance condition in Eq. (2.42), we obtain affinities as,

$$f_\rho = \ln \frac{j_{+\rho}}{j_{-\rho}}, \tag{2.44}$$

which applies to any elementary step. If $j_{+\rho} > j_{-\rho}$, i.e., $j > 0$, then affinity $f_\rho > 0$ and reaction proceed in the forward direction. Whereas, $j_{+\rho} < j_{-\rho}$, i.e., $j < 0$, then affinity $f_\rho < 0$ and reaction proceeds in the backward direction.

Example of Local detailed balance in Brusselator: Exploiting the local detailed balance condition stated in Eq. (2.43) for the Brusselator CRN in Eq. (2.14), we obtain

$$\begin{aligned}
\ln \frac{\mathrm{k}_1}{\mathrm{k}_{-1}} &= \mu^o_A - \mu^o_X, \\
\ln \frac{\mathrm{k}_2}{\mathrm{k}_{-2}} &= \mu^o_X - \mu^o_Y + \mu^o_B - \mu^o_D, \\
\ln \frac{\mathrm{k}_3}{\mathrm{k}_{-3}} &= \mu^o_Y - \mu^o_X, \\
\ln \frac{\mathrm{k}_4}{\mathrm{k}_{-4}} &= \mu^o_X - \mu^o_E.
\end{aligned}$$

2.4.6 Diffusion affinity

Similar to the chemical reactions, we can define the thermodynamic driving force for the diffusion in a one-dimensional system owing to the spatial gradient of concentrations as

$$F_\sigma(r,t) = -\frac{\partial \mu_\sigma(r,t)}{\partial r}, \tag{2.45}$$

and it is called diffusion affinity. In the above expression of the diffusion affinity, substituting the chemical potential expression as shown in Eq. (2.40), we arrive at

$$F_\sigma(r,t) = -\frac{1}{z_\sigma}\frac{\partial z_\sigma(r,t)}{\partial r}. \tag{2.46}$$

At the equilibrium of the RDS, this diffusion affinity and fluxes vanish.

2.4.7 Gibbs free energy for equilibrium distribution

A closed RDS will always equilibrate, and equilibrium concentration distributions z_σ^{eq} are homogeneous. Therefore, we can write $F_\sigma^{eq} = 0$. For this equilibrium concentration distribution, z_σ^{eq}, reaction affinities vanish and we have, $f_\rho^{eq} = \sum_\sigma \mu_\sigma^{eq} S_\rho^\sigma = 0$. Comparing this expression with the conservation laws definitions of the closed system in Eq. (2.10), we can specify the equilibrium chemical potential in terms of the conservation laws as,

$$\mu_\sigma^{eq} = \sum_\lambda R_\lambda l_\sigma^\lambda, \tag{2.47}$$

with R_λ being the real coefficient. Thus, conservation laws can aid in specifying the equilibrium chemical potential. Now, comparing this equilibrium chemical potential expression in Eq. (2.47) with the expression of chemical potential in Eq. (2.40), we arrive at $\sum_\lambda R_\lambda l_\sigma^\lambda = \mu_\sigma^o + \ln z_\sigma^{eq}$. From this relation, we acquire the equilibrium concentration distribution of species as

$$z_\sigma^{eq} = \exp -(\mu_\sigma^o - \sum_\lambda R_\lambda l_\sigma^\lambda). \tag{2.48}$$

Further, from Eq. (2.47), we can obtain $\sum_\sigma \mu_\sigma^{eq} z_\sigma^{eq} = \sum_\sigma \sum_\lambda R_\lambda l_\sigma^\lambda z_\sigma^{eq} = \sum_\lambda R_\lambda L_\lambda = \sum_\sigma \sum_\lambda R_\lambda l_\sigma^\lambda z_\sigma = \sum_\sigma \mu_\sigma^{eq} z_\sigma$. So, we can assert

$$\sum_\sigma \mu_\sigma^{eq}(z_\sigma - z_\sigma^{eq}) = 0. \tag{2.49}$$

Using the equilibrium chemical potential definition in terms of conservation laws, we

can express the equilibrium Gibbs free energy for the closed system from Eq. (2.41) as

$$G^{eq} = G(z_\sigma^{eq}) = G_0 + \sum_\lambda R_\lambda L^\lambda - \sum_{\sigma \neq 0} z_\sigma^{eq}. \tag{2.50}$$

2.4.8 Entropy change in irreversible processes

For an isothermal system at temperature T, one can represent the change in entropy as an addition of two contributions, $dS = d\Sigma_e + d\Sigma$, where $d\Sigma_e$ captures reversible entropy change due to the flow of matter and energy between the system and reservoirs and $d\Sigma$ is known as entropy production in the system[143,20]. In the upcoming passages, we will derive this relation regarding entropy in the irreversible processes starting from some fundamental relations of thermodynamics.

From laws of thermodynamics to Gibbs-Helmholtz equation

In this thesis, we consider that chemical reservoirs (chemostats) are at thermodynamic equilibrium, and the system can be at an equilibrium or nonequilibrium state. For a homogeneous closed system, we can write the first law of thermodynamics, $dQ = dU + PdV$, where P is the pressure, V is the volume, U is the internal energy, and Q is the general heat. Then incorporating the second law corresponding to reversible processes, we obtain $dU = TdS - PdV$.

Now, the enthalpy is defined in terms of internal energy U as $H = U + PV$. This enthalpy definition yields $dH = dU + PdV + VdP$. Further, exploiting the relation mentioned above $dU = TdS - PdV$, we acquire $dH = TdS + VdP$. Since $dQ = TdS$, this relation results in $dH = dQ$ at the constant pressure. This relation means that the change in enthalpy is equal to the absorbed heat.

Further, the Gibbs free energy can be defined in terms of enthalpy and entropy as $G = H - TS$ and thus $dG = dH - TdS - SdT$. Then, inserting $dH = TdS + VdP$ into this, we achieve $dG = VdP - SdT$. This equation of the Gibbs free energy suggests that temperature, T, and pressure, P are natural variables of Gibbs free energy. Thus we can

alternatively write $dG = \frac{\partial G}{\partial P}dP + \frac{\partial G}{\partial T}dT$. Comparing this with the previous fundamental equation of dG we obtain, $V = \frac{\partial G}{\partial P}$ and $S = -\frac{\partial G}{\partial T}$. Now inserting this expression of S into the Gibbs free energy definition in terms of entropy and enthalpy, $G = H - TS$, we acquire $G = H + T(\frac{\partial G}{\partial T})$. Therefore, $H = G - T(\frac{\partial G}{\partial T}) = G - \frac{T^2}{T}(\frac{\partial G}{\partial T}) = -T^2\frac{\partial(\frac{G}{T})}{\partial T}$. This equation of enthalpy is called Gibbs-Helmholtz equation[119].

Molar entropy and enthalpy of species

Now inserting Gibbs free energy of ideal dilute solution from Eq. 2.41, we obtain

$$S = -\frac{\partial G}{\partial T} = \sum_{\sigma}(-\frac{\partial \mu_{\sigma}^{o}}{\partial T} - R\ln z_{\sigma} + R)z_{\sigma}. \tag{2.51}$$

Further defining $-\frac{\partial \mu_{\sigma}^{o}}{\partial T} = \Sigma_{\sigma}^{o}$ and $\Sigma_{\sigma}^{o} - R\ln z_{\sigma} = \Sigma_{\sigma}$, we can represent the entropy as,

$$S = \sum_{\sigma}(\Sigma_{\sigma} + R)z_{\sigma}, \tag{2.52}$$

where Σ_{σ} is the molar entropy and Σ_{σ}^{o} is the standard molar entropy[119] of species, σ.

Similarly, we can also obtain an expression for molar enthalpy from the Gibbs-Helmholtz equation. Thus, we express,

$$H = -T^2\frac{\partial(\frac{G}{T})}{\partial T} = -T^2\sum_{\sigma}\frac{\partial(\frac{\mu_{\sigma}^{o}}{T})}{\partial T}z_{\sigma} = \sum_{\sigma}H_{\sigma}^{o}z_{\sigma}, \tag{2.53}$$

where $H_{\sigma}^{o} = -T^2\frac{\partial(\frac{\mu_{\sigma}^{o}}{T})}{\partial T}$ is the standard molar enthalpy corresponding to species σ. From Eq. (2.53), we express the time derivative of the enthalpy as, $\frac{dH}{dt} = \sum_{\sigma}H_{\sigma}^{o}\frac{dz_{\sigma}}{dt} \implies \sum_{\sigma}H_{\sigma}^{o}\frac{dz_{\sigma}}{dt} = \frac{dQ}{dt}$. Now $H_{\sigma}^{o} = -T^2\frac{\partial(\frac{\mu_{\sigma}^{o}}{T})}{\partial T} = -T\frac{\partial \mu_{\sigma}^{o}}{\partial T} + \mu_{\sigma}^{o} = T\Sigma_{\sigma}^{o} + \mu_{\sigma}^{o}$. After rearranging, we obtain the relation between standard chemical potential, standard molar entropy, and standard molar enthalpy as follows,

$$\mu_{\sigma}^{o} = H_{\sigma}^{o} - T\Sigma_{\sigma}^{o}. \tag{2.54}$$

Using the above relation we can represent the chemical potential as $\mu_\sigma = \mu^o_\sigma + RT \ln z_\sigma = H^o_\sigma - T\Sigma^o_\sigma + RT \ln z_\sigma = H^o_\sigma - T(\Sigma^o_\sigma - R \ln z_\sigma)$. Since $\Sigma^o_\sigma - R \ln z_\sigma = \Sigma_\sigma$, we finally express,

$$\mu_\sigma = H^o_\sigma - T\Sigma_\sigma. \tag{2.55}$$

Reaction entropy and enthalpy:

Now using the expression of entropy, $S = \frac{-\partial G}{\partial T}$ and inserting the Gibbs free energy of reaction, ΔG_ρ, we acquire the reaction entropy[119] as, $\Delta S_\rho = \frac{-\partial \Delta G_\rho}{\partial T} = \frac{-\partial \Delta G_\rho}{\partial T} = -\sum_\sigma S^\sigma_\rho \frac{\partial \mu_\sigma}{\partial T}$. Further, chemical potential relation in Eq. (2.55) aids in the mathematical expression of the reaction entropy, $\Delta S_\rho = \sum_\sigma S^\sigma_\rho \Sigma_\sigma$.

Reaction enthalpy[119,20] can be calculated from the Gibbs-Helmholtz equation presented above, $H = G - T(\frac{\partial G}{\partial T}) = -T^2 \frac{\partial (\frac{G}{T})}{\partial T}$. Substituting the Gibbs free energy of reaction, ΔG_ρ in the above equation and exploiting the chemical potential expression, we obtain the reaction enthalpy as $\Delta H_\rho = -\sum_\sigma S^\sigma_\rho T^2 \frac{\partial (\frac{\mu_\sigma}{T})}{\partial T} = -\sum_\sigma S^\sigma_\rho T^2 \frac{\partial (\frac{\mu^o_\sigma}{T})}{\partial T} = \sum_\sigma S^\sigma_\rho H^o_\sigma$.

Entropy balance equation in RDS

The time derivative of enthalpy can be expressed in terms of reaction enthalpy, $\frac{dH}{dt} = H^o_\sigma \frac{dz_\sigma}{dt} = \sum_\rho j_\rho \sum_\sigma S^\sigma_\rho H^o_\sigma = \sum_\rho j_\rho \Delta H_\rho$. Since the time derivative of enthalpy captures the reversible heat exchange rate, we can now define the rate of heat exchange in terms of reaction enthalpy as, $\frac{dH}{dt} = \frac{dQ}{dt} = \sum_\rho j_\rho \Delta H_\rho$.

From Eq. (2.52), we can write $\frac{dS}{dt} = \frac{d \sum_\sigma (\Sigma_\sigma + R) z_\sigma}{dt} = \sum_\sigma (\frac{d\Sigma_\sigma}{dt} z_\sigma + \Sigma_\sigma \frac{dz_\sigma}{dt} + R \frac{dz_\sigma}{dt})$. Now substituting $\Sigma_\sigma = \Sigma^o_\sigma - R \ln z_\sigma$, we derive

$$\frac{dS}{dt} = \sum_\sigma (\Sigma_\sigma \frac{dz_\sigma}{dt}). \tag{2.56}$$

For RDS as shown in Eq. (2.29), we have $\frac{dz_\sigma}{dt} = -\frac{\partial J_\sigma}{\partial r} + \sum_\rho S^\sigma_\rho j_\rho$ and therefore, $\frac{dS}{dt} = \sum_\sigma [\Sigma_\sigma (-\frac{\partial J_\sigma}{\partial r} + \sum_\rho S^\sigma_\rho j_\rho)]$. Exploiting Eq. (2.55), we obtain,

$$\sum_\sigma [\Sigma_\sigma (-\frac{\partial J_\sigma}{\partial r} + \sum_\rho S^\sigma_\rho j_\rho)] = \sum_\sigma [(\frac{H^o_\sigma - \mu_\sigma}{T})(-\frac{\partial J_\sigma}{\partial r} + \sum_\rho S^\sigma_\rho j_\rho)]. \tag{2.57}$$

In Eq. (2.57), the first part, $\sum_\sigma(\frac{H^o_\sigma-\mu_\sigma}{T})(-\frac{\partial J_\sigma}{\partial r}) = \sum_\sigma(-\frac{\partial[(\frac{H^o_\sigma-\mu_\sigma}{T})J_\sigma]}{\partial r} - J_\sigma\frac{\partial(\frac{H^o_\sigma-\mu_\sigma}{T})}{\partial r}) = \sum_\sigma(-J_\sigma\frac{\partial(\frac{H^o_\sigma-\mu_\sigma}{T})}{\partial r}) = \frac{1}{T}\sum_\sigma J_\sigma\frac{\partial\mu_\sigma}{\partial r} = \frac{1}{T}\sum_\sigma J_\sigma F_\sigma = \frac{d\Sigma_D}{dt}$, where we have exploit the fact that no divergence from the system related to the diffusion exists. $\frac{d\Sigma_D}{dt}$ is the entropy production rate due to diffusion.

Further, we identify, $\frac{1}{T}\sum_\rho j_\rho\sum_\sigma S^\sigma_\rho\mu_\sigma = \frac{1}{T}\sum_\rho j_\rho f_\rho$, as the product of reaction flux and reaction affinity. This $\frac{1}{T}\sum_\rho j_\rho f_\rho = \frac{d\Sigma_R}{dt}$ is called reaction entropy production rate[87]. Whereas, the part, $\sum_\sigma(\frac{H^o_\sigma}{T}\sum_\rho S^\sigma_\rho j_\rho) = \sum_\sigma\frac{H^o_\sigma}{T}\frac{dz_\sigma}{dt} = \frac{1}{T}\sum_\sigma\frac{d(H^o_\sigma z_\sigma)}{dt} = \frac{1}{T}\frac{dH}{dt} = \frac{1}{T}\frac{dQ}{dt}$, at constant pressure and is recognized as the reversible heat exchange rate between system and reserviors. This $\frac{Q}{T} = \Sigma_e$ is also called entropy flow. Therefore, collecting all these terms, we arrive at the time derivative of S as

$$\frac{dS}{dt} = \frac{d\Sigma_D}{dt} + \frac{d\Sigma_R}{dt} + \frac{d\Sigma_e}{dt} = \frac{d\Sigma}{dt} + \frac{d\Sigma_e}{dt}, \tag{2.58}$$

where $\frac{d\Sigma}{dt} = \frac{d\Sigma_D}{dt} + \frac{d\Sigma_R}{dt}$ is the total entropy production rate comprising of reaction and diffusion entropy production rates (EPRs). In nonequilibrium thermodynamics, Eq. (2.58) can be regarded as the entropy balance equation[20] demonstrating the relation between entropy change, entropy production, and entropy flow. We can further represent Eq. (2.58) as $\frac{d\Sigma}{dt} = \frac{dS}{dt} - \frac{d\Sigma_e}{dt}$. The entropy flow part, $-\frac{d\Sigma_e}{dt}$ captures the entropy change in the environment (considering heat is supplied by the environment), and $\frac{dS}{dt}$ represents the system entropy change of the system. Therefore, we assert that the entropy production rate encapsulates the total entropy change in the both system and environment, and by the virtue of second law of thermodynamics entropy production rate has to be positive, $\frac{d\Sigma}{dt} \geq 0$.

Explicit expressions of reaction and diffusion entropy production

Reaction entropy production rates read, $\frac{d\Sigma_R}{dt} = \frac{1}{T}\sum_\rho f_\rho j_\rho$. Now utilizing the definition of net flux, j_ρ in Eq. (2.6) and the expression of affinity in terms of reaction fluxes from

Eq. (2.44), we derive the following expression of the reaction entropy production rate,

$$\frac{d\Sigma_R}{dt} = \frac{1}{T}\sum_{\rho}(j_{+\rho} - j_{-\rho}) \ln \frac{j_{+\rho}}{j_{-\rho}}. \tag{2.59}$$

While, the diffusion entropy production rate has the following expression, $\frac{d\Sigma_D}{dt} = \frac{1}{T}\sum_{\sigma} J_\sigma F_\sigma$. The diffusive flux, J_σ, is provided by Fick's law presented in Eq. (2.26), and diffusion affinity is given by Eq. (2.46). Thus, collecting the mathematical expression of diffusive flux and force, we drive the expression of the diffusion EPR as,

$$\frac{d\Sigma_D}{dt} = \frac{1}{T}\sum_{\sigma} \frac{D_{\sigma\sigma'}}{z_\sigma}\frac{\partial z_{\sigma'}}{\partial r}\frac{\partial z_\sigma}{\partial r}, \tag{2.60}$$

where $\sigma = \sigma'$ for the self diffusion and $\sigma \neq \sigma'$ for the cross diffusion.

Example of diffusion entropy production rate: For the two variable systems like Brusselator RDS, we can represent the diffusion entropy production rate in the presence of both cross and self diffusion as, $\frac{d\Sigma_D}{dt} = \frac{1}{T}\Big[D_{11}\frac{\|\frac{\partial x}{\partial r}\|^2}{x} + D_{22}\frac{\|\frac{\partial y}{\partial r}\|^2}{y} + D_{12}\frac{\|\frac{\partial y}{\partial r}\|\|\frac{\partial x}{\partial r}\|}{x} + D_{21}\frac{\|\frac{\partial x}{\partial r}\|\|\frac{\partial y}{\partial r}\|}{y}\Big]$, where x and y are concentration of two relevant intermediate species of these RDS and the last two terms are related to cross diffusion.

2.4.9 Connection between Gibbs free energy and EPR

From the Gibbs free energy expression in Eq. (2.41), we derive,

$$\frac{dG}{dt} = \sum_{\sigma}(\mu_\sigma \frac{dz_\sigma}{dt} + z_\sigma \frac{d\mu_\sigma}{dt} - \frac{dz_\sigma}{dt}) = \sum_{\sigma} \mu_\sigma \frac{dz_\sigma}{dt}. \tag{2.61}$$

From the RDS presented in Eq. (2.29), we can express $\frac{dz_\sigma}{dt} = -\frac{\partial J_\sigma}{\partial r} + \sum_\rho S^\sigma_\rho j_\rho$. Therefore, $\frac{dG}{dt} = \sum_\sigma \mu_\sigma \frac{dz_\sigma}{dt} = \sum_\sigma \mu_\sigma(-\frac{\partial J_\sigma}{\partial r} + \sum_\rho S^\sigma_\rho j_\rho)$. Now substituting $\sum_\sigma \mu_\sigma \frac{\partial J_\sigma}{\partial r} = \sum_\sigma(\frac{\partial(\mu_\sigma J_\sigma)}{\partial r} - J_\sigma \frac{\partial \mu_\sigma}{\partial r})$, we acquire $\frac{dG}{dt} = \sum_\sigma(-\frac{\partial(\mu_\sigma J_\sigma)}{\partial r} + J_\sigma \frac{\partial \mu_\sigma}{\partial r}) + \sum_\sigma \mu_\sigma \sum_\rho S^\sigma_\rho j_\rho$. No divergence of the system corresponding to the diffusion aids us in expressing,

$$\frac{dG}{dt} = \sum_{\sigma} J_\sigma \frac{\partial \mu_\sigma}{\partial r} + \sum_{\sigma}\mu_\sigma \sum_{\rho} S^\sigma_\rho j_\rho. \tag{2.62}$$

Identifying the driving forces, i.e., diffusion affinity, $F_\sigma(r,t) = -\frac{\partial \mu_\sigma}{\partial r}$ and reaction affinity, $f_\rho = -\sum_\sigma S^\sigma_\rho \mu_\sigma$ in the above equation, we alternatively represent Eq. (2.62) as,

$$\frac{dG}{dt} = -\sum_\sigma J_\sigma F_\sigma - \sum_\rho f_\rho j_\rho = T[-\frac{d\Sigma_D}{dt} - \frac{d\Sigma_R}{dt}] = -T\frac{d\Sigma}{dt} \leq 0. \tag{2.63}$$

2.4.10 Kullback-Leibler divergence (Relative entropy)

Kullback-Leibler (KL) divergence or relative entropy of information theory[144] is always positive, and in a chemical system, it captures the dissimilarity between a concentration distribution, z_σ, and reference concentration, z'_σ.

Positivity of the Kullback-Leibler divergence, D_{KL}, can be shown by using the fact that $-\ln z \geq 1 - z$, where z is an arbitrary positive variable. Now considering $z = \frac{z'_\sigma}{z_\sigma}$ with z_σ and z'_σ being two different concentration distributions, we can write,

$$-\ln \frac{z'_\sigma}{z_\sigma} \geq 1 - \frac{z'_\sigma}{z_\sigma} \implies -\ln \frac{z'_\sigma}{z_\sigma} - (1 - \frac{z'_\sigma}{z_\sigma}) \geq 0. \tag{2.64}$$

Now, KL divergence for the non-normalized concentration distribution reads,

$$D_{KL}(z_\sigma || z'_\sigma) = \sum_\sigma z_\sigma \ln \frac{z_\sigma}{z'_\sigma} - (z_\sigma - z'_\sigma)$$

$$\implies D_{KL}(z_\sigma || z'_\sigma) = \sum_\sigma z_\sigma [-\ln \frac{z'_\sigma}{z_\sigma} - (1 - \frac{z'_\sigma}{z_\sigma})]. \tag{2.65}$$

Since the relation within the bracket in Eq. (2.65) is always non-negative according to the relation in (2.64), and concentration distribution z_σ is positive, $D_{KL}(z_\sigma || z'_\sigma) \geq 0$.

2.4.11 Connection between Gibbs free energy and KL divergence

For two arbitrary concentration distributions, z_σ and z'_σ related to an RDS with the same solvent, we can write the difference between Gibbs free energy using Eq. (2.41) as

$$G(z_\sigma) - G(z'_\sigma) = \sum_\sigma z_\sigma \ln z_\sigma - z_\sigma \ln z'_\sigma + z_\sigma \ln z'_\sigma - z'_\sigma \ln z'_\sigma - (z_\sigma - z'_\sigma) + \mu^o_\sigma (z_\sigma - z'_\sigma)$$

. Further by rearranging and inserting $\mu^o_\sigma + \ln z'_\sigma = \mu'_\sigma$, we can write

$$G(z_\sigma) - G(z'_\sigma) = \sum_\sigma z_\sigma \ln \frac{z_\sigma}{z'_\sigma} - (z_\sigma - z'_\sigma) + \mu'_\sigma(z_\sigma - z'_\sigma).$$

Now identifying the KL divergence expression in Eq. (2.65), we finally express

$$G(z_\sigma) - G(z'_\sigma) = D_{KL}(z_\sigma||z'_\sigma) + \sum_\sigma \mu'_\sigma(z_\sigma - z'_\sigma). \tag{2.66}$$

The above expression reveals how the difference between nonequilibrium Gibbs free energy corresponding to two arbitrary distributions can be related to KL divergence. If we consider the concentration distribution, z'_σ to be equilibrium, z^{eq}_σ, and corresponding chemical potential as $\sum_\sigma \mu^{eq,}_\sigma$ then exploiting the relation in Eq. (2.49), we arrive at a relation between equilibrium and nonequilibrium Gibbs free energy of the system as

$$G(z_\sigma) = G(z^{eq}_\sigma) + D_{KL}(z_\sigma||z^{eq}_\sigma). \tag{2.67}$$

As the minimum value of, $D_{KL}(z_\sigma||z^{eq}_\sigma)$ can be zero (for $z_\sigma = z^{eq}_\sigma$), the above equation implies that the nonequilibrium Gibbs free energy of the closed system is minimized to $G(z^{eq}_\sigma)$ at equilibrium. Further, Eq. (2.67) suggests that G or D_{KL} can be regarded as a Lyapunov function[87] in the closed system.

2.4.12 Chemical work: First law in open system

For an open system, we have an additional flux term, $\mathcal{J}_C$ in the rate equation related to the material exchange between the system and chemostats. Then from Eq. (2.53), we can extend the expression time derivative of enthalpy as, $\frac{dH}{dt} = \sum_\sigma H^o_\sigma \frac{dz_\sigma}{dt} = \frac{dQ}{dt} + \sum_C H^o_C \mathcal{J}_C$ ($H^o_C \mathcal{J}_C$ is only nonzero for chemostatted species). Utilizing Eq. (2.55), we further deduce, $\frac{dH}{dt} = \frac{dQ}{dt} + \sum_C(\mu_C \mathcal{J}_C + T\Sigma_C \mathcal{J}_C)$. Here the part, $\frac{1}{T}\frac{dQ}{dt} + \sum_C(\Sigma_C \mathcal{J}_C)$ is the total entropy flow rate of the open system, $\frac{d\Sigma_e}{dt}$, with the term $\Sigma_C \mathcal{J}_C$ being associated with

the exchange of chemical species between system and chemostats. Thus, we express

$$\frac{dH}{dt} = T\frac{d\Sigma_e}{dt} + \sum_C \mu_C \mathcal{J}_C, \tag{2.68}$$

where $\sum_C \mu_C \mathcal{J}_C$ is defined as the chemical work[99,106] rate, $\dot{w}_{chem}$ done by chemostats. Eq. (2.68) can be regarded as the first law of thermodynamics in open CRN.

2.4.13 Nonequilibrium Landauer principle

For the open RDS, we have an additional, $\mathcal{J}_C$ term corresponding to chemostatted species in $\frac{dz_\sigma}{dt}$, and Eq. (2.61) suggests that the additional term will also modify the time derivative of Gibbs free energy. Therefore, Eq. (2.62) now have an additional term, $\sum_C \mu_C \mathcal{J}_C$, which is chemical work rate. So, in the open RDS, Eq. (2.63) becomes

$$\dot{w}_{chem} - \frac{dG}{dt} = T\frac{d\Sigma}{dt} \geq 0, \tag{2.69}$$

where the positivity of the entropy production rate ensures that the chemical work rate of the chemostats on the open RDS has to be higher than the time derivative of the Gibbs free energy. The EPR in Eq. (2.69) has contributions from reaction and diffusion.

Now integrating Eq. (2.69) between an initial ('i') and final ('f') concentration distribution, z_{σ_i} and z_{σ_f}, respectively, we acquire, $w_{chem} - (G_f - G_i) = T(\Sigma_f - \Sigma_i)$. Now utilizing Eq. (2.67), it is possible to express this equation in the following form as $w_{chem} - (G_f(z^{eq}_{\sigma_f}) + D_{KL}(z_{\sigma_f}||z^{eq}_{\sigma_f}) - (G_i(z^{eq}_{\sigma_i}) + D_{KL}(z_{\sigma_i}||z^{eq}_{\sigma_i}))) = T(\Sigma_f - \Sigma_i) \implies w_{chem} - (G_f(z^{eq}_{\sigma_f}) - G_i(z^{eq}_{\sigma_i})) - (D_{KL}(z_{\sigma_f}||z^{eq}_{\sigma_f}) - D_{KL}(z_{\sigma_i}||z^{eq}_{\sigma_i})) = T(\Sigma_f - \Sigma_i) \implies w_{chem} - \Delta G^{eq} - \Delta D_{KL} = T\Delta\Sigma$, where we have denoted $\Delta G^{eq} = G_f(z^{eq}_{\sigma_f}) - G_i(z^{eq}_{\sigma_i})$, $\Delta D_{KL} = D_{KL}(z_{\sigma_f}||z^{eq}_{\sigma_f}) - D_{KL}(z_{\sigma_i}||z^{eq}_{\sigma_i})$, and $\Delta\Sigma = \Sigma_f - \Sigma_i$ in the last expression. Defining $w_{chem} - \Delta G^{eq} = w^{irr}_{chem}$ as the irreversible chemical work[106], we can obtain

$$w^{irr}_{chem} = T\Delta\Sigma + \Delta D_{KL}, \tag{2.70}$$

which can be regarded as nonequilibrium Landauer principle[63,145,106]. Since, $T\Delta\Sigma$ is

always positive, we can assert from the above relation that $w^{irr}_{chem} \geq \Delta D_{KL}$.

2.4.14 Reference chemical potentials and equilibrium concentration distributions for open system

In an open system, conservation laws are classified into broken and unbroken ones as discussed in Sec. 2.2.8, and the equilibrium chemical potential of chemostatted species in the closed system can be identified as a reference chemical potential of the chemostatted species[107,146]. For the unbroken conservation laws, entries related to chemostatted species are 0, and therefore, the reference chemical potential of the chemostatted species can be expressed in terms of the broken conservation laws as,

$$\mu^{ref}_{C} = \sum_{\lambda_b} R_{\lambda_b} l^{\lambda_b}_{C}, \tag{2.71}$$

with R_{λ_b} being the real coefficient, and can be recognized as broken generalized forces[106]. For chemostatted species, using Eq. (2.48), we can write, $z^{eq}_{C} = \exp -(\mu^{o}_{C} - \sum_{\lambda_b} R_{\lambda_b} l^{\lambda_b}_{C})$. The subset of chemostatted species, C_b, will set reference chemical potentials, $\mu^{ref}_{C_b}$ in the system, and in the case of homogeneous concentration of chemostatted species, these reference potentials simplify to $\mu^{ref}_{C_b} = \mu_{C_b}$ for all spatial point. Exploiting the reference chemical potentials of the chemostatted species, C_b, we can determine the reference chemical potential of the chemostatted species, C_u, and intermediate species, I. By definition, the reference chemical potentials of the chemostatted species, C_b, read, $\mu^{ref}_{C_b} = \sum_{\lambda_b} R_{\lambda_b} l^{\lambda_b}_{C_b}$ from Eq. (2.71). From this we can derive the broken generalized force as, $\sum_{\lambda_b} R_{\lambda_b} = \mu^{ref}_{C_b} \sum_{\lambda_b} {l^{\lambda_b}_{C_b}}^{-1}$. Further, for the set of chemostatted species, C_u, reference chemical potential can be written from Eq. (2.71) as, $\mu^{ref}_{C_u} = \sum_{\lambda_b} R_{\lambda_b} l^{\lambda_b}_{C_u} = \mu^{ref}_{C_b} {l^{\lambda_b}_{C_b}}^{-1} l^{\lambda_b}_{C_u}$ (inserting $\sum_{\lambda_b} R_{\lambda_b} = \mu^{ref}_{C_b} \sum_{\lambda_b} {l^{\lambda_b}_{C_b}}^{-1}$). For the intermediate species, reference chemical potentials can be expressed as $\mu^{ref}_{I} = \sum_{\lambda} R_{\lambda} l^{\lambda}_{I} = \sum_{\lambda_u} R_{\lambda_u} l^{\lambda_u}_{I} + \sum_{\lambda_b} R_{\lambda_b} l^{\lambda_b}_{I}$. After substituting $\sum_{\lambda_b} R_{\lambda_b} = \mu^{ref}_{C_b} \sum_{\lambda_b} {l^{\lambda_b}_{C_b}}^{-1}$, reference chemical potentials of intermediate species become $\mu^{ref}_{I} = \sum_{\lambda_u} R_{\lambda_u} l^{\lambda_u}_{I} + \mu^{ref}_{C_b} \sum_{\lambda_b} {l^{\lambda_b}_{C_b}}^{-1} l^{\lambda_b}_{I}$. In the absence of any unbroken conservation laws, μ^{ref}_{I} reduces to $\mu^{ref}_{I} = \mu^{ref}_{C_b} \sum_{\lambda_b} {l^{\lambda_b}_{C_b}}^{-1} l^{\lambda_b}_{I}$. These reference chemical potentials

aid in describing the equilibrium concentration distribution and using Eq. (2.48), we can generally express the reference equilibrium concentration distribution as,

$$z_\sigma^{eq} = \exp -(\mu_\sigma^o - \mu_\sigma^{ref}). \tag{2.72}$$

Example of reference chemical potentials and equilibrium distribution: For the Brusselator CRN investigation in this thesis, we choose the combination, (A, B) as the reference chemostatted species and therefore are the elements of the subset, C_b. The corresponding inverse of the identity matrix, $l_C^{\lambda_b}$ is ${l_C^{\lambda_b}}^{-1} = \begin{pmatrix} 1 & 0 \\ 0 & 1 \end{pmatrix}$. Here, reference chemical potentials of species A and B are $\mu_A^{ref} = \mu_A$ and $\mu_B^{ref} = \mu_B$. For chemostatted species belonging to subset, C_u, i.e. D and E here, the reference chemical potential emerges as $\mu_D^{ref} = \mu_{C_b}^{ref} {l_{C_b}^{\lambda_b}}^{-1} l_d^{\lambda_b} = \mu_B$, and $\mu_E^{ref} = \mu_{C_b}^{ref} {l_{C_b}^{\lambda_b}}^{-1} l_e^{\lambda_b} = \mu_A$. Since both of the conservation laws are broken, we can find the reference chemical potential of intermediate species of the Brusselator as follows, $\mu_X^{ref} = \mu_{C_b}^{ref} \sum_{\lambda_b} {l_{C_b}^{\lambda_b}}^{-1} l_x^{\lambda_b} = \mu_A$, and $\mu_Y^{ref} = \mu_{C_b}^{ref} \sum_{\lambda_b} {l_{C_b}^{\lambda_b}}^{-1} l_y^{\lambda_b} = \mu_A$.

After identifying the reference chemical potential of species, we can express the reference equilibrium chemical distribution of the species in the Brusselaor using Eq. (2.72). For species A, and B we obtain, $a^{eq} = \exp(\mu_A - \mu_A^o) = \exp(\mu_A^o + \ln a - \mu_A^o) = a$, and $b^{eq} = \exp(\mu_B - \mu_B^o) = \exp(\mu_B^o + \ln b - \mu_B^o) = b$. Since, $\mu_D^{ref} = \mu_B$, equilibrium distribution of the species D is $d^{eq} = \exp(\mu_B - \mu_D^o) = \exp(\mu_B^o + \ln b - \mu_D^o) = b \exp(\mu_B^o - \mu_D^o)$. From Eq. (2.4.5), we derive, $\mu_B^o - \mu_D^o = \ln \frac{k_2 k_3}{k_{-2} k_{-3}}$ and therefore, $d^{eq} = b \frac{k_2 k_3}{k_{-2} k_{-3}}$. Similarly, for the species E, $\mu_E^{ref} = \mu_A$ and $e^{eq} = a \frac{k_1 k_4}{k_{-1} k_{-4}}$. We can also acquire the explicit expression of the equilibrium distribution of the intermediate species, X and Y in the same fashion, $x^{eq} = a \frac{k_1}{k_{-1}}$, and $y^{eq} = a \frac{k_1 k_{-3}}{k_3 k_{-1}}$.

2.5 Moieties exchange in the open system and its cost

As conservation laws represent moieties, we will now define the concentration of moieties exchanged with the environment in the open system, where conservation laws are broken.

We quantify concentrations of moieties exchanged through the chemostatted species as

$$M_{C_b} = \sum_{\lambda_b} {l_{C_b}^{\lambda_b}}^{-1} L_{\lambda_b}, \tag{2.73}$$

where L_{λ_b} is the broken component defined in Sec. 2.2.8. Time derivative of the moieties can be expressed as, $\frac{dM_{C_b}}{dt} = \sum_{\lambda_b} {l_{C_b}^{\lambda_b}}^{-1} \sum_{\sigma} l_{\sigma}^{\lambda_b} \frac{dz_\sigma}{dt} = \sum_{\lambda_b} {l_{C_b}^{\lambda_b}}^{-1} (\sum_{\rho} (\sum_I l_I^{\lambda_b} S_\rho^I + \sum_C l_C^{\lambda_b} S_\rho^C) j_\rho + \sum_C l_C^{\lambda_b} \mathcal{J}_C)$, where we exploit rate equation of the open system from Eq. (2.11). Further, the definition of the general conservation law in the open system in Eq. (2.12) implies that, $\sum_I l_I^{\lambda_b} S_\rho^I + \sum_C l_C^{\lambda_b} S_\rho^C = 0$. Therefore, the rate of change of moieties concentration becomes, $\frac{dM_{C_b}}{dt} = \sum_{\lambda_b} {l_{C_b}^{\lambda_b}}^{-1} \sum_C l_C^{\lambda_b} \mathcal{J}_C = \sum_{\lambda_b} {l_{C_b}^{\lambda_b}}^{-1} \sum_{C_b} l_{C_b}^{\lambda_b} \mathcal{J}_{C_b} + \sum_{\lambda_b} {l_{C_b}^{\lambda_b}}^{-1} \sum_{C_u} l_{C_u}^{\lambda_b} \mathcal{J}_{C_u}$, by employing the decomposition of chemostatted species into two subsets $C = C_b \bigcup C_u$. Finally, we obtain the change of moieties concentration exchanged with the environment as

$$\frac{dM_{C_b}}{dt} = \mathcal{J}_{C_b} + \sum_{\lambda_b} {l_{C_b}^{\lambda_b}}^{-1} \sum_{C_u} l_{C_u}^{\lambda_b} \mathcal{J}_{C_u}. \tag{2.74}$$

Since we have presented the reference chemical potential of reference chemostatted species, C_b, as$\mu_{C_b}^{ref}$ previously, we can capture energetics corresponding to the rate of moieties exchanged with the environment as $\mu_{C_b}^{ref} \frac{dM_{C_b}}{dt}$. From Eq. (2.74), we express, $\mu_{C_b}^{ref} \frac{dM_{C_b}}{dt} = \mu_{C_b}^{ref} (\mathcal{J}_{C_b} + \sum_{\lambda_b} {l_{C_b}^{\lambda_b}}^{-1} \sum_{C_u} l_{C_u}^{\lambda_b} \mathcal{J}_{C_u})$. We can also represent the energetic of the rate of moieties exchanged with environment as, $\mu_{C_b}^{ref} \frac{dM_{C_b}}{dt} = \frac{d(\mu_{C_b}^{ref} M_{C_b})}{dt} - (\frac{d\mu_{C_b}^{ref}}{dt}) M_{C_b}$. Thus, we acquire the following relation,

$$\frac{d(\sum_{C_b} \mu_{C_b}^{ref} M_{C_b})}{dt} - \sum_{C_b} (\frac{d\mu_{C_b}^{ref}}{dt}) M_{C_b} = \sum_{C_b} \mu_{C_b}^{ref} (\mathcal{J}_{C_b} + \sum_{\lambda_b} {l_{C_b}^{\lambda_b}}^{-1} \sum_{C_u} l_{C_u}^{\lambda_b} \mathcal{J}_{C_u}). \tag{2.75}$$

Now previously, we defined the rate of chemical work as $\dot{w}_{chem} = \sum_C \mu_C \mathcal{J}_C$, and considering the decomposition of chemostatted species in open system, this rate of chemical work can be represented as, $\dot{w}_{chem} = \sum_{C_b} \mu_{C_b} \mathcal{J}_{C_b} + \sum_{C_u} \mu_{C_u} \mathcal{J}_{C_u}$. Utilizing this relation of chemical work rate in Eq. (2.75), we arrive at $\frac{d(\sum_{C_b} \mu_{C_b}^{ref} M_{C_b})}{dt} - \sum_{C_b} (\frac{d\mu_{C_b}^{ref}}{dt}) M_{C_b} -$

$\dot{w}_{chem} = \sum_{C_b} \mu_{C_b}^{ref} (\mathcal{J}_{C_b} + \sum_{\lambda_b} {l_{C_b}^{\lambda_b}}^{-1} \sum_{C_u} l_{C_u}^{\lambda_b} \mathcal{J}_{C_u}) - \sum_{C_b} \mu_{C_b} \mathcal{J}_{C_b} - \sum_{C_u} \mu_{C_u} \mathcal{J}_{C_u}$. Further, by rearranging the above relation, we obtain,

$$\frac{d(\sum_{C_b} \mu_{C_b}^{ref} M_{C_b})}{dt} - \sum_{C_b} (\frac{d\mu_{C_b}^{ref}}{dt}) M_{C_b} - \dot{w}_{chem} = \sum_{C_b} (\mu_{C_b}^{ref} - \mu_{C_b}) \mathcal{J}_{C_b} + (\sum_{C_b} \mu_{C_b}^{ref} \sum_{\lambda_b} {l_{C_b}^{\lambda_b}}^{-1} \sum_{C_u} l_{C_u}^{\lambda_b} - \sum_{C_u} \mu_{C_u}) \mathcal{J}_{C_u}. \tag{2.76}$$

2.5.1 Fundamental nonconservative force:

Here, we introduce the definition of the fundamental nonconservative forces[107,146] related to chemostatted species as

$$\mathcal{F}_C = \mu_C - \sum_{C_b} \mu_{C_b}^{ref} \sum_{\lambda_b} {l_{C_b}^{\lambda_b}}^{-1} l_C^{\lambda_b}. \tag{2.77}$$

For the set of chemostatted species, C_b, expresssion of fundamental force reduces to $\mathcal{F}_{C_b} = \mu_{C_b} - \mu_{C_b}^{ref}$. For homogeneous chemostatted species distribution, the reference chemical potential $\mu_{C_b}^{ref}$ is equal to μ_{C_b}, as mentioned earlier. Therefore, there is no fundamental force associated with the chemostatted species set, C_b, $\mathcal{F}_{C_b} = 0$. Whereas, for the chemostatted species subset, C_u, the fundamental force read $\mathcal{F}_{C_u} = \mu_{C_u} - \sum_{C_b} \mu_{C_b} \sum_{\lambda_b} {l_{C_b}^{\lambda_b}}^{-1} l_{C_u}^{\lambda_b}$, which can be interpreted as the difference between chemical potentials of dissimilar chemostatted species coupled by reactions[107,146]. These fundamental forces generate steady currents among chemostats. As the part ${l_{C_b}^{\lambda_b}}^{-1} l_{C_u}^{\lambda_b}$ is identified as $\mu_{C_u}^{ref}$ previously, we can simply write $\mathcal{F}_{C_u} = \mu_{C_u} - \mu_{C_u}^{ref}$. Utilizing the definition of the fundamental forces, we arrive at the following compact form of Eq. (2.77),

$$\frac{d(\sum_{C_b} \mu_{C_b}^{ref} M_{C_b})}{dt} - \sum_{C_b} (\frac{d\mu_{C_b}^{ref}}{dt}) M_{C_b} - \dot{w}_{chem} = -\sum_{C_b} \mathcal{F}_{C_b} \mathcal{J}_{C_b} - \sum_{C_u} \mathcal{F}_{C_u} \mathcal{J}_{C_u} = -\sum_{C} \mathcal{F}_C \mathcal{J}_C. \tag{2.78}$$

Example of fundamental force: Since for the Brusselator system, $\mu_D^{ref} = \mu_B$ and $\mu_E^{ref} = \mu_A$, we can acquire the fundamental forces of the Brusselator open system as $\mathcal{F}_D = \mu_D - \mu_B = \mu_D^o - \mu_B^o + \ln \frac{d}{b} = \ln \frac{k_{-2} k_{-3} d}{k_2 k_3 b}$ and $\mathcal{F}_E = \mu_E - \mu_A = \ln \frac{k_{-1} k_{-4} e}{k_1 k_4 a}$.

2.5.2 Nonconservative chemical work rate

In Eq. (2.78), we recognize the term, $-\sum_{C_b}(\frac{d\mu^{ref}_{C_b}}{dt})M_{C_b}$ as the work rate due to driving, $\dot{w}_{driv}$. It quantifies the work rate needed to control the reference chemostatted species by time-dependent driving. For the autonomous systems considered in this thesis, there is no time-dependent driving, and hence no driving work exists, i.e., $\dot{w}_{driv} = 0$. Further, the term $\sum_C \mathcal{F}_C \mathcal{J}_C$ is identified as the nonconservative chemical work rate, $\dot{w}_{ncon}$ needed for sustaining steady currents among chemostats. Thus the nonconservative work holds the concentration of the chemostatted species C_u at constant value by offsetting the effect of chemical reactions. As we shown previously that $\mathcal{F}_{C_b} = 0$, the above equation, $\sum_C \mathcal{F}_C \mathcal{J}_C = \dot{w}_{ncon}$ simplifies to $\sum_C \mathcal{F}_{C_u} \mathcal{J}_{C_u} = \dot{w}_{ncon}$. Further, we do not have work owing to the diffusion of the chemostatted species having homogeneous distribution.

In terms of nonconservative work rates, Eq. (2.78) becomes, $\dot{w}_{chem} = \frac{d(\sum_{C_b} \mu^{ref}_{C_b} M_{C_b})}{dt} + \dot{w}_{driv} + \dot{w}_{ncon}$. Now exploiting Eq. (2.69), we acquire the following equation, $\frac{dG}{dt} + T\frac{d\Sigma}{dt} = \frac{d(\sum_{C_b} \mu^{ref}_{C_b} M_{C_b})}{dt} + \dot{w}_{driv} + \dot{w}_{ncon}$. Now rearranging these terms we arrive at the equation,

$$T\frac{d\Sigma}{dt} = -\frac{d\mathcal{G}}{dt} + \dot{w}_{driv} + \dot{w}_{ncon}, \tag{2.79}$$

where $\mathcal{G}$ is the semigrand Gibbs free energy[107,115], and can be expressed as

$$\mathcal{G} = G - \sum_{C_b} \mu^{ref}_{C_b} M_{C_b}. \tag{2.80}$$

We discuss the semigrand Gibbs free energy in detail in the next section. Eq. (2.79) represents the decomposition of the dissipation into three different parts for a system far from equilibrium. Since for the autonomous system, $\dot{w}_{driv} = 0$, we are left with, $T\frac{d\Sigma}{dt} = -\frac{d\mathcal{G}}{dt} + \dot{w}_{ncon}$. Additionally, if the fundamental conservative forces vanish, then Eq. (2.79) reduces to $\frac{d\mathcal{G}}{dt} = -T\frac{d\Sigma}{dt} \leq 0$. This relation implies that an open RDS can relax to an equilibrium state by minimizing the semigrand Gibbs free energy in the absence of any fundamental force and time-dependent driving.

2.5.3 Proper thermodynamic potential of an open system

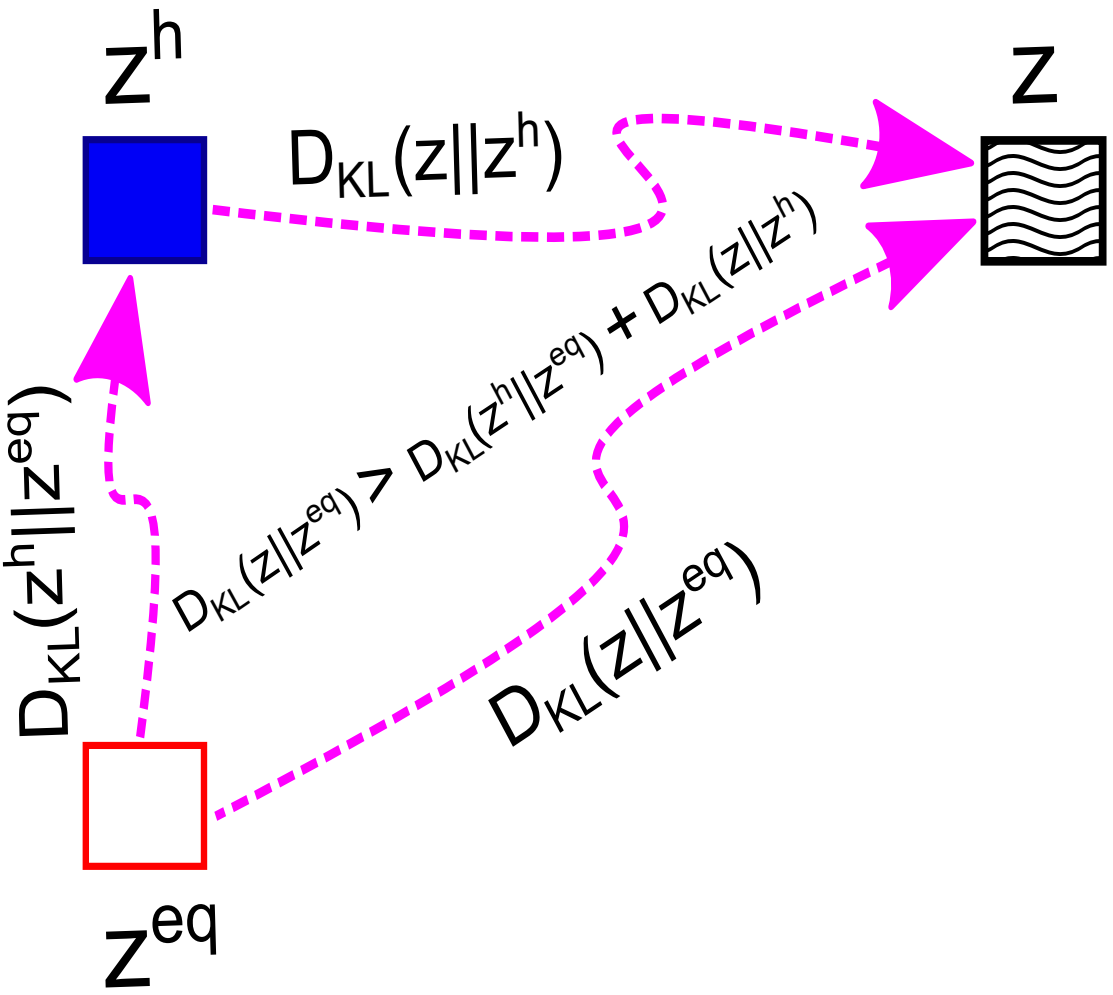

Figure 2.5: Schematic representation of transitions within three different states and their information-theoretic costs. Here, z^{eq} denotes the concentration under a detailed balance situation. z^h refers to the nonequilibrium homogeneous state, while z corresponds to an arbitrary nonequilibrium state with a pattern. Transitions are characterized by the Kullback-Leibler divergence, D_{KL}.

Since the equilibrium Gibbs free energy was characterized by all the conservation laws of the closed RDS, the nonequilibrium Gibbs free energy, G, will be not minimized in the open system due to the existence of the broken conservation laws, l^{λ_b}, even if the system relaxes to an equilibrium concentration distribution. The proper energy content of an open CRN can be acquired by subtracting the energetic cost of moieties exchange from

the nonequilibrium Gibbs free energy of the system. We obtained the semigrand Gibbs free energy expression in Eq. 2.80 by subtracting $\sum_{C_b} \mu_{C_b}^{ref} M_{C_b}$ from the nonequilibrium Gibbs free energy, G. In the semigrand Gibbs free energy definition, we can replace the reference chemical potential, $\mu_{C_b}^{ref}$ and moieties, M_{C_b} in accordance to Eq. (2.71) and Eq. (2.73), respectively $\mathcal{G} = G - \sum_{C_b} \sum_{\lambda_b} R_{\lambda_b} l_{C_b}^{\lambda_b} {l_{C_b}^{\lambda_b}}^{-1} L_{\lambda_b} = G - \sum_{\lambda_b} R_{\lambda_b} L_{\lambda_b}$. We can identify this transformation analogous to the Legendre transfromation of G.

As discussed in the previous section, the reference equilibrium counterpart, $\mathcal{G}^{eq}$ sets the lower bound of semigrand Gibbs free energy, and this $\mathcal{G}^{eq}$ is acquired by exploiting the concentration fields in the detailed balanced condition of the system, z_σ^{eq}. In the above expression of the semigrand Gibbs free energy, if we insert the equilibrium Gibbs free energy expression in Eq. (2.50), we obtain the reference equilibrium counterpart of the semigrand Gibbs free energy as, $\mathcal{G}^{eq} = G^{eq} - \sum_{\lambda_b} R_{\lambda_b} L_{\lambda_b} = G_0 + \sum_\lambda R_\lambda L^\lambda - \sum_{\sigma \neq 0} z_\sigma^{eq} - \sum_{\lambda_b} R_{\lambda_b} L_{\lambda_b} = G_0 + \sum_{\lambda_u} R_{\lambda_u} L_{\lambda_u} - \sum_{\sigma \neq 0} z_\sigma^{eq}$. Now subtracting this equilibrium semigrand Gibbs energy from its nonequilibrium counterpart, we acquire $\mathcal{G} - \mathcal{G}^{eq} = (G - \sum_{\lambda_b} R_{\lambda_b} L_{\lambda_b}) - (G_0 + \sum_{\lambda_u} R_{\lambda_u} L_{\lambda_u} - \sum_{\sigma \neq 0} z_\sigma^{eq})$. Rearranging this expression and utilizing Eq. (2.50) and Eq. (2.67), this difference emerges as $\mathcal{G} - \mathcal{G}^{eq} = (G^{eq} + D_{KL}(z_\sigma || z_\sigma^{eq})) - \sum_\lambda R_\lambda L_\lambda - (G_0 - \sum_{\sigma \neq 0} z_\sigma^{eq}) = (G_0 + \sum_\lambda R_\lambda L^\lambda - \sum_{\sigma \neq 0} z_\sigma^{eq} + D_{KL}(z_\sigma || z_\sigma^{eq})) - \sum_\lambda R_\lambda L_\lambda - (G_0 - \sum_{\sigma \neq 0} z_\sigma^{eq}) = D_{KL}(z_\sigma || z_\sigma^{eq}))$. Thus, the semigrand Gibbs free energy and its reference equilibrium counterpart are connected as

$$\mathcal{G} = \mathcal{G}^{eq} + D_{KL}(z_\sigma || z_\sigma^{eq}). \tag{2.81}$$

Since $D_{KL}(z_\sigma || z_\sigma^{eq}) \geq 0$, we can assert that nonequilibrium semigrand Gibbs free energy is larger than its equilibrium counterpart and it takes minimum value for the equilibrium distribution. Instead of an equilibrium state, if we consider the initial state as an arbitrary homogeneous state, z_σ^h, the energetic cost of reaching the homogeneous state from an equilibrium state can be quantified as

$$\mathcal{G}^h = \mathcal{G}^{eq} + D_{KL}(z_\sigma^h || z_\sigma^{eq}). \tag{2.82}$$

Now, by subtracting Eq. (2.81) and (2.82), we acquire the difference between semigrand Gibbs free energy of nonequilibrium inhomogeneous and initial homogeneous states as

$$\mathcal{G} - \mathcal{G}^h = D_{KL}(z_\sigma||z_\sigma^{eq}) - D_{KL}(z_\sigma^h||z_\sigma^{eq}) = D_{KL}(z_\sigma||z_\sigma^h) + \ln\frac{z_\sigma^h}{z_\sigma^{eq}}(z_\sigma - z_\sigma^h), \tag{2.83}$$

where $D_{KL}(z_\sigma||z_\sigma^h)$ is the KL divergence between concentrations, z_σ and z_σ^h.

Notably, the above general relation in Eq. (2.83) reveals that the switching from equilibrium to nonequilibrium inhomogeneous state via a nonequilibrium homogeneous state has a lower information-theoretic cost (KL divergence) in comparison to the direct transition between equilibrium and inhomogeneous states. The above analysis is practical and general, as applicable to arbitrary CRNs. These transitions and corresponding relations are illustrated in Fig. 2.5, where σ is omitted in concentration to maintain concise notations. For the two-variable Brusselator system with a homogeneous concentration of chemostatted species, the relation in (2.83) yields,

$$\mathcal{G} - \mathcal{G}^h = D_{KL}(z_\sigma||z_\sigma^{eq}) - D_{KL}(z_\sigma^h||z_\sigma^{eq}) = D_{KL}(z_\sigma||z_\sigma^h) + \ln\frac{k_{-1}x^h}{k_{+1}a}(x - x^h) + \ln\frac{k_{-1}k_{+3}y^h}{k_{+1}k_{-3}a}(y - y^h). \tag{2.84}$$

2.5.4 Landauer principle with semigrand Gibbs free energy

Similar to Sec. 2.4.13, if we integrate Eq. (2.79) between initial and final concentration distributions and consider no time-dependent driving, then we appear at

$$T\Delta\Sigma + \Delta D_{KL} = -\Delta\mathcal{G}^{eq} + w_{ncon}, \tag{2.85}$$

with the aid of the relation in Eq. 2.81. Since $T\Delta\Sigma$ is positive, we obtain the nonequilibrium Landauer principle in terms of semigrand Gibbs free energy as

$$w_{ncon} - \Delta\mathcal{G}^{eq} \geq \Delta D_{KL}. \tag{2.86}$$

This model will be a simplification and an idealization, and consequently a falsification. It is to be hoped that the features retained for discussion are those of greatest importance in the present state of knowledge.

- A. M. Turing

3

Thermodynamic cost of the overlapping of Turing and Hopf patterns in the presence of cross diffusion

3.1 Pattern through instabilities in a general RDS description

The traditional Turing pattern[4,1,11,72,147] appeared in reaction-diffusion system (RDS) with very different self-diffusion coefficients of activator and inhibitor, resembles the patterns of the living tissues[7,21,148,149]. Whereas, traveling waves[2,3,150] generated in such systems are prevalent in the cellular rhythms[8,151,152] and many such situations. In RDS, diffusion-induced stationary Turing pattern generates due to Turing instabilities, whereas nonlinearity-originated Hopf instability results in temporal oscillation. We can have both the Hopf and Turing instabilities in an RDS. However, the onsets of Turing and Hopf instabilities can be well-separated in the presence of very different diffusion

coefficients corresponding to two species of the RDS. By adjusting these diffusion coefficients, it is possible to modify the onsets of these two instabilities and bring them close together and then we can have a spatiotemporal pattern in the RDS due to the interaction of the spatial mode of the Turing instability and temporal mode of the Hopf instability[28]. Diverse numerical and analytical analysis of this Turing-Hopf interplay and real-world resemblance of these spatiotemporal patterns have been discussed in the context of different dynamical systems[153,154,155,156].

Brusselator RDS is one of the well-studied and simplest prototypical models in which both Turing and Hopf instabilities can arise. Hence, we have utilized the Brusselator model to demonstrate the overlapping of Turing and Hopf instabilities. However, unlike the previous studies, we would extend the scope of studying the spatiotemporal pattern of the Turing-Hopf overlapping to the nonequilibrium thermodynamic regime. Indeed, quantifying the thermodynamic costs of various patterns and the interplay of various instabilities in nonlinear systems are of crucial theoretical interest. This perspective is recently adopted in encapsulating the thermodynamic cost of the Turing pattern in the presence of self diffusion only[107] and chemical waves[157]. Till now, such thermodynamic description for the Turing-Hopf overlapping regime is missing. Hence, our goal is to shed light on the nonequilibrium thermodynamic consequences of patterns that originated due to the overlapping of Turing and Hopf instabilities in the Brusselator RDS. Moreover, we have incorporated cross diffusion in our reaction-diffusion description of the Brusselator that enables Turing instability even in the presence of equal self-diffusion coefficients. When the self-diffusion coefficients are equal, an appropriate selection of cross-diffusion coefficients in RDS can move the onset of Turing and Hopf instabilities close enough and, thus, consequently lead to the overlapping of these two instabilities, triggering a broad spectrum of intricate spatiotemporal patterns to emerge. This study would also quantify the thermodynamic cost of the limit cycle oscillation in the presence of cross diffusion. On the level of methodology, we have here modified the conventional Krylov-Bogolyubov (KB) averaging method[135] to accommodate the cross-diffusion description.

The results presented in this chapter, which investigate the thermodynamic cost due to the overlapping of Turing and Hopf instabilities, were previously published in *Kumar et al., 2020, Physical Review E, 101:042204.*

The plan of this chapter is as follows: After providing the brief context and motivation of our investigation in this section, we will discuss the Brusselator reaction-diffusion system (RDS) in the presence of self and cross diffusion and present the conditions and critical values of the Turing and Hopf instabilities in the next section. Following this, we will delve into the dynamics of the Turing-Hopf overlapping scenario in Sec. 3.3. We will then turn our attention to amplitude equations, discussing formalisms for both Turing and Hopf instabilities in dedicated sections, Sec. 3.4 and Sec. 3.5. The parameter spaces of Turing and Hopf instabilities will be explored for different sets of RDS parameters in Sec. 3.6. In Sec. 3.7, illustrations of concentration fields and amplitude profiles are provided. Then entropic and energetic pictures of Turing-Hopf overlapping will be depicted in Sec. 3.8 and Sec. 3.9, respectively. Finally, we will conclude the chapter.

3.2 Turing and Hopf instabilities in the Brusselator RDS

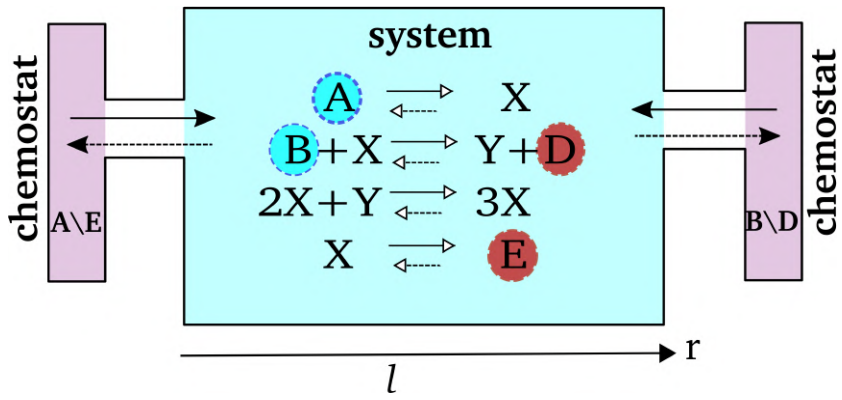

Figure 3.1: Schematic representation of the Brusselator setup. Purple compartments on both sides represent chemostats for maintaining constant concentrations of specified species. Reactions occur within a finite system of length l presented in the middle.

The Brusselator chemical reaction network (CRN), comprising six chemical species and four reversible chemical reactions, is presented in Fig. 3.1. Details about this chemical reaction network are discussed in the previous chapter. As can be seen from the schematic, reactions are occurring along one spatial dimension $r \in [0, l]$ of a finite system of length l. Under the assumption that all the reverse rate constants, $k_{-\rho}$, are negligible in comparison to the forward reaction rate constants, k_ρ, we study the Brusselator RDS presented by Eq. (2.30) in the presence of both self and cross diffusion. In the absence of any diffusion, Brusselator reaction dynamics yield

$$\begin{aligned} \dot{x} &= k_1 a - (k_2 b + k_4)x + k_3 x^2 y \\ \dot{y} &= k_2 b x - k_3 x^2 y, \end{aligned} \tag{3.1}$$

which have steady-state $x_0 = \frac{k_1}{k_4} a, y_0 = \frac{k_2 k_4}{k_1 k_3} \frac{b}{a}$. Selecting the Brusselator CRN for exhibiting the Turing and Hopf patterns in this investigation, we exclude the possibility of subcritical Hopf instability here.

For Brusselator RDS, we obtain conditions of both Hopf and Turing instabilities from linear stability analysis at the steady state. In this regard, the Jacobian matrix of the Brusselator dynamics in (3.1) can be represented as,

$$\mathcal{J} = \begin{pmatrix} -(k_2 b + k_4) + 2k_3 x_0 y_0 & k_3 {x_0}^2 \\ k_2 b - 2k_3 x_0 y_0 & -k_3 {x_0}^2 \end{pmatrix}. \tag{3.2}$$

Thus, elements of this Jacobian matrix, $\mathcal{J}$ can be designated as, $J_{11} = -(k_2 b + k_4) + 2k_3 x_0 y_0$, $J_{12} = k_3 {x_0}^2$, $J_{21} = k_2 b - 2k_3 x_0 y_0$, $J_{22} = -k_3 {x_0}^2$. It is worth mentioning that the Oregonator[158,159], the simplest model for mimicking BZ oscillations, yields a Jacobian matrix with the sign structure (pure activator-inhibitor) opposite to the Brusselator Jacobian matrix (cross activator-inhibitor). Due to this opposite sign structure, cross diffusion can modify these two RDS pictures differently.

3.2.1 Generating Turing instability in Brusselator RDS

In the previous chapter, we have seen the impact of cross diffusion in dictating the Turing instability within a general framework. In the presence of cross diffusion, the Turing pattern generation within the Busselator model in a three-dimensional domain[160] has also been illustrated by using finite volume element approximation. Here, we obtain a critical value of the control parameter and wave number in the 1D Brusselator RDS from the general conditions of Turing instability presented in the previous chapter. Using Eq. (2.31), the Jacobian of the Brusselator RDS can be expressed as

$$\begin{aligned} \mathcal{J}_{\mathcal{D}} &= \mathcal{J} - q^2\mathcal{D} \\ &= \begin{pmatrix} -(k_2 b + k_4) + 2k_3 x_0 y_0 & k_3 {x_0}^2 \\ k_2 b - 2k_3 x_0 y_0 & -k_3 {x_0}^2 \end{pmatrix} - q^2 \begin{pmatrix} D_{11} & D_{12} \\ D_{21} & D_{22} \end{pmatrix}. \end{aligned} \tag{3.3}$$

Substituting all elements of the Jacobian matrix, $\mathcal{J}$ and the determinant, $det(\mathcal{J})$ for the Brusselator into Eq. (2.36), we acquire a quadratic equation of $b^{\frac{1}{2}}$ and then by solving it, we arrive at the critical value of the control parameter, b as

$$b_{cT} = \left(\frac{[D_{11}\frac{k_1^2 k_3}{{k_4}^2} + D_{21}\frac{k_1^2 k_3}{{k_4}^2}]a^2 + 2[det(\mathcal{D})]^{\frac{1}{2}}[\frac{k_1^2 k_3}{k_4}]^{\frac{1}{2}} a + D_{22}k_4}{D_{22}k_2 + D_{12}k_2} \right). \tag{3.4}$$

For this study, we have considered forward rate constants as $k_1 = k_2 = k_3 = k_4 = 1$, and therefore, from Eq. (3.4), we can obtain the critical value of the control parameter as $b_{cT} = \frac{[D_{11}+D_{21}]a^2 + 2[det(\mathcal{D})]^{\frac{1}{2}} a + D_{22}}{D_{22}+D_{12}}$.

Further, the necessary and sufficient conditions yield the intrinsic critical wave number equation of the Brusselator RDS at the onset of Turing instability,

$$q_{cT} = \left[\frac{k_1^2 k_3}{k_4} \frac{a^2}{det(\mathcal{D})} \right]^{\frac{1}{4}}. \tag{3.5}$$

At the onset of Turing instability, eigenvalues can be expressed as $\lambda_+ = Tr(\mathcal{J}_{\mathcal{D}}) = k_2 b_{cT} - k_4 - \frac{k_3 {k_1}^2}{{k_4}^2} a^2 - (D_{11} + D_{22}) q_{cT}^2$ and $\lambda_- = 0$. If we insert, mathematical ex-

pression of b_{cT}, q_{cT}, and consider $k_1 = k_2 = k_3 = k_4 = 1$, λ_+ expression becomes $\lambda_+ = \frac{[D_{11}+D_{21}]a^2+2[det(\mathcal{D})]^{\frac{1}{2}}a+D_{22}}{D_{22}+D_{12}} - 1 - a^2 - (D_{11}+D_{22})\left[\frac{a^2}{det(\mathcal{D})}\right]^{\frac{1}{2}}$. This expression of the eigenvalue implies that this eigenvalue only depends on the concentration of chemostatted species, A, and diffusion coefficients. The negative value of $Tr(\mathcal{J}_{\mathcal{D}})$ suggests that eigenvalue $\lambda_- = 0$ at the onset of Turing instability will govern the whole system dynamics. Now, for the Turing instability in the Brusselator RDS, the critical eigenvector, U_{cT} corresponding to the eigenvalue is

$$U_{cT} = \begin{pmatrix} 1 \\ -\frac{k_4}{(D_{12}+D_{22})q_{cT}{}^2} - \frac{(D_{21}+D_{11})}{(D_{12}+D_{22})} \end{pmatrix} = \begin{pmatrix} 1 \\ -\frac{k_4}{k_1}\sqrt{\frac{k_4}{k_3}}\frac{\sqrt{det(\mathcal{D})}}{(D_{12}+D_{22})a} - \frac{(D_{21}+D_{11})}{(D_{12}+D_{22})} \end{pmatrix}.$$

Above the critical value of the control parameter of the Brusselator, a sufficiently small yet finite band of Fourier modes around the critical wave number, q_{cT}, becomes equally excited and contributes to the nonlinear growth of the pattern. However, within a finite system of length l, the critical wave number of the Turing instability that satisfies $q_{cT} = \frac{n\pi}{l}$ is only accessible in the presence of a zero flux boundary condition. Here, we set the integer value n in such a way that the admissible critical wave number remains nearest to the intrinsic critical wave number, q_{cT}. In terms of the cross-diffusion coefficients, Turing instability in the Brusselator RDS is more favorable when D_{21} is negative and D_{12} is positive[132,133]. However, we should not consider too much negative D_{21} or positive D_{12} in Brusselator RDS to avoid the suppression of the Turing instability[132]. These conditions in cross-diffusion coefficients to acquire favorable Turing instability circumstances will be inverted for the RDS like the Oregonator, as then we have the opposite cross-kinetic behavior compared to the Brusselator, as discussed earlier.

3.2.2 Hopf instability

As mentioned earlier, besides the diffusion-driven spatial Turing pattern, Brusselator RDS can also afford a type III-o[4] oscillatory Hopf instability with the critical wave number $q_{cH} = 0$. For the Hopf instability in the system, the stability condition related

to the trace needs to be broken, i.e., $Tr(\mathcal{J}_{\mathcal{D}})_{|q=0}$ becomes positive while the determinant condition still holds. Therefore, at the onset of the Hopf instability, we can write $Tr(\mathcal{J}_{\mathcal{D}})_{|q=0} = 0$, i.e., $J_{11} + J_{22} = 0$ or $J_{11} = -J_{22}$. From this, we can figure out the critical value of the control parameter as $b_{cH} = \frac{k_4}{k_2} + \frac{k_1^2 k_3}{k_2 {k_4}^2} a^2$. The corresponding critical frequency of the oscillation is, $f_{cH} = \sqrt{\frac{k_1^2 k_3}{k_4}} a$ and critical eigenvector reads $U_{cH} = \left(1 + \frac{i}{a}\sqrt{\frac{k_4}{k_3}}\frac{1}{k_1} \quad , -(1 + \frac{{k_4}^3}{k_3 {k_1}^2}\frac{1}{a^2})\right)^{\mathbf{T}}$.

3.3 Concentration fields of intermediate species for Turing-Hopf overlappings

Concentration fields of the intermediate species can exhibit different spatiotemporal profiles within the different control parameter ranges depending on the dispositions of Turing and Hopf instabilities. The resulting concentration pattern can be traced in the critical wave number and frequency of Turing and Hopf regimes, respectively. Within reaction-diffusion systems (RDS), the evolution equations of concentrations can be expressed by employing a solitary Fourier mode represented as $\exp(\lambda(q)t + iqr)$, where growth rate has wave number, q dependence.

3.3.1 Turing instability regime

For the marginal stability situation of the homogeneous state of the system, the concentration field evolution of the intermediate species near the onset of Turing instability for the single fastest-growing mode can be represented as

$$z_{IT} = z_{I0} + \mathcal{A}_{\mathcal{T}} U_{cT} \exp\left(iq_{cT} r\right) + C.C., \tag{3.6}$$

where $z_{I0} \in [x_0, y_0]$ is the uniform base state set by steady-state values of two intermediate species and $\mathcal{A}_{\mathcal{T}}$ is the Turing amplitude rendering essential features of the Turing

pattern. The corresponding long-time solution of Eq. (3.6) is given by

$$\begin{pmatrix} x \\ y \end{pmatrix} = \begin{pmatrix} x_0 \\ y_0 \end{pmatrix} + \left[\begin{pmatrix} 1 \\ -\frac{k_4}{k_1}\sqrt{\frac{k_4}{k_3}}\frac{\sqrt{det(\mathcal{D})}}{(D_{12}+D_{22})a} - \frac{(D_{21}+D_{11})}{(D_{12}+D_{22})} \end{pmatrix} \mathcal{A}_{\mathcal{T}} 2\cos q_{cT} r \right], \tag{3.7}$$

where $\mathcal{A}_{\mathcal{T}}$ is the Turing amplitude for the long time limit and will be determined in the later part of this chapter.

3.3.2 Hopf instability regime

Akin to the Turing instability, the perturbation part of the Hopf instability can be represented by incorporating Hopf amplitude into the linear stability description of the system in the temporal dimension. Therefore, we can write the perturbation part of the Hopf instability as

$$\delta z_I = \mathcal{A}_{\mathcal{H}} U_{cH} \exp\left(i f_{cH} t\right) + C.C., \tag{3.8}$$

where $\mathcal{A}_{\mathcal{H}}$ is the Hopf amplitude and is generally a complex entity. We will later derive the amplitude of the spatially uniform nonlinear oscillations corresponding to the Hopf instability as $\mathcal{A}_{\mathcal{H}} = \mathcal{A}_{\mathcal{RH}} \exp(i\beta\lambda t)$ with $\mathcal{A}_{\mathcal{RH}}$ being the real part of the amplitude. Inserting this form of the amplitude into Eq. (3.8), we can express the final form of the perturbation equation as

$$\begin{pmatrix} \delta x \\ \delta y \end{pmatrix} = \mathcal{A}_{\mathcal{RH}} \begin{pmatrix} 2\cos\left(f_{cH} t + \beta\lambda t\right) - \frac{2}{a}\sqrt{\frac{k_4}{k_3}}\frac{1}{k_1}\sin\left(f_{cH} t + \beta\lambda t\right) \\ -2(1 + \frac{{k_4}^3}{k_3 {k_1}^2}\frac{1}{a^2})\cos\left(f_{cH} t + \beta\lambda t\right) \end{pmatrix}. \tag{3.9}$$

For the control parameter above the critical value of b_{cH}, this perturbation part will lead to the limit-cycle oscillation in the Brusselator system.

3.3.3 Three scenarios of Turing and Hopf overlapping

In this study of the Brusselator RDS, we aim to go beyond the conventional Turing pattern formation situation and have considered equal self-diffusion coefficients for the

activator and inhibitor and non-zero cross-diffusion coefficients. For this general Brusselator RDS, the critical values of the control parameter, b, for Turing and Hopf instabilities are derived in the previous section. Now, equating these two critical values' equations, i.e., $b_{cT} = b_{cH}$, we can acquire a specific point, a_{TH}, corresponding to the concentration of chemostatted species, A. For a_{TH}, the onset of Turing and Hopf instabilities will coincide within the (a, b) parameter plane. This coinciding point is known as the codimension-two point[153]. From $b_{cT} = b_{cH}$, we obtain quadratic equation of a and then, by solving it, we arrive at

$$a_{TH} = \left[\frac{k_4^3}{k_3 k_1^2}\right]^{\frac{1}{2}} \left(\frac{[det(\mathcal{D})]^{\frac{1}{2}} \pm \sqrt{det(\mathcal{D}) - [D_{22} + D_{12} - D_{11} - D_{21}]D_{12}}}{[D_{22} + D_{12} - D_{11} - D_{21}]}\right). \tag{3.10}$$

For the equal self-diffusion coefficients, $D_{11} = D_{22}$ and $k_1 = k_2 = k_3 = k_4 = 1$, Eq. (3.10) becomes, $a_{TH} = \frac{[det(\mathcal{D})]^{\frac{1}{2}} \pm \sqrt{det(\mathcal{D}) - [D_{12} - D_{21}]D_{12}}}{[D_{12} - D_{21}]}$. In the vicinity of this codimension-two point, the critical intrinsic wave number related to the Turing instability can be expressed as $q_{cT}|_{a=a_{TH}} = q_{cTH} = \left[\frac{k_1^2 k_3}{k_4} \frac{a_{TH}^2}{det(\mathcal{D})}\right]^{\frac{1}{4}}$ and the critical frequency of a homogeneous Hopf mode will be $f_{cTH} = a_{TH}$.

For the one-dimensional system, the concentration dynamics arising in the presence of Turing and Hopf instabilities can be described by taking the superposition of Turing mode in Eq. (3.6) and Hopf mode in Eq. (3.8). Hence, the spatiotemporal dynamics of the concentration field due to the overlapping of Turing and Hopf instabilities can be written as

$$z_{ITH} = z_{I0} + \mathcal{A}_{\mathcal{T}} U_{cT} \exp\left(i q_{cT} r\right) + \mathcal{A}_{\mathcal{H}} U_{cH} \exp\left(i f_{cH} t\right) + C.C. \tag{3.11}$$

The above concentration field expression has been exploited to assess all the thermodynamic entities within the Turing-Hopf overlapping regime.

In this study, we have considered the following three scenarios of Turing and Hopf instabilities' overlapping to generate spatiotemporal patterns in the concentration fields of intermediate species.

- **Turing instability first:** Initially stationary spatial Turing pattern emerges as the control parameter is changed. Then, the Hopf instability appears as the control parameter is further changed and thus crosses the onset point of the Hopf instability.

- **Hopf instability first:** The homogeneous oscillatory pattern appears first, and then this limit-cycle pattern gets modulated by the generation of the Turing pattern with further change in the control parameter.

- **Codimension-two point (CoD2):** Degenerate point regarding the Turing and Hopf instabilities will also generate spatiotemporal patterns as both instabilities grow simultaneously in the system.

Now, we need to acquire the amplitude corresponding to both of these instabilities in the presence of cross diffusion. Then, we can quantify concentration profiles in all three scenarios with the aid of Eq. (3.10).

3.4 Hopf amplitude equation: Krylov-Bogolyubov (KB) method

We see in the previous section that scenarios of Turing and Hopf overlapping, their relative strength and stability can be investigated analytically by incorporating their respective amplitudes into a linear stability description of the system near the onset of instability. Since the usual multiscale method[4,5] of deriving amplitude equations, especially for reaction-diffusion systems with cross diffusion, is rather cumbersome, we employ here a simple method of derivation based on the Krylov-Bogolyubov (KB) averaging method to obtain the relevant Ginzburg-Landau equation.

To implement the KB method, we define two new variables. One is the total concentration of intermediate species, $z = x + y$, and another variable is $u = a - x$. It is possible to rewrite Eq. (3.1) of the Brusselator model for these two new variables. Since all the forward rate constants are considered unity in this investigation, the steady state solution in terms of new variables becomes $u_s = 0$ and $z_s = \frac{b}{a} + a$. A new variable

$\zeta = z - z_s$ is further defined to shift the fixed point into the origin, and now we acquire the following two differential equations,

$$\begin{aligned} \dot{\zeta} &= u \\ \dot{u} &= (b - 1 - a^2)u + (2a - \frac{b}{a})u^2 - u^3 - (a - u)^2\zeta, \end{aligned} \tag{3.12}$$

which can be represented in terms of a single second-order equation with a form similar to the generalized Rayleigh equation[161,162],

$$\ddot{\zeta} + \Omega^2\zeta = \lambda[2(1 + c_1u - c_2u^2)u - \frac{1}{\lambda}(u^2 - 2\Omega u)\zeta]. \tag{3.13}$$

Here, we exploit the following expressions of the newly introduced parameters, $\Omega = a$, $\lambda = \frac{b-1-a^2}{2}$, $c_1 = \frac{(2a-\frac{b}{a})}{2\lambda}$, $c_2 = \frac{1}{2\lambda}$.

Now considering $2(1 + c_1u - c_2u^2)u - \frac{1}{\lambda}(u^2 - 2\Omega u)\zeta = h$ in Eq. (3.13), we obtain

$$\ddot{\zeta} + \Omega^2\zeta = \lambda h. \tag{3.14}$$

From the definition of ζ and u, we can write, $x_{rr} = -u_{rr}$, and $y_{rr} = \zeta_{rr} + u_{rr}$. Therefore, in the presence of both self- and cross-diffusion coefficients for the general Brusselator reaction-diffusion system, we can have the following expression

$$\begin{aligned} \dot{\zeta} &= u + (D_{22} + D_{12} - D_{11} - D_{21})u_{rr} + (D_{22} + D_{12})\zeta_{rr} \\ \dot{u} &= -\Omega^2\zeta + \lambda h + (D_{11} - D_{12})u_{rr} - D_{12}\zeta_{rr} \end{aligned} \tag{3.15}$$

Incorporating equations in (3.15), we extend Eq. (3.14) into the following general form of the reaction-diffusion system,

$$\begin{aligned} \ddot{\zeta} + \Omega^2\zeta = \lambda h + (D_{22} + D_{12} - D_{11} - D_{21})\dot{u}_{rr} + (D_{22} + D_{12})\dot{\zeta}_{rr} \\ +(D_{11} - D_{12})u_{rr} - D_{12}\zeta_{rr}. \end{aligned} \tag{3.16}$$

Under the approximation of small λ, Eq. (3.16) can admit solutions similar to the simple

harmonic motion,

$$\zeta(r,t) = \mathcal{A}(r,t)\cos(\Omega t - \phi(r,t)) \tag{3.17a}$$

$$u(r,t) = \dot{\zeta}(r,t) = -\Omega\mathcal{A}(r,t)\sin(\Omega t - \phi(r,t)). \tag{3.17b}$$

We have considered that both amplitude, $\mathcal{A}$ and phase, ϕ vary very slowly. We acquire all the required spatial derivatives by exploiting Eq. (3.17a) and (3.17b) as,

$$\zeta_{rr} = (2\mathcal{A}_r\phi_r + \phi_{rr}\mathcal{A})\sin(\Omega t - \phi) + (\mathcal{A}_{rr} - \mathcal{A}\phi_r^2)\cos(\Omega t - \phi) \tag{3.18a}$$

$$u_{rr} = \Omega(\mathcal{A}\phi_r^2 - \mathcal{A}_{rr})\sin(\Omega t - \phi) + \Omega(2\mathcal{A}_r\phi_r + \phi_{rr}\mathcal{A})\cos(\Omega t - \phi). \tag{3.18b}$$

Further, using expressions in Eq. (3.17a) and (3.17b), we acquire the following amplitude dynamics,

$$\dot{\mathcal{A}} = -\frac{1}{\Omega}[\lambda h - \Omega^2(D_{22} + D_{12} + \frac{D_{12}}{\Omega^2} - D_{11} - D_{21})\zeta_{rr} + (D_{22} + D_{11})u_{rr}]\sin(\Omega t - \phi), \tag{3.19}$$

and phase dynamics,

$$\dot{\Phi} = \frac{1}{\Omega\mathcal{A}}[\lambda h - \Omega^2(D_{22} + D_{12} + \frac{D_{12}}{\Omega^2} - D_{11} - D_{21})\zeta_{rr} + (D_{22} + D_{11})u_{rr}]\cos(\Omega t - \phi). \tag{3.20}$$

Now, inserting the spatial derivatives and after ironing out the fast oscillation parts via averaging, the amplitude and phase dynamics of the generalized Brusselator RDS yield as

$$\dot{\mathcal{A}} = \mathcal{A}\lambda - p_1\frac{3\lambda c_2\Omega^2}{4}A^3 + \frac{\Omega}{2}(D_{22} + D_{12} + \frac{D_{12}}{\Omega^2} - D_{11} - D_{21})(2\mathcal{A}_r\phi_r + \phi_{rr}\mathcal{A}) + \frac{(D_{11} + D_{22})}{2}(\mathcal{A}_{rr} - \mathcal{A}\phi_r^2), \tag{3.21a}$$

$$\dot{\Phi} = -p_2\frac{\Omega}{8}\mathcal{A}^2 + \frac{(D_{11}+D_{22})}{2}(\frac{2\mathcal{A}_r\phi_r}{\mathcal{A}} + \phi_{rr}) - \frac{\Omega}{2}(D_{22} + D_{12} + \frac{D_{12}}{\Omega^2} - D_{11} - D_{21})(\frac{\mathcal{A}_{rr}}{\mathcal{A}} - \phi_r^2). \tag{3.21b}$$

The non-negative term $2\lambda c_1$ in Eq. (3.13) is related to the unidirectional acceleration from the unstable stationary point. For taking this effect into consideration, correction factors p_2 and p_1 are incorporated into the dynamics[163].

3.4.1 Coefficients of CGLE

The lowest-order amplitude equation capable of encapsulating the crucial features of the oscillatory behavior owing to Hopf instability is the complex Ginzburg Landau equation (CGLE)[5,27,28]. This CGLE description is only valid near the onset of Hopf instability. The form of the phase and amplitude dynamics obtained by the KB method in Eq. (3.21b) and (3.21a) complies with the following unscaled CGLE equation:

$$\frac{\partial Z}{\partial t} = \lambda Z + (\alpha_{\mathcal{R}} + i\alpha_{\mathcal{I}})\partial_r^2 Z - (\beta_{\mathcal{R}} - i\beta_{\mathcal{I}}) \mid Z \mid^2 Z. \tag{3.22}$$

By substituting $Z = \mathcal{A}\exp(-i\phi)$ in Eq. (3.22) and then splitting the real and imaginary parts, we achieve the following equations

$$\frac{\partial \mathcal{A}}{\partial t} = \lambda\mathcal{A} - \beta_{\mathcal{R}}\mathcal{A}^3 + \alpha_{\mathcal{I}}(2\mathcal{A}_r\phi_r + \phi_{rr}\mathcal{A}) + \alpha_{\mathcal{R}}(\mathcal{A}_{rr} - \mathcal{A}\phi_r^2), \tag{3.23a}$$

$$\frac{\partial \phi}{\partial t} = -\beta_{\mathcal{I}}\mathcal{A}^2 + \alpha_{\mathcal{R}}(\frac{2\mathcal{A}_r\phi_r}{\mathcal{A}} + \phi_{rr}) - \alpha_{\mathcal{I}}(\frac{\mathcal{A}_{rr}}{\mathcal{A}} - \phi_r^2). \tag{3.23b}$$

Near the Hopf instability onset point, the above eqs. (3.23a) and (3.23b) represent the evolution of the amplitude and phase, respectively, and are the deductions of the unscaled CGLE.

Now we can acquire all the coefficients of the unscaled CGLE by comparing Eq. (3.23a) and (3.23b) with Eq. (3.21a) and (3.21b) obtained by the KB method, $\lambda = \frac{b-1-a^2}{2}$, $\beta_{\mathcal{R}} = p_1\frac{3\lambda c_2\Omega^2}{4}$, $\beta_{\mathcal{I}} = p_2\frac{\Omega}{8}$, $\alpha_{\mathcal{R}} = \frac{(D_{11}+D_{22})}{2}$, $\alpha_{\mathcal{I}} = \frac{\Omega}{2}(D_{22} + D_{12} + \frac{D_{12}}{\Omega^2} - D_{11} - D_{21})$. We will further implement the scaled variables, $\mathcal{A} = \frac{\mathcal{A}}{\sqrt{\beta_{\mathcal{R}}}}$, $r = \frac{r}{\sqrt{\alpha_{\mathcal{R}}}}$, which leads to the

following form of amplitude and phase equations:

$$\frac{\partial \mathcal{A}}{\partial t} = \lambda\mathcal{A} - \mathcal{A}^3 + \alpha(2\mathcal{A}_r\phi_r + \phi_{rr}\mathcal{A}) + (\mathcal{A}_{rr} - \mathcal{A}\phi_r^2), \tag{3.24a}$$

$$\frac{\partial \phi}{\partial t} = -\beta\mathcal{A}^2 + (\frac{2\mathcal{A}_r\phi_r}{\mathcal{A}} + \phi_{rr}) - \alpha(\frac{\mathcal{A}_{rr}}{\mathcal{A}} - \phi_r^2). \tag{3.24b}$$

The above two equations correspond to the following normalized CGLE[134,28,4] near the onset of Hopf instability in spatially extended system,

$$\frac{\partial Z}{\partial t} = \lambda Z + (1 + i\alpha)\partial_r^2 Z - (1 - i\beta) \mid Z \mid^2 Z. \tag{3.25}$$

The coefficients of the normalized CGLE are solely the ratio between the imaginary and real parts of the complex coefficients of the unscaled CGLE in Eq. (3.22), $\alpha = \frac{\alpha_{\mathcal{I}}}{\alpha_{\mathcal{R}}} = \frac{\Omega(D_{22}+D_{12}+\frac{D_{12}}{\Omega^2}-D_{11}-D_{21})}{(D_{11}+D_{22})}$ and $\beta = \frac{\beta_{\mathcal{I}}}{\beta_{\mathcal{R}}} = \frac{p_2}{p_1}\frac{1}{3a}$. The expression of the coefficient, α, acquired by using KB averaging in the Brusselator RDS, including the cross diffusion, matches exactly its expression derived using the rigorous multiscale approach[164]. The mathematical expression of the coefficient, α, suggests that both the self and cross diffusion explicitly impact the Hopf instability at the amplitude level. While the other coefficient, β, of the normalized CGLE is independent of the diffusion and has a standard expression of $\beta = \frac{4-7a^2+4a^4}{3a(2+a^2)}$ [5] for the Brusselator system. Hence, considering the proper expression of correction factors p_1 and p_2 in the β expression acquired in our KB method, we can recover the standard expression of β mentioned above.

When the normalized CGLE in Eq. (3.25) admits a simple and general asymptotic oscillatory solution of the form $Z = \mathcal{A}_{\mathcal{RH}} \exp(i\omega_0 t)$, where ω_0 is the shift in the frequency from the critical frequency, f_{cH}, we can obtain the properties of uniform nonlinear oscillations. Therefore, inserting this asymptotic solution into the normalized CGLE and comparing the imaginary part and the real part, we can express ${\mathcal{A}_{\mathcal{RH}}}^2 = \lambda$ and $\omega_0 = \beta{\mathcal{A}_{\mathcal{RH}}}^2 = \beta\lambda$. The ω_0 expression provides the bulk frequency of the system. Therefore, nonlinear oscillations associated with Hopf instability can be represented as

$$\mathcal{A}_{\mathcal{H}} = \sqrt{\lambda}\exp(i\beta\lambda t) \tag{3.26}$$

3.5 Turing amplitude equation (TAE)

The essential feature of the Turing pattern can be captured by using the Turing Amplitude Equation (TAE), a real counterpart of the CGLE. Near the Turing instability onset point, the one-dimensional TAE with the lowest order can be constructed utilizing the symmetry argument[4] and it has the following form,

$$\frac{\partial Z}{\partial t} = \lambda_T Z + \varrho \partial_r^2 Z - g \mid Z \mid^2 Z \tag{3.27}$$

where λ_T is defined in a fashion akin to the λ for the Hopf instability. Here, ϱ and g are the other two coefficients of the TAE. By inserting $Z = \mathcal{A}\exp(-i\phi)$ into Eq. (3.27) and separating the real and imaginary parts, we acquire the following equations

$$\frac{\partial \mathcal{A}}{\partial t} = \lambda_T \mathcal{A} - g\mathcal{A}^3 + \varrho(\mathcal{A}_{rr} - \mathcal{A}\phi_r^2) \tag{3.28a}$$

$$\frac{\partial \phi}{\partial t} = \varrho(\frac{2\mathcal{A}_r\phi_r}{\mathcal{A}} + \phi_{rr}). \tag{3.28b}$$

We are only interested in the bifurcation scenario of the Turing pattern here. Hence, it will be enough to have only the parameter λ_T in TAE. So, by introducing the scales, $\mathcal{A} = \frac{\mathcal{A}}{\sqrt{g}}$, $r = \frac{r}{\sqrt{\varrho}}$ in the amplitude and spatial dimension of Eq. (3.28a) and (3.28b), we can get rid of the coefficients, g and ϱ. Further, considering the constant phase due to the translational invariance of the spatial pattern, we obtain

$$\frac{\partial \mathcal{A}}{\partial t} = \lambda_T \mathcal{A} - \mathcal{A}^3 + \mathcal{A}_{rr}, \tag{3.29a}$$

$$\frac{\partial \phi}{\partial t} = 0 \tag{3.29b}$$

where b_{cT} in $\lambda_T = \frac{b - b_{cT}}{2}$ is supplied by Eq. (3.4), and it includes the effect of self and cross diffusion. These two equations, i.e., Eq. (3.29a) and (3.29b) are the deduction of the following normalized TAE,

$$\frac{\partial Z}{\partial t} = \lambda_T Z + \partial_r^2 Z - \mid Z \mid^2 Z. \tag{3.30}$$

Similar to the above form of the amplitude equation can be found from the normalized CGLE by setting α and β to zero in the CGLE equation. The Turing amplitude can be achieved from Eq. (3.29a) as the following time-dependent homogeneous solution,

$$\mathcal{A}_{\mathcal{T}}{}^2 = \mathcal{A}_s^2\Big[\frac{1}{1-\mathcal{A}_0\exp\left(-2\lambda_T(t-t_0)\right)}\Big], \tag{3.31}$$

which yields $\mathcal{A}_{\mathcal{T}} = \sqrt{\lambda_T}$ for the long time limit. Therefore, we employ $\mathcal{A}_{\mathcal{T}} = \sqrt{\lambda_T}$ in Eq. (3.7) to get the full concentration dynamics of the intermediate species within the Turing instability regime.

Utilizing these amplitudes, we generate concentration profiles with the aid of Eq. (3.10) corresponding to three scenarios of Truing-Hopf overlapping in the parameter space of the control parameter, b lying in the vicinity of instabilities' onset.

3.6 Parameter space of Turing and Hopf instabilities and Turing-Hopf overlapping

In Fig. 3.2 (a), we illustrate the regimes of Turing and Hopf instabilities in (b, a) parameter space and their overlapping. Exploiting Eq. (3.4), we obtain the Turing line, and it is presented by a solid line. While the Hopf line is shown as a dashed line. The circular label in the figure denotes the critical Turing-Hopf point (CTHP), representing the intersection of Turing and Hopf lines. In Fig. 3.2 (b), we examine the variation in the Turing and Hopf line as a function of the newly obtained parameter, $D_{cr} = D_{12}[1 + \frac{1}{a^2}] - D_{21}$ solely in terms of cross-diffusion coefficients. This D_{cr} also exists in both the amplitude and phase dynamics in Eq. (3.21a) and (3.21b), respectively. Experimentally, the self- and cross-diffusion coefficients, are derived for the three-component [131], four-component [131,165] and five-component [166] $BZ - AOT$ system [167,168] implementing the modified Taylor dispersion method. These experimental works demonstrate the capability of cross diffusion in shifting the Turing onset and thus generating the Turing pattern within the system initially close to the instability onset. To illustrate this finding, we have also collected elements of the diffusion matrix,

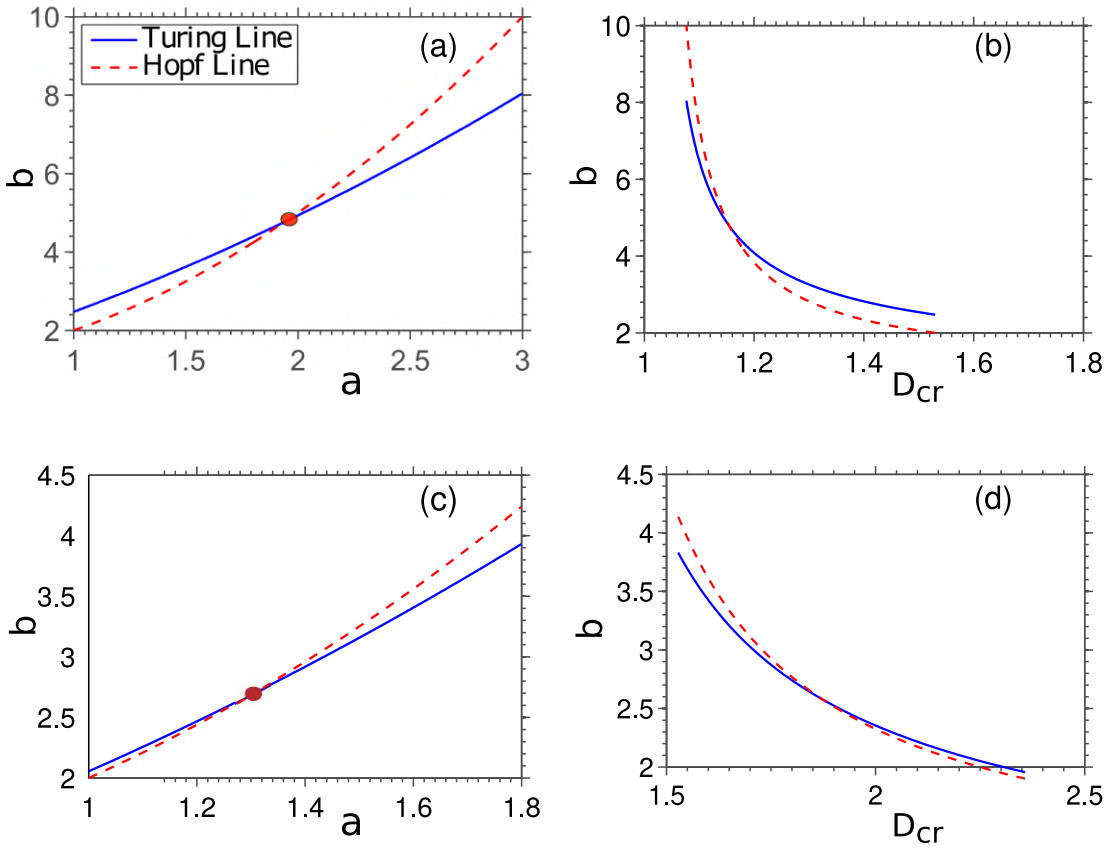

Figure 3.2: In both (a) and (b), the solid line represents the Turing line associated with Eq. (3.4), while the dashed curve corresponds to the Hopf line. In (a), the intersection point of the Turing and Hopf lines occurs at $[a_{TH} \approx 1.9438,\ b_{cT} = b_{cH} \approx 4.7785]$. A new parameter, $D_{cr} = D_{12}[1 + \frac{1}{a^2}] - D_{21}$ containing solely cross-diffusion coefficients is introduced in (b) to explore the effect of cross diffusion on the Turing and Hopf lines. Diffusion coefficients, $D_{11} = D_{22} = 1$, $D_{12} = 0.51$, and $D_{21} = -0.51$ are used in (a) and (b). Whereas, in (c) and (d), the experimental magnitudes of the diffusion coefficients, $D_{11} = 1.28; D_{12} = 1.26; D_{21} = -0.005; D_{22} = 1.51$ of the pentanary $BZ - AOT$ system are considered to obtain figures similar to the previous figures.

$D_{11} = 1.28$, $D_{12} = 1.26$, $D_{21} = -0.005$, and $D_{22} = 1.51$ from the empirical data of the pentanary $BZ - AOT$ system[166]. The corresponding parameter spaces of the Turing and Hopf instability are illustrated in Fig. 3.2 (c) and 3.2 (d). Here, we assume that the diffusion coefficients remain unchanged in the presence of additional components in the system[165]. It is worth noting that the cross diffusion's effect on the onset of Turing instability for the $BZ - AOT$ system was studied for the system involving two different self-diffusion coefficients. However, Fig. 3.2 (b) suggests that D_{cr}, comprising solely

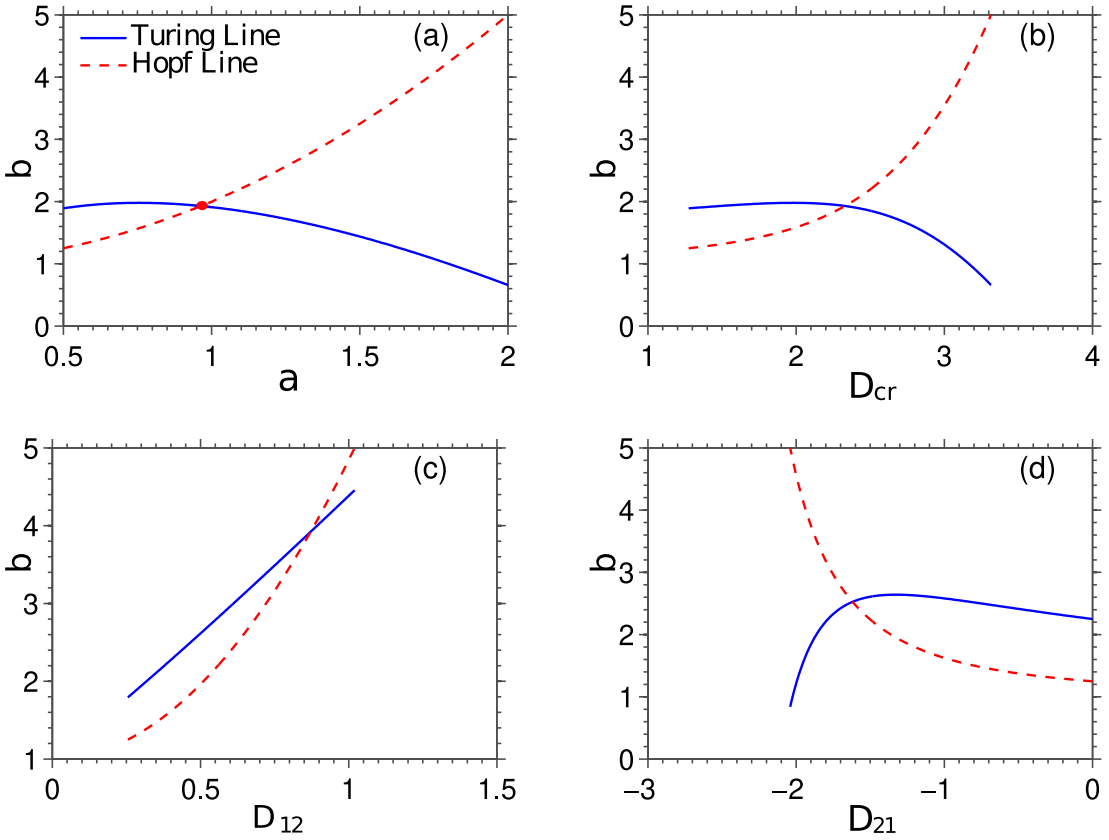

Figure 3.3: For the Brusselator system, Turing and Hopf lines for diffusion coefficients, $D_{11} = D_{22} = 1$, $D_{12} = 0.51x_0$, $D_{21} = -0.51y_0$ are illustrated in both (a) and (b). (a) The intersection point of the Turing and Hopf lines moves to the lower a and b values due to concentration-dependent cross-diffusion coefficients. In (b), the parameter space of $D_{cr} = D_{12}[1 + \frac{1}{a^2}] - D_{21}$ is presented instead of a to capture the effect of concentration-dependent cross-diffusion coefficients on Turing and Hopf line. The impact of individual cross-diffusion coefficients, D_{12} and D_{21} are depicted in the lower panel of the figure.

of cross-diffusion coefficients, can modify the onset of instabilities even for the system having equal self-diffusion coefficients[164].

When cross diffusion exhibits a linear dependence on the concentration, the cross-diffusion coefficients of the Brusselator RDS can be expressed as $D_{12} = D_{12}x_0$ and $D_{21} = D_{21}y_0$, where $x_0 = \frac{k_1}{k_4}a$ and $y_0 = \frac{k_2k_4b}{k_1k_3a}$ represent the steady-state concentrations of X and Y, respectively, in the spatially homogeneous system. As A and B are chemostatted species and the kinetic rate constants remain constant, D_{21} and D_{12} are effectively constant. The intersection of the Turing and Hopf lines, as depicted

in Fig. 3.3 (a), is shifted to lower values of a and b due to this concentration dependence. In both figures, the Turing line is drastically changed due to the consideration of concentration-dependence of the cross-diffusion coefficients. Further, considering only one non-zero cross-diffusion coefficient at a time, we demonstrate the impact of the individual cross-diffusion coefficient of the system on the intersection of Turing and Hopf lines in Fig. 3.3 (c) and (d), while keeping self-diffusion coefficients equal. By examining Fig. 3.3 (a) and 3.3 (d), we can assert that the alteration of the Turing line induced by the concentration-dependent D_{21} is comparable to the effect of concentration a on the Turing line. Analyzing Fig. 3.3 (b), (c), and (d), it can be inferred that, for this Brusselator RDS, D_{21} has a more pronounced impact on the Turing line. The more general concentration dependence of cross-diffusion terms goes beyond the scope of this thesis.

3.7 Amplitude and concentration profiles of Hopf and Turing instabilities

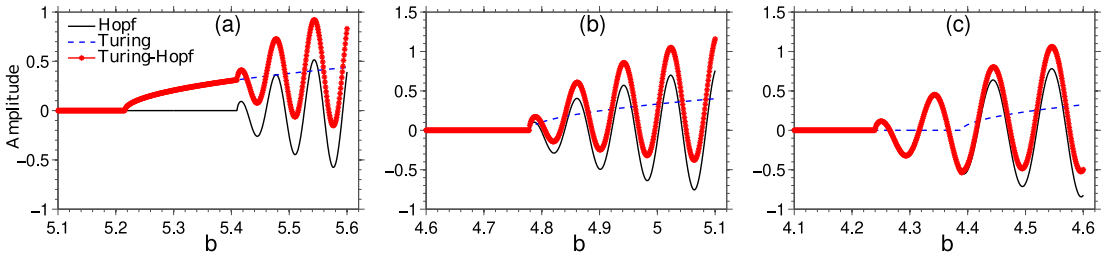

Figure 3.4: The analytically obtained Hopf amplitude as a function of the control parameter, b at time $t = 150$, is represented as the solid black line. The Turing amplitude is presented as the blue $'-\,-'$ line. While the solid line with marker $'*'$ refers to the overlapping of the Turing and Hopf amplitudes. Amplitude profiles are shown for (a) $a = 2.1$: Turing first, (b) CoD2, (c) $a = 1.8$: Hopf first.

All results here and in subsequent sections are obtained at a constant absolute temperature ($T = 300K$) and pressure. The constant temperature throughout the system implies that the heat diffusion rate is much faster than the diffusion rate of species. For the Brusselator CRN, chemical reaction rate constants are specified as

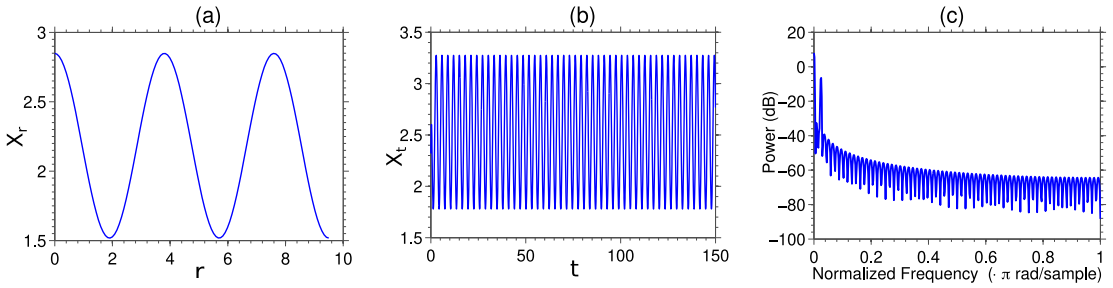

Figure 3.5: Concentration dynamics over the spatial and temporal dimensions are shown in (a) and (b) as X_r and X_t, respectively, for the scenario when the Turing and Hopf mode onset points appear simultaneously in the 1D Brusselator RDS. Here $a = a_{TH}$, $b = 4.9998$. The spatial oscillatory curve in (a) is obtained at a fixed time ($t = 150$). The temporal dynamics in (b) correspond to an arbitrary spatial point in the system. The power spectral density estimate of the discrete-time concentration of the activator obtained via Welch's method is presented (c).

$k_{-\rho} = 10^{-4} << k_\rho = 1$, and diffusion coefficients are fixed at $D_{11} = D_{22} = 1$, $D_{12} = 0.51$, and $D_{21} = -0.51$. A one-dimensional system of length $l = 9.50$ has been employed throughout this study unless otherwise indicated.

We have illustrated the amplitude variation of Hopf and Turing instability with a control parameter, b, in Fig. 3.4. For this purpose, we exploit Hopf and Turing amplitude expressions in Eq. (3.26) and (3.31), respectively. From illustrations, one can notice that as the control parameter, b, is varied through the onset points of Turing and Hopf instabilities, the oscillatory behavior of nonlinear-originating Hopf instability dominates over diffusion-driven Turing instability at an arbitrary spatial and temporal point ($t = 150$) of the system. Conversely, the Turing-Hopf amplitude lines in these figures also depict the extent of the impact of the Turing instability on modifying the oscillatory amplitude of the Hopf instability. Consequently, we can say that the radius of the corresponding limit cycles will also be modulated. So, these profiles reflect the implicit effect of diffusion on the Hopf limit cycle incurred via Turing instability[169]. All these amplitude profiles give a clear idea of the local concentration dynamics within the parameter space of the Turing and Hopf instability and their overlapping regimes. Moreover, these figures quantify the dynamics of both Turing and Hopf instabilities at the fundamental level.

The spatial concentration dynamics, X_r, and temporal concentration profile, X_t are

depicted in Fig. 3.5 for a specific value of the control parameter, b. Both profiles demonstrate periodic behavior owing to Turing and Hopf instability, respectively. The spatial oscillatory behavior in Fig. 3.5 (a) has a wave number close to the critical wave number corresponding to the Turing instability. Whereas the temporal oscillatory profile in Fig. 3.5 (b) has a normalized finite frequency as indicated by the peak in power spectral density in Fig. 3.5 (c). To generate profiles in Fig. 3.5, we only consider the situation when Turing and Hopf instabilities onset occur simultaneously at a point in the parameter space. The main features of these profiles remain roughly the same for the other two scenarios and are not shown here.

3.8 Entropic cost of Turing-Hopf overlapping

The entropy production rate in the 1D Brusselator RDS has been derived to shed light on the correspondence between the evolution of this central element of nonequilibrium thermodynamics and the dynamics of the spatiotemporal pattern owing to Turing-Hopf overlapping. For the encapsulating entropic cost in the subsequent studies, we take three different values of a using the parameter space in Fig. 3.2 to realize the three scenarios discussed before, i.e., $a = 2.1$ corresponding to the appearance of Turing instability before Hopf instability, $a \approx 1.9438$ for CoD2, and $a = 1.8$ related to the first appearance of Hopf instability in the system.

For a particular scenario of Turing-Hopf overlapping, we have investigated the total entropy production rate (EPR) due to the variation in the concentration of one of the reference chemostatted species, b, keeping the concentration of another reference chemostatted species, a, fixed. A nonzero total EPR changes continuously and yields oscillatory behaviors for all three scenarios. Comparing the space-integrated global concentration of the activator (or inhibitor) on the right column of Fig. 3.6 with the corresponding total EPR on the left column of the figure, we can assert that the total EPR is quantitatively proportional to the global concentration of the intermediate species in the RDS. In other words, total EPR reflects the global concentration dynamics of

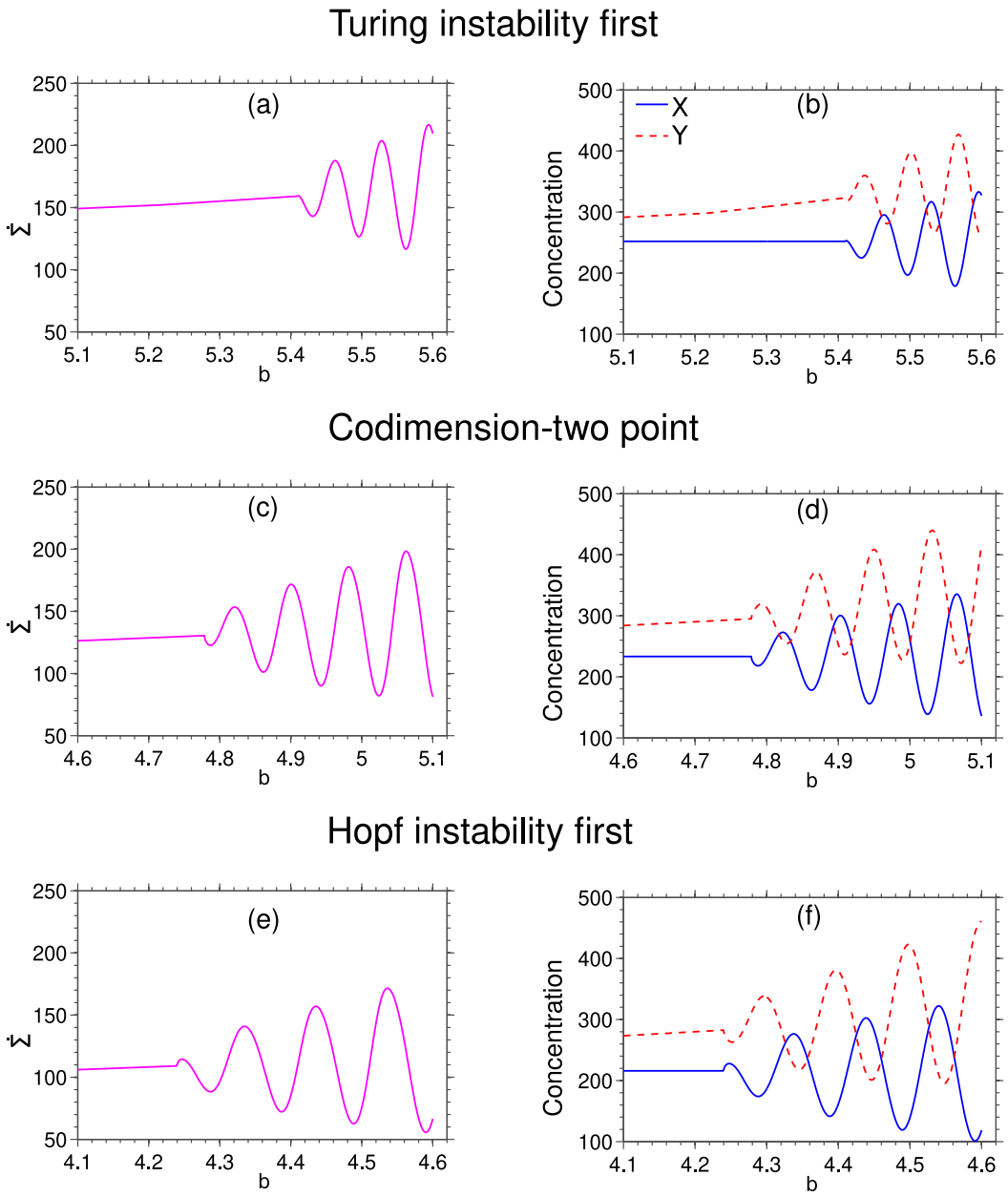

Figure 3.6: Total entropy production rate (left column) with the control parameter, b, is presented for a 1D Brusselator RDS at a specific time, $t = 150$, and absolute temperature, $T = 300K$. The space-integrated global concentration fields of the intermediate species X and Y with b are displayed in the right column. Three distinct scenarios of Turing-Hopf overlapping are explored by exploiting three values of parameter a: (a), (b) $a = 2.1$, Turing first; (c), (d) CoD2; (e), (f) $a = 1.8$, Hopf first. Across all cases, it is evident from the figures that the entropy production rate is directly proportional to the global concentration of X (or Y).

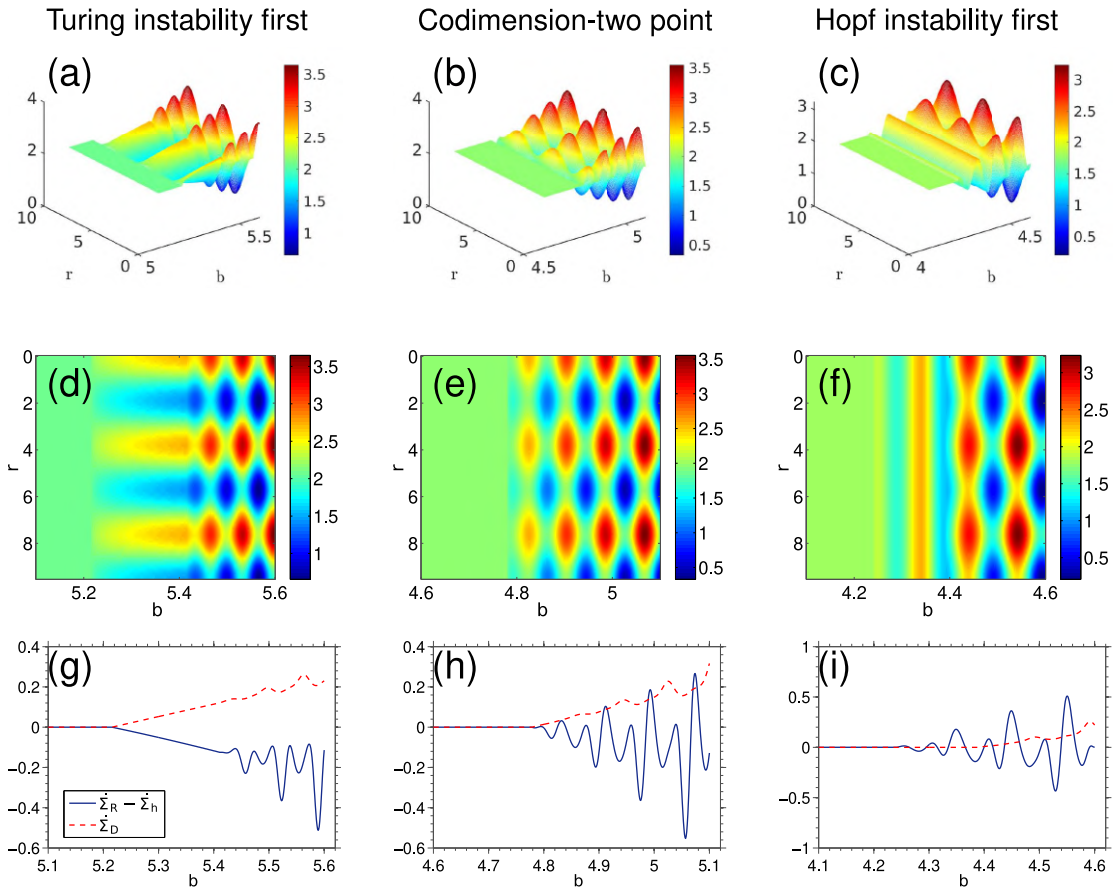

Figure 3.7: 3D concentration fields of the species, X, as a function of the control parameter, b, are depicted in the first row. Whereas figures of the second row illustrate the images of corresponding 3D concentration fields. The 'jet' colormap is utilized to represent the contrast in the concentration field. The entropy production rates (EPR) related to the reaction($\dot{\Sigma}_R$) and diffusion($\dot{\Sigma}_D$) with the control parameter, b, are presented in the last row. The solid blue lines denote the difference between the EPR related to the reaction part and the homogeneous part of the RDS. The $'-$ $-'$ lines refer to the contribution in EPR due to the diffusion. Here, 'r' refers to the extended spatial dimension. All profiles are obtained at a specific time point, $t = 150$.

RDS operating within the various Turing-Hopf overlapping regimes. This result infers that the total EPR of the nonlinear RDS can be a qualitative and quantitative measure of spatiotemporal pattern formation. Additionally, in all three scenarios, these profiles seemingly exhibit qualitatively similar features[169].

The concentration fields of the intermediate species, X, with the variation of the control parameter, b, are illustrated for the Turing-Hopf overlapping in the first two rows of Fig. 3.7. These concentration fields are acquired from the analytical Eq. (3.11).

Reaction and diffusion entropy production rates (EPR), defined in the previous chapter, corresponding to these concentration profiles are also illustrated in the last row. The decomposition of the EPR into the diffusion and reaction parts reveals their proper contribution to the total EPR. It also renders the impact of the Turing-Hopf overlapping and cross-diffusion coefficients on these two parts separately. In Fig. 3.7 (g), as the critical point of Turing instability is approached by varying the control parameter, a nonzero EPR associated with both the reaction and diffusion yields. The reaction and diffusion EPR curves appear analogous to the dynamical bifurcation characteristics. Then, the emergence of Hopf instability into the picture for the higher value of the control parameter modifies the reaction part of the EPR due to its innate oscillatory dynamics and results in irregular oscillatory characteristics of the reaction EPR. The diffusion EPR represented by the dotted line in the same figure is also slightly modified by the Hopf instability to a finite extent. This modification of the diffusion EPR by Hopf instability suggests an indirect association between the limit cycle of Hopf instability and diffusion. For the scenario presented in Fig. 3.7 (i), initially, Hopf instability only exists in the lower value of the control parameter in the RDS, and the diffusion EPR is zero. Only the reaction EPR reflects the signature of the Hopf instability. Then, as the control parameter value exceeds the critical point of the Turing instability, diffusion EPR becomes nonzero owing to the Turing pattern. Thus, the onset of the Turing instability is reflected through the thermodynamic entity, despite the first appearance of the Hopf instability in the system[169]. It can be an interesting result, as within the dynamical framework of RDS, Hopf instability often screens the Turing pattern when the former precedes the later instability. Thus, exploiting the decomposition of the thermodynamic entity can aid in revealing all the instabilities in RDS by reflecting their signatures prominently. Finally, for the scenario in Fig. 3.7 (h), we observe the sufficient change of both the reaction and diffusive EPR from the initial zero values as the Turing and Hopf instabilities emerge simultaneously. Thus, we capture the reaction and diffusive EPR of the concentration profiles in all three scenarios shown in the first two rows of Fig. 3.7.

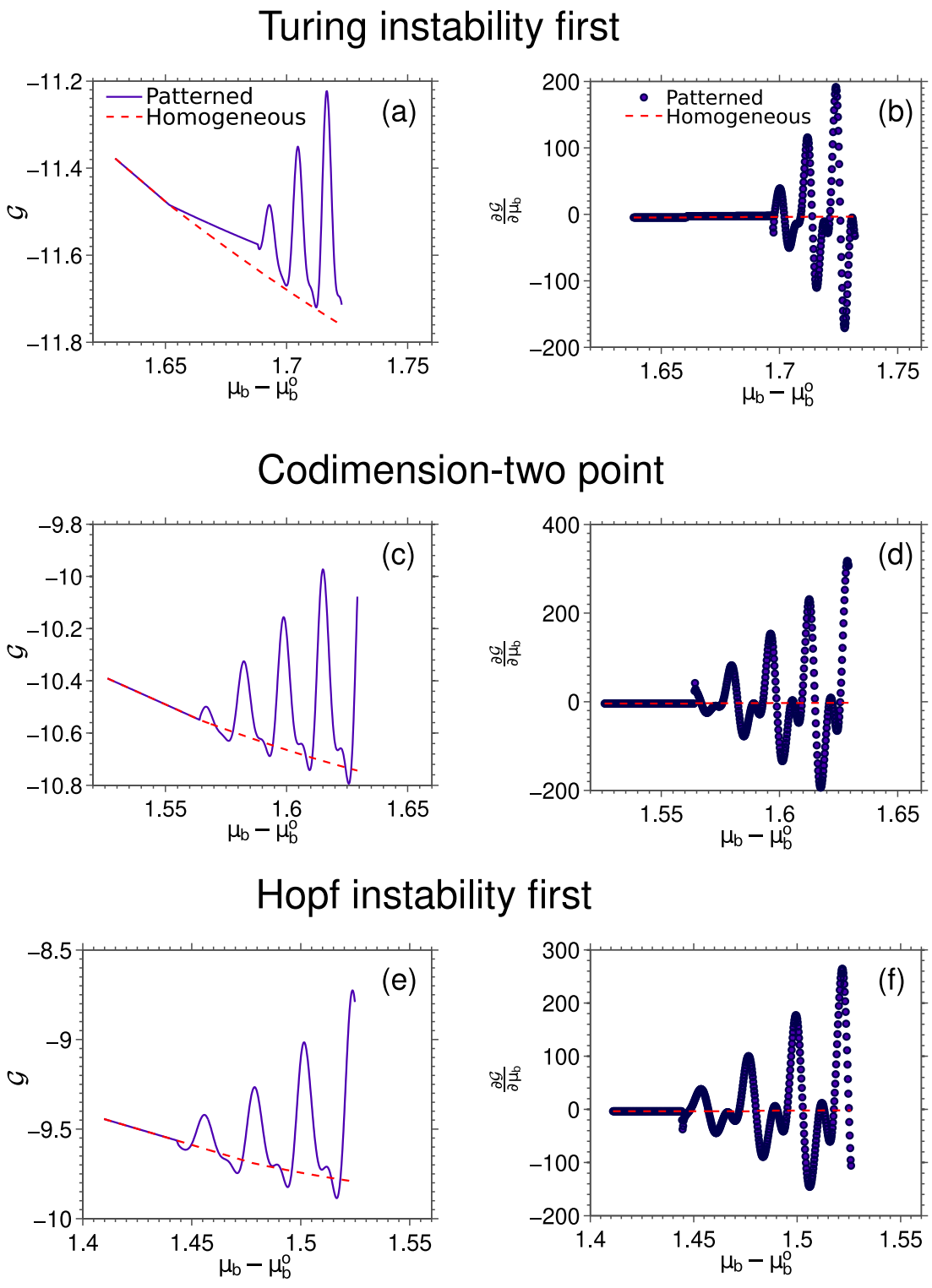

Figure 3.8: Semigrand Gibbs (SGG) free energy (left column) and its slope (right column) are illustrated as the function of the chemical potential of the control parameter b in the 1D Brusselator RDS for the previously mentioned three distinct scenarios. The dotted lines correspond to a homogeneous state with no pattern. Concentration profiles were captured at the $t = 150$.

3.9 Energetic cost of Turing-Hopf overlapping

In the open CRN of the Brusselator exhibiting Turing and Hopf instability, we need to implement semigrand Gibbs free energy to capture the proper energetics of the system, at least in a global sense. The semigrand Gibbs (SGG) free energy profiles concerning the chemical potential of the chemostatted species, B, are depicted in the left column of Fig. 3.8. For all scenarios, the semigrand Gibbs free energy profiles associated with the homogeneous part (dotted lines) essentially set the baseline of the semigrand Gibbs free energy curves acquired for patterns in the RDS. Slope profiles of the SGG are presented in the right column of Fig. 3.8. These slope profiles concerning control parameter change provide a clear idea regarding transitions in the thermodynamic entity and thus can serve as an indicator for detecting various pattern-forming mechanisms at the thermodynamic level. In Fig. 3.8, due to Turing and Hopf overlapping, we obtain oscillation in the SGG profiles with μ_b. A series of transitions can be noticed in the slope profiles of all three scenarios of the RDS with varying chemostatted species B.

3.10 Chapter conclusions

In this chapter, we determined the thermodynamic cost of spatiotemporal patterns arising in the realm of Turing-Hopf instabilities overlapping in a prototypical RDS. Particularly, we systematically quantified the proper nonequilibrium potential and the entropy production rate for the Brusselator RDS in the presence of both self and cross diffusion. Considering three distinct scenarios of Turing and Hopf overlapping, we showed the drastic modification of the dynamic and thermodynamic entities by the cross-diffusion coefficients and chemostatted species concentration. We also encapsulated the implicit effect of the diffusion on the Hopf limit cycle through the Turing instability.

This study also paves the way to relate the dynamic phenomena of the Turing-Hopf overlapping with the notion of the nonequilibrium thermodynamic phase transitions. The finding of the proportionality of the total EPR with the global concentration dynamics of the RDS can be an important result to be explored in upcoming chapters.

Furthermore, the illustration of the parameter space of the Turing- Hopf overlapping using experimentally found self- and cross-diffusion coefficients, means this dynamic and thermodynamic framework can be extended to the experimental setting. Additionally, we implemented a less cumbersome modified KB averaging method for obtaining the amplitude equation in the presence of the self-and cross-diffusion coefficients. The amplitude acquired by this analytical method for equal self-diffusion coefficients can be useful in explaining and describing the dynamical events in the experiment settings[163].

We found that the expressions of the Turing critical values of the control parameter and wave number explicitly contain cross-diffusion coefficients in the absence of the 'local activation and long-range inhibition' condition. Hence, Turing instability presented in this study was essentially driven by. Therefore, this thermodynamic framework is applicable beyond the conventional Turing pattern. However, one should recall the crucial limitation mentioned previously regarding cross diffusion in this thermodynamic study. The cross diffusion has to obey Fick's laws of diffusion to be incorporated into this nonequilibrium thermodynamic scheme. Within the realm of Fick's laws, this framework for Turing-Hopf overlapping can be extended to the RDS with superdiffusive species[170]. Another thing to keep in mind is that we only inspected the overlapping of Turing and Hopf instability and excluded Turing-Hopf interplay and subharmonics. To capture the complete richness of the Turing-Hopf interaction and corresponding thermodynamics, one can resort to the computational scheme.

It was not easy for a person brought up in the ways of classical thermodynamics to come around to the idea that the gain of entropy eventually is nothing more nor less than the loss of information.

- Gilbert N. Lewis

4

Thermodynamics of traveling waves and Benjamin-Feir instability in glycolysis

4.1 Glycolytic waves in a simple RDS and importance of thermodynamic quantification

In the previous chapter, we measured the thermodynamic cost of the spatiotemporal pattern generated due to the overlapping Turing and Hopf instability in an abstract chemical oscillator model. Now, we will focus solely on the general form of the oscillator behavior and corresponding thermodynamic quantification within a nonequilibrium environment. Generally, oscillatory behavior is a crucial and ubiquitous phenomenon in living systems[7,11,4,8,151,152,171]. Despite the diverse origins of this oscillatory behavior, we can connect them with a universal underlying principle. In this chapter, we describe the oscillation of chemical species associated with a particular biological event in cells, glycolysis. Glycolysis is a pivotal energy-generating pathway of metabolism, and

it consists of a collection of reactions catalyzed by enzymes. Through this glycolysis chemical reaction network, glucose breaks into pyruvate, and the high-energy molecule adenosine triphosphate (ATP) is generated. From very simplified ones to sophisticated complex ones[69,172,173,174,175], diverse theoretical models have been proposed to describe the oscillatory behavior of glycolysis. In this regard, diffusion was incorporated into the reaction kinetics of the glycolysis in the Goldbeter model[172] to visualize the spatial effects. This spatially extended model and its altered version[176] exhibited a range of spatiotemporal phenomena in glycolysis. These behaviors span from traveling waves to spatiotemporal chaos and closely resemble the glycolytic waves observed in experimental setup[177]. Later, the experimental demonstration of generating traveling waves utilizing the yeast extracts is showcased in an open spatial reactor[178]. The theoretical reaction-diffusion system (RDS) based on the Selkov model[179,163] has shown its capability in capturing and elaborating vital features of traveling waves observed in this experiment setup. Motivated by the strength of the spatially extended Selkov model in reliably generating glycolytic traveling waves, we have also chosen the two-variable Selkov model for depicting the oscillatory behavior of glycolysis. The simplicity and clarity of this two-variable Selkov RDS will provide scope to focus solely on desirable dynamical features of glycolysis and generalize findings and understandings to any activator-inhibitor type RDS. Moreover, in the previous studies[163] of the glycolytic traveling waves involving amplitude equation formalism, equal self-diffusion coefficients were considered. We here generalize the amplitude equation description by taking into account all the diffusion coefficients (self and cross), which can assume any range of values. Thus, our theoretical framework provides more flexibility in exploring and investigating various generic features and robustness. Further, we have opted for the homogeneous concentration of the control parameter in this chapter instead of the inhomogeneous control parameter[163,180] or periodic substrate influx[181] considered for investigating features like phase reversal, chaotic oscillation, or oscillation entrainment. Consequently, the features and dynamic phenomena captured within the oscillatory regime of the system are solely attributed to the tuning of the uniform chemostatted species concentration and diffusion coefficients.

Till now, the main focus in investigating glycolysis waves has been limited to controlling the spatiotemporal pattern[11,4], identifying key influential factors governing oscillatory behavior, and understanding the entrainment of intrinsic glycolytic oscillations. However, the broader role of glycolysis waves in processing and spreading biological information[182,183,184], and thereby influencing the coordination among metabolic or other cellular events, raises questions related to entropic cost, energetics, or efficiency of glycolytic waves. Thermodynamic depiction of glycolytic waves will also enhance our understanding of general nonlinear systems featuring limit cycles or waves, at a fundamental level. Moreover, our investigation aims to provide insights into how various instabilities dictated by coefficients of the amplitude equation leave their imprints on the evolution of thermodynamic entities near the Hopf instability point. This line of study can also aid in identifying the advantages and drawbacks of different popular glycolysis pathways[13] and thus can supply a completely different perspective for comparing these pathways.

Results presented in this chapter related to the investigation of the thermodynamic cost of glycolytic traveling waves were previously published in *Kumar et al., 2021, Physical Review E, 104:014221.*

This chapter is organized as follows: After outlining the aim and motivation of our investigation in this section, we will discuss the simple model of glycolysis, the Selkov model, and its reversible variant in Sec. 4.2. Following this, we will present the conservation laws and emergent cycles of the Selkov CRN in Sec. 4.3. We will then focus on the Hopf instability and traveling wave dynamics within the Selkov RDS in Sec. 4.4. Then coefficients of CGLE are derived for Selkov RDS using the KB averaging method in Sec. 4.5. The closed form of amplitude, phase, and allowed wave number are derived in the next section. Subsequently, amplitudes and concentration dynamics related to Hopf instability and traveling wave will be illustrated in Sec. 4.7. In Sec. 4.8, the thermodynamic cost of glycolytic patterns is quantified. Finally, the chapter will conclude by summarizing our findings and prospects.

4.2 Connecting Selkov Model with Reversible Selkov Model

The kinetic model proposed by E. E. Selkov to encapsulate the self-oscillations of the glycolysis[69] can be represented in terms of the following chemical reactions:

$$\begin{aligned}
\rho = 1: &\quad \mathrm{S_1} + \mathrm{ES_2^2} \underset{\mathrm{k_{-1}}}{\overset{\mathrm{k_1}}{\rightleftharpoons}} \mathrm{S_1ES_2^2} \\
\rho = 2: &\quad \mathrm{S_1ES_2^2} \xrightarrow{\mathrm{k_2}} \mathrm{ES_2^2} + \mathrm{S_2} \\
\rho = 3: &\quad 2\,\mathrm{S_2} + \mathrm{E} \underset{\mathrm{k_{-3}}}{\overset{\mathrm{k_3}}{\rightleftharpoons}} \mathrm{ES_2^2}
\end{aligned} \tag{4.1}$$

Here, S_1 and S_2 refer to ATP and ADP, respectively. The free enzyme, E, can be identified as phosphofructokinase, and it plays an important role in generating self-oscillation in glycolysis. This free enzyme is initially inactive and is considered to exhibit activation only by combining with the product, ADP, to form the complex, ES_2^2. Phosphofructokinase is also strongly inhibited by the substrate, ATP. So, this simple kinetic model includes the substrate inhibition and product activation of the enzyme. We assume that all reactions occur in an ideally mixed medium.

The concentration dynamics of the CRN in Eq. (4.1) obey the following equations,

$$\begin{aligned}
\frac{ds_1}{dt} &= z_1 - k_1 s_1 x_1 + k_{-1} x_2, \\
\frac{ds_2}{dt} &= k_2 x_2 - k_3 s_2^2 e + k_{-3} x_1 - k_2 s_2, \\
\frac{dx_1}{dt} &= (k_{-1} + k_2) x_2 - k_1 s_1 x_1 + k_3 s_2^2 e - k_{-3} x_1, \\
\frac{dx_2}{dt} &= k_1 s_1 x_1 - (k_{-1} + k_2) x_2, \\
\frac{de}{dt} &= -k_3 s_2^2 e + k_{-3} x_1,
\end{aligned} \tag{4.2}$$

where $x_1 = [ES_2^2]$, $x_2 = [S_1ES_2^2]$, $s_1 = [S_1]$, $s_2 = [S_2]$ denote concentrations of the chemical species and e represents the concentration of the free enzyme. Additionally, z_1 and $k_2 s_2$ specify the substrate supply and the product removal rate, respectively. Now,

employing a dimensionless analysis in Eq. (4.2), we obtain

$$\frac{d\zeta_1}{d\theta} = z' - (1 + \frac{k_{-1}}{k_2})\frac{\zeta_1 x_1}{e_0} + \frac{k_{-1}}{k_2}\frac{x_2}{e_0}, \tag{4.3a}$$

$$\frac{d\zeta_2}{d\theta} = \alpha_2[\frac{x_2}{e_0} - \frac{k_{-3}}{k_2}\frac{e}{e_0}\zeta_2^2 + \frac{k_{-3}}{k_2 e_0}x_1 - X_2\zeta_2], \tag{4.3b}$$

$$\epsilon\frac{dx_1}{d\theta} = x_2 - x_1\zeta_1 - \frac{K_3}{K_1+1}[x_1 - \zeta_2^2 e], \tag{4.3c}$$

$$\epsilon\frac{dx_2}{d\theta} = \zeta_1 x_1 - x_2, \tag{4.3d}$$

$$\epsilon\frac{de}{d\theta} = \frac{K_3}{K_1+1}[x_1 - \zeta_2^2 e], \tag{4.3e}$$

where $\theta = \frac{k_1 k_2 e_0 t}{k_{-1}+k_2}$, $z' = \frac{z_1}{k_2 e_0}$, $\alpha_2 = \frac{k_2+k_{-1}}{k_1}\sqrt{\frac{k_3}{k_{-3}}}$, $X_2 = \frac{1}{e_0}\sqrt{\frac{k_{-3}}{k_3}}$, $\epsilon = \frac{e_0 k_1 k_2}{(k_{-1}+k_2)^2}$, $K_3 = \frac{k_{-3}}{k_2}$, $K_1 = \frac{k_{-1}}{k_2}$. Here, $\zeta_1 = \frac{k_1}{k_{-1}+k_2}s_1$ and $\zeta_2 = \sqrt{\frac{k_3}{k_{-3}}}s_2$ are considered as relative concentrations of substrate and product, respectively. The total enzyme concentration is $e_0 = x_1 + x_2 + e$. The factor ϵ on the left side of Eq. (4.3c), (4.3d), and (4.3e), can be considered as very small, $\epsilon \ll 1$, and the dynamical system in Eq. (4.3) can be approximately expressed by Eq. (4.3a) and (4.3b) with x_1, x_2, e being substituted by their steady-state values, $x_1^{s.s.} = \frac{e_0\zeta_2^2}{1+\zeta_2^2(1+\zeta_1)}$, $x_2^{s.s.} = \frac{e_0\zeta_1\zeta_2^2}{1+\zeta_2^2(1+\zeta_1)}$, and $e^{s.s.} = \frac{e_0}{1+\zeta_2^2(1+\zeta_1)}$. This operation eventually leads to the following rate equations of the relative concentrations of substrate and product,

$$\frac{d\zeta_1}{d\theta} = z' - \frac{\zeta_1\zeta_2^2}{1+\zeta_2^2(1+\zeta_1)}, \tag{4.4a}$$

$$\frac{d\zeta_2}{d\theta} = \alpha_2[\frac{\zeta_1\zeta_2^2}{1+\zeta_2^2(1+\zeta_1)} - X_2\zeta_2]. \tag{4.4b}$$

Now, we consider the rescaled quantities $\tau = X_2^2 z'^{-2}\theta$, $x = X_2^{-1}z'\alpha_2\zeta_1$, $y = X_2^{-1}z'\zeta_2$, $\nu = X_2^{-3}z'^4\alpha_2$, $\omega = X_2^{-1}z'^2\alpha_2$, $\kappa = z'X_2{}^{-1}\alpha_2$ in Eq. (4.4a) and (4.4b), and it yields,

$$\frac{dx}{d\tau} = \nu - \frac{xy^2}{1+\frac{z'}{\nu}y^2(\kappa+x)} \tag{4.5a}$$

$$\frac{dy}{d\tau} = \frac{xy^2}{1+\frac{z'}{\nu}y^2(\kappa+x)} - \omega y. \tag{4.5b}$$

In glycolysis, concentration dynamics exhibit self-oscillation for the slow glycolytic flux, i.e., $z' \ll 1$. Under this condition, we can assert $1 + \frac{z}{\nu} y^2(\kappa + x) = 1$ and finally arrive at the simplified form of the Selkov system,

$$\begin{aligned} \frac{dx}{d\tau} &= \nu - xy^2 \\ \frac{dy}{d\tau} &= xy^2 - \omega y. \end{aligned} \tag{4.6}$$

It is important to note that the product formation reaction, $\rho = 2$ of the Selkov CRN in Eq. (4.1), is irreversible. However, the nonequilibrium thermodynamic description of any CRN demands all elementary chemical reactions of the CRN to be reversible. Hence, for general convenience, we resort to a completely reversible version of the Selkov model[185]. The CRN of the reversible version of Selkov model[185] can be represented by following elementary reactions,

$$\begin{aligned} \rho = 1: &\quad \mathrm{A} \underset{\mathrm{k_{-1}}}{\overset{\mathrm{k_1}}{\rightleftharpoons}} \mathrm{S} \\ \rho = 2: &\quad \mathrm{S} + 2\,\mathrm{P} \underset{\mathrm{k_{-2}}}{\overset{\mathrm{k_2}}{\rightleftharpoons}} 3\,\mathrm{P} \\ \rho = 3: &\quad \mathrm{P} \underset{\mathrm{k_{-3}}}{\overset{\mathrm{k_3}}{\rightleftharpoons}} \mathrm{B}, \end{aligned} \tag{4.7}$$

where substrate, S and product, P denote ATP and ADP, respectively. These S and P are intermediate species of this CRN, $\{S, P\} \in I$ and A and B are chemostatted species of the network, $\{A, B\} \in C$. The dynamics of the reversible Selkov CRN can be elucidated by solving the following concentration dynamics of the intermediate species,

$$\begin{aligned} \frac{ds}{dt} &= k_1 a - k_2 s p^2 \\ \frac{dp}{dt} &= k_2 s p^2 - k_3 p, \end{aligned} \tag{4.8}$$

where we assume $k_\rho \gg k_{-\rho}$. Further, we introduce the following scaled variables in Eq. (4.8), $\tau = \frac{k_2 t}{c_1^2}$, $\nu = \frac{c_1^3 k_1 a}{k_2}$, $x = c_1 s$, $y = c_1 p$, $\omega = \frac{c_1^2 k_3}{k_2}$, with c_1 being an arbitrary

constant.Now, we can express the reversible Selkov dynamics as

$$\begin{aligned} \frac{dx}{d\tau} &= \nu - xy^2 \\ \frac{dy}{d\tau} &= xy^2 - \omega y. \end{aligned} \tag{4.9}$$

The dynamics of the original Selkov model in Eq. (4.6) is equivalent to the dynamical representation of the reversible Selkov model in Eq. (4.9). So, for the further investigation of the glycolysis in this chapter, we would utilize the CRN representation and dynamical description of the reversible Selkov model the glycolysis.

For the reversible Selkov CRN in Eq. (4.7), forward reaction rate constants of the first and second elementary reactions are taken as $k_1 = k_2 = 1$. Therefore, the control parameter of the system becomes $\nu = a$. Whereas, the forward reaction rate constant of the third elementary reaction, $k_3 = 2$, results in another fixed system parameter as $\omega = 2$. We will employ the notation t for time throughout this chapter.

4.3 Conservation laws and emergent cycles of the Selkov CRN

From the reversible Selkov model in Eq. (4.7), we obtain the stoichiometric matrix as,

$$S_\rho^\sigma = \begin{array}{c} \\ S \\ P \\ A \\ B \end{array} \begin{array}{c} \begin{array}{ccc} R_1 & R_2 & R_3 \end{array} \\ \begin{pmatrix} 1 & -1 & 0 \\ 0 & 1 & -1 \\ -1 & 0 & 0 \\ 0 & 0 & 1 \end{pmatrix} \end{array}. \tag{4.10}$$

From Eq. (4.10), we obtain the conservation law of the closed Selkov CRN as,

$$l_\sigma^{\lambda=1} = \begin{array}{c} \begin{array}{cccc} X & Y & A & B \end{array} \\ \begin{pmatrix} 1 & 1 & 1 & 1 \end{pmatrix} \end{array}.$$

Therefore, the corresponding component can be represented as $L_1 = s + p + a + b$. The conservation law of the closed Selkov CRN, $l_\sigma^{\lambda=1}$ will be broken as the system will be opened by chemostatting. This Selkov CRN has no stoichiometric cycle. Since there are two chemostatted species in the Selkov CRN and one conservation law is broken in the open Selkov CRN, the open reversible Selkov CRN must admit one independent emergent cycle. This emergent cycle is given by,

$$c_1 = \begin{matrix} 1 \\ 2 \\ 3 \end{matrix} \begin{pmatrix} 1 \\ 1 \\ 1 \end{pmatrix}.$$

Over this emergent cycle, the intermediate species state remains intact, but chemostatted species of the CRN are exchanged between the system and chemostats.

4.4 Hopf instability to traveling waves within Selkov RDS

When disregarding the spatial dimension in the system, the Hopf instability with uniform oscillation (wave number $q = 0$) can only exist in the system. In a more general situation corresponding to the reaction-diffusion representation of the glycolysis model, we can have traveling waves with a nonzero finite wave number.

4.4.1 Hopf instability in the Selkov CRN

The system in Eq. (4.9) yields a unique steady-state, $x_0 = \frac{\omega^2}{\nu}$, $y_0 = \frac{\nu}{\omega}$. For the linear stability analysis at this steady state, we need to examine the Jacobian matrix of the system,

$$\mathcal{J} = \begin{pmatrix} -{y_0}^2 & -2x_0y_0 \\ {y_0}^2 & 2x_0y_0 - \omega \end{pmatrix}, \tag{4.11}$$

where elements of the Jacobian matrix, $\mathcal{J}$ are explicitly identified as, $J_{11} = -{y_0}^2$, $J_{12} = -2x_0y_0$, $J_{21} = {y_0}^2$, $J_{22} = 2x_0y_0 - \omega$. Therefore, the determinant and trace of $\mathcal{J}$ are $det(\mathcal{J}) = \frac{\nu^2}{\omega}$ and $Tr(\mathcal{J}) = \omega - (\frac{\nu}{\omega})^2$, respectively. The onset of Hopf instability demands $Tr(\mathcal{J}) = 0$, and this condition leads to the critical value of the control parameter, $\nu_{cH} = \omega\sqrt{\omega}$. Hence, the determinant becomes $det(\mathcal{J}) = \omega^2$ at this onset point, and eigenvalues are derived as $\lambda_{\pm} = \pm i\omega$. The imaginary part of the eigenvalue, λ, gives the critical frequency of the Hopf instability, $f_{cH} = \omega$ and hence the approximate period of the limit cycle is $T = \frac{2\pi}{\omega}$. Further, the critical eigenvector, U_{cH}, corresponding to the eigenvalue, $\lambda = i\omega$ is, $U_{cH} = \begin{pmatrix} 1-i \\ -1 \end{pmatrix}$.

4.4.2 Traveling wave in the Selkov RDS

Now considering spatial dimension, we can extend Selkov dynamics in Eq. (4.9) to a reaction-diffusion system (RDS) similar to the general form of RDS in Eq. (2.29),

$$\begin{aligned} \dot{x} &= \nu - xy^2 + D_{11}x_{rr} + D_{12}y_{rr} \\ \dot{y} &= xy^2 - \omega y + D_{21}x_{rr} + D_{22}y_{rr} \end{aligned} \tag{4.12}$$

for one spatial dimension $r \in [0, l]$ of a finite system of length l. For the RDS in Eq. (4.12), the Jacobian matrix, $\mathcal{J}$ of the Selkov dynamics modifies to

$$\mathcal{J}_{\mathcal{D}} = \mathcal{J} - q^2\mathcal{D} = \begin{pmatrix} -{y_0}^2 & -2x_0y_0 \\ {y_0}^2 & 2x_0y_0 - \omega \end{pmatrix} - q^2 \begin{pmatrix} D_{11} & D_{12} \\ D_{21} & D_{22} \\ . & \end{pmatrix} \tag{4.13}$$

Therefore, trace of $\mathcal{J}_{\mathcal{D}}$ is $Tr(\mathcal{J}_{\mathcal{D}}) = Tr(\mathcal{J}) - q^2Tr(\mathcal{D}) = \omega - (\frac{\nu}{\omega})^2 - (D_{11} + D_{22})q^2$ and the determinant is $det(\mathcal{J}_{\mathcal{D}}) = det(\mathcal{D})q^4 - [D_{11}J_{22} + D_{22}J_{11} - D_{12}J_{21} - D_{21}J_{12}]q^2 + det(\mathcal{J})$. Here, $det(\mathcal{D})$ is the determinant of the matrix containing diffusion coefficients. The onset of traveling waves in this reaction-diffusion system demands two criteria to be fulfilled, $Tr(\mathcal{J}_{\mathcal{D}}) = 0$, and $det(\mathcal{J}_{\mathcal{D}}) > 0$. Utilizing the trace criteria, $Tr(\mathcal{J}_{\mathcal{D}}) = 0$, the

critical control parameter value for oscillatory instability is specified as,

$$\nu_{ctw} = \omega\sqrt{\omega - (D_{11} + D_{22})q^2}. \tag{4.14}$$

The wave number q needs to obey the relation $q = \frac{2n\pi}{l}$ imposed by the periodic boundary conditions within the finite domain of length l. Here n is an integer. Further, the determinant condition, $det(\mathcal{J}_{\mathcal{D}}) > 0$, adds another constraint to the wave number selection. Therefore, the traveling waves in this Selkov RDS have to satisfy the condition, $(D_{22}^2 + D_{12}D_{21} + D_{12}D_{11} + D_{12}D_{22})q^4 + (2D_{11}\omega - D_{12}\omega + 2D_{21}\omega)q^2 - \omega^2 \leq 0$ derived from the determinant condition. We can obtain a critical value of the wave number utilizing the equality condition from the above quadratic equation of q^2 as, $q_c^2 = \frac{\omega[-(2D_{11}-D_{12}+2D_{21})\pm\sqrt{(2D_{11}+2D_{21})^2+(2D_{22}+D_{12})^2}]}{2(D_{22}^2+D_{12}D_{21}+D_{12}D_{11}+D_{12}D_{22})}$.

From the traveling waves, we can acquire the Hopf instability as a special case of traveling waves by setting $q = 0$, and we recover the critical control parameter value of the Hopf instability, $\nu_{cH} = \omega\sqrt{\omega}$.

4.5 Amplitude equation of Hopf instability and traveling waves in the presence of cross diffusion

4.5.1 KB averaging method for the Selkov RDS

Similar to the previous chapter, we exploit the modified KB averaging method[169] to obtain the dynamical equation of magnitude and phase corresponding to the spatially extended reversible Selkov CRN, where both self and cross diffusions are taken into account.

Initially, defining two new variables, $z = x + y$ and $u = \nu - \omega y$, we can rewrite the dynamics of the Selkov CRN in Eq. (4.9) into the following form:

$$\begin{aligned} \dot{z} &= u \\ \dot{u} &= -\omega(u - \nu) - \omega^{-2}(\omega z + u - \nu)(u - \nu)^2 \end{aligned} \tag{4.15}$$

which yields the steady state of the Selkov system as $u_s = 0$ and $z_s = \frac{\omega^2}{\nu} + \frac{\nu}{\omega}$. Further, we shift the steady state point to the origin by setting up a new variable, $\zeta = z - z_s$ and by exploiting the dynamical equation of u and ζ it is possible to derive a single second-order equation,

$$\ddot{\zeta} + \Omega^2\zeta = \lambda[2(1 + c_1u - c_2u^2)u - \frac{\Omega^2}{\lambda}(\nu^{-2}u^2 - 2\nu^{-1}u)\zeta]. \tag{4.16}$$

In the above equation, we define following parameters, $\Omega = \frac{\nu}{\sqrt{\omega}}, \lambda = \frac{\omega - \omega^{-2}\nu^2}{2}, c_1 = \frac{(2\omega^{-2}\nu - \frac{\omega}{\nu})}{2\lambda}, c_2 = \frac{\omega^{-2}}{2\lambda}$. Now if we consider $2(1 + c_1u - c_2u^2)u - \frac{\Omega^2}{\lambda}(\nu^{-2}u^2 - 2\nu^{-1}u)\zeta = h$ in Eq. (4.16), we arrive at

$$\ddot{\zeta} + \Omega^2\zeta = \lambda h. \tag{4.17}$$

For the Selkov RDS in Eq. (4.12) comprising both self and cross diffusion, Eq. (4.17) gets modified to the following equation,

$$\ddot{\zeta} + \Omega^2\zeta = \lambda h + (D_{22} + D_{12} - D_{11} - D_{21})\dot{u}_{rr} + (D_{22} + D_{12})\dot{\zeta}_{rr} + (D_{11} - D_{12})u_{rr} - D_{12}\zeta_{rr}. \tag{4.18}$$

Under the assumption of small λ, Eq. (4.18) can admit simple harmonic function like solutions,

$$\zeta(r,t) = \mathcal{A}(r,t)\cos(\Omega t + \phi(r,t)) \tag{4.19a}$$

$$u(r,t) = \dot{\zeta}(r,t) = -\Omega\mathcal{A}(r,t)\sin(\Omega t + \phi(r,t)), \tag{4.19b}$$

utilizing Eq. (4.19a) and (4.19b), we derive the dynamics of the amplitude and phase as,

$$\begin{aligned}\dot{\mathcal{A}} = -\frac{1}{\Omega}[\lambda h - \Omega^2(D_{22} + D_{12} + \frac{D_{12}}{\Omega^2} - D_{11} - D_{21})\zeta_{rr} \\ +(D_{22} + D_{11})u_{rr}]\sin(\Omega t + \phi),\end{aligned} \tag{4.20}$$

$$\begin{aligned}\dot{\Phi} = \frac{1}{\Omega\mathcal{A}}[\lambda h - \Omega^2(D_{22} + D_{12} + \frac{D_{12}}{\Omega^2} - D_{11} - D_{21})\zeta_{rr} \\ +(D_{22} + D_{11})u_{rr}]\cos(\Omega t + \phi).\end{aligned} \tag{4.21}$$

The final dynamical equations of amplitude and phase are then acquired by taking the average similar to the previous chapter,

$$\dot{\mathcal{A}} = \mathcal{A}\lambda - p_1\frac{3\lambda c_2\Omega^2}{4}A^3 - \frac{\Omega}{2}(D_{22} + D_{12} + \frac{D_{12}}{\Omega^2} - D_{11} - D_{21})(2\mathcal{A}_r\phi_r + \phi_{rr}\mathcal{A}) + \frac{(D_{11}+D_{22})}{2}(\mathcal{A}_{rr} - \mathcal{A}\phi_r^2), \quad (4.22)$$

$$\dot{\Phi} = -p_2\frac{\Omega^3}{8\nu^2}\mathcal{A}^2 - \frac{(D_{11}+D_{22})}{2}(\frac{2\mathcal{A}_r\phi_r}{\mathcal{A}} + \phi_{rr}) - \frac{\Omega}{2}(D_{22} + D_{12} + \frac{D_{12}}{\Omega^2} - D_{11} - D_{21})(\frac{\mathcal{A}_{rr}}{\mathcal{A}} - \phi_r^2). \quad (4.23)$$

Correction factors, $p_1 = \frac{c_2}{c_1}$ and $p_2 = \frac{2c_1}{\nu c_2}$ are included in Eq. (3.21a) and (3.21b) to capture the modulation on the radius and phase of the limit cycle as a result of unidirectional acceleration from unstable steady state[163].

4.5.2 Coefficients of CGLE for reversible Selkov model

We discussed in the previous chapter that CGLE reliably reflects the oscillatory dynamics near the onset of Hopf instability. Assuming the same velocity for all the traveling waves and considering a comoving coordinate, $r = r - velocity \times t$, we can implement the same amplitude equation in Eq. (3.22) for the traveling waves. By substituting $Z = \mathcal{A}\exp(i\phi)$ in Eq. (3.22) and then separating the real and imaginary parts we acquire,

$$\frac{\partial\mathcal{A}}{\partial t} = \lambda\mathcal{A} - \beta_{\mathcal{R}}\mathcal{A}^3 - \alpha_{\mathcal{I}}(2\mathcal{A}_r\phi_r + \phi_{rr}\mathcal{A}) + \alpha_{\mathcal{R}}(\mathcal{A}_{rr} - \mathcal{A}\phi_r^2), \quad (4.24a)$$

$$\frac{\partial\phi}{\partial t} = \beta_{\mathcal{I}}\mathcal{A}^2 + \alpha_{\mathcal{R}}(\frac{2\mathcal{A}_r\phi_r}{\mathcal{A}} + \phi_{rr}) + \alpha_{\mathcal{I}}(\frac{\mathcal{A}_{rr}}{\mathcal{A}} - \phi_r^2). \quad (4.24b)$$

By comparing the above equations deduced from CGLE with the phase and amplitude equations (4.22) and (4.23) derived using the modified KB method, we obtain the following coefficients corresponding to Selkov RDS: $\beta_r = p_1\frac{3\lambda c_2\Omega^2}{4}$, $\beta_i = -p_2\frac{\Omega^3}{8\nu^2}$, $\alpha_r = -\frac{(D_{11}+D_{22})}{2}$, $\alpha_i = -\frac{\Omega}{2}(D_{22} + D_{12} + \frac{D_{12}}{\Omega^2} - D_{11} - D_{21})$. Using the scaled variables,

$\mathcal{A} = \frac{\mathcal{A}}{\sqrt{\beta_r}}$ and $r = \frac{r}{\sqrt{\alpha_r}}$ in Eq. (4.24a) and (4.24b), we can obtain

$$\frac{\partial \mathcal{A}}{\partial t} = \lambda\mathcal{A} - \mathcal{A}^3 - \alpha(2\mathcal{A}_r\phi_r + \phi_{rr}\mathcal{A}) + (\mathcal{A}_{rr} - \mathcal{A}\phi_r^2), \tag{4.25a}$$

$$\frac{\partial \phi}{\partial t} = \beta\mathcal{A}^2 + (\frac{2\mathcal{A}_r\phi_r}{\mathcal{A}} + \phi_{rr}) + \alpha(\frac{\mathcal{A}_{rr}}{\mathcal{A}} - \phi_r^2), \tag{4.25b}$$

which corresponds to the normal form of CGLE as in (3.25). Despite the universal form of the normal CGLE, coefficients of the CGLE for the Selkov RDS will be different from the Brusselator RDS in the previous chapter and are identified as $\alpha = \frac{\alpha_i}{\alpha_r} = \frac{\Omega(D_{22}+D_{12}+\frac{D_{12}}{\Omega^2}-D_{11}-D_{21})}{(D_{11}+D_{22})}$ and $\beta = \frac{\beta_i}{\beta_r} = -\frac{p_2}{p_1}\frac{\sqrt{\omega}\omega}{3\nu}$.

4.6 Amplitude and phase of the RDS

Assuming slow temporal variation of the amplitude, we can express $\mathcal{A}$ as its steady state using Eq. (4.25a). Hence,

$$\mathcal{A}^2 = \lambda - \alpha(\frac{2\mathcal{A}_r\phi_r}{\mathcal{A}} + \phi_{rr}) + (\frac{\mathcal{A}_{rr}}{\mathcal{A}} - \phi_r^2). \tag{4.26}$$

Further, due to long-range phase variation, we can simplify the steady state amplitude in Eq. (4.26) to

$$\mathcal{A}^2 = \lambda - \alpha\phi_{rr} - \phi_r^2. \tag{4.27}$$

By inserting steady state amplitude in Eq. (4.27) into Eq. (4.25b), we derive the following phase dynamics

$$\frac{\partial \phi}{\partial t} = \beta\lambda + (1 - \alpha\beta)\phi_{rr} - (\alpha + \beta)\phi_r^2. \tag{4.28}$$

Benjamin-Feir(BF) instability criterion

In the above phase equation, the criterion, $(\alpha + \beta) < 0$, is associated with the exchange between inward and outward rotating spiral. Another criterion known as the Newell criterion, $(1 - \alpha\beta) < 0$, sets the onset of the Benjamin-Feir (BF) instability[186,4] from the uniform oscillation. This BF instability was first found in deep-water waves[186]. It

is a long-wave side-band instability and generates irregularities in the wave number and frequency of a previously uniform traveling wave.

Closed form of the phase

Now defining the new phase variable as, $\psi = \phi - \beta\lambda t$ in Eq. (4.28), we arrive at

$$\frac{\partial \psi}{\partial t} = (1 - \alpha\beta)\psi_{rr} - (\alpha + \beta)\psi_r^2. \tag{4.29}$$

By employing the derivation concerning space and setting $\psi_r = u$, the following equation akin to Burger's equation is obtained,

$$\frac{\partial u}{\partial t} = (1 - \alpha\beta)u_{rr} - (\alpha + \beta)2uu_r. \tag{4.30}$$

Further, we transform Eq. (4.29) into a linear equation by applying the Cole-Hopf transformation, $\psi = -[\frac{1-\alpha\beta}{\alpha+\beta}] \ln \chi$,

$$\frac{\partial \chi}{\partial t} = (1 - \alpha\beta)\chi_{rr}. \tag{4.31}$$

Considering $\chi = G(t) \exp{(\alpha + \beta)qr}$ as the trial solution of Eq. (4.31), we derive a simple solution as $\chi = G_0 \exp{((1 - \alpha\beta)(\alpha + \beta)^2 q^2 t + (\alpha + \beta)qr)}$ with G_0 being an arbitrary inital value. Eventually, from the relation between χ and ψ we express the closed form of the system phase as

$$\phi = \beta\lambda t - \frac{1 - \alpha\beta}{\alpha + \beta}[\ln G_0 + (1 - \alpha\beta)(\alpha + \beta)^2 q^2 t + (\alpha + \beta)qr]. \tag{4.32}$$

Dispersion relation

The normal form of the CGLE can accept an asymptotic plane wave solution,

$$Z = \mathcal{A} \exp i(\omega_0 t + qr), \tag{4.33}$$

with ω_0 being the frequency shift from the critical frequency f_{cH} and q being a unique wave number selected by the unique spiral frequency. Then, we can obtain the following relations

$$q^2 = \lambda - \mathcal{A}^2 \tag{4.34a}$$

$$\omega_0 = \beta\mathcal{A}^2 - \alpha q^2 = \beta\lambda - (\beta + \alpha)q^2. \tag{4.34b}$$

from Eq. (3.25). Hence, any modification of the system's frequency will induce a change in the wave number, q, by the nonlinear dispersion relation given in Eq. (4.34b). By inserting $q = q_{cH} = 0$ in (4.34b), the frequency of uniform oscillation (bulk frequency) is obtained. Further, the group velocity can be represented as $v_g = \frac{\partial \omega_q}{\partial q} = -2(\beta + \alpha)q$.

4.6.1 Stability of plane wave and wave number selection

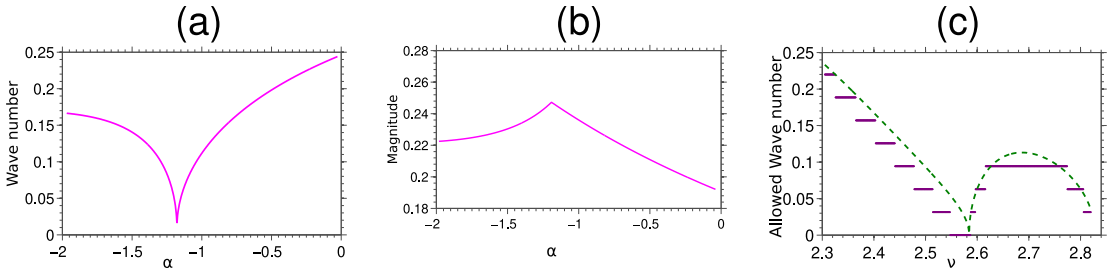

Figure 4.1: The wave number with the coefficient α is illustrated in (a). (b) Variation of the magnitude of the complex amplitude as a function of the same coefficient, α. In both figures, we change the cross-diffusion coefficient, D_{12} from -0.00001 to -0.0005 and D_{21} from 0.00001 to 0.0005 while keeping other parameters fixed, i.e., $D_{11} = D_{22} = 0.00051$, $\nu = 2.45$ and $w = 2$. (c) Discrete allowed values of wave number near the onset of Hopf instability for $D_{11} = D_{22} = 0.00051$, $D_{12} = -0.0002$, $D_{21} = 0.0002$, and $\omega = 2$ are shown by the solid line. The dashed line represents the continuous wave number in the limit of infinite size.

Unlike the equilibrium system, the wave number selection in a finite system under far-from-equilibrium conditions is a challenging problem to be addressed[4], primarily because the wave number intricately relies on factors such as control parameter values, boundary conditions, dynamical processes, perturbations, and methodologies. In this regard, we can assess the stability of the asymptotic plane wave solution of the CGLE

by introducing a small perturbation about the nonlinear wave state. Consequently, the perturbed plane wave will exhibit the following structure

$$Z = (\mathcal{A} + A_{per}) \exp i(qr + \omega_0 t), \tag{4.35}$$

where A_{per} can be expressed in the following form using the complex growth rate, σ,

$$A_{per} = A_+ \exp(iKr + \sigma t) + \tilde{A_-} \exp(-iKr + \tilde{\sigma} t). \tag{4.36}$$

Here, $\tilde{A}$ and $\tilde{\sigma}$ denote the complex conjugation of A and σ, respectively and K represents different perturbation modes. Substituting Eq. (4.35) into Eq. (3.25) and neglecting the higher order of the perturbation, we obtain the following,

$$\begin{aligned}\frac{\partial A_{per}}{\partial t} + i\omega_0(\mathcal{A} + A_{per}) = \lambda(\mathcal{A} + A_{per}) - (1 - i\beta)(\mathcal{A}^3 + 2\mathcal{A}^2 A_{per} + \mathcal{A}^2 \tilde{A}_{per}) \\ +(1 + i\alpha)({\partial_r}^2 A_{per} + 2iq\partial_r A_{per} - q^2(\mathcal{A} + A_{per})).\end{aligned} \tag{4.37}$$

Now substituting the perturbed plane wave Eq. (4.36) into Eq. (4.37) and rearranging terms, following equality is derived

$$\begin{aligned}[A_+\sigma + i\omega_0 A_+ - \lambda A_+ + (1 - i\beta)(2\mathcal{A}^2 A_+ + \mathcal{A}^2 A_-) + \\ (1 + i\alpha)(K + q)^2 A_+] \exp(iKr + \sigma t) \\ +[\tilde{A}_-\tilde{\sigma} + i\omega_0 \tilde{A}_- - \lambda \tilde{A}_- + (1 - i\beta)(2\mathcal{A}^2 \tilde{A}_- + \mathcal{A}^2 \tilde{A}_+) + \\ (1 + i\alpha)(K - q)^2 \tilde{A}_-] \exp(-iKr + \tilde{\sigma} t) \\ +i\omega_0 \mathcal{A} - \lambda \mathcal{A} + (1 - i\beta)\mathcal{A}^3 + (1 + i\alpha)q^2 \mathcal{A} = 0.\end{aligned} \tag{4.38}$$

From Eq. (4.38), by equating coefficients of $\exp(iKr + \sigma t)$ and $\exp(-iKr + \tilde{\sigma} t)$ to 0, a

homogeneous system is acquired as,

$$(\sigma + (1 - i\beta)\mathcal{A}^2 + (1 + i\alpha)(K^2 + 2qK))A_+ + (1 - i\beta)\mathcal{A}^2 A_- = 0 \tag{4.39a}$$

$$(\sigma + (1 + i\beta)\mathcal{A}^2 + (1 - i\alpha)(K^2 - 2qK))A_- + (1 + i\beta)\mathcal{A}^2 A_+ = 0, \tag{4.39b}$$

which can be represented in a compact form, $H \begin{pmatrix} A_+ \\ A_- \end{pmatrix} = 0$ with

$$H = \begin{bmatrix} \sigma + (1 - i\beta)\mathcal{A}^2 & \\ +(1 + i\alpha)(K^2 + 2qK) & (1 - i\beta)\mathcal{A}^2 \\ & \\ (1 + i\beta)\mathcal{A}^2 & \sigma + (1 + i\beta)\mathcal{A}^2 \\ & +(1 - i\alpha)(K^2 - 2qK) \end{bmatrix}.$$

Now by solving the characteristic equation associated with H, we acquire the most positive growth rate σ as,

$$\sigma = -\mathcal{A}^2 - K^2 - 2i\alpha qK + \sqrt{(1 + \beta^2)\mathcal{A}^4 - (\alpha K^2 - \beta\mathcal{A}^2 - 2iqK)^2}. \tag{4.40}$$

For exploring the long wavelength behavior, we expand Eq. (4.40) around $K = 0$. It results in,

$$\sigma = -2iq(\alpha + \beta)K + [\frac{(2q^2(1 + \beta^2) + \beta\alpha\mathcal{A}^2)}{\mathcal{A}^2} - 1]K^2 + O(K^3). \tag{4.41}$$

We aim to determine the threshold of the stable wave number above which the traveling wave exhibits instability. For that purpose, we utilize $\partial_{KK}\sigma = 0$ to set a boundary between stable and unstable wave numbers. Therefore, the wave number at the onset of instability can be represented as

$$q^2 = \frac{\lambda(1 - \alpha\beta)}{2\beta^2 - \alpha\beta + 3}. \tag{4.42}$$

Eq. (4.42) provides the band of allowed wave number of the traveling waves near the critical wave number of the Hopf instability.

As mentioned earlier, the wave number q needs to satisfy $q = \frac{2n\pi}{l}$ (n is an integer) under the periodic boundary conditions. Hence, the wave number has to be quantized. A discrete wave number set corresponding to plane waves emerges with the variation of the control parameter of the system. Furthermore, the perturbation wave number, K, also has to be fit within the finite domain. So, under the periodic boundary conditions, we express the allowed wave number as, $q \pm K = \frac{2m\pi}{l}$, where m is also an integer and generally $m \neq n$. Here, we maintain the perturbation wave number at a minimum finite value by keeping $|m - n| = 1$ near the critical wave number of the Hopf instability. In this way, we acquire a discontinuous overall change in the allowed wave numbers for the control parameter variation.

We have linearly unstable plane waves within the BF instability regime. However, these linearly unstable waves can have physical relevance due to the convective nature of this instability. Adjacent to the BF instability onset, q approaches zero. Therefore, Eq. (4.40) yields the following expression of σ,

$$\sigma_{q=0} = -\lambda - K^2 + \sqrt{\lambda^2 - \alpha^2 K^4 + 2\alpha\beta K^2 \lambda}. \tag{4.43}$$

Now expanding Eq. (4.43) for $K \to 0$ and then setting the Taylor expansion of $\sigma_{q=0}$ to zero, the following expression is achieved

$$K_c^2 = \frac{2\lambda(\alpha\beta - 1)}{\alpha^2(1 + \beta^2)}. \tag{4.44}$$

When the value of the control parameter keeps the system near the BF instability onset or within the BF instability regime, the linearly unstable modulated waves with the discrete allowed wave numbers taken from the band, $|K| < K_c$ is considered to persist in the system. The role of the finite domain size in specifying the wave number within the nonequilibrium environment is discussed in detail in ref.[129].

It is evident from the expression in Eq. (4.42) that the wave number, q, depends ex-

plicitly on the coefficients α and β of the amplitude equation. Further, Eq. (4.44) also suggests the explicit dependence of the K_c on coefficients α and β. Since the coefficient, α contains the cross-diffusion terms, we depict the relationship between wave numbers and α in Fig. 4.1 (a) to reveal the implicit dependence of the wave number on the cross diffusion. We have obtained the profile by simultaneously varying the cross-diffusion coefficients while keeping all other parameters, including self-diffusion coefficients, fixed. Here, the zero wave number point signifies the onset of the BF instability, implying that it is feasible to enter or exit the BF instability regime solely by adjusting the cross-diffusion coefficients of the system. Nonetheless, the continuous variation of the wave number is only possible for infinite system size consideration. Likewise, we have demonstrated the change in the magnitude of the complex amplitude concerning α in Fig. 4.1 (b). This magnitude essentially determines the radius of the limit cycle in the system, and Fig. 4.1 (b) suggests that the alterations in the radius can be achieved solely by manipulating the cross-diffusion coefficients[187]. In Fig. 4.1 (a), the wave number within the BF instability regime decreases towards the onset of the BF instability point, and concurrently in Fig. 4.1 (b), the magnitude gradually increases. Conversely, outside the instability regime, a decrease in magnitude is observed with an increase in wave number. In Fig. 4.1 (c), we depict the wave number in proximity to the critical wave number of the Hopf instability, as a function of the control parameter ν. The discrete wave numbers, denoted by the solid and bold lines, represent allowed values for the traveling wave at different control parameter values and other parameter values mentioned in the figure. These discrete wave numbers are valid within a finite domain with periodic boundary conditions and are determined using analytically derived expressions for continuous wave numbers, (4.42) and (4.44). As we vary the control parameter towards the onset of the BF instability point while keeping all other parameters constant, the wave number gradually decreases and converges towards the critical value associated with Hopf instability. Subsequently, we again consider discrete and finite wave numbers within the BF instability region. The dashed line in the same figure illustrates the corresponding continuous wave number profile, applicable as wave numbers in the limit

of infinite system size.

4.7 Amplitude and concentration dynamics of homogeneous oscillation and traveling waves: Benjamin-Feir instability

4.7.1 Analytical expression of concentration evolution for traveling waves

As discussed earlier, the Hopf instability and traveling waves can be found within a specific range of the control parameter, ν, depending on whether the selected wave number is zero or a finite nonzero value. The temporal concentration pattern due to Hopf instability can be acquired from an equation similar to Eq. (3.8) in the previous chapter. However, all the entities and parameters will be now procured from the Selkov RDS.

However, the evolution of the concentration fields of the intermediate species, z_{ITW} for traveling waves near the onset of oscillation is slightly different due to the presence of the spatial variation in the amplitude part owing to nonzero wave number of traveling waves and are expressed as

$$z_{ITW} = z_{I0} + \mathcal{A}_{\mathcal{TW}} U_{cH} \exp\left(i f_{cH} t\right) + C.C., \tag{4.45}$$

with z_{I0} being the uniform base state representing the steady state of the Selkov system here. In Eq. (4.45), $\mathcal{A}_{\mathcal{TW}}$ is the amplitude part within the oscillatory regime, and its real part is obtained from Eq. (4.34a). Therefore, the final general concentration dynamics within the oscillatory regime are derived as

$$\begin{pmatrix} x \\ y \end{pmatrix} = \begin{pmatrix} x_0 \\ y_0 \end{pmatrix} + \sqrt{\lambda - q^2} \begin{pmatrix} 2\cos\left(\omega_0 t + f_{cH} t + qr\right) + 2\sin\left(\omega_0 t + f_{cH} t + qr\right) \\ -2\cos\left(\omega_0 t + f_{cH} t + qr\right) \end{pmatrix}. \tag{4.46}$$

The concentration dynamics represented in Eq. (4.46) encapsulate the essential features of both Hopf homogeneous oscillation and traveling waves within the oscillatory para-

metric regime.

4.7.2 Illustration of amplitude and concentration dynamics in Selkov RDS

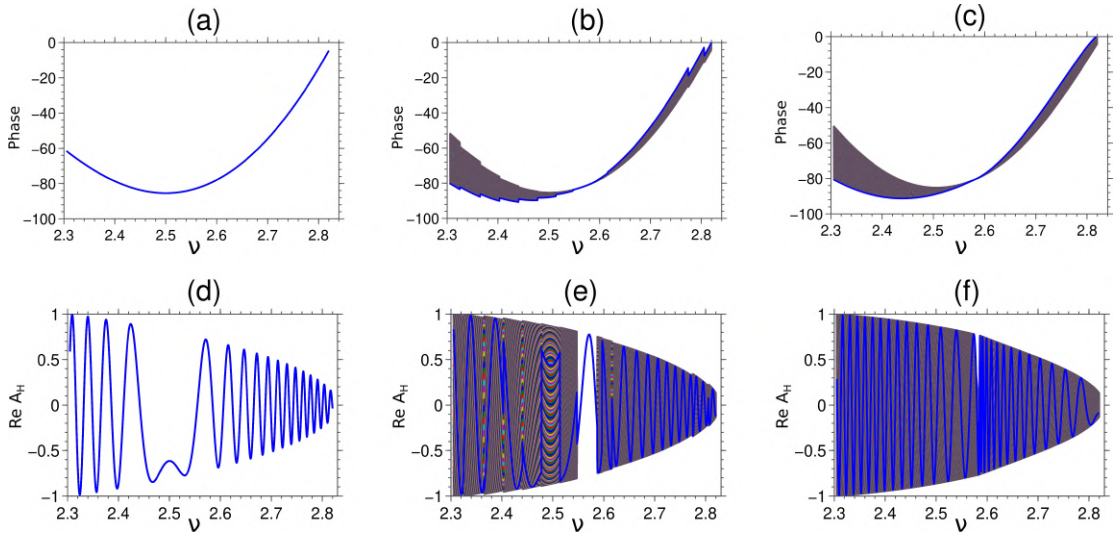

Figure 4.2: The phase dynamics of 1D Selkov RDS corresponding to the Hopf instability (a) and traveling waves (b) with the control parameter, ν, are represented in the upper panel of the figure. The phase dynamics of traveling waves in the limit of infinite system size is illustrated in (c). The variations of the normalized real amplitude, 'Re A_H' concerning the control parameter ν at a specific time point, $t = 400$, are illustrated in the lower panel of the figure: (d) Hopf instability (e) traveling waves for discrete and (f) continuous wave number. Here, diffusion coefficients are: $D_{11} = D_{22} = 0.00051$, $D_{12} = -0.0002$, $D_{21} = 0.0002$. We consider the finite domain of length $l = 200$, and the parameter ω is fixed at 2.

Amplitude and concentration dynamics of the 1D Selkov RDS in the regime of oscillatory instability for uniform oscillation and traveling waves are presented in 4.2. All figures are procured in the 1D system of length, $l = 200$, and we take 520 grid points. A time step of size 0.16 is used. All snapshots are taken at the time point $t = 400$. The diffusion coefficients of this spatially extended system are $D_{11} = D_{22} = 0.00051$, $D_{12} = -0.0002$, and $D_{21} = 0.0002$. We assume weakly reversible reactions with reverse chemical reaction rate constants being $k_{-\rho} = 10^{-4}$ and forward reaction rate constants being $k_1 = k_2 = 1$ and $k_3 = 2$ in Eq. (4.7). Since both the theoretical[188] and experimental[189] studies suggest the temperature dependence of the glycolytic oscillation, we keep

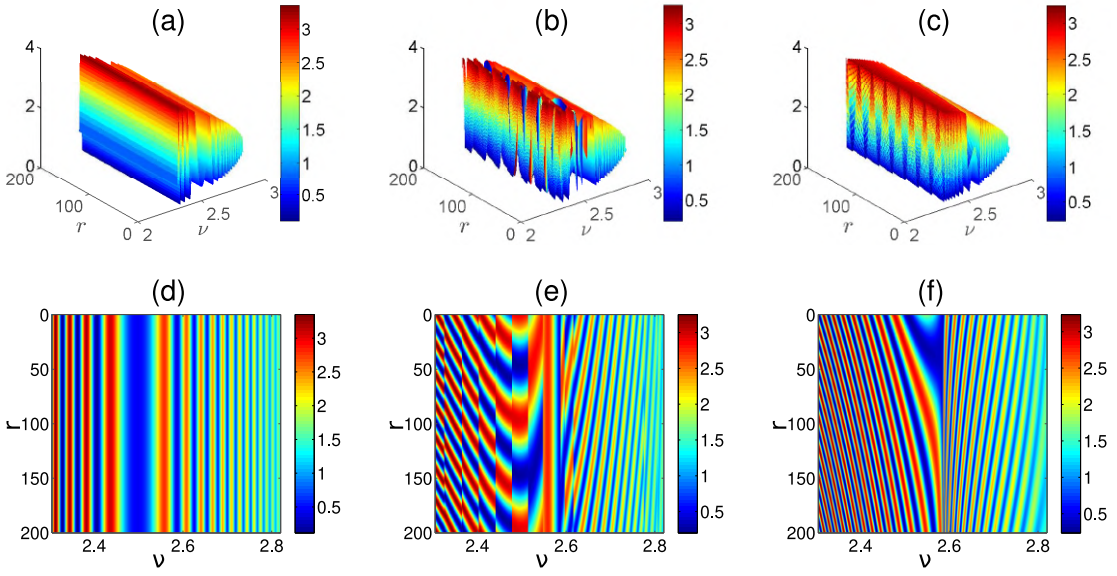

Figure 4.3: The 3d concentration field of the intermediate species, X, as a function of the control parameter, ν, is illustrated in the upper panel: (a) Hopf instability, (b) traveling waves with discrete wave number, and (c) traveling waves with continuous family of wave numbers. Here, we implement the 'jet' colormap to capture the contrast in the concentration field. The corresponding images of concentration fields are presented in the lower panel of the figure. All other system parameter values are the same as in the previous figure.

the temperature constant throughout. This constant temperature assumption implies much faster heat diffusion relative to the concentration of intermediate species in this reaction-diffusion system. The system is initially characterized by steady-state values of two intermediate species. These system parameters and situations remain intact unless otherwise indicated. A self-sustained oscillation emerges below the ν_{cH} for the parameter $\omega = 2$. Implementing CGLE as the backbone of our analytical investigation restricts us to only a small parametric space in the vicinity of ν_{cH}. Concentration dynamics of the intermediate species over a range of relevant control parameter values are illustrated in Fig. 4.3 utilizing the general analytical evolution equation of concentrations, Eq. (4.46).

The lower and upper panels of Fig. 4.2 illustrate dynamics of the real part of the amplitude field, A_H in the normalized form and the phase, ϕ, respectively with the control parameter near the oscillatory instability regime. The dynamics of A_H is obtained from Z in Eq. (4.33) utilizing Eq. (4.34a) and (4.34b). Hence, the real part of A_H

variation includes features of both the phase and magnitude of the amplitude. Whereas, the variation of the phase is exhibited using Eq. (4.32). For the Hopf instability, the selected wave number is zero, and therefore we notice an irregular oscillatory profile of the real part of the Hopf amplitude field, A_H with the variation of ν in Fig. 4.2 (d). The different magnitudes of the oscillatory concentration profile regarding the different control parameter values suggest the modification of the radius of the Hopf limit cycles. This Hopf amplitude curve provides information about the essential concentration dynamics within the Hopf instability regime at a fundamental level. The corresponding Phase variation is illustrated in Fig. 4.2 (a). Analyzing the dynamics of amplitude and phase, we can assert that the 'double-well' shaped low-amplitude region of the normalized amplitude profile (at $\nu = 2.5$) in Fig. 4.2 (d) is associated with a local minimum of the phase in Fig. 4.2 (a). While for traveling waves with allowed discrete wave numbers, no notable change in the normalized real part of the amplitude profile is noticed in Fig. 4.2 (e) corresponding to the local minima of the phase in Fig. 4.2 (b). However, as the spatial distribution of the phase ceases to a point near $\nu = 2.6$ in Fig. 4.2 (b), the normalized amplitude exhibits a spatially homogeneous region in Fig. 4.2 (e). In both Hopf instability and traveling wave, we observe a gradual increment in the magnitudes of normalized amplitudes as we decrease the control parameter value away from the onset point of the oscillatory instability. In the scenario related to infinite system size limit, i.e., for traveling wave with continuous wave number band, both the phase and normalized amplitude in Fig. 4.2 (c) and 4.2 (f), respectively exhibit more smooth transitions relative to discrete wave number counterpart of the traveling wave. Further, the homogeneous region of the normalized amplitude is not evident. The 3d concentration fields and corresponding field images of the intermediate species, X, derived by employing the analytical Eq. (4.46), are illustrated in the upper and lower panels of Fig. 4.3. For Hopf instability, a wide low-concentration regime can be seen over the control parameter space ranging from $\nu = 2.4$ to $\nu = 2.6$ in Fig. 4.3 (d). There exists a one-to-one correspondence between this wide low-concentration regime and the 'double-well' shaped low-amplitude part discussed earlier. In this way, this low-concentration

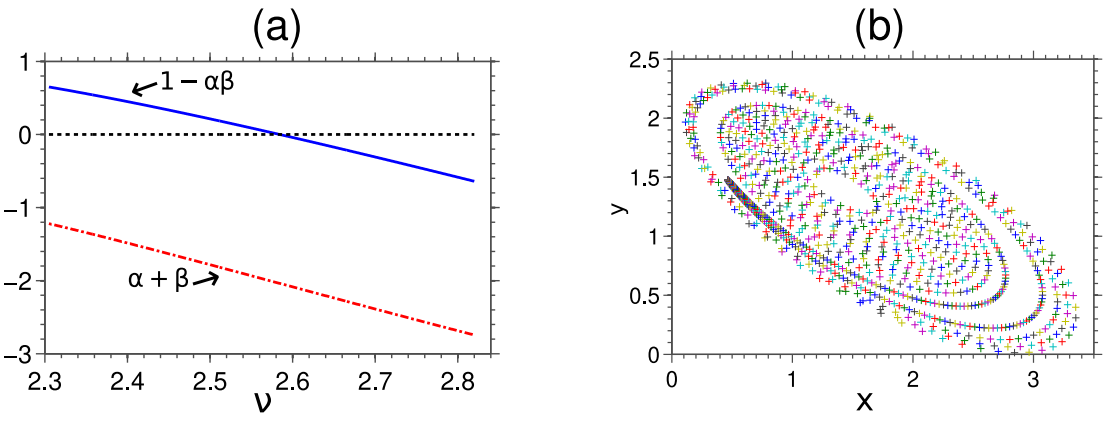

Figure 4.4: (a)The Benjamin-Feir (BF) instability and phase reversal defining conditions acquired from the amplitude equation formalism. As the $1-\alpha\beta$ line crosses the zero line (dashed), we enter the BF instability region. (b) A phase portrait-like illustration for the Hopf instability. Here, dynamics of X and Y species' concentrations are acquired by varying ν at a fixed time point $t = 400$.

regime is associated with the sign change of the phase's slope, from negative to positive. Before discussing more about this wide low-concentration region, we look into the variation of two mathematical expressions comprising the amplitude equation's coefficients. More specifically, the variations of $\alpha+\beta$ and $1-\alpha\beta$ with control parameter ν represented by the red dotted line and the solid blue line, respectively in Fig. 4.4 (a). The dotted black line in the figure corresponds to $\alpha+\beta=0$ or $1-\alpha\beta=0$ condition. The $\alpha+\beta$ line in Fig. 4.4 (a) never crosses the zero line in this RDS implying no scenario of exchange between inward and outward rotating spiral. Whereas, the $1-\alpha\beta$ line intersects the zero-line near $\nu=2.6$ referring to the generation of BF instability with the control parameter variation. Now, observing the normalized Hopf amplitude in Fig. 4.2 (d), we assert that the abrupt low-amplitude profile arises before the onset point of BF instability. This low-amplitude part is the reason behind the wide low-concentration region of the concentration field illustrated in Fig. 4.3 (d). Beyond the onset of the instability point, damped oscillatory-type behavior emerges. Furthermore, we notice a clear turnback in the phase portrait-like representation in Fig. 4.4 (b) corresponding to this wide low-concentration region in the X concentration field of the Hopf instability. Hence, we assert that the direction change in the concentration phase portrait corresponding to the Hopf instability is essentially associated with the sign change of

the phase slope. A previous study of glycolytic wave propagation[180] also reported a pulsating regime within the temporal concentration dynamics of X due to the phase reversal with time in the presence of inhomogeneous substrate influx. We will study the Selkov RDS with inhomogeneous substrate influx in the next chapter.

Now, for the traveling waves with discrete allowed wave numbers, the 3D concentration field of X and the corresponding concentration field image are exhibited in Fig. 4.3 (b) and (e), respectively. Within the stable oscillatory region of the RDS, traveling wave patterns are presented for discrete wave numbers corresponding to the linearly stable wave number limit. When the control parameter tuning takes the system beyond the BF instability onset point, we still obtain a modulated wave pattern in Fig. 4.3 (e) as the system can select nonzero wave numbers due to the convective nature of BF instability. In this regard, the disconnectedness observed in the traveling wave pattern is a result of the involvement of different discrete wave numbers related to the distinct control parameter values. The modification in the amplitude dynamics while passing the BF instability point dictates the changes in the traveling wave pattern around the BF instability. The spatially homogeneous part of the amplitude dynamics, related traveling waves corresponds to the zero wave number selection around BF instability onset. Despite the selected wave number for the traveling waves at the onset of BF instability is the same as the wave number of the Hopf instability, we must treat them as two distinct dynamic phenomena.

For the infinite size limit, wave numbers of traveling waves can take continuous values represented by a dashed line in Fig. 4.1 (c). For this scenario, we obtain a different concentration pattern of traveling waves in comparison to its discrete wave number counterpart. The 3D concentration field of X and the corresponding concentration field image related to the traveling wave with continuous wave number are demonstrated in Fig. 4.3 (c) and (f), respectively. This contrast in the concentration patterns of traveling waves with discrete and continuous wave numbers is expected, provided different amplitude dynamics are acquired in these two scenarios.

Thus, we can better understand and predict the concentration dynamics with ν in

Fig. 4.3 by accessing different instability conditions in terms of coefficients, α, and β. The α coefficient, a crucial entity in defining the instability conditions at the level of the amplitude dynamics, contains both the self and cross-diffusion coefficients. Therefore, the cross diffusion can solely shift parametric regimes and thus impact the temporal concentration pattern to a significant extent, particularly in the system with equal self-diffusion coefficients.

4.8 Thermodynamic cost of glycolytic patterns

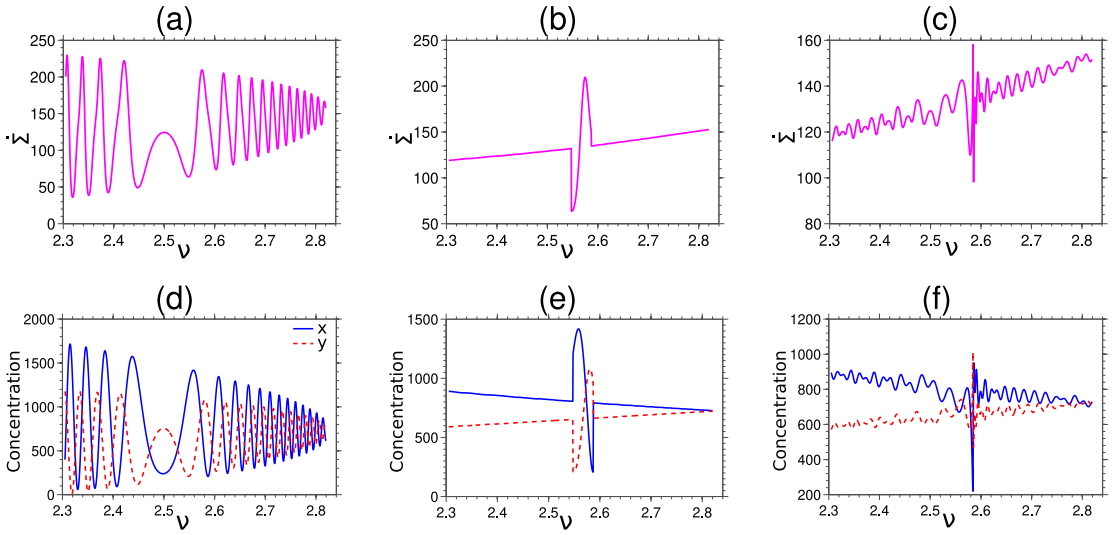

Figure 4.5: (a) The total entropy production rate (EPR) of the Hopf instability concerning the control parameter ν is measured. (d) Variation in the global concentration fields of intermediate species X and Y for the Hopf instability as a function of ν. (b) Total EPR of traveling waves with discrete wave numbers and (e) corresponding global concentration fields of intermediate species with the control parameter variation (c) Total EPR and (f) corresponding global concentration fields for traveling waves in the limit of infinite size are illustrated.

We quantify the nonequilibrium thermodynamic cost of the concentration patterns discussed above in terms of total entropy production rate (EPR) and semigrand Gibbs free energy (SGG). The total EPR and SGG variations concerning the control parameter, ν, keeping the other parameter, $\omega = 2$ fixed, are depicted in both Hopf and traveling wave scenarios.

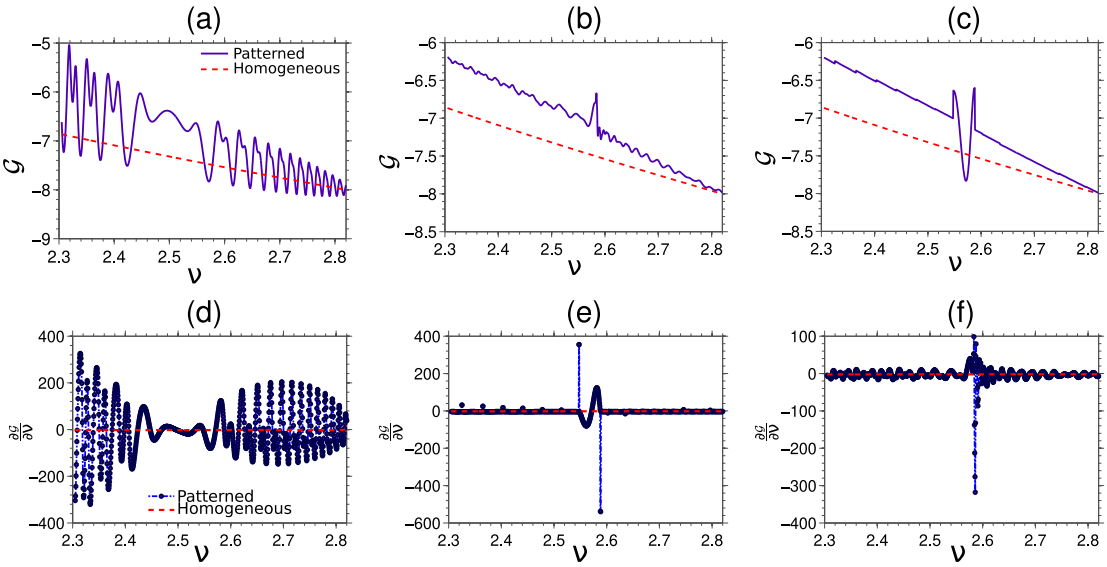

Figure 4.6: For the Hopf instability, (a) the variation of the semigrand Gibbs free energy (SGG) and (b) the corresponding slope against the control parameter, ν, are demonstrated. The variations of the same entities for traveling waves with discrete wave numbers are illustrated in (b) and (e), respectively. For traveling waves in the infinite size limit, we depict the variation of (c) SGG and (f) the corresponding slope. The dotted lines represent the unstable homogeneous state in all cases.

4.8.1 EPR of glycolytic oscillations

For the system experiencing Hopf instability, a nonzero total EPR exhibits oscillatory behavior in Fig. 4.5 (a). When we compare this total EPR profile with the profile of the global concentration of the intermediate species, X and Y in Fig. 4.5 (d), it becomes evident that the total EPR is quantitatively proportional to the global concentration of Y. Furthermore, they exhibit qualitatively analogous profiles, similar to the previous chapter. This similarity suggests that the total EPR of a dissipative system can serve as a quantitative and qualitative measure of the system's temporal behavior. The EPR for traveling waves with discrete wave numbers in Fig. 4.5 (b) displays a pulse-type structure around the BF instability onset point. Additionally, a clear upward trend in the total EPR of traveling waves concerning the control parameter, ν, is observed. However, the oscillatory nature of traveling waves is not clear for this discrete wave number scenario. Whereas, the total EPR variation throughout the control parameter ν range demonstrates irregular oscillations in Fig. 4.5 (c) for the traveling wave in the

limit of infinite system size. This EPR profile experiences a sharp change around the onset point of BF instability[187]. Similar to the scenario of Hopf instability, the total EPRs of traveling waves in both situations reflect the space-integrated global dynamics of Y concentration depicted in Fig. 4.5 (e) and (f). Consequently, the total EPR of this dissipative system is capable of encapsulating both quantitative and qualitative aspects of purely temporal and spatiotemporal concentration dynamics of the system, regardless of its size.

4.8.2 SGG of the glycolytic waves

The semigrand Gibbs free energy (SGG) profiles and corresponding slopes against the control parameter ν are depicted in Fig. 4.6. The SGG profile with ν for the Hopf instability is displayed in Fig. 4.6 (a). The SGG profile illustrates a $(2:1)$ periodic oscillation and the wide low-concentration part of the concentration field can be identified around $\nu = 2.5$ as a relatively slow-changing region in the SGG profile. The corresponding slope of the SGG for Hopf instability is presented in Fig. 4.6 (d), and this slope profile more prominently exhibits the slow change in the SGG around $\nu = 2.5$. For traveling waves with discrete wave numbers, the SGG profile and corresponding slope are presented in Fig. 4.6 (b) and (e), respectively. Similar to the total EPR, the SGG related to the discrete wave number scenario of the traveling waves does not exhibit prominent oscillatory behavior. However, due to the generation of the spatial pattern, the SGG profile of the traveling waves maintains a well-separation from its homogeneous counterpart, except around the onset of the BF instability. The additional energetic cost in the presence of the spatial pattern arises due to the work for varying the wave number of the traveling wave. Around the onset of the BF instability point, the wave number of the traveling wave matches with the wave number of the Hopf instability, and the SGG profile passes through a minimum. Similar to the total EPR, the slope of the SGG corresponding to the traveling waves in the finite system size also exhibits a pulse-like structure around the onset of BF instability in Fig. 4.6 (e). In contrast to the situation with discrete wave numbers, the SGG for traveling waves in the infinite size

limit in Fig. 4.6 (c) displays a prominent oscillatory pattern and reaches a maximum at the onset of BF instability. In the case of the traveling waves in the infinite size limit, we also note a close resemblance in the profiles of the total EPR and the slope of the SGG, illustrated in Fig. 4.6 (f). These similarities suggest a proportional relationship between the slope of the SGG and the total EPR of the system for all three scenarios.

4.9 Chapter conclusions

In this chapter, we systematically encapsulate the uniform oscillation and traveling wave dynamics of the Selkov reaction-diffusion system by employing a CGLE-based framework in the presence of both self and cross diffusion. By deriving the coefficients of the amplitude equation for the general Selkov RDS explicitly, we have illustrated the impact of the diffusion coefficients of the system on the amplitude and phase of the system. Besides these, the implicit dependence of the traveling wave's wave number on the cross diffusion has also been demonstrated. Further, leveraging the rigorous nonequilibrium thermodynamics description, we acquire the entropic and energetic characterization of the temporal and spatiotemporal patterns of the system.

In the previous chapter, we obtained the proportionality of total EPR with the global concentration profile in different Turing-Hopf overlapping regimes. Similarly, we observe in this chapter that total EPR is qualitatively and quantitatively analogous to the global concentration dynamics for uniform oscillation and traveling waves. We also illustrate a pulse-like shape at the onset of BF instability in the total EPR profile corresponding to the traveling wave with finite wave numbers. Whereas, for the scenario with continuous wave number, the total EPR profile exhibits a sharp change at the onset of the BF instability. This study reveals the semigrand Gibbs free energy (SGG) variation corresponding to the Hopf instability is more complex and colossal than the same thermodynamic potential corresponding to traveling waves. Additionally, the two contrasting natures of SGG profiles around the BF instability onset point, associated with discrete and continuous wave numbers of traveling waves, underscore the importance

of accounting for finite boundary effects for conducting a proper investigation of the traveling wave in a real scenario.

The recipe provided here for associating dynamic signatures in glycolysis RDS with central nonequilibrium thermodynamic entities can be extended to more complex dynamic situations. For example, this recipe can be applicable for capturing the thermodynamics of the spiral waves[3] and their phase reversal scenarios[190,191,192]. However, this recipe may not be suitable for capturing the dynamics and thermodynamics of the anti-wave to wave transition, as this transition can occur away from the Hopf onset point[193]. We have seen in the previous chapter that the cross diffusion in a two-variable RDS can generate diffusion-driven Turing instability in the system[194,195]. However, the generation and characterization of the Turing pattern and the interaction between the Turing and traveling wave patterns in the presence of both self and cross diffusion in Selkov RDS will be an interesting topic to be explored in our future work. In the presence of cross diffusion, there is also a possibility of the emergence of spatiotemporal chaos within the large-system size[196]. However, investigating the dynamics and thermodynamics of this type of spatiotemporal chaotic behavior is out of the scope of this chapter. In the next chapter of this thesis, we will implement a similar thermodynamic framework for the collective dynamics of chemical oscillators.

One of the pleasures of looking at the world through mathematical eyes is that you can see certain patterns that would otherwise be hidden.

- Steven Strogatz

5

Thermodynamic characterization of chimeras in a coupled continuum system

5.1 Chimera emergence and need of Thermodynamic Picture

The thesis has previously briefly mentioned the concept of the chimera state. This chapter aims to delve deep into this state within the framework of a globally coupled chemical system and proposes a recipe for characterizing this state using nonequilibrium thermodynamic entities. Dynamically, the chimera state is distinguished by the spatial coexistence of coherent and incoherent behaviors[25]. This coexistence of distinctly different behaviors in the collective dynamics of identical entities subjected to the same coupling scheme is counterintuitive[26]. Thus, this state is distinct from the partially incoherent states previously observed in the collective behavior of nonidentical oscillators with varied frequencies[197,5]. In those cases, the population splits into different states due to inherent heterogeneity in the oscillator group. The intriguing and subtle nature

of the chimera makes it one of the most debated collective phenomena. Nevertheless, chimeras have been reported in different theoretical models[198,199,200,201,202,203,204] and diverse experimental setups, spanning optical setting[205], nonlocally coupled chemical oscillatory system[206], mechanical oscillator networks[207] and laser array[208,209]. Chimeras are the natural link between the coherence and incoherence[210] of the coupled nonlinear system. This state serves as a mediator for the transition from a coherent to an incoherent state or from cluster to coherent state[211,212,213].

Initially, it seems that chimera could only be present in the nonlocally coupled identical phase oscillators. For example, chimeras were demonstrated in the reaction-diffusion models only in the presence of effective nonlocal coupling and under the applicability of the phase reduction method. However, the finding of 'amplitude-mediated chimeras'[30] in the nonlocally coupled complex Ginzburg-Landau equation (CGLE) connected this counterintuitive state to the amplitude of the system. The evidence of amplitude chimeras[214] further solidifies the claim of chimera in the amplitude dynamics of the coupled system. Then, chimeras were also observed in the global (all-to-all coupling) coupling[31,215] and local coupling scheme[216]. These advancements significantly broaden the scope of chimera investigation into more diverse scenarios of collective dynamics. Now, in the realm of coupled chemical reaction systems, diverse chimera variants have been observed in nonlocally coupled chemical oscillators, both experimentally and theoretically[206,217,218,219,220]. Specifically, the report of chimera in a population of nonlocally coupled discrete photosensitive Belousov-Zhabotinsky (BZ) chemical oscillators[206] was one of the first experimental evidence of chimeras. However, in a globally coupled chemical reaction system, prior research only reported oscillatory cluster patterns[221,222] or turbulent state[223]. Hence, in this chapter, we aim to fill the gap by generating and elucidating the chimera state within a prototypical continuum chemical oscillatory system having a global coupling scheme. This emergence of chimera within the globally coupled framework of chemical oscillators will enrich the exploration of various possible patterns in chemical systems.

The main focus of the chimera investigation centers on comprehending chimeras

across different coupling schemes, considering various coupling strengths and diverse types of oscillator assemblies. Till now, these studies have been limited solely to the dynamic aspect of the state. For instance, in the global coupling scheme, diverse complex bifurcation scenarios and mechanisms of creation and destruction of dynamical states associated with the chimera are studied in detail[224,212]. However, a proper thermodynamic characterization of this chimera state is still lacking. Nevertheless, the appearance of an analogous state in the networks of neurons[225], large-scale hydrodynamical system[226,227] and possible connection of chimeras with diverse brain states, such as unihemispheric sleep[228,229] in various aquatic and avian species, seeks a systematic thermodynamic investigation of this state to unveil the general underlying principles and signatures of these similar states. This chapter aims to address this gap by focusing on characterizing the chimera state using nonequilibrium thermodynamic entities. This investigation of the chimera state can broaden the current insight into the spatial coexistence of qualitatively different states. Beyond theoretical understandings, thermodynamic quantification can serve useful purposes in identifying potential applications of such states or exploring their relevance in real-world scenarios.

This chapter builds upon our prior work in *Kumar et al., 2022, Physical Review E, 105:034208*, to explore the thermodynamic signature of the chimera state in a globally coupled chemical oscillator system.

This chapter is structured as follows: After a brief introduction to chimera states and the importance of a thermodynamic picture in their study, we will explain the implementation of the global coupling scheme in the Brusselator RDS in Sec. 5.2. In Sec. 5.3, we will introduce the ansatz, which will be crucial in describing the concentration dynamics of the coupled system. This section will be followed by a discussion about the connection between dynamics and entropy production rate at the chimera state in Sec. 5.4. Then, in the next chapter, we will suggest the equivalence between chimera energetics and Gabor elementary function. Finally, we will conclude the chapter by mentioning our key findings.

5.2 Brusselator RDS and Implementation of global coupling

We will realize the chimera state in a globally coupled Brusselator continuum chemical oscillator system. We further assume that the individual Brusselator is operating within the regime of Hopf instability. Unlike the previous description of the Brusselator chemical reaction network in this thesis, we have only considered the self diffusion of the intermediate species X and Y for the collective dynamics investigation to avoid further complications. In the presence of self diffusion only, the general reaction-diffusion system (RDS) of the Brusselator in Eq. (2.30) simplifies to,

$$\begin{aligned} \dot{x} &= k_1 a - (k_2 b + k_4 + k_{-1})x + (k_{-2} d + k_3 x^2)y - k_{-3} x^3 + k_{-4} e + D_{11} x_{rr} \\ \dot{y} &= k_2 b x - k_{-2} d y + k_{-3} x^3 - k_3 x^2 y + D_{22} y_{rr}, \end{aligned} \tag{5.1}$$

where D_{11}, and D_{22} stand as self-diffusion coefficients of intermediate species X and Y, respectively, as also mentioned in previous chapters. In this RDS, conditions for the onset of Hopf instability yield the critical value of the control parameter of the Brusselator, b, as $b_{ctw} = \frac{k_4}{k_2} + \frac{k_1^2 k_3}{k_2 {k_4}^2} a^2 + \frac{(D_{11}+D_{22})}{k_2} q^2$, where the wave number, q is in accordance with the relation, $q = \frac{2n\pi}{l}$, respecting periodic boundary conditions within the finite domain l with n being an integer. However, our investigation here narrows down specifically to the consideration of $q = 0$, focusing solely on the Hopf instability.

In this thesis, we will not incorporate the global coupling explicitly into the RDS of the Brusselator. Instead, we visualize the effective global coupling within the system by introducing linear and nonlinear global coupling at the level of the Brusselator amplitude description. This coupling at the level of the amplitude dynamics is sufficient to encapsulate the fundamental system dynamics, as we only focus solely on amplitude-mediated chimera states. This strategy reduces the complexity of the analysis.

In the absence of global coupling, the dynamics of the Brusselator RDS in Eq. 5.1 can be equivalently represented by the CGLE shown in Eq. 3.25 with the specific form of CGLE coefficients near the onset of Hopf instability. As discussed in the preceding chapters, due to the universal form of CGLE, these coefficients aid in capturing the

distinctive characteristics of a particular system. The coefficients α and β of the normal form of CGLE in Eq. 3.25 are determined by employing the Krylov-Bogolyubov (KB) averaging method[135,169] on the Brusselator RDS in Eq. 5.1. Thus, for the Brusselator RDS here, the coefficients of the CGLE are derived as $\alpha = \frac{\Omega(D_{22}-D_{11})}{(D_{11}+D_{22})}$, $\beta = \frac{p_2}{p_1}\frac{1}{3a}$, and $\lambda = \frac{b-1-a^2}{2}$, with the ratio of correction factors being $\frac{p_1}{p_2} = \frac{4-7a^2+4a^4}{(2+a^2)}$. The parameter Ω in the coefficient α of CGLE is determined using the KB method as $\Omega = a$, where a represents the concentration of chemostatted species, A. These explicit expressions of the coefficients of the CGLE in terms of the system parameters of the Brusselator RDS establish a direct link between the CGLE and the Brusselator RDS in Eq. 5.1.

To model the coupled continuum system at the level of the amplitude, we need to resort our amplitude equation from the CGLE in Eq. (3.25) to the MCGLE in (2.39). A comparative analysis reveals that the MCGLE in (2.39) and the CGLE in (3.25) share three common terms. However, the last two terms on the right of MCGLE are additional to account for the nonlinear global coupling, incorporating a new coefficient denoted as ν. A discrete manifestation of this continuous system involves resorting to a globally coupled Stuart Landau oscillator system[31]. Upon spatial averaging of Eq. (2.39), this MCGLE yields an oscillatory mean field, $\langle Z \rangle = Z_0 = \eta \exp(-i\nu t)$. η and ν are identified as the amplitude and the frequency of the oscillation, respectively. From Eq. (2.39), we determine the threshold value of the η as $\eta_c = \sqrt{\frac{\lambda}{2}}$, below which uniform oscillation becomes unstable irrespective of other parameters. Notably, the coefficient λ in the above expression is the coefficient of Brusselator CGLE, encompassing the Brusselator model parameters, namely, a and b. Consequently, the coupling parameter η is dictated by the Brusselator's parameters, reinforcing the connection between our globally coupled amplitude equation and the Brusselator system. We interpret η as the coupling strength of the system. In this context, it is crucial to note that in prior investigations of globally coupled CGLE[230,223], the coupling strength was included in the amplitude equation as a multiplicated factor of the coupling term. In contrast, η does not explicitly appear in the considered MCGLE. The nonlinear global coupling described in the MCGLE can be visualized as an effective external force acting on each Brusselator.

5.3 Ansatz for obtaining spatiotemporal chimera concentration

In previous chapters, we have captured the concentration dynamics of the nonlinear RDS by incorporating the complex entity, amplitude, into the standard linearized description of the nonlinear system. This amplitude, near the onset of the Hopf instability, was obtained from the CGLE using analytical approximations, and it encapsulates the essential nonlinear characteristics of the system. Inspired by this standard method, we ansatz that the concentration fields of the chimera state within a globally coupled Brusselator system can be acquired by merging the numerical solution of the MCGLE into the linear stability description of the Brusselator RDS. The concentrations of intermediate species in the chimera state yield the nonequilibrium nature of the system and above ansatz thus facilitating the implementation of our nonequilibrium thermodynamic framework here. Therefore, this approach is pivotal in establishing the link between the dynamics of the globally coupled system and the nonequilibrium thermodynamic framework.

5.3.1 Concentration dynamics of chimera

To determine the amplitude in the presence of the global coupling, we numerically solve the equation (2.39) using a pseudospectral method combined with an exponential time differencing algorithm[29]. In the simulation of the MCGLE, a timestep of size 0.01 is employed, and system length $l = 500$ is discretized into 2048 grid points. Periodic boundary conditions are implemented. A uniform state with additional noise is set as the initial state of the system. Throughout the numerical simulation, all coefficients of Eq. (2.39) are specified in terms of the parameters of the Brusselator in Eq. (5.1). By combining the numerically derived amplitude field with the linear stability description of the nonlinear system, the chimera concentration dynamics of the Brusselator system are expressed using the following equation:

$$z_{IH} = z_{I0} + A_M U_{cH} \exp(i f_{cH} t) + C.C. \tag{5.2}$$

where A_M represents the real part of the numerically derived amplitude field from Eq. (2.39), z_{I0} is the initial uniform concentration field determined by steady-state values of two intermediate species, and $f_{cH} = \sqrt{\frac{k_1^2 k_3}{k_4}}a$ denotes the critical frequency of the Brusselator within the Hopf instability regime. Thus, incorporating the numerically obtained amplitude into the linear stability representation of the Brusselator system would elucidate the essential feature of the chimera in the concentration dynamics. In this investigation, The dynamics of the chimera concentration are derived from Eq. (5.2) employing 2001 amplitude snapshots within the time span from $t = 2000$ to $t = 2600$.

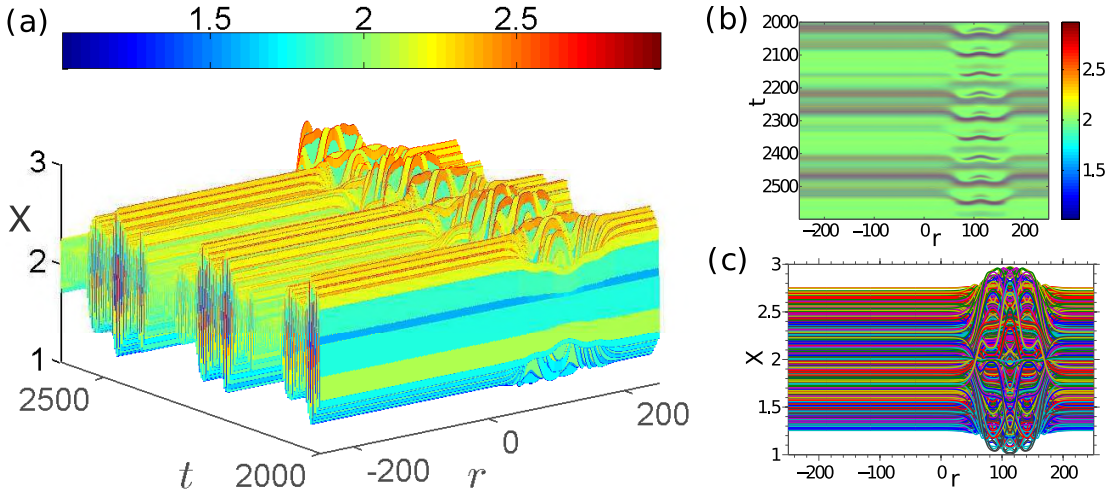

Figure 5.1: (a) The 3D spatiotemporal activator concentration field at the chimera state in the globally coupled Brusselator system, and (b) the corresponding image, along with (c) the concentration dynamics of the activator over the spatial dimension. The concentration dynamics is obtained from Eq. (5.2) employing 2001 amplitude snapshots within the time span from $t = 2000$ to $t = 2600$. For the MCGLE simulation, we utilize a timestep of 0.01 and discretize the one-dimensional system length, $l = 500$, into 2048 grid points. The parameters of Brusselaor RDS used were $D_{11} = 4, D_{22} = 3.2, a = 2, b = 5.28,$ and $k_{-\rho} = 10^{-4} \ll k_\rho = 1$.

A uniform base state is set as the initial state of the system. The pseudospectral simulation of the MCGLE considers a time step of 0.01 and 2048 grid points over the one-dimensional system of length, $l = 500$. All depictions are generated using diffusion coefficients $D_{11} = 4$, $D_{22} = 3.2$, along with fixed chemostatted species concentrations $a = 2, b = 5.28$. Similar to the Brusselator investigation in the prior chapter, chemical reaction rate constants are set as $k_{-\rho} = 10^{-4} \ll k_\rho = 1$. For this thermodynamic

investigation of the chimera state, we consider coupling parameters as $\eta = 0.66\sqrt{\lambda}$ and $\nu = \frac{\lambda}{10}$ throughout this chapter.

Figure 5.1 portrays the spatiotemporal evolution of the activator concentration within the system at the Chimera state. In Fig. 5.1(a), the appearance of the chimera state within the 3D concentration field of the activator is illustrated. The corresponding space-time realization of the chimera is shown in Fig. 5.1(b), revealing an embedded incoherent regime within the coherence counterparts of the state. The incoherence nature of the activator concentration field is evident in Fig. 5.1(c), with the turbulent concentration around $r \approx 100$. Moreover, it is also observed from the chimera concentration field that the coherence region evolves with time.

5.4 Connection between chimera dynamics and entropy production

The space-integrated concentration, X_s, and time-integrated concentration, X_m, are determined from the spatiotemporal concentration field of the activator, X, by taking the sum over the spatiotemporal concentration data over the spatial and temporal domains, respectively. The temporal evolution of space-integrated concentration, X_s, in Fig. 5.2(a) exhibits a beat interference pattern characterized by a periodic envelope of the temporal profile. A similar beat phenomenon was recently found in the chemical system of a periodically forced pH oscillator[231]. We suggest that the emergence of this beat pattern in the temporal dimension of the chimera is linked to the global coupling scheme within the amplitude equation.

The temporal behavior of the entropy production rate in Fig. 5.2(b) seems to qualitatively mirror the characteristics observed in the space-integrated concentration in Fig. 5.2(a). However, in Fig. 5.2(c), the power spectrum of the space-integrated concentration displays two distinct lines, while the EPR power spectrum demonstrates a series of evenly spaced spectral lines with diminishing power in the frequency domain. These frequency components, associated with the spectral lines in the EPR power spectrum, are determined by a central frequency, f_o, and the spacing between consecutive lines, δf,

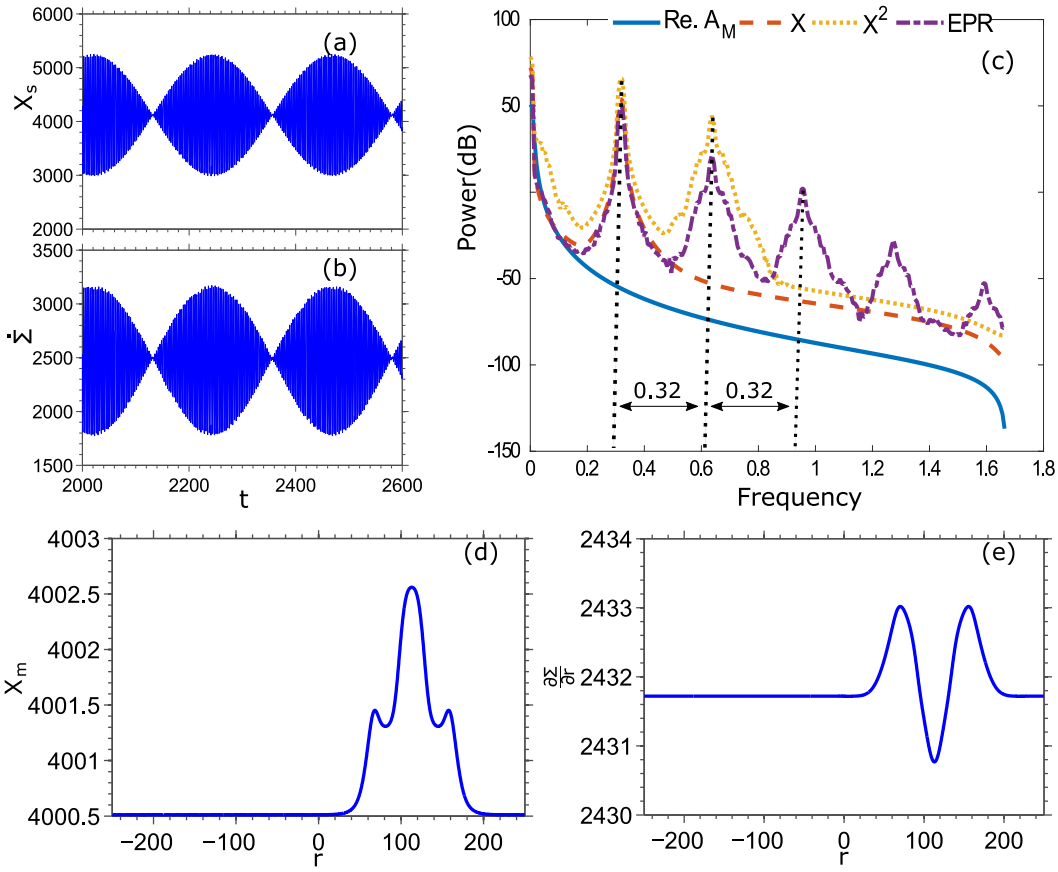

Figure 5.2: (a) X_s denotes the space-integrated concentration, and its temporal variation displays a beat interference pattern. (b) The entropy production rate (EPR) bears a qualitative resemblance to the temporal dynamics of the global concentration. (c) We obtain the power spectrum of the space-integrated amplitude, concentration, and EPR at the chimera state by implementing Welch's power spectral density estimate. (d) The time-integrated concentration X_m at the chimera state is illustrated over the spatial axis. (e) The spatial EPR of the chimera state is depicted. The space-integrated concentration, X_s, and time-integrated concentration, X_m, are calculated by summing the spatiotemporal concentration field of the activator X along the spatial and temporal dimensions, respectively. For all these figures, the concentrations of chemostatted species are held constant at $b = 5.28$, $a = 2$, and $d = e = 10^4$ with d, e representing the concentration of D, E, respectively.

as $f_n = n(\delta f) + f_o$, where 'n' is an integer. This feature revealed in the frequency domain of the entropy production rate is due to the underlying mixing of frequency components of concentrations in the representation of the EPR and the inherent nonlinearity within the system. This appearance of new frequencies is evident from the emergence of an additional frequency line in the power spectrum of the space-integrated X^2 in the same

figure. All these power spectra in Fig. 5.2(c) are obtained using Welch's power spectral density estimate[232] with a Hann window and an appropriate discrete Fourier transform (DFT) length in MATLAB.

The time-integrated activator concentration in Fig. 5.2(d) and the spatial EPR in Fig. 5.2(e) demonstrate an even-symmetric structure. This even-symmetric profile is related to the incoherence state of the chimera, and an otherwise flat profile is associated with the coherent regions. The uniform nature of the global coupling might be the reason behind the symmetry observed in both dynamic and thermodynamic entities of the incoherent state. The time-integrated concentration reveals a composite pulse structure within the incoherence regime, displaying an increased concentration at the axis of symmetry. Moving away from this axis, the principal concentration peak of the pulse diminishes into a secondary peak preceded by a notch on both sides. The spatiotemporal realization of the chimera's incoherent state can be visualized as the inclusion of significant spatial amplitude fluctuations over time in this symmetric time-integrated profile.

The spatial EPR in Fig. 5.2(e) displays a symmetric double-humped structure, where a global minimum aligns with the peak in the time-integrated concentration. The hump in this EPR profile is associated with the secondary peak in the concentration profile and acts as an indicator of the transition from incoherence to coherence region. Hence, the transition between coherence and incoherence costs the most significant spatial increase in dissipation. This regular structured behavior, characteristic of the incoherent state of the chimera, resonates with previously demonstrated highly ordered time-average states of the chaotic spatiotemporal pattern[233].

5.5 Chimera energetics as the Gabor elementary function

Figure 5.3(a) illustrates that the semigrand Gibbs free energy (SGG) of the chimera state is consistently higher in comparison to its homogeneous counterpart due to their association through a non-negative relative entropy of concentration distributions. The

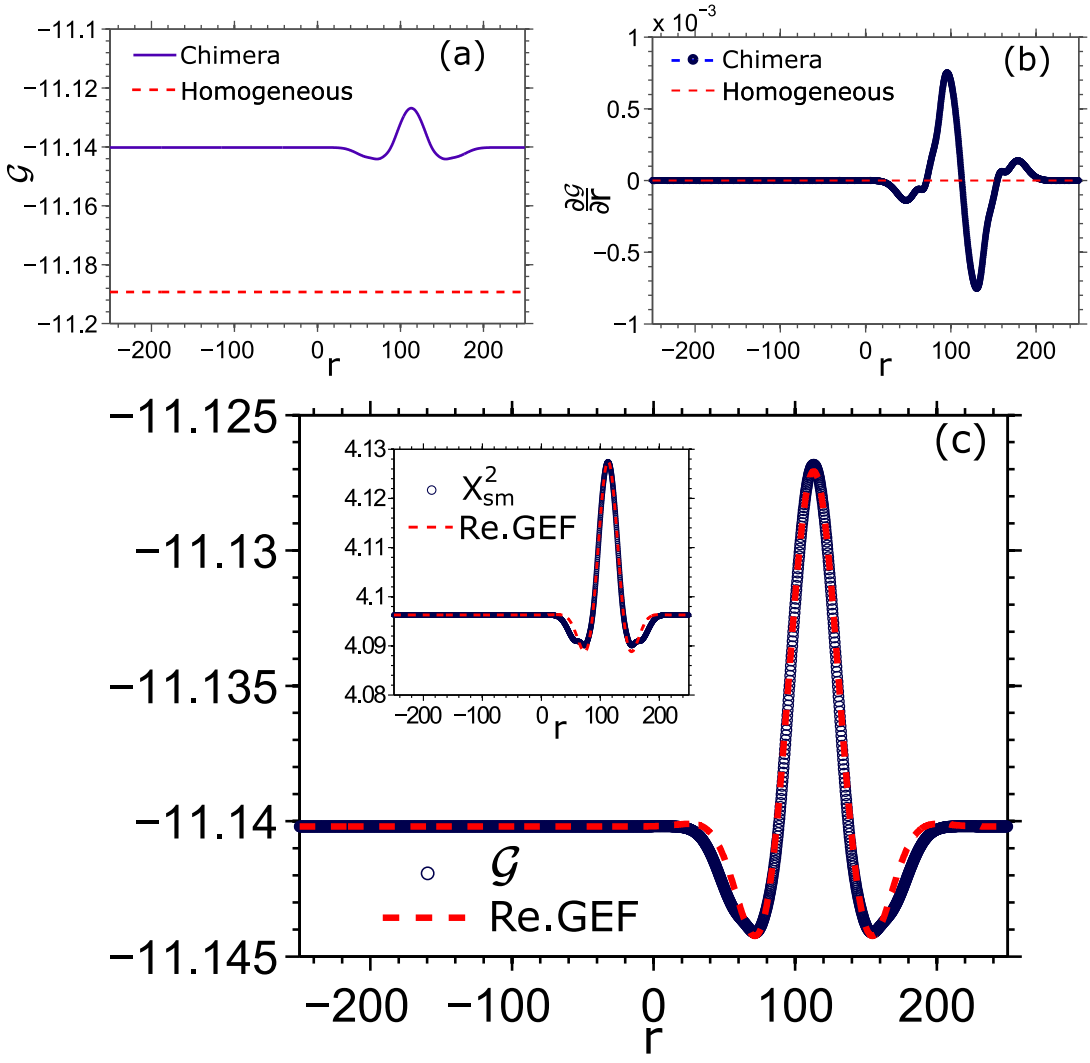

Figure 5.3: (a) The semigrand Gibbs free energy (SGG) of the chimera state is illustrated as a solid blue line, while its (b) corresponding slope is represented by a blue line with circular dots. The red dotted lines in both figures represent the same entities in the homogeneous state. The homogeneous counterpart refers to a uniform field established by the steady state of the system. (c) The real part of the Gabor elementary function (GEF) is fitted to the SGG of the chimera state. Inset: a reasonable fit between GEF and time sample-averaged X^2. All parameters are the same as in Fig. 5.1.

homogeneous counterpart relates to a uniform concentration field set by the steady state of the system. The nature of the transition between coherence and incoherence states within the chimera is distinctly evident in the energetic portrayal of the system, displayed through the semigrand Gibbs free energy profile in Fig. 5.3(a), and its spatial

gradient in Fig. 5.3(b). Specifically, a notch on both sides marks the transition from coherence to incoherence state, and this feature is connected to the previously mentioned maximum spatial dissipation rate during this transition. Furthermore, within this Chimera, the core of the incoherent state yields a symmetric peak, hinting at the lower energetic stability of the incoherence part compared to its coherent region.

Interestingly, we have discovered that the characteristics of the semigrand Gibbs free energy in the chimera state resemble a 1D Gabor elementary function (GEF)[64]. The GEF is a Gaussian-modulated complex exponential function, $\exp\left(-\frac{r^2}{2\tilde{w}^2} - i\tilde{k}r\right)$, where $\tilde{w}$ stands for the standard deviation of the Gaussian envelope and $\tilde{k}$ signifies the preferred wave number. Consequently, the SGG of the chimera can be equivalently expressed in terms of a scaled and translated improved family of the GEF, denoted as $\mathcal{G} \equiv \mathcal{G}_c + Q\exp\left(-\frac{(r-r_0)^2}{2\tilde{w}^2} - i\tilde{k}(r-r_0)\right)$. Here, Q represents the scaling factor, r_0 is the center location, and $\mathcal{G}_c$ stands for the SGG of coherence regimes, acting as the shift factor. This family of GEFs in the expressed form maintains the lowest possible bound of joint uncertainty in space and wave number, with $\sigma_r\sigma_k = \frac{1}{2}$.

Due to the implementation of the real part of amplitude in describing the concentration dynamics of the chimera, the semigrand Gibbs free energy characteristics render an even symmetry in Fig. 5.3(a). Therefore, the real component of the 1D GEF with a suitable choice of parameters fits reasonably well with the SGG profile as shown in Fig. 5.3(c). This fascinating alignment between the energetics of the chimera and the GEF enables the utilization of the interpretability of the Gabor function to predict and control the information transmission capacity of the chimera state within a specified spatial domain. For instance, we can readily assert that Gabor's information uncertainty principle[64,234,235] related to the localization trade-off in two conjugate dimensions is also equally applicable to the SGG of the chimera. Additionally, the link between the SGG and the GEF implies that diverse energy profiles of chimeras at different parameter settings can be produced by dilation and translation of a particular GEF associated with a distinct SGG profile.

b	$\mathcal{G}_c$	$(Q, \tilde{w})$	$(r_0, \tilde{k})$	$(\sigma_r\sigma_k)_c$	$(\sigma_r\sigma_k)_s$
5.24	-11.11	(0.011, 37.50)	(137.70, 0.063)	2.36	2.46
5.28	-11.14	(0.013, 30.79)	(113.04, 0.060)	1.68	2.14
5.32	-11.17	(0.017, 30.50)	(112.30, 0.0485)	1.14	2.00
5.38	- 11.21	(0.024, 27.50)	(111.82, 0.043)	0.82	1.90

Table 5.1: The joint uncertainty metric of the real, $(\sigma_r\sigma_k)_c$ and imaginary, $(\sigma_r\sigma_k)_s$ components of the Gabor elementary functions (GEFs) for various values of b.

We have identified distinct parameters such as preferred wave number, $\tilde{k}$, center location, r_0, scaling factor, Q, and Gaussian envelope width, $\tilde{k}$ (see table 5.1)-associated with GEFs related to the energetics of chimera at different control parameter values. These GEFs delineated here exhibit trade-offs between spatial and wave number localization. Notably, table 5.1 suggests that, unlike the whole GEF case, the real and imaginary components of GEFs possess a joint uncertainty metric dependent on the Gaussian width. This metric can independently serve as an indicator of the chimera energetics.

The representation of chimera energetics through the Gabor function highlights the role of the constraint put by the information uncertainty principle in shaping the thermodynamic evolution of the system containing the chimera state. Besides these, the quantification of time-integrated chimera concentration dynamics through the GEF offers crucial insights for evaluating the chimera state from an information-theoretic perspective; for instance, the wave number selectivity for the coherent profile can be estimated by considering the center wave number $(\tilde{k})$ of the GEF fitted to the time sample-averaged X^2 (illustrated in the inset in Fig. 5.3(c)).

5.6 Chapter Conclusions

To sum up, our work in this chapter delves into the emergence of chimera within a globally coupled continuum chemical oscillatory system and captures the nonequilibrium thermodynamic signatures of this counterintuitive state. Subsequently, we identify the equivalence of the chimera energetics with the Gabor representation having the minimum possible joint uncertainty metric. The beat characteristics observed in

the temporal entropy production rate and the symmetric curves evident in the spatial entropy production rate of the chimera state can serve as key diagnostic elements for detecting the nature of chimeras across diverse coupling schemes and collective systems. This thermodynamic characterization of the chimera can also be extended to traditional chimeras in a ring of nonlocally connected oscillators[236] or multichimera states resulting from strong nonlinear coupling[237]. Furthermore, this insight into the thermodynamics of the chimera can be expanded to explore the relationship between the chimera state and synchronous states in Kuramoto-type networks[238]. For instance, thermodynamic signatures can aid in qualitatively differentiating the chimera from other symmetry-breaking states within such populations. Therefore, detailed comparative investigations aiming to analyze the entropic and energetic signatures across various classes of chimeras[239,240] are essential.

Moreover, rendering the energy characteristics of the chimera through a Gabor representation would complement the information thermodynamic[107] aspect of the pattern formation. The Gabor equivalence of the chimera energetics would significantly contribute to accessing the similarities between the chimera state and various seemingly analogous states[225,228,226,227], providing crucial insight into the understanding of the broader spatial pattern of partial synchrony. The thermodynamic quantification of the chimera and its information-theoretic connection presented here can enhance the efficiency of a chimera-based architecture[241]. This understanding may also broaden the application potential of the state beyond the laboratory, ranging from image representation [242,243] to the representation of the primary visual system[244].

In this study, it is imperative to highlight that, in this work, we have refrained from delineating the coupling mechanism at the level of activator and inhibitor concentrations. The precise functional expression of the nonlinear global coupling (presented in MCGLE) within the confines of a reaction-diffusion framework is an aspect we aim to investigate in our future research. We anticipate that implementing coupling directly at the concentration level will assist in extracting the numerical concentration dynamics without reducing the coupled system.

The irreversibility of time is the mechanism that brings order out of chaos.

Ilya Prigogine

6

Collective dynamical states around chimera: thermodynamic signatures

6.1 Beyond the chimera state in the coupled continuum system

In the previous chapter, thermodynamic study in the globally coupled system was focused exclusively on the chimera state. Recent works in stochastic thermodynamics have addressed the thermodynamic cost of the coherent biochemical oscillations[245,246]. In this chapter, we aim to broaden the scope of this line of research to encompass more general scenarios by incorporating diverse generic states derived around the chimera state within the global coupled system and then capturing the dynamic and thermodynamic signatures of these generic collective states. The transitions between different dynamical states, ranging from coherence and incoherence to chimeras and cluster states, to gain a deeper understanding of the emergence and exclusiveness of those states within a globally coupled chemical system. Moreover, the transitions between the coherent

and incoherent states of collective systems are ubiquitous phenomena[247,248,249], and a general understanding of the transition between coherent and incoherent states remains an important issue in coupled nonlinear systems. Therefore, examining parametric transitions from a thermodynamic perspective can provide the fundamental underlying fingerprints of those similar transitions.

In this chapter, we generate various spatiotemporal states in a coupled Brusselator continuum chemical oscillator system. These spatiotemporal states are achieved by adjusting the coupling parameters of the system while keeping the internal parameters of each chemical oscillator fixed. In this investigation, the individual Brusselator is at the Hopf instability regime and so it can be described by the complex Ginzburg Landau equation (CGLE)[134,4] near the onset of the instability. In the presence of nonlinear global coupling, the Brusselator CGLE is extended to a modified CGLE (MCGLE) as shown in (2.39) of the previous chapter. To establish a connection between the states of a globally coupled chemical system and their nonequilibrium thermodynamic representation, we employ a similar approach as in the previous chapter. This approach enables us to model the concentration fields of these various spatiotemporal states by combining the numerical solution of the MCGLE with the linear stability description of the reaction-diffusion system (RDS). Once we have identified and characterized different spatiotemporal patterns in the coupled system, we proceed to systematically quantify the nonequilibrium thermodynamic properties of these states. Through this investigation, we uncover some intriguing resemblances between essential dynamic and thermodynamic quantities, irrespective of collective behaviors. These findings can be crucial in the context of the connection between the dynamics and thermodynamics of more general coupled systems.

This chapter delves into the thermodynamic signatures of various collective states observed near the chimera state in a globally coupled Brusselator system, building upon the findings of *Kumar et al., 2023, Physical Review E, 108:044218.*

The following key areas will be covered in this chapter: After outlining the motivation and research aim in this section, we will delve into methods for acquiring

various spatiotemporal collective states within the MCGLE regime in Sec. 6.2. Subsequently, Sec. 6.3 will introduce metrics for characterizing these diverse dynamical states. Building upon this foundation, Sec. 6.4 will identify distinct dynamical states within the globally coupled system. In Sec. 6.5, we will explore the nonequilibrium thermodynamic entities associated with each identified collective state. Finally, the conclusion will summarize the key findings and discuss the broader implications of this research.

6.2 Implementing MCGLE in acquiring spatiotemporal states

The oscillatory mean-field, $\langle Z \rangle = Z_0 = \eta \exp(-i\nu t)$ derived in the MCGLE description, could potentially originate from chemical reactions outside the chemical reaction network (CRN) or some external input connected to the individual CRN. We assume that any changes in the dynamics of this external source instantly affect the entire system. Furthermore, we have complete control over the dynamics of this external source. Given the flexibility and arbitrariness in the nature of the external source responsible for generating coupling, we do not explicitly define the functional forms of the coupling parameters. Instead, we provide specific values for these parameters. In the context of this work, we should emphasize that the weak-coupling approximation is not a requirement for amplitude-mediated states[30,31,215] in the MCGLE.

Different spatiotemporal states in the system are generated by discretely varying the frequency, ν of the oscillatory mean-field, Z_0 relative to the fixed amplitude $\eta = 0.67\sqrt{\lambda}$ of the field. The frequency values are represented in terms of the mean-field amplitude throughout this chapter.

Similar to the previous chapter, MCGLE in Eq. (2.39) is solved numerically by the pseudospectral method incorporated with an exponential time stepping algorithm[29]. For each specific value of ν, we initialize the system in a uniform state. During the simulation of the MCGLE, we use a time step size of 0.01, and the system length is set to $l = 500$, which is discretized into 2048 grid points. Periodic boundary conditions are applied. We capture amplitude snapshots for each collective state corresponding to

different ν values within the time interval from $t = 2000$ to $t = 3000$. For all states, the parameters of the individual Brusselator RDS are fixed at $b = 5.24$, $a = 2$, $D_{11} = 4$, $D_{22} = 3.2$, and $k_{-\rho} = 10^{-4} \ll k_\rho = 1$.

6.2.1 Collective concentration dynamics of the system

In the spirit of Ansatz in the previous chapter, we then combine the amplitude field obtained from the MCGLE simulation with the standard linearized description of the single nonlinear system to acquire the collective concentration dynamics of intermediate species, z_I of the Brusselator system,

$$z_{IH} = z_{I0} + Z_M U_{cH} \exp(i f_{cH} t) + C.C. \tag{6.1}$$

Here Z_M is the numerically obtained amplitude field from the Eq. (2.39), and z_{I0} is steady-state values of two intermediate species.

6.3 Metrics for characterizing different dynamical states

We utilize two quantitative metrics, namely, the strength of incoherence (SI), S, and the discontinuity measure (DM), H[250], to characterize the different dynamical states in this globally coupled system. These metrics were originally designed for systems with nonlocal coupling. However, we devise these statistical measures based on the local standard deviation for identifying dynamical states in the globally coupled continuum system.

From the spatiotemporal concentration distribution of the activator, x, we derive a transformed variable over the time range t as $\mathcal{X}_{i,t} = x_{i,t} - x_{i+1,t}$ with $i = 1, 2, ..., N-1$ being the grid points of spatial length, l. Then, by calculating the standard deviation of this variable and averaging it over time, $\sigma = \left\langle \sqrt{\frac{1}{N}\sum_{i=1}^{N}[\mathcal{X}_{i,t} - < \mathcal{X}_{i,t} >]^2} \right\rangle_t$, we can differentiate the coherent state from the incoherent and chimera states. Here, $< \mathcal{X}_{i,t} >= \frac{1}{N}\sum_{i=1}^{N} \mathcal{X}_{i,t}$ and $\langle ... \rangle_t$ denotes the average over time. An infinitesimal σ value suggests a coherent state, whereas relatively higher σ values indicate incoher-

ent and chimera states. As incoherent and chimera states may yield similar orders of σ, we require an additional criterion to distinguish chimera from incoherent states. To address this issue, we calculate local standard deviation for a suitable bin number P, $\sigma_{loc} = \left\langle \sqrt{\frac{1}{n}\sum_{j=np-n+1}^{pn}[\mathcal{X}_{j,t} - < \mathcal{X}_{i,t} >]^2} \right\rangle_t$ with $n = \frac{N-1}{P}$ and $p = 1, 2, ..., P$. Then, a Heaviside step function, $\Theta(\delta - \sigma_{loc})$ with threshold, $\delta = 0.0003|\mathcal{X}_{max} - \mathcal{X}_{min}|$ aids in distinguishing these states. Now, the strength of incoherence (SI) is defined as $S = 1 - \frac{\sum_{p=1}^{P}\Theta(\delta - \sigma_{loc}(p))}{P}$. Additionally, the discontinuity measure, $H = \frac{\sum_{i=1}^{P}|\Theta_i - \Theta_{i+1}|}{2}$, can be employed to differentiate the multichimera from the chimera state.

We will use the combinations of S and H to identify different dynamical states. More specifically, the following combinations correspond to particular states in this scheme[251]:

$$\begin{cases} (S = 0, H = 0) & \Rightarrow coherent, \\ (S = 1, H = 0) & \Rightarrow incoherent, \\ (0 < S < 1, H = 1) & \Rightarrow chimera, \\ (0 < S < 1, 2 \leq H \leq \frac{P}{2}) & \Rightarrow multichimera. \end{cases} \tag{6.2}$$

6.4 Different dynamical states in globally coupled system

The following collective states are obtained for various frequency values of the mean field relative to its amplitude.

6.4.1 Quasiperiodic coherent state

If the frequency of the mean field is sufficiently larger than the amplitude of the mean field, the system exhibits spatially coherent behavior. For instance, we consider the spatiotemporal concentration corresponding to $\nu = 100\eta$ in Fig. 6.1. Snapshots of the concentrations in the lower panel of Fig. 6.2 (a) yield closed orbits in the complex plane. The temporal dynamics of an arbitrarily selected spatial point in the upper panel display quasiperiodic behavior with a modulated amplitude. Consequently, the spatiotemporal

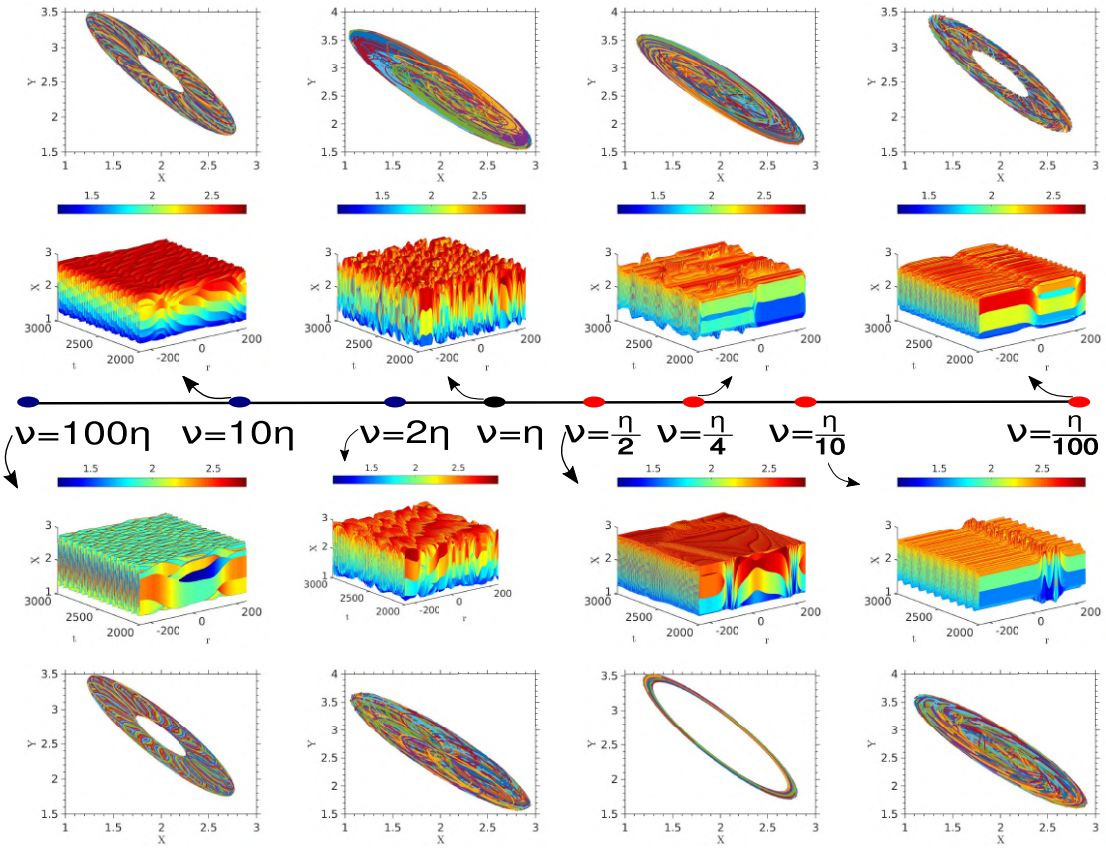

Figure 6.1: The spatiotemporal concentration dynamics of the system are shown for different mean-field frequencies while maintaining a fixed amplitude of the mean-field at $\eta = 0.67\sqrt{\lambda}$. The frequency values are represented relative to the amplitude and are marked by filled circles along the line. Inner panel: 3D concentration fields of the activator for various frequencies, with activator concentration values represented using a color map. Outer panel: Spatiotemporal concentration dynamics of X and Y as phase portraits correspond to different mean-field frequencies. Parameters of individual RDS are fixed at $D_{11} = 4$, $D_{22} = 3.2$, $a = 2$, $b = 5.24$, and $k_{-\rho} = 10^{-4} \ll k_\rho = 1$.

dynamics in the phase portrait for $\nu = 100\eta$ in Fig. 6.1 reveal a circular motion on a torus. We classify this state as a quasiperiodic coherent state.

For a relatively lower frequency value, $\nu = 10\eta$, the system also demonstrates quasiperiodic coherent behavior with a complex torus attractor in the phase portrait in Fig. 6.1. However, this state is less coherent than the previous state, with the appearance of small distortion on the circular orbit of the snapshot in Fig. 6.2 (b). So, the quasiperiodic behavior of the temporal dynamics in the upper panel is also different than the previous one. For both states, we calculate SI and DM as $S = 0$ and $H = 0$, as expected for

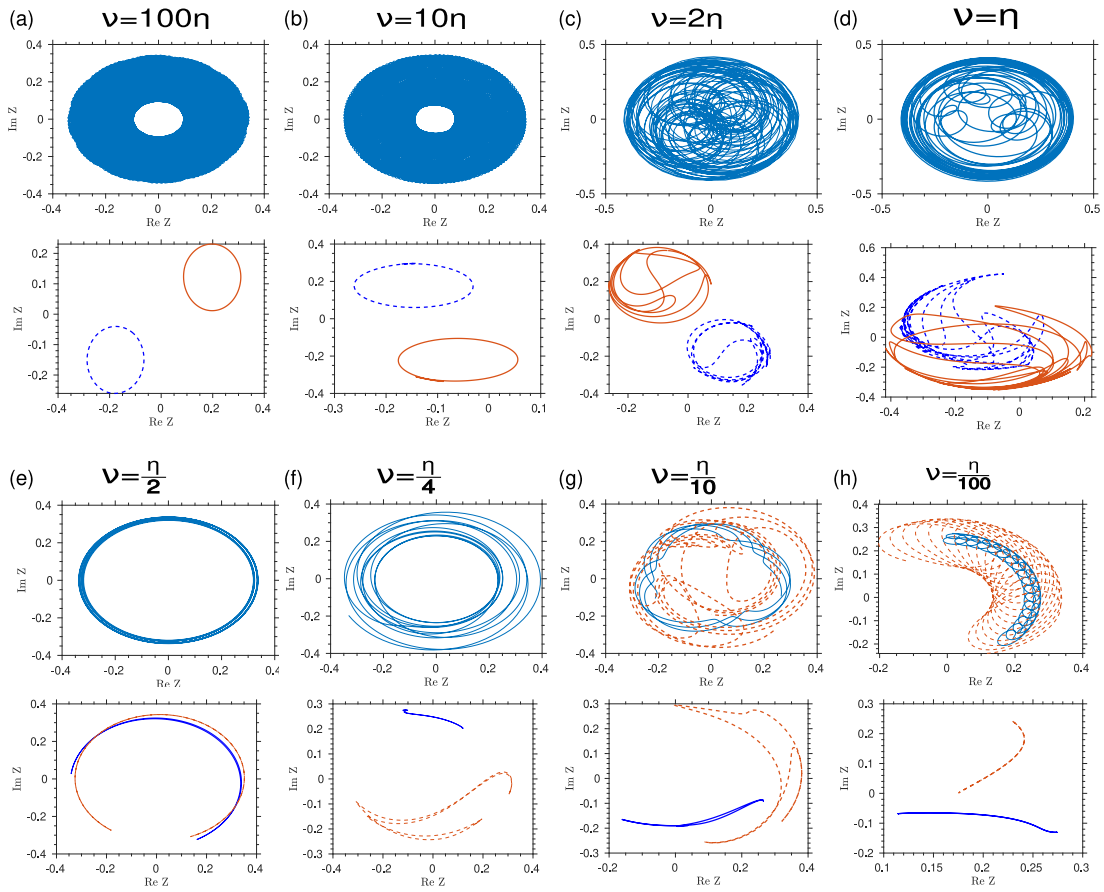

Figure 6.2: Amplitude dynamics in the complex plane represent various states at different coupling parameters. Upper panel: Temporal dynamics at an arbitrary spatial node are presented in a complex plane. For cases (g) and (h), we depict the temporal dynamics for two different spatial nodes using solid and dashed lines. Lower panel: For each case of coupling parameters, the snapshot of the amplitude at an arbitrary time point is provided in the complex plane. Two different profiles, represented by solid and dashed lines, correspond to two different time points.

coherent states in the system.

6.4.2 Tree-like transition state

As we explore lower frequencies, a noticeable transformation occurs in the phase portrait of the snapshots. The cyclic orbit that was initially present eventually splits and takes on the form of a circular arc. At even lower frequencies, such as $\nu = 2\eta$, a multifold trajectory emerges, as shown in the lower panel of Fig. 6.2 (c). This multifold trajectory

signifies the onset of incoherence in the spatial dynamics of the system. The temporal dynamics in the upper panel undergo a transition from intricate quasiperiodic motion to chaotic flow. Consequently, the torus attractor ceases to exist in the corresponding spatiotemporal phase portrait in Fig. 6.1.

For lower frequencies, the spatiotemporal concentration field exhibits tree-like patterns[252], which appear locally over certain spatial regimes. This tree-like pattern becomes more pronounced as the frequency is further reduced, as evident in the spatiotemporal field corresponding to $\nu = 2\eta$ in Fig. 6.1.

We find that the combination of SI and DM indicates a multichimera state[237] at $\nu = 2\eta$, which is possibly due to the loss of spatial coherence at multiple parts of the concentration field. However, we refer to these partially synchronized states as 'tree-like transitioning states'. A similar transitioning state has been reported previously in Couette flow[253].

6.4.3 Incoherent state

As we further decrease the frequency, the state with a complex tree-like pattern subsequently evolves into a concentration field with spatiotemporal intermittency[254,255]. With a discrete reduction in frequency, we notice the emergence of irregular patches scattered throughout the spatiotemporal dimensions of the concentration dynamics, particularly around the equal value of the amplitude and frequency.

For an equal value of the frequency and the amplitude, the spatiotemporal concentration field is presented in Fig. 6.1. For $\nu = \eta$, we observe a highly complex trajectory in the phase portrait of the snapshots, and the temporal dynamics within the phase portrait follow a peculiar attractor, as illustrated in Fig. 6.2 (d). This state is characterized as an incoherent state, and the overall incoherence nature of this state is evident in the corresponding phase portrait of the activator-inhibitor concentration in Fig. 6.1. The metrics SI and DM, with values $S = 1$ and $H = 0$, also support the classification of this state as an incoherent state.

6.4.4 Transitioning cluster state

As we continue to reduce the frequency while keeping the amplitude, η fixed, the incoherent nature gradually diminishes as the size of the patches in the spatiotemporal dynamics notably increases, resulting in simpler spatiotemporal intermittency on the surface of the concentration. Due to further frequency variations, a transition can occur from this spatiotemporal intermittency to a tree-like perturbation[252] state. The tree-like perturbation state for $\nu = \frac{\eta}{2}$ is illustrated in Fig. 6.1. The spatiotemporal turbulence in the phase portrait now transforms into a thin cyclic orbit. So, unlike the incoherent regimes, the temporal dynamics phase portrait in Fig. 6.2 (e) displays multiple cyclic attractors. In the lower panel, snapshots of spatial grids in the complex plane reveal two distinct circular arc attractors at higher time points, suggesting the existence of at least two groups. Although the combination of SI and DM values indicates a multichimera state at $\nu = \frac{\eta}{2}$ due to the loss of spatiotemporal coherence on multiple occasions, we classify this state as an amplitude cluster state. This state is considered a prerequisite for the emergence of chimera states in the globally coupled system[212].

6.4.5 Multichimera state

For even lower frequencies, $\nu = \frac{\eta}{4}$, we observe the emergence of multiple modulated amplitude clusters in the phase portrait of the temporal dynamics of the spatial grid in Fig. 6.2 (e). Meanwhile, the snapshots of the spatial grids exhibit folded double-layer trajectories. The cluster states in this coupling parameter move irregularly with time, causing shifts in the positions of coherence and incoherence regions. Consequently, multiple sharp incoherence clusters expand within the spatiotemporal concentration field in Fig. 6.1, leading to the appearance of chimera states with the coexistence of multiple coherent and incoherent clusters. A chimera state with a chaotic motion of coherent and incoherent regimes over time has been previously described as a finite-size effect[256]. In the context of this continuum system, we identify this spatiotemporal pattern as a multicluster chimera, as also supported by the combination of SI and DM values.

6.4.6 Chimera state

For further lower frequencies, specifically for $\nu = \frac{\eta}{10}$, a conventional amplitude-mediated chimera state emerges in the spatiotemporal concentration field, as shown in Fig. 6.1. This identification of the chimera state is consistent with the combination of SI and DM values, $(0 < S < 1, H = 1)$.

In the phase portrait, Fig. 6.2 (g), the modulated amplitude dynamics are observed for the spatial grid within the coherence regime. The coexisting incoherence counterpart, represented by the dashed line, yields more intricate phase trajectories. The snapshots of spatial dynamics reveal distorted ρ-shaped profiles[230,215], which undergo modifications over time. The nonlinear nature of global coupling introduces complexity in the ρ-shaped profiles.

6.4.7 Chimera to coherent transition

As the mean-field frequency decreases, a type-II cluster pattern[212] emerges, accompanied by modulated amplitude in the temporal dynamics. Initially, this pattern exhibits quasiperiodic behavior, but as the value of ν decreases further, it begins to split, as illustrated in Fig. 6.2 (h). At $\nu = \frac{\eta}{100}$, we acquire two out-of-phase coherence clusters in the concentration field, as shown in Fig. 6.1). The phases of these clusters alternate after some time, with a small incoherent patch situated at the boundary of the clusters. The combination of SI and DM, $(S = 0, H = 0)$, identifies this pattern as a coherent state.

For all these states, the time-averaged profiles of a transformed variable, $\mathcal{X}_{i,t}$ yield an odd symmetry. This indicates an even symmetric center of mass for the activator concentration. Concentration regimes associated with coherent states have $\mathcal{X}_{i,t}$ around the origin of the vertical axis. Whereas, for regimes corresponding to incoherent states, $\mathcal{X}_{i,t}$ deviates from that origin[251].

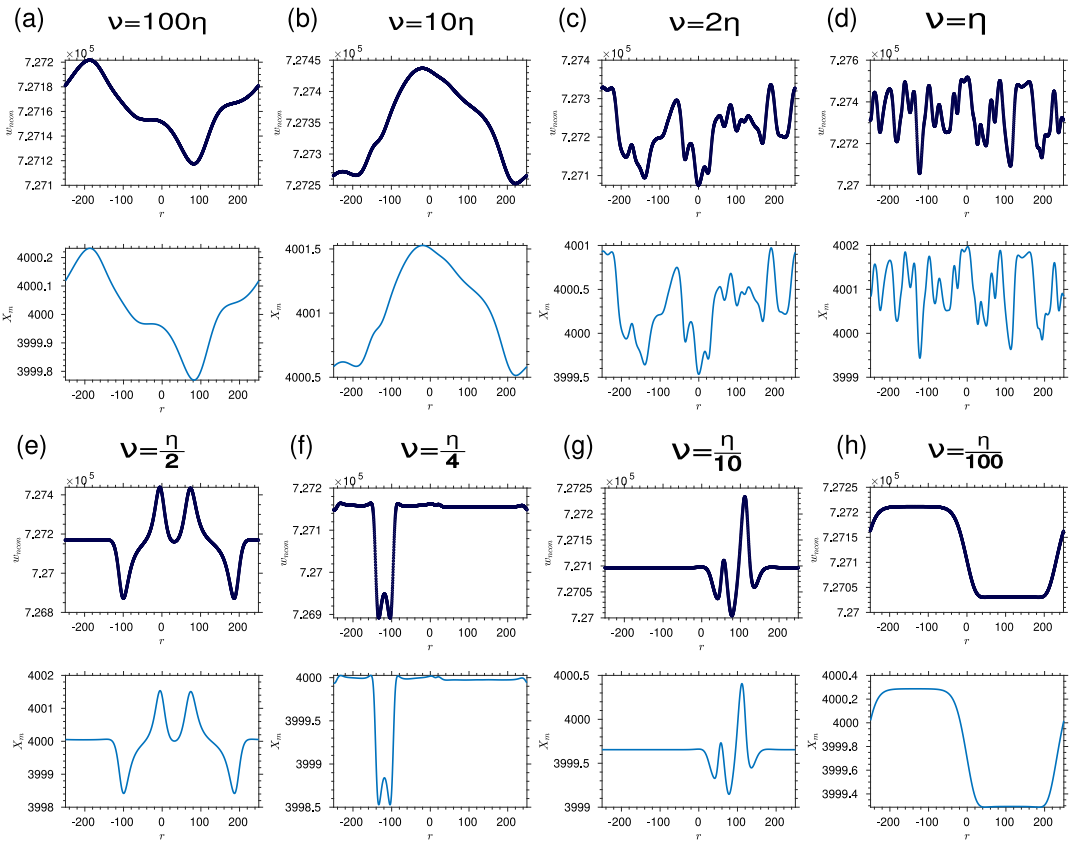

Figure 6.3: The nonconservative work performed on the system for different states associated with various frequencies is presented in the upper panel. The corresponding time-integrated concentration profile, X_m, is depicted in the lower panel. The nonconservative work and X_m profiles exhibit similar qualitative characteristics.

The nonequilibrium thermodynamic signatures corresponding to the various collective states discussed above are depicted in Fig. 6.3, 6.4, and 6.5. From Fig. 6.3, it becomes evident that the nonconservative work profiles shown in the upper panel for all the states bear a qualitative resemblance to the time-integrated profiles of the activator concentration, X_m, in the lower panel. This correspondence arises due to the presence of the activator concentration in the dominant forward reaction currents, j_{+2} and j_{+4}, which are integral components of the non-conservative work expression. A substantial portion of the nonconservative work is exploited in the generation of spatial entropy

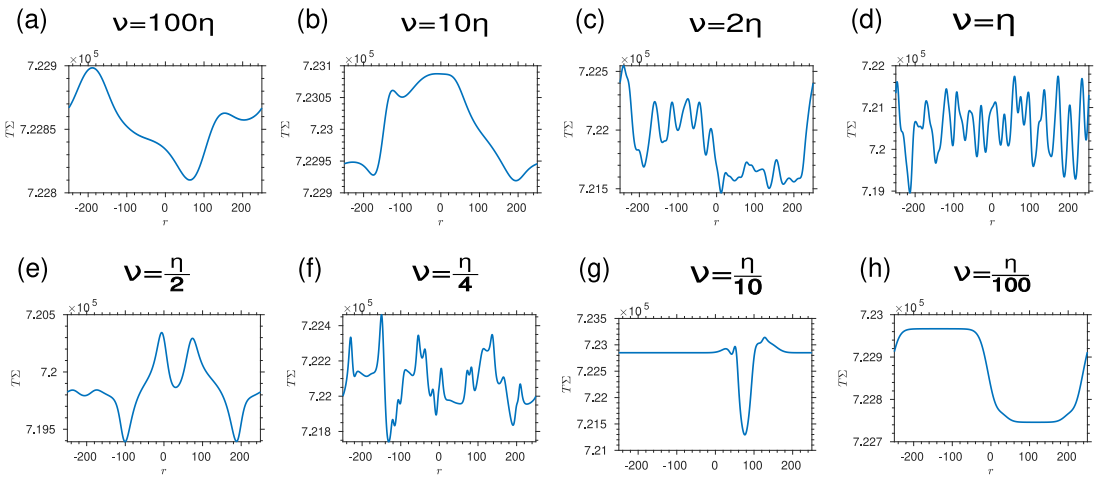

Figure 6.4: The entropy production of various states within the coupled system is displayed over the spatial length of the system. (a), (b), and (h) depict the entropy production for coherent states at different frequencies. (c) and (e) illustrate the entropy production for two distinct transitioning states. (f) and (g) show the entropy production for multichimera and chimera states, respectively. (d) displays the entropy production for the incoherent state.

in Fig. 6.4. Another aspect of nonequilibrium thermodynamics is presented through

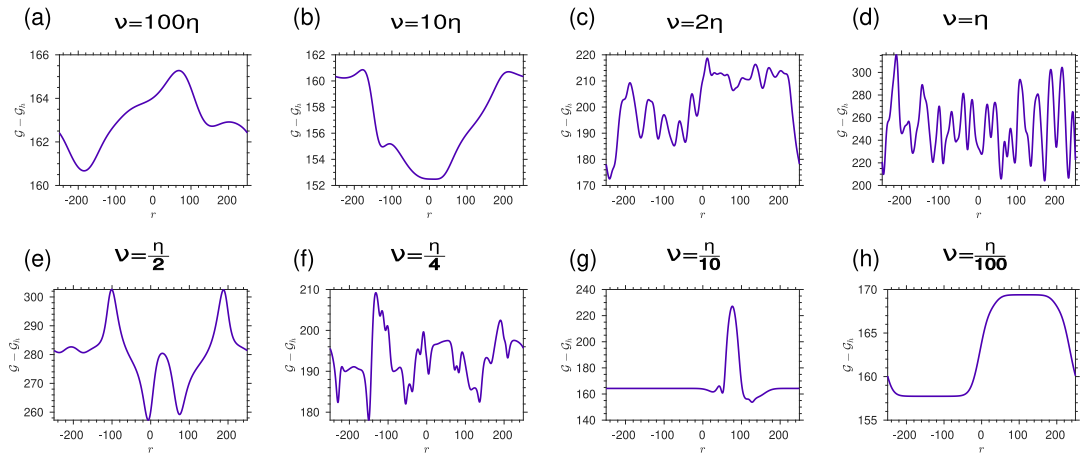

Figure 6.5: Semigrand Gibbs free energy profiles associated with the states obtained by varying the frequency. In each case, we subtract the semigrand Gibbs free energy of a common initial homogeneous state from the semigrand Gibbs free energy profiles of the states.

the semigrand Gibbs free energy profiles of various nonequilibrium states within the system, as depicted in Fig. 6.5. In these profiles, the semigrand Gibbs free energy of the initial homogeneous state is subtracted from the semigrand Gibbs free energy

of all states. Consequently, these profiles convey the amount of information generated along the spatial dimension in transitioning from a homogeneous reference state to these various states. Since all the conservation laws are broken in this context, the semigrand Gibbs free energy, as represented at the local level, serves as the proper thermodynamic potential for the system[146].

As the shift between different states involves changes in the frequency of the mean field, the profiles of semigrand Gibbs free energy and entropy production at the local level go through significant alterations and aid in distinguishing different states. In all these instances, semigrand Gibbs free energy and spatial entropy production profiles exhibit similarity but are entirely out of phase. It is worth mentioning that the entropy production and local free energy flow due to the diffusion flux are minimal here.

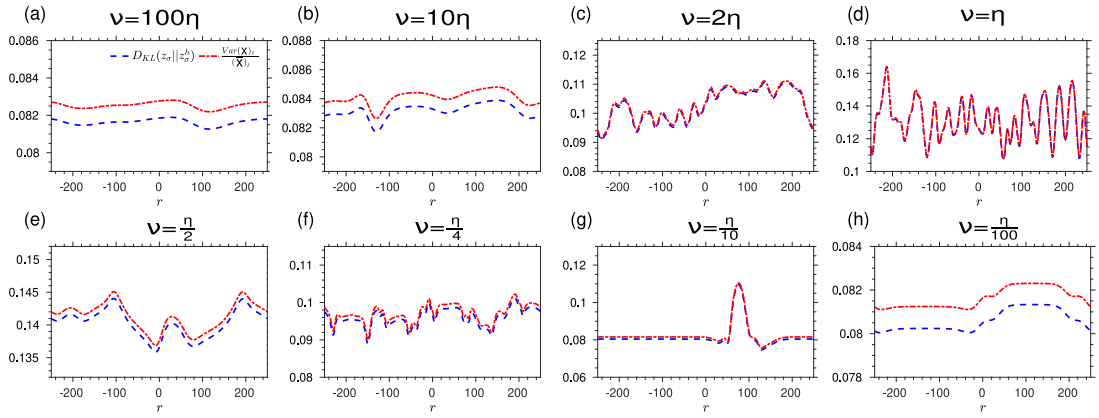

Figure 6.6: The equivalence of Kullback-Leibler divergence obtained between the nonequilibrium inhomogeneous and homogeneous concentrations with an entity resembling the Fano factors $\frac{Var(x)_t}{(\overline{x})_t}$. Here, $Var(x)_t$ represents the variance, and $(\overline{x})_t$ is the average of the activator concentration in the inhomogeneous state over time. z_σ^h corresponds to the nonequilibrium homogeneous concentrations and z_σ represents concentrations of species at the nonequilibrium inhomogeneous state. In coherence states (a), (b), and (h), the range for the two equivalence entities is very small, emphasizing the seemingly pronounced difference between these entities.

6.5.1 Equivalence of KL divergence and Fano factor-like entity

For different values of ν, we have illustrated the KL divergence, $D_{KL}(z_\sigma||z_\sigma^h)$ (represented by dashed lines) acquired between the nonequilibrium inhomogeneous state, z_σ

and homogeneous reference state, z_σ^h of the coupled system, and a measure akin to the Fano factor, $\frac{Var(x)_t}{(\overline{x})_t}$ (depicted as a dash-dotted line) in Fig. 6.6. In this context, $Var(x)_t$ stands for the variance, and $(\overline{x})_t$ represents the average of the activator concentration in the inhomogeneous state over time. Figure 6.6 compellingly demonstrates that the KL divergence, $D_{KL}(z_\sigma||z_\sigma^h)$ and the Fano factor-like measurement exhibit both qualitative and quantitative similarities, displaying an equal degree of variability[251]. Most significantly, the semigrand Gibbs free energy expression in Eq. (2.84) contains $D_{KL}(z_\sigma||z_\sigma^h)$, and thus the aforementioned equivalence emphasizes a strong connection between the proper nonequilibrium thermodynamic potential and variance of the concentration dynamics of the globally coupled system.

6.5.2 Distinct Signatures of coherence states

In Fig. 6.3, 6.4, and 6.5 (a), all the thermodynamic entities exhibit a sine waveform with harmonic distortion for the coherence state at $\nu = 100\eta$ as depicted in fig. 6.1. However, for the coherence state associated with $\nu = 10\eta$, the sine wave profiles in these entities are distorted by a different harmonic. We note that the spatial entropy production profile in Fig. 6.4 (b) and semigrand Gibbs energy profile in Fig. 6.5 (b) corresponding to the coherence state at $\nu = 10\eta$ exhibit an additional cusp which possibly manifests the slight distortion in concentration dynamics as shown in the complex plane in Fig. 6.2 (b). In contrast, when considering the coherent state with a much lower frequency, $\nu = \frac{\eta}{100}$, the profiles in Fig. 6.3, fig. 6.4, and fig. 6.5 (h) take the form of clipped sine waveforms, with roughly equal amplitudes observed in both the upper and lower portions. Meanwhile, $D_{KL}(z_\sigma||z_\sigma^h)$ and the Fano factor-like entity for the coherence states in Fig. 6.6 (a), (b), and (h) demonstrate remarkably small ranges, thereby making even the slightest magnitude differences between these two measures appear significantly prominent.

6.5.3 Signatures of tree-like transition and incoherence states

In the case of the tree-like transition state corresponding to $\nu = 2\eta$, the nonconservative work in Fig. 6.3 (c) takes on a more intricate waveform. This profile exhibits multiple notches and irregular oscillatory behavior with varying amplitudes over the spatial dimension. This behavior arises due to occasional losses of spatial coherence in the presence of the tree-like pattern. The entropy production and semigrand Gibbs free energy profiles in this state display stronger modulation compared to the coherence states. They have one part with a more regular multifold spatial period relative to the out-of-phase other part. The erratic part of these thermodynamic profiles indicates that the loss of coherence due to the tree-like pattern dominates in that spatial region.

For the incoherence state corresponding to $\nu = \eta$, thermodynamic entities in Fig. 6.3, 6.4, and 6.5 (d) show a more pronounced breakup of oscillations, and continuous aperiodic behaviors emerge over the spatial length.

Due to the comparatively wide range of values for $D_{KL}(z_\sigma||z_\sigma^h)$ and the Fano factor-like entity in the tree-like transition and incoherence states in fig. 6.6 (c), and (d), respectively, the two measures seem to exhibit a notable degree of overlap.

6.5.4 Signatures of transitioning cluster state

As for the transitioning cluster state, the concentration dynamics of the system become more regular than the incoherence state, and the aperiodic continuous wave profile corresponding to the incoherence state converts into a symmetric profile for nonconservative work in Fig. 6.3 (e). This profile exhibits a combination of two distinct behaviors. One part is characterized by a flat portion, followed by a transition to a double-peaked structure with comparatively higher amplitude. In both the entropy production and semigrand Gibbs energy profiles, in fig. 6.4 and 6.5 (e), two nearly symmetric structures with the same phase but varying magnitudes are interconnected. At the point where these structures connect, maxima appear in the semigrand Gibbs free energy profile. In contrast to the nonconservative work profile, the entropy production and semigrand

Gibbs energy profiles display a wavy structure throughout, without a flat regime.

Figure fig. 6.6 (e) highlights that the range of values for similar entities, $D_{KL}(z_\sigma||z_\sigma^h)$ and $\frac{Var(x)_t}{(\overline{x})_t}$ for this state, falls within an intermediate range, between that of the coherence and incoherence states.

As for the transitioning cluster state, the concentration dynamics of the system become more regular than the incoherence state, and the aperiodic continuous wave profile corresponding to the incoherence state converts into a symmetric profile for nonconservative work in Fig. 6.3 (e). This profile exhibits a combination of two distinct behaviors. One part is characterized by a flat portion, followed by a transition to a double-peaked structure with comparatively higher amplitude.

6.5.5 Signatures of multichimera and chimera state

In the case of the multichimera state, at $\nu = \frac{\eta}{4}$, the nonconservative work profile Fig. 6.3 (f) exhibits a global minimum with spatial double-periodic structure. Additionally, there are some secondary minima and maxima, although these are not prominent markers. Examining the profiles for entropy production and semigrand Gibbs free energy in Fig. 6.4 and Fig. 6.5 (f), respectively, we find that they display entirely distinct signatures in comparison to the corresponding work profile. The entropy production and semigrand Gibbs free energy illustrate numerous complex structures characterized by multiple peaks of varying amplitudes corresponding to the incoherent regimes. These structures are linked through relatively flat profiles corresponding to the coherent regions. This wave-like profile indicates that the multiple patches are not stationary over the spatiotemporal dimension; instead, the boundaries of the incoherent domains undergo erratic spatiotemporal motion. In this context, it is essential to emphasize that the nonconservative work is directly related to the addition of the KL divergence, $D_{KL}(z_\sigma||z_\sigma^h)$, and entropy production for all the states. Therefore, even though the work profile appears profoundly dissimilar from the individual profiles of entropy production and semigrand Gibbs free energy in this state, the former can still be derived from the appropriately scaled $D_{KL}(z_\sigma||z_\sigma^h)$ and entropy production.

For the conventional chimera state at $\nu = \frac{\eta}{10}$, the nonconservative work profile Fig. 6.3 (g) shows a flat line that corresponds to the coherent state, while the incoherent regime is characterized by an asymmetric profile. The entropy production over spatial dimension in Fig. 6.4 (g) demonstrates hump-like structures with a global minimum located between them. The global minimum is indicative of the central region within the incoherent part of the chimera state. The hump observed in this entropy production profile serves as a marker denoting the transition from coherence to incoherence. The semigrand Gibbs free energy in Fig. 6.5 (g) resembles a modulated pulse-like structure for the incoherent regime, with a peak signifying the core of the incoherent state. Notches on both sides of this peak mark the transition from coherence to incoherence, corresponding to the aforementioned humps in the spatial entropy production profile.

The variations in the entities $D_{KL}(z_\sigma||z_\sigma^h)$ and $\frac{Var(x)_t}{(\overline{x})_t}$ also illustrate similarity for the multichimera and chimera states in Fig. 6.6 (f) and (g), respectively. The range of values for these two entities is comparable to that found in transitional states.

In coherence, incoherence, and the transitioning cluster state between incoherence and chimera, we observe closely similar signatures in the nonconservative work and entropy production profiles. However, when it comes to chimera, multichimera, and the tree-like transition state between coherence and incoherence, we notice distinct signatures in profiles of nonconservative work and entropy production. Since the nonconservative work here qualitatively reflects the time-integrated concentration dynamics, we can conclude that the signatures of the system's dynamics at the level of the first raw moment differ from those of spatial entropy production in the cases of chimera, multichimera, and the tree-like transition state of the globally coupled system.

6.6 Chapter conclusions

To sum up, this chapter has illuminated the emergence of various states and the transitions between them in a globally coupled continuum chemical oscillatory system and quantified the associated nonequilibrium thermodynamic entities to capture their unique

thermodynamic signatures. We have provided a detailed comparative analysis of these states, offering valuable insights into differentiating different dynamical states of globally coupled CRNs qualitatively. The spatial entropy production profiles presented in this study can serve as a diagnostic tool for identifying diverse collective systems with varying coupling schemes. Additionally, we have obtained profiles of nonconservative work and semigrand Gibbs free energy for all states, revealing the connections between thermodynamic and dynamic aspects and among different thermodynamic entities. Most importantly, the intriguing link between the semigrand Gibbs free energy and the variance of the activator concentration is asserted by illustrating similarities between information-theoretic cost and a Fano-factor-like measure. This result has the potential to enhance our comprehension of complex systems at the intersection of thermodynamics and dynamics. Furthermore, we notice that the Fano-factor-like measure for all states is significantly lower than the constant value ($= 1$) associated with a situation related to a Poisson process, which confirms that the underlying dynamics of these "under-dispersed" states are more intricate than those described by a Poisson process.

While our study has focused on collective dynamics within the context of a specific chemical oscillator, the principal constituents used in this nonequilibrium thermodynamic investigation of collective dynamics are applicable to a wide range of systems where such dynamical states have been previously observed. Therefore, exploring similar thermodynamic aspects is feasible for those systems. For example, following the approach outlined in this study, the nonequilibrium thermodynamic analysis of glycolytic oscillations[187] can be expanded to encompass the collective dynamical states of such biological phenomena. The quantification of semigrand Gibbs free energy for different dynamic states and the information-theoretic connections conferred here can prove valuable in elucidating various patterns of brain dynamics and function[241]. Additionally, the significant relationship between semigrand Gibbs free energy and the variance of activator concentration, illustrated in the global coupling framework of the chemical oscillator, should be further explored in the context of local and nonlocal coupling schemes to assess its generality.

All our life processes - walking, talking, moving, feeding - are essentially chemical reactions.

Aaron Ciechanover

7

Kinetic proofreading: elucidating the interplay among energy, dissipation, and error rate in CRN

7.1 Incorporating CRN thermodynamic scheme into proofreading

Biosynthesis processes exhibit remarkably high accuracy. To rationalize this extraordinary accuracy, J. J. Hopfield and J. Ninio independently proposed a strategy adopted by biological systems known as kinetic proofreading[257,258]. This proofreading mechanism comes into play when the right substrate needs to be selected amidst similar alternatives during fundamental biological events such as DNA replication[259,260], RNA transcription[261,262], or protein synthesis[263]. The reaction network model for these core biological events achieved high fidelity under kinetic proofreading when strongly driven out of equilibrium. Essentially, the kinetic proofreading mechanism can be visualized by

a cyclic receptor-ligand binding model[117,118,264] coupled with Adenosine triphosphate (ATP) hydrolysis. Here, we consider that our kinetic proofreading network (KPN) is operating at a nonequilibrium steady state (NESS) characterized by nonzero dissipation[265]. Consequently, for the kinetic proofreading mechanism, a trade-off between the dissipation and error rate can exist[12,266,267], and understanding this trade-off scenario can help in identifying optimal operating regimes of the network. Hence, the error-dissipation trade-off has been investigated in different variants of proofreading networks associated with various biological processes.

While much attention has been devoted to understanding the intricate interplay between error and dissipation, the explicit utilization and modulation of energy in this chemical fuel-driven error-correcting mechanism remain inadequately addressed. However, given the pivotal role of overall energy expenditure in shaping and carrying out biological processes[268,269], the energetic cost of detecting the right substrate would impose a significant constraint on the functioning of kinetic proofreading networks, especially considering the limited energy budget in a biological environment. So, in this chapter, utilizing the nonequilibrium thermodynamic framework of an open chemical reaction network (CRN), we aim to depict the proper energetic picture of an arbitrarily driven KPN under the concentration and flux control[270] of the chemostatted species. Thus, we can encapsulate the overall performance of the KPN in terms of error, dissipation, and energy representation and unveil the correspondence among these entities. In this regard, the quantification of proper thermodynamic potential, particularly concerning externally controlled chemical fuel, can offer valuable insights into the concepts of chemical work and the thermodynamic efficiency of biological information processing mechanisms. Moreover, given the existence of multiple regimes with varying discriminatory abilities for proofreading networks[271], it will be intriguing to explore how the system's energy, within a nonequilibrium environment, is allocated to different discriminatory regimes with diverse trade-off situations. The analogy of different proofreading regimes with stages of microtubule growth[266] and nonequilibrium sensing[272] also demands a thorough thermodynamic depiction of such proofreading regimes to shed light

on the underlying general principles applicable to biological information processing[273]. Throughout this work, we will access error rates and associated dissipation by merely controlling the chemostatted species concentration and magnitude of binding energy without changing the network structurally.

This chapter examines the interplay of energy, dissipation, and error rate in the kinetic proofreading network using results from *Kumar et al., 2022, Physica A, 603:127735.*

This chapter is structured as follows: After outlining our motive in investigating the kinetic proofreading network in this section, we will focus on the network description of the kinetic proofreading and the key assumptions of this study in Sec. 7.2. Then the nonequilibrium steady state of the network will be presented in Sec. 7.3. In Sec. 7.4, building upon the network description, conservation laws, stoichiometric cycles, and emergent cycles of the kinetic proofreading network will be acquired. Next, the thermodynamic response and potential of the network are illustrated in Sec. 7.5 and Sec. 7.6. Profiles connecting the error, dissipation, and semigrand Gibbs free energy are provided in Sec. 7.7. Subsequently, the network's performance measuring entity, the Q value will be introduced in Sec. 7.8. Finally, we summarize our results in the chapter conclusions.

7.2 CRN of Kinetic Proofreading and assumptions

We have implemented a simple two-cycle CRN shown in Fig. 7.1 (a) for describing the kinetic proofreading mechanism. In this double-cycle proofreading network, one cycle corresponds to the 'right' ('R') substrate pathway, whereas the other cycle belongs to the 'wrong' ('W') substrate. This network describes the binding of protein E with substrate 'R' (or 'W'), leading to the formation of intermediate complexes ER, ER^* (or EW, EW^*), which then disassociate into enzyme and product. Similar to the previous chapters, we can categorize all species in the proofreading network in Fig. 7.1 (a) into two disjoint sets of I and C,

$$\underbrace{\{E, ER, ER^*, EW, EW^*\}}_{I} \bigcup \underbrace{\{R, ATP, ADP, R_p, W, W_p\}}_{C},$$

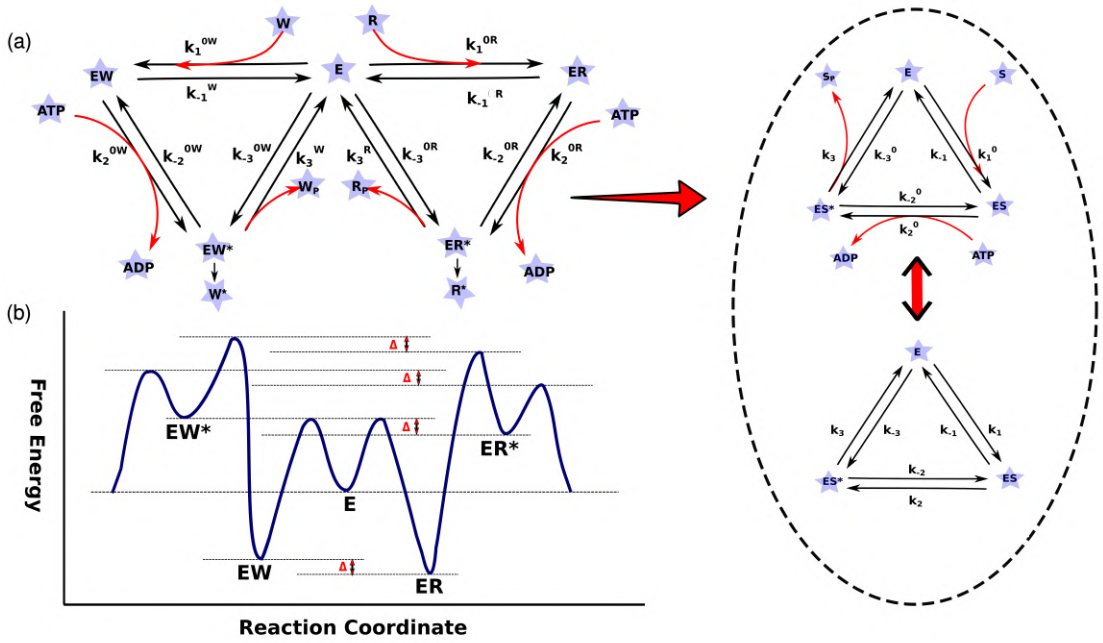

Figure 7.1: (a) Two cycles of the kinetic proofreading model are related to two very similar substrates: 'right'('R') and 'wrong'('W'). 'R*' and 'W*' are associated with the synthesis rates, which are considered sufficiently low to be neglected here. Species 'W', 'R', 'ATP', 'ADP', 'R$_p$' and 'W$_p$' have constant concentrations over the time scale of interest and are chemostatted species in this network. (b) The hypothetical image of the free energy landscape is illustrated here. Right: Individual cycles of the kinetic proofreading network can be represented by a single cyclic network, as shown in the upper panel. By absorbing the chemostatted concentration within rate constants, we obtain pseudo-first-order rate constants as $k_1 = k_1^0(S)$, $k_{-3} = k_{-3}^0(S_p)$, $k_{+2} = k_{+2}^0(ATP)$ and $k_{-2} = k_{-2}^0(ADP)$. Exploiting these pseudo-first-order rate constants, the single cyclic model in the upper panel can be mapped into a three-state system in the lower panel.

where I represents the set of intermediate species, and C is the set of chemostatted species. To maintain a general perspective, R_p and W_p instead of commonly used R and W have been considered in the third step of the proofreading network.

7.2.1 Low synthesis limit

We will study the interplay between error, dissipation, and thermodynamic potential under the condition of a fixed synthesis rate and assume that the fixed synthesis rate is considerably low relative to all other rate constants. Consequently, we can disregard this

nominal synthesis rate, and our findings regarding error rate and thermodynamics are applicable within the context of a slow synthesis rate. In the kinetic proofreading literature, this assumption of sufficiently low synthesis rates is made across various scenarios, such as T-cell receptor activation[274], mitigation of intrinsic biochemical noise[117,264], and an analogy between nonequilibrium sensing and kinetic proofreading[272].

7.2.2 Energetic discrimination

For proofreading networks, kinetic discrimination arises due to the difference in activation barrier heights[12], whereas energetic discrimination exists due to the difference in the binding energy of intermediates[257,258]. In general, both of these discriminations can appear in the proofreading network. These two scenarios of discrimination can be utilized effectively in a combined manner[275]. However, in recent studies of kinetic proofreading[271,266,276], an energetic discrimination regime has been solely considered to explore essential features of the proofreading model, including the error-dissipation scenario. This study will also exploit energetic discrimination only. For energetic discrimination, the minimum error rate can be acquired for vanishingly small dissipation.

7.2.3 Discrimination via dissociation

In a biological system, the discrimination between two similar substrates often occurs during the unbinding process rather than the binding process[257,274,276]. In this investigation, we also consider this aspect of biological discrimination, introducing the discrimination factor solely in the dissociation rates. All other rate constants associated with the right and wrong substrate pathways are equal due to the structural similarity of the two substrates. Specifically, k_{-1}^R and k_3^R of the right substrate pathway are linked with the wrong substrate pathway counterparts as $\frac{k_{-1}^R}{k_{-1}^W} = \frac{k_3^R}{k_3^W} = \exp^{-\Delta} = \sigma < 1$ where Δ represents the difference in free-energy barriers.

7.2.4 Mean field approximation

From the schematic diagram in Fig. 7.1 (a), we can express the relation $eR^* + eR + eW + eW^* + e = e_0$, where e_0 represents the total enzyme concentration and eR, eR^*, eW, eW^* denote the concentrations of species ER, ER^*, EW, EW^*, respectively. We assume that the total enzyme concentration can also be written as $e_0 = e_0^R + e_0^W$ to simplify the problem, with the general condition $e_0^R \neq e_0^W$. In this two-cycle model, this assumption of partitioning the total enzyme concentration into two independent parts is a mean-field approximation. This approach can also be extended to a general kinetic proofreading network by considering an appropriate number of independent parts for the total enzyme concentration. For our numerical study, we assume equal total enzyme concentrations for both pathways, i.e., $e_0^R = e_0^W$. This assumption leads to $eR^* + eR + e^R = e_0^R$ and $e^W + eW + eW^* = e_0^W$ where $e = e^R + e^W$ and e^R and e^W represent the free enzyme concentrations corresponding to 'right' and 'wrong' pathways, respectively. With these considerations, we can mathematically map this two-cycle proofreading model into a single-cycle model, as illustrated in the right panel of Fig. 7.1, where the substrate S in the figure can be R or W depending on the pathway considered.

7.3 Nonequilibrium steady states of the proofreading network

The kinetics of the single cycle involving the right substrate can be expressed as:

$$\frac{\partial eR}{\partial t} = k_1^R(e_0^R - eR^* - eR) - (k_{-1}^R + k_{+2}^R)(eR) + k_{-2}^R(eR^*) \tag{7.1a}$$

$$\frac{\partial eR^*}{\partial t} = k_{-3}^R(e_0^R - eR^* - eR) - (k_{-2}^R + k_{+3}^R)(eR^*) + k_{+2}^R(eR). \tag{7.1b}$$

In the above expressions, we implement the concept of pseudo-first-order rate constants[117,118], and $k_1 = k_1^0(R)$, $k_{-3} = k_{-3}^0(R_p)$, $k_{+2} = k_{+2}^0(ATP)$ and $k_{-2} = k_{-2}^0(ADP)$ are pseudo-first-order rate constants. Here, ATP, ADP, R, and $\mathrm{R_p}$ are concentration of chemostatted species and $k_1^0(R)$, k_{-3}^0, k_{+2}^0, and k_{-2}^0 reaction rate constants.

Utilizing the condition $eR^* + eR + e^R = e_0^R$, we obtain the following steady-state

concentrations from Eqs. (7.1a) and (7.1b),

$$eR_{ss} = \frac{(k^R_{-2}k^R_{-3} + k^R_1 k^R_3 + k^R_1 k^R_{-2})e^R_0}{(k^R_1 k^R_{-2} + k^R_1 k^R_3 + k^R_1 k^R_2) + (k^R_{-1}k^R_{-3} + k^R_2 k^R_{-3} + k^R_{-2}k^R_{-3}) + (k^R_{-1}k^R_{-2} + k^R_{-1}k^R_3 + k^R_2 k^R_3)} \tag{7.2a}$$

$$eR^*_{ss} = \frac{(k^R_1 k^R_2 + k^R_{-1}k^R_{-3} + k^R_2 k^R_{-3})e^R_0}{(k^R_1 k^R_{-2} + k^R_1 k^R_3 + k^R_1 k^R_2) + (k^R_{-1}k^R_{-3} + k^R_2 k^R_{-3} + k^R_{-2}k^R_{-3}) + (k^R_{-1}k^R_{-2} + k^R_{-1}k^R_3 + k^R_2 k^R_3)} \tag{7.2b}$$

$$e^R_{ss} = \frac{(k^R_{-1}k^R_{-2} + k^R_{-1}k^R_3 + k^R_2 k^R_3)e^R_0}{(k^R_1 k^R_{-2} + k^R_1 k^R_3 + k^R_1 k^R_2) + (k^R_{-1}k^R_{-3} + k^R_2 k^R_{-3} + k^R_{-2}k^R_{-3}) + (k^R_{-1}k^R_{-2} + k^R_{-1}k^R_3 + k^R_2 k^R_3)}. \tag{7.2c}$$

Now, unlike an equilibrium steady state, a clockwise steady-state flux exists for each cycle of the kinetic proofreading network at this nonequilibrium steady state (NESS). Each cycle of the proofreading network comprises three elementary reactions, and the net fluxes of these reactions can be acquired as $j_1 = k_1(e) - k_{-1}(es); j_2 = k_2(es) - k_{-1}(es^*)$ and $j_3 = k_3(es^*) - k_{-3}(e)$. Therefore, the steady-state cycle flux in the clockwise direction for a single cycle emerges as

$$j^R_{ss} = \frac{(k^R_1 k^R_2 k^R_3 - k^R_{-1}k^R_{-2}k^R_{-3})e^R_0}{(k^R_1 k^R_{-2} + k^R_1 k^R_3 + k^R_1 k^R_2) + (k^R_{-1}k^R_{-3} + k^R_2 k^R_{-3} + k^R_{-2}k^R_{-3}) + (k^R_{-1}k^R_{-2} + k^R_{-1}k^R_3 + k^R_2 k^R_3)}. \tag{7.3}$$

For the wrong substrate pathway, the expressions for eW_{ss}, eW^*_{ss}, e^W_{ss} and j^W_{ss} remain the same, with all the superscript changed from 'R' to 'W' in each term. From a thermodynamic viewpoint, all reaction steps must be reversible. The driving force associated with the NESS cycle flux is the net chemical potential around the single cycle, $\mu_L = \mu_{e,es} + \mu_{es,es^*} + \mu_{es^*,e} = \ln \frac{k_1 k_2 k_3}{k_{-1}k_{-2}k_{-3}} = \ln \gamma$. Since the rate constants $k_1, k_{\pm 2}, k_{-3}$ are equal in both 'W' and 'R' pathways and k_{-1} and k_3 are linked through a common factor $\exp^{-\Delta}$, both the 'W' and 'R' cycles experience an equal driving force. Unless specified otherwise, we have employed the following rate constants throughout our study, $k^R_1 = k^W_1 = 5$, $k^R_3 = 1$, $k^R_{-1} = 50$, $k^R_{-2} = k^W_{-2} = 10^{-3}$ and $k^R_{-3} = k^W_{-3} = 10^{-3}$ [277]. Here, the chosen Reaction rate constants are of the order of rate constants associated with

crucial proofreading steps in the experimental study of the tRNA selection network in Escherichia coli[278]. Specifically, rate constants $k^R_{-2} = k^W_{-2}$ and $k^R_{-3} = k^W_{-3}$ are set to be very small to render reaction steps 2 and 3 in both pathways nearly irreversible. For this double-cycle proofreading model, one could also utilize parameter values related to DNA replication as provided in ref.[277] and proceed with the numerical analysis conducted here. Rate constants with equal magnitudes for the 'R' and 'W' cycles will be used without a superscript in subsequent discussions.

7.3.1 Basin-like profile of error rate

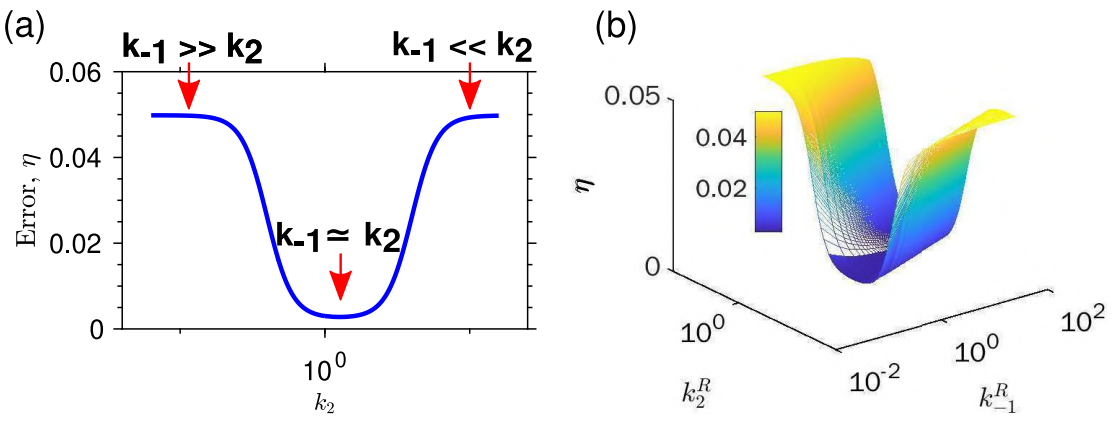

Figure 7.2: (a) The error rate exhibits a basin-like characteristic when solely varying k_2 over a range from 10^{-6} to 10^6. The other rate constants (or pseudo-first-order rate constants) of the proofreading network are held constant at $k_1 = 5$, $k^R_3 = 1$, $k^R_{-1} = 50$, $k_{-2} = 10^{-3}$, and $k_{-3} = 10^{-3}$. (b) A 3D counterpart of the error basin is illustrated by simultaneously changing both k_{-1} and k_{+2}. Here, k_{+2} is varied from 10^{-5} to 10^5, while k_{-1} is changed within the range of 0.5 to 50. The remaining rate constants are the same as in (a). The binding energy difference is set to $\Delta = 3$ in both figures.

Initially, we will investigate the error rate profile variation with pseudo-first-order rate constants. In the limit of slow synthesis rate, the error rate of the kinetic proofreading network at NESS is defined[271] as follows:

$$\eta = \frac{eW^*_{ss}}{e^W_{ss}} \frac{e^R_{ss}}{eR^*_{ss}}. \tag{7.4}$$

Here, eW^*_{ss} and eR^*_{ss} are steady-state concentrations of EW^* and ER^*, respectively,

and the concentration of enzyme corresponding 'R' and 'W' cycles is given by e_{ss}^{R} and e_{ss}^{W}. Under equilibrium conditions, the error rate of the kinetic proofreading network would be $\eta = \exp^{-\Delta}$. However, within a nonequilibrium environment, it is possible to achieve an error rate as low as $\eta = \exp^{-2\Delta}$.

Utilizing Eqs. (7.2b) and (7.2c), we can express the error rate from equation (7.4) as,

$$\eta = \frac{(k_1^W k_2^W + k_{-1}^W k_{-3}^W + k_2^W k_{-3}^W)(k_{-1}^R k_{-2}^R + k_{-1}^R k_3^R + k_2^R k_3^R)}{(k_1^R k_2^R + k_{-1}^R k_{-3}^R + k_2^R k_{-3}^R)(k_{-1}^W k_{-2}^W + k_{-1}^W k_3^W + k_2^W k_3^W)}. \tag{7.5}$$

The natural dominance of reaction step 2 over step 3 in the proofreading network for producing the substrate-enzyme complex eR^* or eW^* implies $k_1 >> k_{-3}$ in Fig. 7.1. Furthermore, the preference of step 3 in the formation of $R_{\rm p}$ (or $W_{\rm p}$) from eR^* (or eW^*) suggests $k_3 >> k_{-2}$. Now, under these assumptions, $k_1 >> k_{-3}$, and $k_3 >> k_{-2}$, our analysis focuses on how the error rate of the proofreading network is modified due to the relative strength between rate constants k_{-1} and k_{+2}. For this purpose, we have considered three distinct scenarios based on the relative strength between rate constants k_{-1} and k_{+2} and have identified orders of the error rate in each of these situations.

- When $k_{-1} >> k_{+2}$ with $\gamma = \frac{k_1^R k_2^R k_3^R}{k_{-1}^R k_{-2}^R k_{-3}^R} \approx 1$, the general expression of the error rate in Eq. (7.5) results in $\eta_1 = \frac{k_{-1}^W}{k_{-1}^R} \frac{(k_{-1}^R k_3^R)}{(k_{-1}^W k_3^W)} = \exp^{-\Delta} = \sigma$.

- When $k_{-1} \simeq k_{+2}$ with $\gamma >> 1$, the error rate in Eq. (7.5) becomes $\eta_2 = \frac{(k_{-1}^R k_3^R)}{(k_{-1}^W k_3^W)} \frac{(1+\frac{k_2^R}{k_{-1}^R})}{(1+\frac{k_2^W}{k_{-1}^W})} = \sigma^2 \frac{(1+\frac{k_2^R}{k_{-1}^R})}{(1+\frac{k_2^W}{k_{-1}^W})} = \sigma^2$.

- Finally, the condition $k_{-1} << k_{+2}$ with $\gamma >> 1$ yields error rate as, $\eta_3 = \frac{k_3^R}{k_3^W} = \sigma$.

This outcome highlights the subtle role of the relative magnitudes of rate constants k_{-1} and k_{+2} on the modification of the error rate. By employing either k_2 or k_{-1} as a control parameter in this scheme, we can access different discriminatory regimes. Notably, under the condition $k_{-1} << k_{+2}$, despite the system being significantly far from equilibrium, there is no observed enhancement in the error rate compared to equilibrium conditions.

From the general expression of the error rate in Eq. (7.5), we acquire an error rate profile in Fig. 7.2 (a) by varying solely the rate constant, k_{+2}, while the binding energy difference Δ and all other rate constants are held constant. As we move from the $k_{-1} >> k_{+2}$ to the $k_{-1} \simeq k_{+2}$ regime by adjusting the k_{+2}, Fig. 7.2 (a) illustrates an abrupt decline in the error rate. Eventually, the error rate reaches its minimum value, σ^2. The plateau observed in Fig. 7.2 (a) corresponds to the $k_{-1} \simeq k_{+2}$ regime, characterized by the error rate σ^2. Subsequently, as we change the parameter space from the $k_{-1} \simeq k_{+2}$ region to the $k_{-1} << k_{+2}$ regime, a basin-like profile of the error rate emerges as the error rate approaches the equilibrium error rate value, σ, within the nonequilibrium environment. This graphical representation of the general error rate in Fig. 7.2 (a) validates the analytical results obtained under these conditions.

In Fig. 7.2 (b), a 3D counterpart of the error basin[279] in Fig. 7.2 (a) is acquired by simultaneously varying both k_{-1} and k_{+2}. This three-dimensional figure provides a lucid illustration of how the error rate is modulated due to the relative strengths of k_{-1} and k_{+2}. Therefore, this representation can be crucial for ensuring the maximum accuracy of the proofreading scheme by controlling either k_{-1} or k_2 or both rate constants simultaneously while keeping Δ $(= 3)$ constant.

The key insight derived from this analysis is that the error rate η is not constant under the nonequilibrium conditions; rather, it strongly relies on the relative strengths of the rate constants k_{-1} and k_{+2}. We assert that within the nonequilibrium operating regime of the KPN, two distinct regimes with different discrimination abilities can exist depending on the relative strength of rate constants k_{-1} and k_{+2}. Notably, unlike the ref.[277], here k_{+2} is the pseudo-first-order rate constant denoted as $k_2 = k^0_{+2}(ATP)$ in Fig. 7.2. The association of ATP concentration with the pseudo-first-order rate constant, k_2, implies that we can utilize ATP concentration as a control parameter to achieve an equivalent error rate profile. In general, since pseudo-first-order rate constants incorporate the concentration of chemostatted species by definition, we can similarly modify the dynamic and thermodynamic profiles of the network by controlling the concentration of these species.

7.3.2 The error rate and impact of the binding energy difference

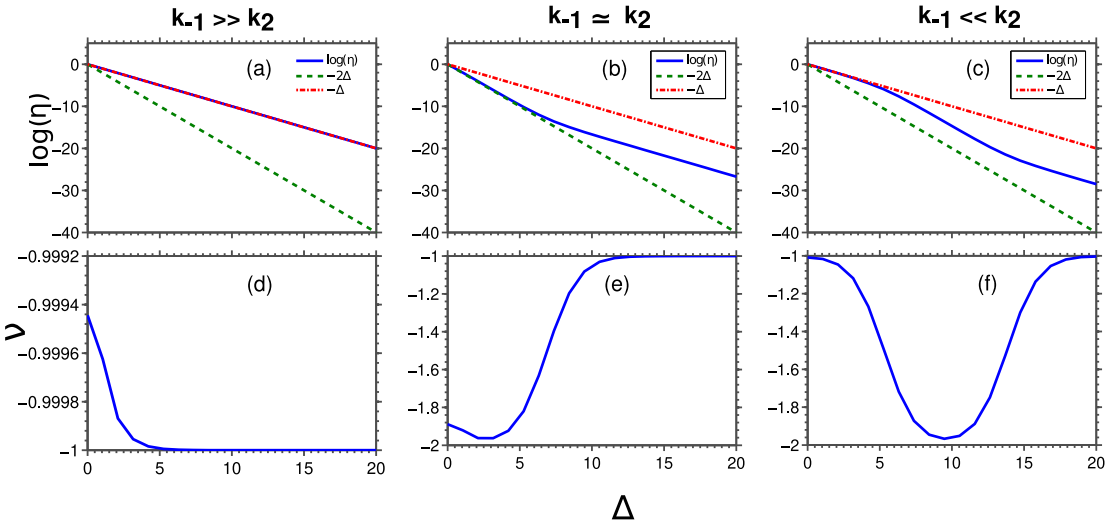

Figure 7.3: In panels (a), (b), and (c), we present the relationship between $\log \eta$ and Δ for three distinct regions associated with $k_{-1} >> k_{+2}$, $k_{-1} \simeq k_{+2}$, and $k_{-1} << k_{+2}$, respectively. The corresponding variations of the discriminatory index, $\nu = \frac{\partial \log(\eta)}{\partial \Delta}$ across the range of Δ, are illustrated for regimes $k_{-1} >> k_{+2}$, $k_{-1} \simeq k_{+2}$, and $k_{-1} << k_{+2}$ in (d), (e), and (f), respectively.

To encapsulate the influence of the binding energy difference, Δ, on the error rate of the network, we have depicted the variation of $\log(\eta)$ concerning Δ. The analysis is conducted separately for three different regimes corresponding to the relative strengths of k_{-1} and k_{+2}. Then, similar to the discriminatory index introduced in ref.[271], we have implemented an index ν defined as $\nu = \frac{\partial \log(\eta)}{\partial \Delta}$, - essentially representing the slope of the $\log(\eta)$ versus Δ plot. This index aids in evaluating the discriminatory capability of those local regimes. For instance, this definition results in $\nu = -1$ for the equilibrium condition since $\eta = \exp^{-\Delta}$ in this regime.

The error rate, η, and newly defined quantity, ν, for the three previously mentioned regimes are illustrated by varying the binding energy difference, Δ.

- $k_{-1} >> k_{+2}$ regime: $\log(\eta)$ aligns with a line representing $\exp -\Delta$ throughout the entire Δ range, as illustrated in Fig. 7.3 (a). With all other parameters maintained at constant values, it can be affirmed that the error rate within this

regime remains unaffected by changes in Δ. This observation is further supported by Fig. 7.3 (d) as $\nu = -1$ is maintained across the entire Δ range.

- $k_{-1} \simeq k_{+2}$ regime: $\log(\eta)$ curve in Fig. 7.3 (b) closely tracks the line associated with $\exp -2\Delta$ up to a certain magnitude of Δ. However, beyond this point, the curve deviates from this line as Δ increases further. From Fig. 7.3 (e) it is evident that the value of ν switches from -2 to -1 as Δ reaches higher magnitudes. Consequently, the accuracy is compromised compared to its maximum level in the parameter region of a relatively higher binding energy difference. The error rate in this scenario can be characterized by $\eta = \exp -(1+\beta)\Delta$ where $0 < \beta < 1$.

- $k_{-1} << k_{+2}$ regime: $\log(\eta)$ initially follows $\exp -\Delta$ line in Fig. 7.3 (c), as anticipated from the error basin in Fig. 7.2 (a). However, as Δ extends beyond a certain threshold, the $\log(\eta)$ curve gradually deviates from the $\exp -\Delta$ line and approaches the $\exp -2\Delta$ line. This deviation for higher Δ values suggests the possibility of achieving relatively more effective proofreading in this regime compared to the region with lower Δ. Interestingly, the error rate curve returns towards the $\exp -\Delta$ line upon further increments of Δ above a certain threshold. The entire observation in Fig. 7.3 (c) is also validated by the variation of ν between -1 and -2 in Fig. 7.3 (f). Hence, within this regime, proofreading is the most effective for the intermediate range of binding energy differences.

Thus, the comprehensive graphical examination in Fig. 7.3 reveals the correlation between the error rate of the kinetic proofreading network and the magnitude of Δ within the nonequilibrium environment. This correlation implies that the parameter space corresponding to a specific error rate can be expanded, contracted, or shifted by employing the binding energy difference as a control parameter[279].

7.4 Conservation laws, and cycles of the proofreading network

The kinetic proofreading reaction network illustrated in Fig. 7.1 (a) consists of six elementary chemical reactions and involves eleven distinct species. Therefore, according

to the discussions in Chapter 2, the proofreading network can be represented by the following stoichiometric matrix of dimensions 11×6,

$$S_\rho^\sigma = \begin{array}{c} \\ E \\ ER \\ ER^* \\ EW \\ EW^* \\ R \\ ATP \\ ADP \\ W \\ R_p \\ W_p \end{array} \begin{array}{c} \begin{array}{cccccc} R_1 & R_2 & R_3 & R_4 & R_5 & R_6 \end{array} \\ \begin{pmatrix} -1 & 0 & 1 & -1 & 0 & 1 \\ 1 & -1 & 0 & 0 & 0 & 0 \\ 0 & 1 & -1 & 0 & 0 & 0 \\ 0 & 0 & 0 & 1 & -1 & 0 \\ 0 & 0 & 0 & 0 & 1 & -1 \\ -1 & 0 & 0 & 0 & 0 & 0 \\ 0 & -1 & 0 & 0 & -1 & 0 \\ 0 & 1 & 0 & 0 & 1 & 0 \\ 0 & 0 & 0 & -1 & 0 & 0 \\ 0 & 0 & 1 & 0 & 0 & 0 \\ 0 & 0 & 0 & 0 & 0 & 1 \end{pmatrix} \end{array}. \tag{7.6}$$

For the stoichiometric matrix in Eq. (7.6) of the proofreading network, five vectors are acquired as the conservation laws of the closed reaction network, and these conservation laws specify the following components of the kinetic proofreading network: $L_1 = e+eR+eR^*+eW+eW^*$; $L_2 = ATP+ADP$; $L_3 = eR+eW+R-ATP+W$; $L_4 = eR+eR^*+R+R_p$ and $L_5 = -e-2eR-eR^*-eW-R+ATP+W_p$. When this closed CRN of the kinetic proofreading is opened by external chemostatting, components, L_2, L_3, L_4, and l_5 of the closed network are no longer globally conserved quantities of the open network due to the breaking of the associated conservation laws. The unbroken conservation law of the open CRN is derived from the stoichiometric matrix of intermediate species, S_ρ^I

$$l_I^{\lambda_u=1} = \begin{array}{c} \begin{array}{ccccc} E & ER & ER^* & EW & EW^* \end{array} \\ \begin{pmatrix} 1 & 1 & 1 & 1 & 1 \end{pmatrix} \end{array},$$

and corresponding component is $L_{\lambda_u} = e+eR+eR^*+eW+eW^*$. This component essentially describes that the total concentration of the enzyme remains a globally conserved entity for this open network of proofreading.

No stoichiometric cycle exists in this network of kinetic proofreading. However, this network allows the following two independent emergent cycles:

$$c_1 = \begin{matrix}1\\2\\3\\4\\5\\6\end{matrix}\begin{pmatrix}1\\1\\1\\0\\0\\0\end{pmatrix} \qquad \text{and} \qquad c_2 = \begin{matrix}1\\2\\3\\4\\5\\6\end{matrix}\begin{pmatrix}0\\0\\0\\1\\1\\1\end{pmatrix}.$$

These two emergent cycles, c_1 and c_2 represent the following two transitions: R + ATP $\longleftrightarrow$ R_p + ADP and W + ATP $\longleftrightarrow$ W_p + ADP, respectively. Corresponding to the emergent cycles, c_1 and c_2, we can write steady-state flux vectors as

$$j_{c_1} = \begin{matrix}1\\2\\3\\4\\5\\6\end{matrix}\begin{pmatrix}j_{c_1}\\j_{c_1}\\j_{c_1}\\0\\0\\0\end{pmatrix} \qquad \text{and} \qquad j_{c_2} = \begin{matrix}1\\2\\3\\4\\5\\6\end{matrix}\begin{pmatrix}0\\0\\0\\j_{c_2}\\j_{c_2}\\j_{c_2}\end{pmatrix},$$

respectively. Each of these NESS fluxes can be acquired by exploiting any elementary reaction of the proofreading network by using steady-state concentrations of intermediate species, $j_{c_1} = k_1^R(e_{ss}^R) - k_{-1}^R(eR_{ss})$ and $j_{c_2} = k_1^W(e_{ss}^W) - k_{-1}^W(eW_{ss})$. Both j_{c_1} and j_{c_2} yield

a similar mathematical expression as Eq. (7.3), except having two distinct superscripts, 'R' and 'W' in rate constants, respectively.

7.5 Thermodynamic response of different proofreading regimes

The pseudo-first-order rate constants are determined based on the concentrations of chemostatted species in the CRN representation of the kinetic proofreading. So, instead of modifying the rate constants, we can achieve variations in the pseudo-first-order rate constants by adjusting the concentrations of these chemostatted species. Changes in these concentrations can significantly impact the entropic and energetic responses of the system within the nonequilibrium environment[169,187]. In the following study, we will examine the thermodynamic evolution of the proofreading network, focusing on the influence of the influx of chemostatted species, particularly the fuel molecule ATP, and elucidate the connection between the thermodynamic response and dynamics of the network. Measuring energy and dissipation by changing the ATP concentrations will be more natural in such a driven biological system.

7.5.1 Dissipation in proofreading regimes

For the kinetic proofreading network, we can also express the overall dissipation[20] using a flux-force relationship. The steady-state flux of the kinetic proofreading network is determined as the sum of the fluxes of two emerging cycles, $J_{ss} = j_{c_1} + j_{c_2}$. The chemical forces, represented by the reaction affinities acting along these cycles, can be characterized by emergent affinities, $\mu_\epsilon = c_\epsilon \ln \frac{k_\rho}{k_{-\rho}} z_c^{-S_\rho^c}$, with z_c and S_ρ^c being concentrations and stoichiometric elements of chemostatted species, respectively. Consequently, the chemical affinities along c_1 and c_2 are obtained as $\mu_1 = \ln \frac{k_1^R k_2^R k_3^R}{k_{-1}^R k_{-2}^R k_{-3}^R}$ and $\mu_2 = \ln \frac{k_1^W k_2^W k_3^W}{k_{-1}^W k_{-2}^W k_{-3}^W}$. Any nonzero positive affinities, μ_1 and μ_2, will drive the system out of equilibrium. Our assumptions regarding reaction rates ensure that $\mu_1 = \mu_2 = \mu$. Thus, the total dissipation of the proofreading network is acquired as $\dot{\Sigma} = J_{ss}\mu$.

A transition in ATP concentration from low to high levels induces changes in dis-

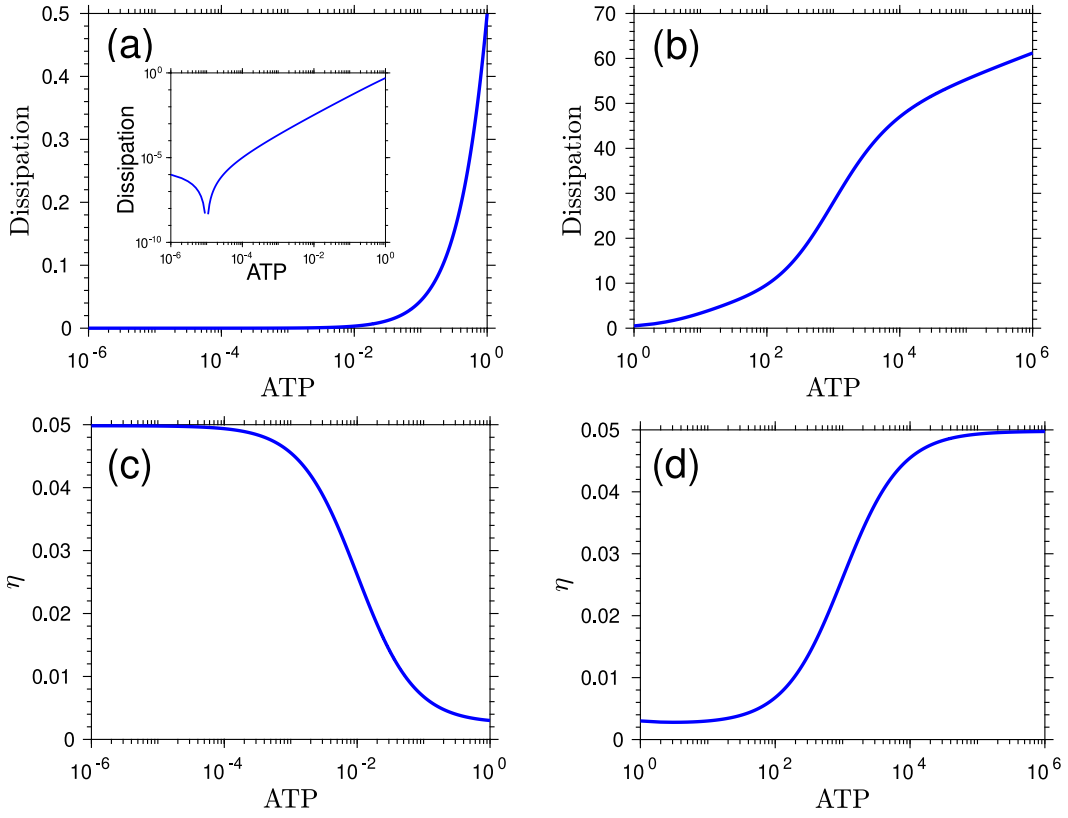

Figure 7.4: (a) Dissipation and (c) error rate of the kinetic proofreading network for an ATP concentration range of $10^{-6} - 10^{0}$ are shown. Inset: We have represented dissipation in log scale to visualize the small dissipation regime. The equilibrium point of the system is identified as the discontinuity due to zero dissipation. For the higher ATP concentration range of $10^{0} - 10^{6}$, the (b) dissipation and (d) error rate of the network are illustrated. The rate constants of the proofreading network are held constant at $k_1 = 5$, $k_2^0 = 1$, $k_3^R = 1$, $k_{-1}^R = 50$, $k_{-2} = 10^{-3}$, and $k_{-3} = 10^{-3}$.

sipation, as depicted in Fig. 7.4. This alteration in ATP concentration, with ADP concentration held constant, implies a gradual rise in the ATP to ADP concentration ratio within the system. We have presented two breakdown figures, Fig. 7.4 (a) and (b) to elucidate the dissipation curve concerning ATP concentration, accompanied by error variations in Fig. 7.4 (c) and (d). When k_{+2}^0 equals 1, maintaining the condition $k_{-1} >> k_{+2}$ for a range of ATP concentrations keeps the system close to equilibrium. At an ATP concentration of 10^{-5} concentration unit, the system remains at the equilibrium, as evident from the discontinuity in the inset plot of Fig. 7.4 (a).

In the left panel of Fig. 7.4, variation of ATP concentration drives the system from an initial near-equilibrium state to a nonequilibrium state. Due to the ATP concentration change, the error rate in Fig. 7.4 (c) gradually decreases from near-equilibrium to the nonequilibrium region. This error rate variation was expected from the error basin illustration in Fig. 7.2 (a) and the corresponding discussion. From Fig. 7.4 (c) and (a), it is evident that dissipation becomes nonzero and increases monotonically as the error rate enters the nonequilibrium error regime from near-equilibrium. This dissipation curve highlights the trade-off nature between error rate and dissipation within this range of ATP concentration. On the right panel of Fig. 7.4, for a much higher ATP concentration range, the error rate increases from its minimum value and approaches the equilibrium magnitude within the nonequilibrium environment in Fig. 7.4 (d). By comparing Fig. 7.4 (b) and (d), we can state that the corresponding dissipation curve qualitatively reflects the same dynamics as the error rate in this regime. A simultaneous increase in the error rate and dissipation for this ATP concentration range suggests a lack of trade-off between error rate and dissipation under these nonequilibrium conditions.

7.6 Thermodynamic potential of the proofreading network

We will now focus on the energy expenditure of the proofreading network by calculating the nonequilibrium thermodynamic potential of the network. By characterizing each chemical species thermodynamically in terms of chemical potential μ_σ, we can derive the nonequilibrium Gibbs free energy of the network, similar to the studies in previous chapters. Then, we capture the semigrand Gibbs free energy of the open network from the nonequilibrium Gibbs free energy. This semigrand Gibbs free energy is often regarded as the proper entity to encapsulate the energetics of the open CRN.

In Fig. 7.5 (a) and (b), we illustrate the Gibbs free energy, semigrand Gibbs free energy, and its slope with changes in ATP concentration across two distinct error rate regimes. For the lower and higher ranges of ATP concentration, the qualitative features of the nonequilibrium Gibbs free energy align with the error rate, presented in (*ii*) and

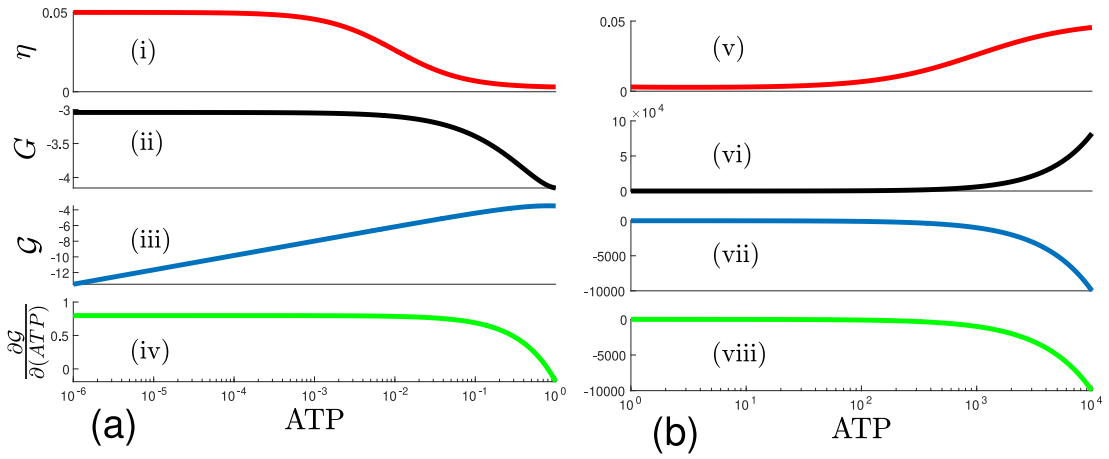

Figure 7.5: In (a), we depict variations in error rate (i), Gibbs free energy (ii), semigrand Gibbs free energy (iii), and the slope of semigrand Gibbs free energy (iv) across the lower ATP concentration range $(10^{-6} - 10^{0})$. Conversely, in (b), the response curves of the same entities for the higher ATP concentration range are illustrated in (v), (vi), (vii), and (viii). The binding energy difference, $\Delta = 3$, has been considered for both scenarios. The rate constants of proofreading network remain constant at $k_1 = 5$, $k_2^0 = 1$, $k_3^R = 1$, $k_{-1}^R = 50$, $k_{-2} = 10^{-3}$, and $k_{-3} = 10^{-3}$.

(vi) of Figs. 7.5 (a) and (b), respectively. However, the error rate and nonequilibrium Gibbs free energy profiles are out of phase. The similarity in profiles of Gibbs free energy and the error rate suggests an interconnection between these two entities.

Within the ATP concentration range corresponding to the minimum error rate, the Gibbs free energy decreases as dissipation starts increasing from zero (Fig. 7.4 (a)). In the higher ATP concentration range, as the error rate increases post the minimum error plateau, the dissipation intensifies (Fig. 7.4 (b)) within a more strongly driven nonequilibrium environment, and the nonequilibrium Gibbs free energy rapidly approaches a significantly positive value. This increase and decrease in Gibbs free energy with increasing ATP concentration stem from the constraint imposed by the relationship between the dissipation and the Gibbs free energy within the nonequilibrium environment. More specifically, the combination of nonequilibrium Gibbs free energy and proofreading network dissipation can quantify the chemical work executed on the system. Therefore, we can conclude that the proofreading network operates with a minimum error rate under small and finite chemical work. The chemical work escalates rapidly in the strongly

driven nonequilibrium regime associated with lower accuracy.

The semigrand Gibbs free energy (SGG) profile, $\mathcal{G}$ in Fig. 7.5 (a), moves upward from a negative value as more ATP accumulates in the system. At the same time, the error rate approaches a minimum. The corresponding slope of the SGG remains initially constant and then transitions from one to zero as the error shifts from the equilibrium value to the minimum one. For a relatively higher ATP concentration in Fig. 7.5 (b), the SGG profile hovers near zero across an extended range of ATP concentrations, while the minimum error rate is maintained within a nonequilibrium environment. However, when the error deviates from its minimum due to further changes in ATP concentration, a sharp and substantial shift toward a negative value is evident in the SGG profile. This significant change is also reflected in the corresponding slope depicted in (*viii*) of Fig. 7.5 (b). The enormous magnitudes of Gibbs free energy and semigrand Gibbs free energy in Fig. 7.5 (b) indicate that the system is considerably distant from equilibrium. So, we conclude that the proofreading system functions with optimal accuracy and dissipation for the close to zero semigrand Gibbs free energy[279]. The near-zero value of semigrand Gibbs free energy signifies a very small magnitude (negative) of the entity relative to its considerably larger (negative) values elsewhere. In Fig. 7.5 (vii), the semigrand Gibbs free energy, appearing to be zero, is actually due to the entity's enormous negative value at higher ATP concentrations.

7.7 Error-Dissipation-Semigrand Gibbs Free Energy Profile

A trade-off between error rate and dissipation can exist if any modification in a parameter cannot simultaneously enhance both. However, this trade-off feature may not be present in some other regimes. Our study delves into the trade-off between dissipation and error rate in various discrimination regimes, corresponding to externally controlled ATP concentration changes. We also illustrate the connection between semigrand Gibbs free energy and this trade-off scenario. Furthermore, considering a distinct binding energy difference, Δ, we analyze the overall performance of the proofreading network

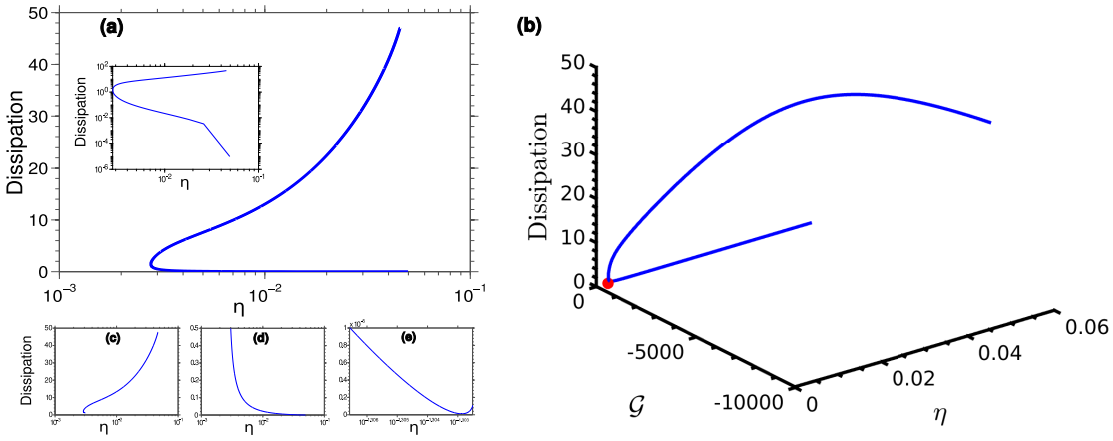

Figure 7.6: Dissipation concerning the error rate is presented in Fig. 7.6 (a) for the ATP concentration range of $10^{-6} - 10^{4}$. Inset: dissipation on a log scale is depicted to gain insight into the small dissipation regime. (e) The dissipation-error profile is illustrated for the regime ($k_{-1} >> k_{+2}$), where the error rate equals the equilibrium error rate and dissipation is negligible. (d) For the $k_{-1} \simeq k_{+2}$ regime, a sharp change in dissipation with error rate is demonstrated. (c) The dissipation-error curve of the $k_{-1} << k_{+2}$ regime is presented. The simultaneous variations of dissipation and semigrand Gibbs free energy with the error rate are shown in (b). The red dot in this figure refers to the optimal working scenario of the proofreading network. The binding energy difference, $\Delta = 3$, is employed for all the illustrations.

concerning error rate and dissipation across the entire ATP concentration range.

A parametric curve illustrating the relationship between error and dissipation, utilizing ATP concentration as the independent variable, is depicted in Fig. 7.6 (a). The curve indicates that dissipation remains negligible until the minimum error is achieved. Figure 7.6 (e) shows the nature of this infinitesimal dissipation change near the equilibrium error regime. Then a sharp and finite increase in the dissipation can be observed in Fig. 7.6 (d) as the error rate reaches near the minimum. This rapid rise suggests that as the error rate decreases further, dissipation inevitably increases due to the inherent trade-off between dissipation and error in this regime. As the error rate again approaches the equilibrium error rate magnitude (for a fixed lower Δ) within the nonequilibrium environment, dissipation monotonically increases owing to further increase in the external driving force, as presented in Fig. 7.6 (c). Thus, it becomes evident that the error rate value does not exclusively determine the dissipation, as the dissipation can vary for the

same error rate depending on the distance from the equilibrium. Moreover, Fig. 7.6 (b) demonstrates the concurrent variation of dissipation and semigrand Gibbs free energy with the error rate, revealing the allocation of the system's proper energy content to the error-dissipation trade-off scenarios. The red dot in the figure denotes the optimal working condition of the network. Here, optimality refers to a specific operating condition or parameter regime where the network achieves both a minimum error rate and minimum dissipation. Therefore, the red dot in Fig. 7.6 (b) represents simultaneous minimum values for error rate and dissipation, along with the corresponding semigrand Gibbs free energy value.

7.8 Performance of proofreading network: Q value

In Fig. 7.7 (a), a dissipation-error profile, akin to Fig. 7.6 (a), is presented for four arbitrary levels of the binding energy difference, Δ. While the error rate decreases significantly for higher Δ values, the maximum dissipation within the same ATP concentration range decreases. The characteristic distinction between curves corresponding to higher and lower values of Δ is also apparent from fig. 7.7 (a). For higher Δ values, the error rate of the proofreading scheme in the nonequilibrium environment tends to get stuck at a lower value over a broader parameter space of ATP concentration. Consequently, a more rapidly increasing nonzero part of the dissipation plot is observed for $\Delta = 3$ compared to the corresponding part for $\Delta = 12$, reflecting the persistent nonequilibrium regime with no improvement in error rate for relatively lower Δ values. Additionally, it is noteworthy from Fig. 7.7 (a) that the dissipation corresponding to the minimum error rate is greater for higher Δ than for lower Δ. Given the equal driving forces considered for different Δ values, these variations in dissipation curves are attributed solely to the different fluxes associated with distinct Δ values.

In a recent investigation[280], the performance of a kinetic proofreading network, representing a biological process, was examined using constraints set by the thermodynamic uncertainty relation[103]. Here, our analysis focuses on the NESS of the kinetic proofread-

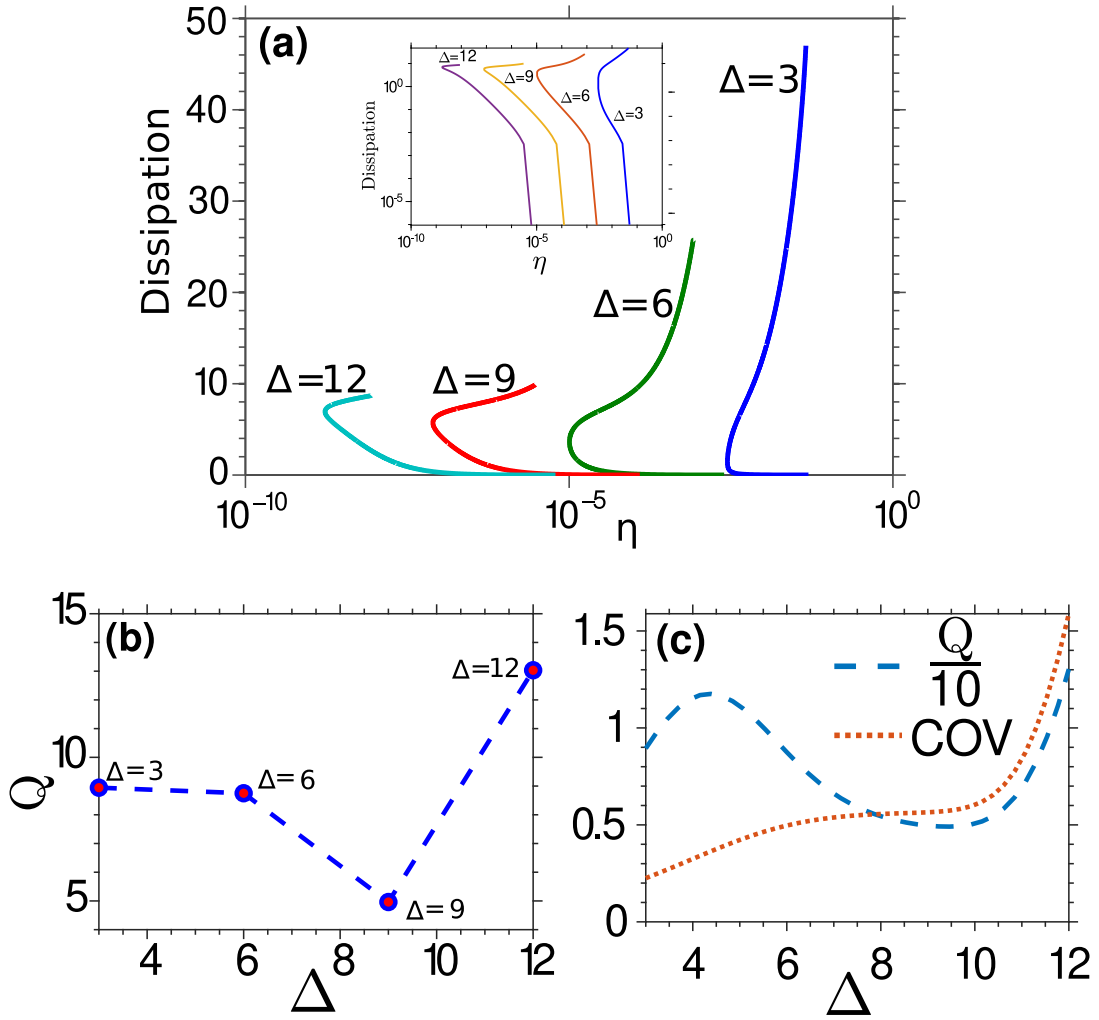

Figure 7.7: (a)Dissipation variation with the error rate is drawn for four different binding energy difference values, $\Delta(=3, 6, 9$ and $12)$. In all scenarios, the ATP concentration spans from 10^{-6} to 10^{4}, with all other parameters held constant. The inset plot depicts dissipation shown on a log scale for the same binding energy difference values. The Q values are illustrated for $\Delta(=3, 6, 9$ and $12)$ in (b). The minimum Q value at $\Delta = 9$ suggests a relatively favorable trade-off between error and dissipation for the entire ATP concentration range. The variations in the Q factor and coefficients of variation (COV) due to the continuous change in Δ are presented in (c). The Q factor profile is scaled by a factor of 0.1 to achieve an appropriate fit.

ing network at a fixed time, considering variations in ATP concentration and energetic discrimination. So, to assess the performance concerning both error and dissipation under different binding energy differences, we introduce a performance measuring metric

at the NESS of the deterministic system during ATP concentration variations. For that purpose, we select the error rate, denoted as $A_o = \eta$, as the observable of interest, which changes with ATP concentration. At the NESS, we represented the mean and standard deviation associated with A_o as $\langle A_o \rangle$ and $\sqrt{(\langle A_o^2 \rangle - \langle A_o \rangle^2)}$, respectively. To capture the variability across the entire ATP concentration range, we introduce the coefficient of variation, $\epsilon = \frac{\sqrt{(\langle A_o^2 \rangle - \langle A_o \rangle^2)}}{\langle A_o \rangle}$. The use of the coefficient of variation can be beneficial here, given the drastically different means associated with distinct Δ values. Now, for a specific Δ, we define the performance measuring metric Q as the product of the average dissipation and the coefficient of variation, expressed as $Q = \left\langle \dot{\Sigma} \right\rangle \epsilon$[279]. Although our Q value definition is inspired by the thermodynamic uncertainty relation, we make necessary modifications to align it with the variables, objectives, and framework of this study.

In Fig. 7.7 (b), the factor Q exhibits a decrease to its minimum value for $\Delta = 9$ after initially showing nearly equal magnitudes for $\Delta = 3$ and $\Delta = 6$. Notably, Fig. 7.7 (b) also highlights that the Q factor for $\Delta = 12$ gets higher and even surpasses the value corresponding to $\Delta = 3$. The trends in the Q factor and coefficients of variation during continuous variations in Δ are depicted in Fig. 7.7 (c). Despite the coefficients of variation associated with the error rate being lower for $\Delta = 3$ and $\Delta = 6$ than those for higher Δ values, the elevated average dissipation values for these two Δ values result in their corresponding Q values exceeding that for $\Delta = 9$. However, for $\Delta = 12$, even a considerably lower average dissipation is insufficient to compensate for the higher coefficient of variation, leading to its Q value being higher than all other Δ values. Consequently, while the average dissipation for the entire ATP concentration range decreases monotonically with increasing Δ, the Q factor exhibits non-monotonic behavior. We assert that a lower Q value better balances error and dissipation, ensuring optimal overall performance across different operating regimes throughout the ATP concentration range[279]. Therefore, for a specific velocity and a fixed energy budget of the kinetic proofreading network, this Q term assists in identifying a specific Δ that achieves optimal overall performance in terms of error and dissipation.

7.9 Chapter Conclusions

We have elucidated the kinetic proofreading mechanism using the substrate selection network, focusing on its energetic discrimination aspects. Our approach involves leveraging the chemical thermodynamic framework and its network property for systematically investigating the operation of the proofreading network. Key outcomes and strengths of our theoretical analysis include the identification and characterization of the impact of the control parameters on the dynamic and thermodynamic elements within the network and the quantification of the proper energy content of this generic biological network. Furthermore, our estimation of nonequilibrium thermodynamic quantities assists in exploring the optimal operating conditions for proofreading, considering factors such as error rates, dissipation, and semigrand Gibbs free energy. Given the association of the proofreading steps of the kinetic proofreading network with futile cycles and chemical fuel consumption, biological systems aim to maintain specificity with minimal dissipation and energy expenditure. Finally, we have introduced a new metric, denoted as Q, to assess the overall performance of the proofreading network.

We categorize different discrimination regimes of kinetic proofreading on the basis of the relative strength between the pseudo-first-order rate constants. Then, we encapsulate the impact of the magnitudes of the binding energy difference, Δ on the error basin profile. These findings imply that we can shift or modify the error rate regimes by adjusting the magnitude of the binding energy difference or chemostatted species' concentration without changing the hardcore network structure. Particularly, the dependence on the binding energy magnitudes will be crucial in the presence of a family of competing substrates in a biological system. Additionally, in a biomolecular system, the impact of enhanced binding discrimination can be decisive in sustaining the system near the thermodynamic uncertainty relation[103] bound or further from this bound[280].

By changing the concentration of chemical fuel, ATP, we have captured the evolution of dissipation and nonequilibrium Gibbs free energy in different discrimination regimes and thus provided a way to connect the chemical work with the error rate. This aspect

will aid in designing more efficient synthetic biological architectures. Besides these, the depiction of the semigrand Gibbs free energy suggests that the optimal network accuracy and dissipation are achieved with near-zero semigrand Gibbs free energy. These findings in the simple two-cycle proofreading network can be advantageous for extending the search of the optimal specificity and dissipation regime in more intricate and general proofreading networks[271,266,276]. This chemostatted concentration-based approach will be beneficial for obtaining the energy expenditure of the general biochemical feedback control mechanisms[281,273].

This investigation holds relevance for systematically analyzing the performance of self-assembled synthetic systems[282,283]. The error basin described in this study fits well with the summation of two logistic functions, and the mathematical structure of such functions will be provided in our forthcoming research. Within the nonequilibrium environment, the identified trade-off and non-trade-off regimes present significant opportunities to explore new control parameters and novel mechanisms based on the structure and energetics of the network. Understanding the proper energy consumption and storage of the network under continuous fuel utilization could provide valuable insights for designing more effective experimental design related to tRNA charging[284], translation by Ribosomes[285], and similar biological events.

The important thing is not to stop questioning.
Curiosity has its own reason for existing.

-Albert Einstein

8

Conclusions and prospects

In this thesis, starting from the chemical reaction network (CRN) representation of the Brusselator and Selkov models, we have developed reaction-diffusion systems (RDS) to capture the concentration dynamics associated with Turing instability, Hopf instability, traveling waves, or their interactions by exploiting the phenomenological amplitude equations relevant to these different instabilities. These concentration dynamics were then used to obtain corresponding nonequilibrium thermodynamic signatures. Notably, we have extended the strategy of capturing the nonequilibrium thermodynamics of single-system dynamics to the collective dynamics of the Brusselator by making an ansatz. In the absence of any diffusion, we have also utilized network properties in the kinetic proofreading network and then encapsulated the thermodynamics of the kinetic proofreading over different discriminatory regimes. Entropy production rate (EPR) and the proper thermodynamic potential were quantified for all investigated phenomena.

While the dynamic and thermodynamic investigation of phenomena were fascinating on their own, comparisons of dynamic and thermodynamic signatures revealed intrigu-

ing connections in far-from-equilibrium environments. For three scenarios of Turing and Hopf overlapping in Brusselator RDS, we have demonstrated the drastic influence of diffusion coefficients and control parameters on dynamic and thermodynamic entities related to spatiotemporal patterns in chapter 3. Importantly, we have considered essentially cross diffusion-driven Turing instability in the presence of equal self-diffusion coefficients of activator and inhibitor, and hence dynamic and thermodynamic entities exhibit pictures beyond the conventional Turing pattern. Chapter 4 explores the implicit effect of cross diffusion on the wave number of traveling waves within the Selkov RDS and the entropic and energetic characterization of the patterns related to Hopf instability and traveling waves around the Benjamin-Feir (BF) instability. At BF instability onset, contrasting entropic and energetic signatures of traveling waves associated with discrete and continuous wave numbers implied the importance of finite boundary effects. We have observed proportionality between total entropy production rate (EPR) and global concentration dynamics in both chapters. Additionally, a less cumbersome Krylov-Bogolyubov (KB) method has been employed to acquire coefficients of amplitude equations in the presence of both self and cross diffusion. In chapter 5, we have realized the chimera state within a globally coupled Brusselator system by implementing coupling at the level of amplitude. We have found that the temporal EPR exhibited 'beat characteristics', a potential diagnostic tool for such states within the global coupling scheme. In particular, we have displayed the equivalence of chimera energetics with the Gabor representation associated with the information uncertainty principle, suggesting its usefulness in comparing chimeras to other seemingly analogous states in diverse settings. Meanwhile, we have considered the same coupled system in chapter 6 and generated a wide range of states around the chimera by varying coupling parameters. The dynamic and thermodynamic signatures of all these states are discussed in detail to differentiate these dynamical states qualitatively. Most importantly, similarities between information-theoretic cost and a Fano-factor-like measure suggest a relationship between semigrand Gibbs free energy and the variance of activator concentration. Chapter 7 has employed the same nonequilibrium thermodynamic framework to investigate the kinetic

proofreading mechanism at a nonequilibrium steady state (NESS). We achieved an error basin profile by varying the concentration of chemical fuel and then illustrated the impact of the magnitudes of the binding energy difference on the error basin profile. By capturing the evolution of thermodynamic quantities, we have identified optimal operating conditions and connected chemical work with error rates. A new metric has been introduced to assess network performance under varying binding energies. These findings within the two-cycle proofreading network offer valuable insights for analyzing self-assembled synthetic systems. Overall, the results from these chapters, applied to various model systems, hold significant potential for advancing our understanding of complex systems at the intersection of dynamics and thermodynamics.

Throughout this thesis, we have primarily focused on the homogeneous concentration distribution of the chemostatted species. However, similar studies can be extended to consider the inhomogeneous concentration of chemostatted species. The dynamical viewpoint of an RDS system with inhomogeneous concentration distributions of chemostatted species has been explored in prior works[180,163,112]. Therefore, investigating the thermodynamic signatures of phenomena such as wave direction shifts with time or other crucial features in the presence of inhomogeneity of chemostatted species will complement the dynamical approach and present an intriguing avenue for future exploration. These nonequilibrium thermodynamic characterizations of dynamical phenomena in RDS can also be extended to non-ideal RDS systems[286] and CRNs involving non-elementary reactions[111]. Moreover, the Ansatz employed in this thesis to obtain collective dynamics warrants further investigation in diverse coupling scenarios and should be compared with the chemical fields obtained through a complete numerical approach with coupling at the level of the RDS.

Another significant aspect to consider would be a comparative study of various alternative glycolytic pathways from both dynamic and thermodynamic viewpoints. Such a study could shed light on different inquiries related to the glycolytic pathway, such as the prevalence of a particular glycolytic pathway in specific organisms, the role of nonequilibrium thermodynamic constraints on glycolytic pathway performance, trade-

offs between ATP yield and thermodynamic cost, or the identification of the most cost-efficient pathway. Some studies in this direction[14,15] have been conducted; however, many questions persist, and several aspects remain unexplored. The nonequilibrium thermodynamic framework used in this thesis for the simple glycolytic RDS can be extended to explore these aspects within different metabolic networks.

The kinetic proofreading network investigated in this thesis is considered to have a negligible catalytic rate. However, the effect of finite and distinct catalytic rates on the error rate of the proofreading network has been illustrated in prior works[287]. In the future, we aim to extend the current framework to capture the interplay between dynamic and thermodynamic entities for the kinetic proofreading network with a finite catalytic rate. Additionally, recent introductions of spatial gradients and diffusion in investigating specificity in biological events[288] have led to the RDS description of the kinetic proofreading network. Our approach, encapsulating the nonequilibrium thermodynamics of RDS, can also be applied to this RDS description, revealing the effect of a spatial gradient in this biological proofreading strategy. The network properties discussed in this thesis will be applied to various synthetic genetic regulatory networks[289] in the future. These studies hold important implications for network engineering, understanding trade-off logic in biological and chemical systems, and evolutionary biology. Nevertheless, this nonequilibrium thermodynamic description of these passive chemical and biological systems can be also leveraged for obtaining a complete thermodynamic description of the active RDS[290].

References

[1] A M Turing. The Chemical Basis of Morphogenesis. *Philosophical transactions of the Royal Society of London. Series B, Biological sciences*, 237(641):37–72, 1952.

[2] AN Zaikin and AM Zhabotinsky. Concentration wave propagation in two-dimensional liquid-phase self-oscillating system. *Nature*, 225(5232):535, 1970.

[3] Arthur T Winfree. Spiral waves of chemical activity. *Science*, 175(4022):634–636, 1972.

[4] Michael Cross and Henry Greenside. *Pattern Formation and Dynamics in Nonequilibrium Systems*. Cambridge University Press, 2009.

[5] Yoshiki Kuramoto. *Chemical Oscillations, Waves, and Turbulence*, volume 19 of *Springer Series in Synergetics*. Springer Berlin Heidelberg, 1984.

[6] Daniel Walgraef. *Spatio-temporal pattern formation: with examples from physics, chemistry, and materials science*. Springer Science & Business Media, 2012.

[7] James Dickson Murray. *Mathematical Biology II: Spatial Models and Biomedical Applications*, volume 2. Springer, 2003.

[8] Albert Goldbeter. *Biochemical oscillations and cellular rhythms: the molecular bases of periodic and chaotic behaviour*. Cambridge university press, 1997.

[9] Alfred Gierer and Hans Meinhardt. A theory of biological pattern formation. *Kybernetik*, 12:30–39, 1972.

[10] Steven H. Strogatz. *Nonlinear Dynamics and Chaos: With Applications to Physics, Biology, Chemistry and Engineering*. Westview Press, 2000.

[11] Irving R Epstein and John A Pojman. *An introduction to nonlinear chemical dynamics: oscillations, waves, patterns, and chaos*. Oxford University Press, 1998.

[12] Charles H. Bennett. Dissipation-error tradeoff in proofreading. *Biosystems*, 11(2):85 – 91, 1979.

[13] Donald Voet and Judith G Voet. *Biochemistry*. John Wiley & Sons, 2010.

[14] Avi Flamholz, Elad Noor, Arren Bar-Even, Wolfram Liebermeister, and Ron Milo. Glycolytic strategy as a tradeoff between energy yield and protein cost. *Proceedings of the National Academy of Sciences*, 110(24):10039–10044, 2013.

[15] Arion I. Stettner and Daniel Segrè. The cost of efficiency in energy metabolism. *Proceedings of the National Academy of Sciences*, 110(24):9629–9630, 2013.

[16] Martin Feinberg. Lectures on chemical reaction networks. 1979.

[17] Anatol M Zhabotinsky. A history of chemical oscillations and waves. *Chaos: An Interdisciplinary Journal of Nonlinear Science*, 1(4):379–386, 1991.

[18] I. Prigogine and R. Lefever. Symmetry Breaking Instabilities in Dissipative Systems. II. *The Journal of Chemical Physics*, 48(4):1695–1700, 2 1968.

[19] Ilya Prigogine and Isabelle Stengers. *Order out of chaos: Man's new dialogue with nature*. Batam Books, 1984.

[20] Dilip Kondepudi and Ilya Prigogine. *Modern Thermodynamics*. John Wiley & Sons, Ltd, Chichester, UK, 11 2014.

[21] Shigeru Kondo and Takashi Miura. Reaction-diffusion model as a framework for understanding biological pattern formation. *science*, 329(5999):1616–1620, 2010.

[22] Ronald Aylmer Fisher. The wave of advance of advantageous genes. *Annals of eugenics*, 7(4):355–369, 1937.

[23] Andrey Nikolaevich Kolmogorov and NS Piskunov. Studies of the diffusion with the increasing quantity of the substance; its application to a biological problem. In *Differential Equations*, pages 106–132. CRC Press, 1996.

[24] Vladimir K. Vanag and Irving R. Epstein. Cross-diffusion and pattern formation in reaction–diffusion systems. *Phys. Chem. Chem. Phys.*, 11:897–912, 2009.

[25] Yoshiki Kuramoto and Dorjsuren Battogtokh. Coexistence of coherence and incoherence in nonlocally coupled phase oscillators. *Nonlinear Phenom. Complex Syst.*, 5(4):380–385, 2002.

[26] Daniel M. Abrams and Steven H. Strogatz. Chimera states for coupled oscillators. *Phys. Rev. Lett.*, 93:174102, Oct 2004.

[27] Igor S Aranson and Lorenz Kramer. The world of the complex ginzburg-landau equation. *Reviews of Modern Physics*, 74:99–143, 8 2002.

[28] Daniel Walgraef. The hopf bifurcation and related spatio-temporal patterns. In *Spatio-Temporal Pattern Formation*, pages 65–85. Springer, 1997.

[29] S.M. Cox and P.C. Matthews. Exponential time differencing for stiff systems. *Journal of Computational Physics*, 176(2):430–455, 2002.

[30] Gautam C. Sethia, Abhijit Sen, and George L. Johnston. Amplitude-mediated chimera states. *Phys. Rev. E*, 88:042917, Oct 2013.

[31] Lennart Schmidt, Konrad Schönleber, Katharina Krischer, and Vladimir García-Morales. Coexistence of synchrony and incoherence in oscillatory media under nonlinear global coupling. *Chaos: An Interdisciplinary Journal of Nonlinear Science*, 24(1):013102, 2014.

[32] Robert J Silbey, Robert A Alberty, George A Papadantonakis, and Moungi G Bawendi. *Physical chemistry*. John Wiley & Sons, 2022.

[33] Ilya Prigogine. Time, structure, and fluctuations. *Science*, 201(4358):777–785, 1978.

[34] Hong Qian and Daniel A Beard. Thermodynamics of stoichiometric biochemical networks in living systems far from equilibrium. *Biophysical chemistry*, 114(2-3):213–220, 2005.

[35] Martin Feinberg. Foundations of chemical reaction network theory. 2019.

[36] Lars Onsager. Reciprocal relations in irreversible processes. ii. *Phys. Rev.*, 38:2265–2279, Dec 1931.

[37] Sadi Carnot. *Réflexions sur la puissance motrice du feu et sur les machines propres à développer cette puissance*. Bachelier, 1824.

[38] Hermann von Helmholtz. *Über die Erhaltung der Kraft*. G. Reimer, 1847.

[39] William Thomson. On the dynamical theory of heat, with numerical results deduced from mr joule's equivalent of a thermal unit, and m. regnault's observations on steam. *Transactions of the Royal Society of Edinburgh*, 20:261–288, 1851.

[40] William Thomson. On a mechanical theory of thermo-electric currents. *Proceedings of the Royal Society of Edinburgh*, 3:91–98, 1857.

[41] William Thomson. On a universal tendency in nature to the dissipation of mechanical energy. *The London, Edinburgh, and Dublin Philosophical Magazine and Journal of Science*, 4(25):304–306, 1852.

[42] R. Clausius. Ueber ein neues, w rme und arbeit betreffendes theorem. *Annalen der Physik und Chemie*, 169(1):500–505, 1854.

[43] Rudolf Clausius. *The mechanical theory of heat*. Macmillan, 1879.

[44] Rudolf Clausius. Über die anwendung des zweiten hauptsatzes der mechanischen w rmetheorie auf die erscheinungen in der natur. *Annalen der Physik und Chemie*, 193(1):1–27, 1865.

[45] Gibbs J Willard. The scientific papers of j.willard gibbs, vol. 1: Thermodynamics, 1961.

[46] Ludwig Boltzmann. Weitere studien über das wärmegleichgewicht unter gasmolekulen. *Wien. Ber*, 66:275–370, 1872.

[47] Rud Wegscheider. Über simultane gleichgewichte und die beziehungen zwischen thermodynamik und reactionskinetik homogener systeme. *Monatshefte für Chemie und verwandte Teile anderer Wissenschaften*, 32:849–906, 1911.

[48] Theophile De Donder and Pierre Van Rysselberghe. *Thermodynamic theory of affinity*. Stanford university press, 1936.

[49] Lars Onsager. Reciprocal relations in irreversible processes. ii. *Phys. Rev.*, 38:2265–2279, Dec 1931.

[50] Ilya Prigogine. Modération et transformation irréversible des systèmes ouverts. *Bulletin de la Classe des sciences. Académie royale de Belgique*, 31:600–606, 1945.

[51] Ludwig Von Bertalanffy. The theory of open systems in physics and biology. *Science*, 111(2872):23–29, 1950.

[52] Ilya Prigogine. Etude thermodynamique des phénomènes irréversibles. *These d'agregation presentee a la taculte des sciences de I'Universite Libre de Bruxelles 1945*, 1947.

[53] G. Nicolis and I. (Ilya) Prigogine. *Self-organization in nonequilibrium systems : from dissipative structures to order through fluctuations*. Wiley, 1977.

[54] E. A. Milne. The Effect of Collisions on Monochromatic Radiative Equilibrium. *Monthly Notices of the Royal Astronomical Society*, 88(6):493–502, 04 1928.

[55] James Clerk Maxwell. *Theory of Heat*. Longmans, Green, and Company, 1871.

[56] Leo Szilard. Über die entropieverminderung in einem thermodynamischen system bei eingriffen intelligenter wesen. *Zeitschrift für Physik*, 53:840–856, 1929.

[57] L. Brillouin. Maxwell's Demon Cannot Operate: Information and Entropy. I. *Journal of Applied Physics*, 22(3):334–337, March 1951.

[58] R. Landauer. Irreversibility and heat generation in the computing process. *IBM Journal of Research and Development*, 5(3):183–191, 1961.

[59] Charles H Bennett. The thermodynamics of computation—a review. *International Journal of Theoretical Physics*, 21:905–940, 1982.

[60] Takahiro Sagawa and Masahito Ueda. Second law of thermodynamics with discrete quantum feedback control. *Phys. Rev. Lett.*, 100:080403, Feb 2008.

[61] Jun Cao and Andre Feito. Landauer's principle and the second law of thermodynamics. *Physical Review E*, 79(041118):041118, 2009.

[62] H.-H. Hasegawa, J. Ishikawa, K. Takara, and D.J. Driebe. Generalization of the second law for a nonequilibrium initial state. *Physics Letters A*, 374(8):1001–1004, 2010.

[63] M. Esposito and C. Van den Broeck. Second law and landauer principle far from equilibrium. *EPL (Europhysics Letters)*, 95(4):40004, aug 2011.

[64] Dennis Gabor. Theory of communication. part 1: The analysis of information. *Journal of the Institution of Electrical Engineers-Part III: Radio and Communication Engineering*, 93(26):429–441, 1946.

[65] C. E. Shannon. A mathematical theory of communication. *The Bell System Technical Journal*, 27(3):379–423, 1948.

[66] Solomon Kullback and Richard A. Leibler. On information and sufficiency. *Annals of Mathematical Statistics*, 22(1):79–86, 1951.

[67] B. P. Belousov. A periodic reaction and its mechanism. 1959.

[68] A. M. Zhabotinsky. Periodical oxidation of malonic acid in solution (a study of the belousov reaction kinetics). *Biofizika*, 9(3):306–311, 1964.

[69] E. E. SEL'KOV. Self-oscillations in glycolysis 1. a simple kinetic model. *European Journal of Biochemistry*, 4(1):79–86, 1968.

[70] Miklos Orban and Irving R. Epstein. Systematic design of chemical oscillators. part 13. complex periodic and aperiodic oscillation in the chlorite-thiosulfate reaction. *The Journal of Physical Chemistry*, 86(20):3907–3910, 1982.

[71] Irving R. Epstein, Kenneth Kustin, Patrick De Kepper, and Miklós Orbán. Oscillating chemical reactions. *Scientific American*, 248(3):112–123, 1983.

[72] Vincent Castets, Etiennette Dulos, Jacques Boissonade, and Patrick De Kepper. Experimental evidence of a sustained standing turing-type nonequilibrium chemical pattern. *Physical Review Letters*, 64(24):2953, 1990.

[73] L. D. Landau. On the theory of phase transitions. In *Collected Papers of L. D. Landau*. Gordon and Breach, New York, 1937.

[74] Lev D Landau. On the problem of turbulence. In *Dokl. Akad. Nauk USSR*, volume 44, page 311, 1944.

[75] V.L. Ginzburg and L.D. Landau. On the theory of superconductivity. *Zh. Eksp. Teor. Fiz.*, 20(10):1064–1082, 1950.

[76] J. T. Stuart. On the non-linear mechanics of wave disturbances in stable and unstable parallel flows. part 1. the basic behaviour in plane poiseuille flow. *Journal of Fluid Mechanics*, 9(3):353–370, 1960.

[77] A. C. Newell and J. A. Whitehead. Finite bandwidth, finite amplitude convection. *Journal of Fluid Mechanics*, 38(2):279–303, 1969.

[78] L. A. Segel. Distant side-walls cause slow amplitude modulation of cellular convection. *Journal of Fluid Mechanics*, 38(1):203–224, 1969.

[79] A. C. Newell and J. A. Whitehead. Review of the finite bandwidth concept. In H. H. E. Leipholz, editor, *Instability of Continuous Systems*. Springer-Verlag, Berlin, 1971.

[80] J. T. Stewartson, K. & Stuart. A non-linear instability theory for a wave system in plane poiseuille flow. *Journal of Fluid Mechanics*, 48(3):529–545, 1971.

[81] Yoshiki Kuramoto and Toshio Tsuzuki. Persistent Propagation of Concentration Waves in Dissipative Media Far from Thermal Equilibrium. *Progress of Theoretical Physics*, 55(2):356–369, 02 1976.

[82] R. Aris. Prolegomena to the rational analysis of systems of chemical reactions. *Arch. Rational Mech. Anal.*, 19:81–99, 1965.

[83] Fritz Horn and Roy Jackson. General mass action kinetics. *Archive for rational mechanics and analysis*, 47:81–116, 1972.

[84] Martin Feinberg. Complex balancing in general kinetic systems. *Archive for rational mechanics and analysis*, 49(3):187–194, 1972.

[85] Fritz Horn. Necessary and sufficient conditions for complex balancing in chemical kinetics. *Archive for Rational Mechanics and Analysis*, 49:172–186, 1972.

[86] Terrell L. Hill. Studies in irreversible thermodynamics iv. diagrammatic representation of steady state fluxes for unimolecular systems. *Journal of Theoretical Biology*, 10(3):442–459, 1966.

[87] J. Schnakenberg. Network theory of microscopic and macroscopic behavior of master equation systems. *Rev. Mod. Phys.*, 48:571–585, Oct 1976.

[88] Sheldon Katz, Joel L. Lebowitz, and H. Spohn. Phase transitions in stationary nonequilibrium states of model lattice systems. *Phys. Rev. B*, 28:1655–1658, Aug 1983.

[89] N.G. VAN KAMPEN. Chapter v - the master equation. In N.G. VAN KAMPEN, editor, *Stochastic Processes in Physics and Chemistry (Third Edition)*, North-Holland Personal Library, pages 96 – 133. Elsevier, Amsterdam, third edition edition, 2007.

[90] Chung Yuan Mou, Jiu-li Luo, and Gregoire Nicolis. Stochastic thermodynamics of nonequilibrium steady states in chemical reaction systems. *The Journal of Chemical Physics*, 84(12):7011–7017, 06 1986.

[91] K. Sekimoto. *Stochastic Energetics*. Lecture Notes in Physics. Springer Berlin Heidelberg, 2010.

[92] C Van den Broeck. Stochastic thermodynamics. In *Selforganization by Nonlinear Irreversible Processes: Proceedings of the Third International Conference Kühlungsborn, GDR, March 18–22, 1985*, pages 57–61. Springer.

[93] Denis J. Evans, E. G. D. Cohen, and G. P. Morriss. Probability of second law violations in shearing steady states. *Phys. Rev. Lett.*, 71:2401–2404, Oct 1993.

[94] G. Gallavotti and E. G. D. Cohen. Dynamical ensembles in nonequilibrium statistical mechanics. *Phys. Rev. Lett.*, 74:2694–2697, Apr 1995.

[95] Jorge Kurchan. Fluctuation theorem for stochastic dynamics. *Journal of Physics A: Mathematical and General*, 31(16):3719–3729, 1998.

[96] J. L. Lebowitz and H. Spohn. A gallavotti-cohen-type symmetry in the large deviation functional for stochastic dynamics. *Journal of Statistical Physics*, 95:333–365, 1999.

[97] C. Jarzynski. Equilibrium free-energy differences from nonequilibrium measurements: A master-equation approach. *Phys. Rev. E*, 56:5018–5035, Nov 1997.

[98] Gavin E. Crooks. Entropy production fluctuation theorem and the nonequilibrium work relation for free energy differences. *Phys. Rev. E*, 60:2721–2726, Sep 1999.

[99] Tim Schmiedl and Udo Seifert. Stochastic thermodynamics of chemical reaction networks. *The Journal of Chemical Physics*, 126(4):044101, 01 2007.

[100] Udo Seifert. Stochastic thermodynamics, fluctuation theorems and molecular machines. *Reports on Progress in Physics*, 75(12):126001, nov 2012.

[101] Luca Peliti and Simone Pigolotti. *Stochastic Thermodynamics: An Introduction*. Princeton University Press, 2021.

[102] Hong Qian, Signe Kjelstrup, Anatoly B Kolomeisky, and Dick Bedeaux. Entropy production in mesoscopic stochastic thermodynamics: Nonequilibrium kinetic cycles driven by chemical potentials, temperatures, and mechanical forces. *Journal of Physics: Condensed Matter*, 28(15):153004, 2016.

[103] Andre C. Barato and Udo Seifert. Thermodynamic uncertainty relation for biomolecular processes. *Phys. Rev. Lett.*, 114:158101, Apr 2015.

[104] Matteo Polettini and Massimiliano Esposito. Irreversible thermodynamics of open chemical networks. I. Emergent cycles and broken conservation laws. *Journal of Chemical Physics*, 141(2), 2014.

[105] M. Polettini, A. Wachtel, and M. Esposito. Dissipation in noisy chemical networks: The role of deficiency. *The Journal of Chemical Physics*, 143(18):184103, 11 2015.

[106] Riccardo Rao and Massimiliano Esposito. Nonequilibrium thermodynamics of chemical reaction networks: Wisdom from stochastic thermodynamics. *Phys. Rev. X*, 6:041064, Dec 2016.

[107] Gianmaria Falasco, Riccardo Rao, and Massimiliano Esposito. Information Thermodynamics of Turing Patterns. *Physical Review Letters*, 121(10):108301, 2018.

[108] J. J. Hopfield, RL. Peterson, and S. Spiegelman. Kinetic Proofreading: A New Mechanism for Reducing Errors in Biosynthetic Processes Requiring High Specificity. *Proceedings of the National Academy of Sciences*, 71(10):4135–4139, 10 1974.

[109] David Andrieux and Pierre Gaspard. Nonequilibrium generation of information in copolymerization processes. *Proceedings of the National Academy of Sciences of the United States of America*, 105(28):9516–21, 7 2008.

[110] Hong Qian. Open-system nonequilibrium steady state: statistical thermodynamics, fluctuations, and chemical oscillations. *The Journal of Physical Chemistry B*, 110(31):15063–15074, 2006.

[111] Francesco Avanzini, Gianmaria Falasco, and Massimiliano Esposito. Thermodynamics of non-elementary chemical reaction networks. *New Journal of Physics*, 22(9):093040, sep 2020.

[112] Premashis Kumar and Gautam Gangopadhyay. Glycolytic wave patterns in a simple reaction-diffusion system with inhomogeneous influx: Dynamic transitions. *ChemPhysChem*, 24(5):e202200643, 2023.

[113] Steffen Klamt, Utz-Uwe Haus, and Fabian Theis. Hypergraphs and cellular networks. *PLoS computational biology*, 5(5):e1000385, 2009.

[114] Daniel A. Beard, Shou dan Liang, and Hong Qian. Energy balance for analysis of complex metabolic networks. *Biophysical Journal*, 83(1):79–86, 2002.

[115] Riccardo Rao and Massimiliano Esposito. Conservation laws and work fluctuation relations in chemical reaction networks. *The Journal of Chemical Physics*, 149(24):245101, 2018.

[116] Pierre Gaspard. Fluctuation theorem for nonequilibrium reactions. *The Journal of Chemical Physics*, 120(19):8898–8905, 04 2004.

[117] Hong Qian. Open-system nonequilibrium steady state: Statistical thermodynamics, fluctuations, and chemical oscillations. *The Journal of Physical Chemistry B*, 110(31):15063–15074, 2006.

[118] Hong Qian. Phosphorylation energy hypothesis: Open chemical systems and their biological functions. *Annual Review of Physical Chemistry*, 58(1):113–142, 2007.

[119] Robert A. Alberty. *Thermodynamics of Biochemical Reactions*. John Wiley & Sons, Inc., Hoboken, NJ, USA, 2 2003.

[120] H. Haraldsdóttir and R. Fleming. Identification of conserved moieties in metabolic networks by graph theoretical analysis of atom transition networks. *PLoS Computational Biology*, 12, 2016.

[121] Kenneth A Johnson and Roger S Goody. The original michaelis constant: translation of the 1913 michaelis–menten paper. *Biochemistry*, 50(39):8264–8269, 2011.

[122] P. Muller. Glossary of terms used in physical organic chemistry (iupac recommendations 1994). *Pure and Applied Chemistry*, 66(5):1077–1184, 1994.

[123] Alfred J. Lotka. Analytical note on certain rhythmic relations in organic systems. *Proceedings of the National Academy of Sciences*, 6(7):410–415, 1920.

[124] James Dickson Murray. Mathematical biology: I. an introduction. 17, 2002.

[125] Vito Volterra. Fluctuations in the abundance of a species considered mathematically. *Nature*, 118(2972):558–560, 1926.

[126] P. Gray and S.K. Scott. Autocatalytic reactions in the isothermal, continuous stirred tank reactor: Isolas and other forms of multistability. *Chemical Engineering Science*, 38(1):29–43, 1983.

[127] John E. Pearson. Complex patterns in a simple system. *Science*, 261(5118):189–192, 1993.

[128] Jessica M. Chung and Enrique Peacock-López. Bifurcation diagrams and turing patterns in a chemical self-replicating reaction-diffusion system with cross diffusion. *The Journal of Chemical Physics*, 127(17):174903, 2007.

[129] Rebecca Hoyle. *Pattern Formation: An Introduction to Methods*. Cambridge University Press, 2006.

[130] Vladimir K Vanag and Irving R Epstein. Cross-diffusion and pattern formation in reaction–diffusion systems. *Physical Chemistry Chemical Physics*, 11(6):897–912, 2009.

[131] Vladimir K. Vanag, Federico Rossi, Alexander Cherkashin, and Irving R. Epstein. Cross-diffusion in a water-in-oil microemulsion loaded with malonic acid or ferroin. taylor dispersion method for four-component systems. *The Journal of Physical Chemistry B*, 112(30):9058–9070, 2008.

[132] Niraj Kumar and Werner Horsthemke. Effects of cross diffusion on turing bifurcations in two-species reaction-transport systems. *Phys. Rev. E*, 83:036105, Mar 2011.

[133] E. P. Zemskov, K. Kassner, M. J. B. Hauser, and W. Horsthemke. Turing space in reaction-diffusion systems with density-dependent cross diffusion. *Phys. Rev. E*, 87:032906, Mar 2013.

[134] G. Nicolis. *Introduction to nonlinear science*. Cambridge University Press, 1995.

[135] Nikolai Mitrofanovich Krylov and Nikolai Nikolaevich Bogoliubov. *Introduction to non-linear mechanics*. Princeton University Press, 1949.

[136] Iljana Miethe, Vladimir García-Morales, and Katharina Krischer. Irregular subharmonic cluster patterns in an autonomous photoelectrochemical oscillator. *Phys. Rev. Lett.*, 102:194101, May 2009.

[137] Vladimir García-Morales, Alexander Orlov, and Katharina Krischer. Subharmonic phase clusters in the complex ginzburg-landau equation with nonlinear global coupling. *Phys. Rev. E*, 82:065202, Dec 2010.

[138] Lennart Schmidt and Katharina Krischer. Chimeras in globally coupled oscillatory systems: From ensembles of oscillators to spatially continuous media. *Chaos: An Interdisciplinary Journal of Nonlinear Science*, 25(6):064401, 2015.

[139] Sindre W Haugland, L. Schmidt, and K. Krischer. Self-organized alternating chimera states in oscillatory media. *Scientific Reports*, 5, 2015.

[140] S. R. De Groot and Peter Mazur. *Non-equilibrium thermodynamics*. Dover Publications, 1984.

[141] Enrico Fermi. *Thermodynamics*. Dover Publications, 1956.

[142] I Prigogine. *Chemical thermodynamics [by] I. Prigogine and R. Defay.* Longmans, [London], 1954.

[143] Ilya Prigogine. *Introduction to Thermodynamics of Irreversible Processes.* New York: John Wiley, 1962.

[144] T. M. Cover and Joy A. Thomas. *Elements of information theory*. Wiley-India, 1999.

[145] Generalization of the second law for a transition between nonequilibrium states. *Physics Letters A*, 375(2):88–92, 2010.

[146] Francesco Avanzini, Gianmaria Falasco, and Massimiliano Esposito. Thermodynamics of chemical waves. *The Journal of Chemical Physics*, 151(23):234103, 2019.

[147] Qi Ouyang and Harry L Swinney. Transition from a uniform state to hexagonal and striped turing patterns. *Nature*, 352(6336):610, 1991.

[148] Dagmar Iber and Denis Menshykau. The control of branching morphogenesis. *Open biology*, 3(9):130088, 2013.

[149] Simon Kretschmer and Petra Schwille. Pattern formation on membranes and its role in bacterial cell division. *Current opinion in cell biology*, 38:52–59, 2016.

[150] Anatol M Zhabotinsky, Milos Dolnik, and Irving R Epstein. Pattern formation arising from wave instability in a simple reaction-diffusion system. *The Journal of chemical physics*, 103(23):10306–10314, 1995.

[151] Martin Falcke. Reading the patterns in living cells—the physics of ca2+ signaling. *Advances in physics*, 53(3):255–440, 2004.

[152] Kevin Thurley, Alexander Skupin, Rüdiger Thul, and Martin Falcke. Fundamental properties of ca2+ signals. *Biochimica et Biophysica Acta (BBA)-General Subjects*, 1820(8):1185–1194, 2012.

[153] De Wit A, Lima, Dewel, and Borckmans. Spatiotemporal dynamics near a codimension-two point. *Physical review. E, Statistical physics, plasmas, fluids, and related interdisciplinary topics*, 54(1):261–271, 7 1996.

[154] W Just, M Bose, S Bose, H Engel, and E Schöll. Spatiotemporal dynamics near a supercritical turing-hopf bifurcation in a two-dimensional reaction-diffusion system. *Physical Review E*, 64(2):026219, 2001.

[155] Lingfa Yang and Irving R Epstein. Oscillatory turing patterns in reaction-diffusion systems with two coupled layers. *Physical review letters*, 90(17):178303, 2003.

[156] M. R. Ricard and S. Mischler. Turing instabilities at hopf bifurcation. *Journal of Nonlinear Science*, 19(5):467–496, 2009.

[157] Francesco Avanzini, Gianmaria Falasco, and Massimiliano Esposito. Thermodynamics of chemical waves. *The Journal of Chemical Physics*, 151(23):234103, 2019.

[158] Richard J. Field, Endre Koros, and Richard M. Noyes. Oscillations in chemical systems. ii. thorough analysis of temporal oscillation in the bromate-cerium-malonic acid system. *Journal of the American Chemical Society*, 94(25):8649–8664, 1972.

[159] Richard J. Field and Richard M. Noyes. Oscillations in chemical systems. iv. limit cycle behavior in a model of a real chemical reaction. *The Journal of Chemical Physics*, 60(5):1877–1884, 1974.

[160] Zhigui Lin, Ricardo Ruiz-Baier, and Canrong Tian. Finite volume element approximation of an inhomogeneous brusselator model with cross-diffusion. *Journal of Computational Physics*, 256:806 – 823, 2014.

[161] Anastasiya I Lavrova, E B Postnikov, and Yurii M Romanovsky. Brusselator — an abstract chemical reaction? *Physics-Uspekhi*, 52(12):1239, dec 2009.

[162] John William Strutt Rayleigh and Robert Bruce Lindsay. *The theory of sound,*. Dover, 1945.

[163] A. I. Lavrova, L. Schimansky-Geier, and E. B. Postnikov. Phase reversal in the Selkov model with inhomogeneous influx. *Physical Review E - Statistical, Nonlinear, and Soft Matter Physics*, 79(5):1–4, 2009.

[164] Evgeny P. Zemskov, Vladimir K. Vanag, and Irving R. Epstein. Amplitude equations for reaction-diffusion systems with cross diffusion. *Physical Review E - Statistical, Nonlinear, and Soft Matter Physics*, 84(3), 2011.

[165] Federico Rossi, Vladimir K. Vanag, Enzo Tiezzi, and Irving R. Epstein. Quaternary cross-diffusion in water-in-oil microemulsions loaded with a component of the belousov−zhabotinsky reaction. *The Journal of Physical Chemistry B*, 114(24):8140–8146, 2010.

[166] Federico Rossi, Vladimir K. Vanag, and Irving R. Epstein. Pentanary cross-diffusion in water-in-oil microemulsions loaded with two components of the belousov–zhabotinsky reaction. *Chemistry – A European Journal*, 17(7):2138–2145, 2011.

[167] Vladimir K. Vanag and Irving R. Epstein. Segmented spiral waves in a reaction-diffusion system. *Proceedings of the National Academy of Sciences*, 100(25):14635–14638, 2003.

[168] Irving R. Epstein and Vladimir K. Vanag. Complex patterns in reactive microemulsions: Self-organized nanostructures? *Chaos: An Interdisciplinary Journal of Nonlinear Science*, 15(4):047510, 2005.

[169] Premashis Kumar and Gautam Gangopadhyay. Energetic and entropic cost due to overlapping of turing-hopf instabilities in the presence of cross diffusion. *Phys. Rev. E*, 101:042204, Apr 2020.

[170] J.C. Tzou, B.J. Matkowsky, and V.A. Volpert. Interaction of Turing and Hopf modes in the superdiffusive Brusselator model. *Applied Mathematics Letters*, 22(9):1432–1437, 9 2009.

[171] A Boiteux, A Goldbeter, and B Hess. Control of oscillating glycolysis of yeast by stochastic, periodic, and steady source of substrate: a model and experimental study. *Proceedings of the National Academy of Sciences*, 72(10):3829–3833, 1975.

[172] A. Goldbeter. Patterns of spatiotemporal organization in an allosteric enzyme model. *Proceedings of the National Academy of Sciences*, 70(11):3255–3259, 1973.

[173] F. Hynne, S. Danø, and P.G. Sørensen. Full-scale model of glycolysis in saccharomyces cerevisiae. *Biophysical Chemistry*, 94(1):121–163, 2001.

[174] Jana Wolf and Reinhart Heinrich. Effect of cellular interaction on glycolytic oscillations in yeast: a theoretical investigation. *Biochemical Journal*, 345(2):321–334, 2000.

[175] Mads F. Madsen, Sune Danø, and Preben G Sørensen. On the mechanisms of glycolytic oscillations in yeast. *The FEBS Journal*, 272(11):2648–2660, 2005.

[176] Lu Zhang, Qingyu Gao, Qun Wang, and Xing Zhang. *Biophys. Chem.*, 125(1):112–116, 2007.

[177] Thomas Mair, Christian Warnke, and Stefan C Müller. *Faraday Discuss.*, 120:249–259, 2001.

[178] Satenik Bagyan, Thomas Mair, Etiennette Dulos, Jacques Boissonade, Patrick De Kepper, and Stefan C. Müller. Glycolytic oscillations and waves in an open spatial reactor: Impact of feedback regulation of phosphofructokinase. *Biophysical Chemistry*, 116(1):67–76, 2005.

[179] Satenik Bagyan, Thomas Mair, Yuri Suchorski, Marcus J. B. Hauser, and Ronny Straube. Spatial desynchronization of glycolytic waves as revealed by karhunen-loève analysis. *The Journal of Physical Chemistry B*, 112(45):14334–14341, 2008. PMID: 18942874.

[180] A.I. Lavrova, S. Bagyan, T. Mair, M.J.B. Hauser, and L. Schimansky-Geier. Modeling of glycolytic wave propagation in an open spatial reactor with inhomogeneous substrate influx. *Biosystems*, 97(2):127 – 133, 2009.

[181] D. V. Verveyko, A. Yu. Verisokin, and E. B. Postnikov. Mathematical model of chaotic oscillations and oscillatory entrainment in glycolysis originated from periodic substrate supply. *Chaos: An Interdisciplinary Journal of Nonlinear Science*, 27(8):083104, 2017.

[182] Howard R. Petty. Spatiotemporal chemical dynamics in living cells: From information trafficking to cell physiology. *Biosystems*, 83(2):217–224, 2006. 5th International Conference on Systems Biology.

[183] Marcelo Behar and Alexander Hoffmann. Understanding the temporal codes of intra-cellular signals. *Current Opinion in Genetics & Development*, 20(6):684–693, 2010. Genetics of system biology.

[184] Jeremy E. Purvis and Galit Lahav. Encoding and decoding cellular information through signaling dynamics. *Cell*, 152(5):945–956, 2013.

[185] Peter H. Richter, Paul Rehmus, and John Ross. Control and Dissipation in Oscillatory Chemical Engines. *Progress of Theoretical Physics*, 66(2):385–405, 08 1981.

[186] Thomas Brooke Benjamin. Instability of periodic wavetrains in nonlinear dispersive systems. *Proceedings of the Royal Society of London. Series A. Mathematical and Physical Sciences*, 299(1456):59–76, 1967.

[187] Premashis Kumar and Gautam Gangopadhyay. Nonequilibrium thermodynamics of glycolytic traveling wave: Benjamin-feir instability. *Phys. Rev. E*, 104:014221, Jul 2021.

[188] E. B. Postnikov, D. V. Verveyko, and A. Yu. Verisokin. Simple model for temperature control of glycolytic oscillations. *Phys. Rev. E*, 83:062901, Jun 2011.

[189] Thomas Mair, Christian Warnke, Kinko Tsuji, and Stefan C. Müller. Control of glycolytic oscillations by temperature. *Biophysical Journal*, 88(1):639–646, 2005.

[190] Vladimir K. Vanag and Irving R. Epstein. Inwardly rotating spiral waves in a reaction-diffusion system. *Science*, 294(5543):835–837, 2001.

[191] Yunfan Gong and David J. Christini. Antispiral waves in reaction-diffusion systems. *Phys. Rev. Lett.*, 90:088302, Feb 2003.

[192] Teng-Chao Li and Bing-Wei Li. Reversal of spiral waves in an oscillatory system caused by an inhomogeneity. *Chaos: An Interdisciplinary Journal of Nonlinear Science*, 23(3):033130, 2013.

[193] Xin Shao, Yabi Wu, Jinzhong Zhang, Hongli Wang, and Qi Ouyang. Inward propagating chemical waves in a single-phase reaction-diffusion system. *Phys. Rev. Lett.*, 100:198304, May 2008.

[194] G. Gambino, M.C. Lombardo, and M. Sammartino. Pattern formation driven by cross-diffusion in a 2d domain. *Nonlinear Analysis: Real World Applications*, 14(3):1755–1779, 2013.

[195] Jessica M. Chung and Enrique Peacock-López. Bifurcation diagrams and turing patterns in a chemical self-replicating reaction-diffusion system with cross diffusion. *The Journal of Chemical Physics*, 127(17):174903, 2007.

[196] Igal Berenstein and Carsten Beta. Spatiotemporal chaos arising from standing waves in a reaction-diffusion system with cross-diffusion. *The Journal of Chemical Physics*, 136(3):034903, 2012.

[197] Arthur T. Winfree. Biological rhythms and the behavior of populations of coupled oscillators. *Journal of Theoretical Biology*, 16(1):15–42, 1967.

[198] Gautam C. Sethia, Abhijit Sen, and Fatihcan M. Atay. Clustered chimera states in delay-coupled oscillator systems. *Phys. Rev. Lett.*, 100:144102, Apr 2008.

[199] Erik A. Martens, Carlo R. Laing, and Steven H. Strogatz. Solvable model of spiral wave chimeras. *Phys. Rev. Lett.*, 104:044101, Jan 2010.

[200] Adilson E Motter. Spontaneous synchrony breaking. *Nature Physics*, 6(3):164–165, 2010.

[201] Grigory Bordyugov, Arkady Pikovsky, and Michael Rosenblum. Self-emerging and turbulent chimeras in oscillator chains. *Phys. Rev. E*, 82:035205, Sep 2010.

[202] Carlo R. Laing. The dynamics of chimera states in heterogeneous kuramoto networks. *Physica D: Nonlinear Phenomena*, 238(16):1569–1588, 2009.

[203] V. M. Bastidas, I. Omelchenko, A. Zakharova, E. Schöll, and T. Brandes. Quantum signatures of chimera states. *Phys. Rev. E*, 92:062924, Dec 2015.

[204] Nikita Kruk, Yuri Maistrenko, and Heinz Koeppl. Self-propelled chimeras. *Phys. Rev. E*, 98:032219, Sep 2018.

[205] Aaron M Hagerstrom, Thomas E Murphy, Rajarshi Roy, Philipp Hövel, Iryna Omelchenko, and Eckehard Schöll. Experimental observation of chimeras in coupled-map lattices. *Nature Physics*, 8(9):658–661, 2012.

[206] Mark R. Tinsley, Simbarashe Nkomo, and Kenneth Showalter. Chimera and phase-cluster states in populations of coupled chemical oscillators. *Nature Physics*, 8(9):662–665, September 2012.

[207] Erik Andreas Martens, Shashi Thutupalli, Antoine Fourrière, and Oskar Hallatschek. Chimera states in mechanical oscillator networks. *Proceedings of the National Academy of Sciences*, 110(26):10563–10567, 2013.

[208] Fabian Böhm, Anna Zakharova, Eckehard Schöll, and Kathy Lüdge. Amplitude-phase coupling drives chimera states in globally coupled laser networks. *Phys. Rev. E*, 91:040901, Apr 2015.

[209] Laurent Larger, Bogdan Penkovsky, and Yuri Maistrenko. Laser chimeras as a paradigm for multistable patterns in complex systems. *Nature communications*, 6(1):7752, 2015.

[210] Oleh E. Omel'chenko, Yuri L. Maistrenko, and Peter A. Tass. Chimera states: The natural link between coherence and incoherence. *Phys. Rev. Lett.*, 100:044105, Jan 2008.

[211] Iryna Omelchenko, Yuri Maistrenko, Philipp Hövel, and Eckehard Schöll. Loss of coherence in dynamical networks: Spatial chaos and chimera states. *Phys. Rev. Lett.*, 106:234102, Jun 2011.

[212] Lennart Schmidt and Katharina Krischer. Clustering as a prerequisite for chimera states in globally coupled systems. *Phys. Rev. Lett.*, 114:034101, Jan 2015.

[213] Yuanzhao Zhang and Adilson E. Motter. Mechanism for strong chimeras. *Phys. Rev. Lett.*, 126:094101, Mar 2021.

[214] Anna Zakharova, Marie Kapeller, and Eckehard Schöll. Chimera death: Symmetry breaking in dynamical networks. *Phys. Rev. Lett.*, 112:154101, Apr 2014.

[215] Gautam C. Sethia and Abhijit Sen. Chimera states: The existence criteria revisited. *Phys. Rev. Lett.*, 112:144101, Apr 2014.

[216] Carlo R. Laing. Chimeras in networks with purely local coupling. *Phys. Rev. E*, 92:050904, Nov 2015.

[217] Simbarashe Nkomo, Mark R. Tinsley, and Kenneth Showalter. Chimera states in populations of nonlocally coupled chemical oscillators. *Phys. Rev. Lett.*, 110:244102, Jun 2013.

[218] Mahesh Wickramasinghe and István Z Kiss. Spatially organized dynamical states in chemical oscillator networks: Synchronization, dynamical differentiation, and chimera patterns. *PloS one*, 8(11):e80586, 2013.

[219] Simbarashe Nkomo, Mark R. Tinsley, and Kenneth Showalter. Chimera and chimera-like states in populations of nonlocally coupled homogeneous and heterogeneous chemical oscillators. *Chaos: An Interdisciplinary Journal of Nonlinear Science*, 26(9):094826, 2016.

[220] Jan Frederik Totz, Julian Rode, Mark R Tinsley, Kenneth Showalter, and Harald Engel. Spiral wave chimera states in large populations of coupled chemical oscillators. *Nature Physics*, 14(3):282–285, 2018.

[221] VK Vanag, L Yang, M Dolnik, AM Zhabotinsky, and IR Epstein. Oscillatory cluster patterns in a homogeneous chemical system with global feedback. *Nature*, 406(6794):389—391, July 2000.

[222] Vladimir K. Vanag, Anatol M. Zhabotinsky, and Irving R. Epstein. Pattern formation in the belousov-zhabotinsky reaction with photochemical global feedback. *The Journal of Physical Chemistry A*, 104(49):11566–11577, 2000.

[223] Florian Mertens, Ronald Imbihl, and Alexander Mikhailov. Turbulence and standing waves in oscillatory chemical reactions with global coupling. *The Journal of Chemical Physics*, 101(11):9903–9908, 1994.

[224] Lennart Schmidt and Katharina Krischer. Two-cluster solutions in an ensemble of generic limit-cycle oscillators with periodic self-forcing via the mean-field. *Phys. Rev. E*, 90:042911, Oct 2014.

[225] Carlo R. Laing and Carson C. Chow. Stationary bumps in networks of spiking neurons. *Neural Computation*, 13(7):1473–1494, 2001.

[226] Dwight Barkley and Laurette S. Tuckerman. Computational study of turbulent laminar patterns in couette flow. *Phys. Rev. Lett.*, 94:014502, Jan 2005.

[227] Yohann Duguet and Philipp Schlatter. Oblique laminar-turbulent interfaces in plane shear flows. *Phys. Rev. Lett.*, 110:034502, Jan 2013.

[228] N. Rattenborg, C. Amlaner, and S. L. Lima. Behavioral, neurophysiological and evolutionary perspectives on unihemispheric sleep. *Neuroscience & Biobehavioral Reviews*, 24(8):817–842, 2000.

[229] Mark J Panaggio and Daniel M Abrams. Chimera states: coexistence of coherence and incoherence in networks of coupled oscillators. *Nonlinearity*, 28(3):R67–R87, feb 2015.

[230] Naoko Nakagawa and Yoshiki Kuramoto. Collective Chaos in a Population of Globally Coupled Oscillators. *Progress of Theoretical Physics*, 89(2):313–323, 02 1993.

[231] Hugh Shearer Lawson, Gábor Holló, Robert Horvath, Hiroyuki Kitahata, and István Lagzi. Chemical resonance, beats, and frequency locking in forced chemical oscillatory systems. *The Journal of Physical Chemistry Letters*, 11(8):3014–3019, 2020. PMID: 32216274.

[232] P. Welch. The use of fast fourier transform for the estimation of power spectra: A method based on time averaging over short, modified periodograms. *IEEE Transactions on Audio and Electroacoustics*, 15(2):70–73, 1967.

[233] B. J. Gluckman, P. Marcq, J. Bridger, and J. P. Gollub. Time averaging of chaotic spatiotemporal wave patterns. *Phys. Rev. Lett.*, 71:2034–2037, Sep 1993.

[234] Marie Farge. Wavelet transforms and their applications to turbulence. *Annual Review of Fluid Mechanics*, 24(1):395–458, 1992.

[235] John G. Daugman. Uncertainty relation for resolution in space, spatial frequency, and orientation optimized by two-dimensional visual cortical filters. *J. Opt. Soc. Am. A*, 2(7):1160–1169, Jul 1985.

[236] DANIEL M. ABRAMS and STEVEN H. STROGATZ. Chimera states in a ring of nonlocally coupled oscillators. *International Journal of Bifurcation and Chaos*, 16(01):21–37, 2006.

[237] Iryna Omelchenko, Oleh E. Omel'chenko, Philipp Hövel, and Eckehard Schöll. When nonlocal coupling between oscillators becomes stronger: Patched synchrony or multichimera states. *Phys. Rev. Lett.*, 110:224101, May 2013.

[238] Tejas Kotwal, Xin Jiang, and Daniel M. Abrams. Connecting the kuramoto model and the chimera state. *Phys. Rev. Lett.*, 119:264101, Dec 2017.

[239] Felix P. Kemeth, Sindre W. Haugland, Lennart Schmidt, Ioannis G. Kevrekidis, and Katharina Krischer. A classification scheme for chimera states. *Chaos: An Interdisciplinary Journal of Nonlinear Science*, 26(9):094815, 2016.

[240] Fatemeh Parastesh, Sajad Jafari, Hamed Azarnoush, Zahra Shahriari, Zhen Wang, Stefano Boccaletti, and Matjaž Perc. Chimeras. *Physics Reports*, 898:1–114, 2021. Chimeras.

[241] Kanika Bansal, Javier O. Garcia, Steven H. Tompson, Timothy Verstynen, Jean M. Vettel, and Sarah F. Muldoon. Cognitive chimera states in human brain networks. *Science Advances*, 5(4):eaau8535, 2019.

[242] I. Daubechies. The wavelet transform, time-frequency localization and signal analysis. *IEEE Transactions on Information Theory*, 36(5):961–1005, 1990.

[243] Tai Sing Lee. Image representation using 2d gabor wavelets. *IEEE Transactions on Pattern Analysis and Machine Intelligence*, 18(10):959–971, 1996.

[244] John G. Daugman. Two-dimensional spectral analysis of cortical receptive field profiles. *Vision Research*, 20(10):847–856, 1980.

[245] Yuansheng Cao, Hongli Wang, Qi Ouyang, and Yuhai Tu. The free-energy cost of accurate biochemical oscillations. *Nature physics*, 11(9):772–778, 2015.

[246] Lukas Oberreiter, Udo Seifert, and Andre C. Barato. Universal minimal cost of coherent biochemical oscillations. *Phys. Rev. E*, 106:014106, Jul 2022.

[247] N. B. Tufillaro, R. Ramshankar, and J. P. Gollub. Order-disorder transition in capillary ripples. *Phys. Rev. Lett.*, 62:422–425, Jan 1989.

[248] E. Braun, S. Rasenat, and V. Steinberg. Mechanism of transition to a weak turbulence in extended anisotropic systems. *Europhysics Letters*, 15(6):597, jul 1991.

[249] Daniel I. Goldman, M. D. Shattuck, Sung Joon Moon, J. B. Swift, and Harry L. Swinney. Lattice dynamics and melting of a nonequilibrium pattern. *Phys. Rev. Lett.*, 90:104302, Mar 2003.

[250] R. Gopal, V. K. Chandrasekar, A. Venkatesan, and M. Lakshmanan. Observation and characterization of chimera states in coupled dynamical systems with nonlocal coupling. *Phys. Rev. E*, 89:052914, May 2014.

[251] Premashis Kumar and Gautam Gangopadhyay. Nonequilibrium thermodynamic signatures of collective dynamical states around chimera in a chemical reaction network. *Phys. Rev. E*, 108:044218, Oct 2023.

[252] Anna Zakharova. *Chimera Patterns in Networks*. Springer, 2020.

[253] Grégoire Lemoult, Liang Shi, Kerstin Avila, Shreyas V Jalikop, Marc Avila, and Björn Hof. Directed percolation phase transition to sustained turbulence in couette flow. *Nature Physics*, 12(3):254–258, 2016.

[254] Hugues Chaté and Paul Manneville. Transition to turbulence via spatio-temporal intermittency. *Phys. Rev. Lett.*, 58:112–115, Jan 1987.

[255] Kunihiko Kaneko. Spatiotemporal intermittency in coupled map lattices. *Progress of Theoretical Physics*, 74(5):1033–1044, 1985.

[256] Oleh E. Omel'chenko, Matthias Wolfrum, and Yuri L. Maistrenko. Chimera states as chaotic spatiotemporal patterns. *Phys. Rev. E*, 81:065201, Jun 2010.

[257] J. J. Hopfield. Kinetic proofreading: A new mechanism for reducing errors in biosynthetic processes requiring high specificity. *Proceedings of the National Academy of Sciences*, 71(10):4135–4139, 1974.

[258] Jacques Ninio. Kinetic amplification of enzyme discrimination. *Biochimie*, 57(5):587 – 595, 1975.

[259] Kenneth A. Johnson. Conformational coupling in dna polymerase fidelity. *Annual Review of Biochemistry*, 62(1):685–713, 1993. PMID: 7688945.

[260] R.M. Schaaper. Base selection, proofreading, and mismatch repair during dna replication in escherichia coli. *Journal of Biological Chemistry*, 268(32):23762–23765, 1993.

[261] A. Blank, Jonathan A. Gallant, Richard R. Burgess, and Lawrence A. Loeb. An rna polymerase mutant with reduced accuracy of chain elongation. *Biochemistry*, 25(20):5920–5928, 1986. PMID: 3098280.

[262] Jean-Francois Gout, Weiyi Li, Clark Fritsch, Annie Li, Suraiya Haroon, Larry Singh, Ding Hua, Hossein Fazelinia, Zach Smith, Steven Seeholzer, Kelley Thomas, Michael Lynch, and Marc Vermulst. The landscape of transcription errors in eukaryotic cells. *Science Advances*, 3(10), 2017.

[263] Hani S. Zaher and Rachel Green. Fidelity at the molecular level: Lessons from protein synthesis. *Cell*, 136(4):746 – 762, 2009.

[264] Hong Qian. Reducing intrinsic biochemical noise in cells and its thermodynamic limit. *Journal of molecular biology*, 362(3):387–392, 2006.

[265] Hao Ge and Hong Qian. Physical origins of entropy production, free energy dissipation, and their mathematical representations. *Phys. Rev. E*, 81:051133, May 2010.

[266] Arvind Murugan, David A. Huse, and Stanislas Leibler. Speed, dissipation, and error in kinetic proofreading. *Proceedings of the National Academy of Sciences*, 109(30):12034–12039, 2012.

[267] Joel D. Mallory, Anatoly B. Kolomeisky, and Oleg A. Igoshin. Trade-offs between error, speed, noise, and energy dissipation in biological processes with proofreading. *The Journal of Physical Chemistry B*, 123(22):4718–4725, 2019. PMID: 31074999.

[268] Michael A. Savageau and Rolf R. Freter. Energy cost of proofreading to increase fidelity of transfer ribonucleic acid aminoacylation. *Biochemistry*, 18 16:3486–93, 1979.

[269] Pankaj Mehta and David J. Schwab. Energetic costs of cellular computation. *Proceedings of the National Academy of Sciences*, 109(44):17978–17982, 2012.

[270] Francesco Avanzini and Massimiliano Esposito. Thermodynamics of concentration vs flux control in chemical reaction networks. *The Journal of Chemical Physics*, 2021.

[271] Arvind Murugan, David A Huse, and Stanislas Leibler. Discriminatory proofreading regimes in nonequilibrium systems. *Phys. Rev. X*, 4:021016, Apr 2014.

[272] David Hartich, Andre C Barato, and Udo Seifert. Nonequilibrium sensing and its analogy to kinetic proofreading. *New Journal of Physics*, 17(5):055026, may 2015.

[273] Ganhui Lan, Pablo Sartori, Silke Neumann, Victor Sourjik, and Yuhai Tu. The energy-speed-accuracy tradeoff in sensory adaptation. *Nature physics*, 8:422 – 428, 2012.

[274] T W McKeithan. Kinetic proofreading in t-cell receptor signal transduction. *Proceedings of the National Academy of Sciences*, 92(11):5042–5046, 1995.

[275] Pablo Sartori and Simone Pigolotti. Kinetic versus energetic discrimination in biological copying. *Physical review letters*, 110 18:188101, 2013.

[276] Felix Wong, Ariel Amir, and Jeremy Gunawardena. Energy-speed-accuracy relation in complex networks for biological discrimination. *Phys. Rev. E*, 98:012420, Jul 2018.

[277] Kinshuk Banerjee, Anatoly B Kolomeisky, and Oleg A. Igoshin. Accuracy of substrate selection by enzymes is controlled by kinetic discrimination. *The journal of physical chemistry letters*, 8 7:1552–1556, 2017.

[278] Hani S. Zaher and Rachel Green. Hyperaccurate and error-prone ribosomes exploit distinct mechanisms during trna selection. *Molecular Cell*, 39(1):110 – 120, 2010.

[279] Premashis Kumar, Kinshuk Banerjee, and Gautam Gangopadhyay. Interplay of energy, dissipation, and error in kinetic proofreading: Control via concentration and binding energy. *Physica A*, 603:127735, 2022.

[280] William D. Piñeros and Tsvi Tlusty. Kinetic proofreading and the limits of thermodynamic uncertainty. *Phys. Rev. E*, 101:022415, Feb 2020.

[281] Hong Qian and Timothy C. Reluga. Nonequilibrium thermodynamics and nonlinear kinetics in a cellular signaling switch. *Phys. Rev. Lett.*, 94:028101, Jan 2005.

[282] David Yu Zhang and Georg Seelig. Dynamic dna nanotechnology using strand-displacement reactions. *Nature chemistry*, 3(2):103–113, 2011.

[283] Bryan Wei, Mingjie Dai, and Peng Yin. Complex shapes self-assembled from single-stranded dna tiles. *Nature*, 485(7400):623–626, 2012.

[284] T Yamane and J J Hopfield. Experimental evidence for kinetic proofreading in the aminoacylation of trna by synthetase. *Proceedings of the National Academy of Sciences*, 74(6):2246–2250, 1977.

[285] Scott C. Blanchard, Ruben L. Gonzalez, Harold D. Kim, Steven Chu, and Joseph D. Puglisi. trna selection and kinetic proofreading in translation. *Nature Structural &Molecular Biology*, 11:1008–1014, 2004.

[286] Timur Aslyamov, Francesco Avanzini, Étienne Fodor, and Massimiliano Esposito. Nonideal reaction-diffusion systems: Multiple routes to instability. *Phys. Rev. Lett.*, 131:138301, Sep 2023.

[287] Kinshuk Banerjee, Anatoly B. Kolomeisky, and Oleg A. Igoshin. Elucidating interplay of speed and accuracy in biological error correction. *Proceedings of the National Academy of Sciences*, 114(20):5183–5188, 2017.

[288] Vahe Galstyan, Kabir Husain, Fangzhou Xiao, Arvind Murugan, and Rob Phillips. Proofreading through spatial gradients. *eLife*, 9:e60415, dec 2020.

[289] Michael B Elowitz and Stanislas Leibler. A synthetic oscillatory network of transcriptional regulators. *Nature*, 403(6767):335–338, 2000.

[290] Tomer Markovich, Étienne Fodor, Elsen Tjhung, and Michael E. Cates. Thermodynamics of active field theories: Energetic cost of coupling to reservoirs. *Phys. Rev. X*, 11:021057, Jun 2021.